

MÖSSBAUER SPECTROSCOPIC STUDIES OF SOME COBALTATES, GARNETS AND ALUMINIUM-IRON ALLOYS

By

VIRENDRA KUMAR



PHY TH
PHY/1984/D
1984 K 96 m

D

KUM

MOS

DEPARTMENT OF PHYSICS

INDIAN INSTITUTE OF TECHNOLOGY KANPUR

JULY, 1984

MÖSSBAUER SPECTROSCOPIC STUDIES OF SOME COBALTATES, GARNETS AND ALUMINIUM-IRON ALLOYS

A Thesis Submitted
in Partial Fulfilment of the Requirements
for the Degree of

DOCTOR OF PHILOSOPHY

By

VIRENDRA KUMAR

to the

DEPARTMENT OF PHYSICS

INDIAN INSTITUTE OF TECHNOLOGY KANPUR
JULY, 1984

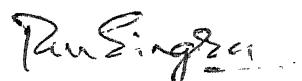
21 DEC 1967
CENTRAL LIBRARY
I / T., Kanbur.

90231
Acc. No. 404.2 001.42 001.42 001.42

PHY-1984-D-KUM-MOS

CERTIFICATE

This is to certify that the work presented in this thesis entitled "'Mössbauer Spectroscopic Studies of Some Cobaltates, Garnets and Aluminium-Iron Alloys'" by Virendra Kumar has been done under my supervision and it has not been submitted elsewhere for a degree or diploma.



R. M. Singru
Professor of Physics
Indian Institute of Technology
KANPUR - 208016, INDIA

July 1984.

ACKNOWLEDGEMENTS

I am deeply grateful to Professor R.M. Singru for his able guidance, invaluable advice and constant encouragement throughout the course of this work.

I wish to express my sincere thanks to Professor T.R. Ramachandran for valuable discussions regarding the planning of the present studies on dilute Al-Fe alloys and for his kind help in interpreting these results.

I am sincerely grateful to Dr. D. Bahadur for helping me at all stages of my research work and particularly for the valuable discussions about the present study of cobaltates and garnets. I wish to thank Dr. D. Bahadur for his help in X-ray diffraction and magnetization measurements.

I wish to thank Professors Y.R. Waghmare, G.K. Mehta and D.C. Khan for their kind help and cooperation.

I take this opportunity to express my thanks to Mr. N. Mohan Rao, Director, Snow and Avalanche Study Establishment for granting me sufficient leave to complete this work. I also thank Col. K.C. Agrawal, Shri N.M. Hariprasad, Shri N. Rangachari and Shri M.V.S. Murty for their encouragement and a keen interest in this work.

I am thankful to Mr. Akhilesh Prasad for useful discussions and for his help in experimental work. Thanks are also due to Mr. R.R. Mishra, Dr. K.R.K. Gandhi and Dr. A.K. Naik who helped me in many ways.

It is impossible to express, through words, my gratitude to my innumerable friends whose association made my stay at Kanpur a memorable event, especially Mr. Atul Sen, Mr. G.S. Raghuvansi and family, Dr. Prem Chand and family, Mr. V.D. Chafekar, Dr. M.B. Patel, Mr. B.P. Singh, Mr. J.P. Singh, Mr. P. Khowash and Miss Anshu Agrawal who really made me feel at home.

Thanks are due to the members of the Central Nuclear Facility for the help provided by them from time to time. In particular I wish to thank Sarvashri K.M.L. Jha, Vishal Saxena, M.M. Gupta, Khalid Masood, A.R. Korde, R.S. Rajput, Ram Nath and Shiv Prakash. I am thankful to Dr. R. Tewari, Computer Centre for his help in my computational work. I thank Mr. L.S. Bajpai for excellent typing, Mr. D. Chakraborty for zeroxing the figures and Mr. H.K. Panda and Mr. L.S. Rathore for cyclostyling the stencils. The timely help received from glass blowing section and physics workshop is gratefully acknowledged.

I express my profound regards to my parents for their constant inspiration. I feel elated in expressing my gratitude to my brothers Dr. S.P. Verma and Mr. Mahendra Pal whose suggestions, help and kind wishes gave me vigour to accomplish this work. I extend my sincere thanks to my brothers, sisters and other family members for their encouragement.

Virendra Kumar

CONTENTS

	<u>Page</u>
LIST OF TABLES	
LIST OF FIGURES	
SYNOPSIS	
CHAPTER 1 : INTRODUCTION	1
1.1 MÖSSBAUER EFFECT	1
1.2 NUCLEAR RESONANCE	1
1.3 HYPERFINE INTERACTIONS	10
1.4 ISOMER SHIFT	11
1.5 SECOND ORDER DOPPLER SHIFT	17
1.6 QUADRUPOLE INTERACTION	20
1.7 MAGNETIC HYPERFINE INTERACTION	24
1.8 COMBINED QUADRUPOLE AND MAGNETIC DIPOLE INTERACTION	28
1.9 GOLDANSKII-KARYAGIN EFFECT	29
1.10 ASYMMETRIC QUADRUPOLE DOUBLET	30
REFERENCES	32
CHAPTER 2 : INSTRUMENTATION AND EXPERIMENTAL METHODS	34
2.1 INTRODUCTION	34
2.2 MÖSSBAUER SPECTROMETER	36
2.3 ELECTRO-MECHANICAL VELOCITY TRANSDUCER	39
2.4 GAMMA-RAY DETECTION AND AMPLIFICATION SYSTEM	39
2.5 MULTICHANNEL ANALYSER	41

	<u>Page</u>
2.6 CRYOSTAT AND FURNACE	43
2.6.1 Cryostat	43
2.6.2 Furnace	45
2.7 MÖSSBAUER SOURCE AND ABSORBER	48
2.7.1 Sources	48
2.7.2 Absorber	50
2.7.3 Absorber Thickness Optimization	51
2.8 GEOMETRY EFFECTS	55
2.8.1 Source-Detector Distance Variation Effect	55
2.8.2 Cosine Smearing Effect	58
2.9 DATA ANALYSIS	58
2.9.1 Hyperfine Field Distribution	60
2.9.2 Computation Method	61
2.10 OTHER MEASUREMENTS	62
REFERENCES	66

CHAPTER 3 :	MÖSSBAUER SPECTROSCOPIC STUDIES OF $\text{LaCo}_{1-x}\text{Ti}_x\text{O}_3$ AND $\text{La}_{1-x}\text{Sr}_x\text{Co}_{1-x}\text{Ti}_x\text{O}_3$ SYSTEMS	68
3.1	INTRODUCTION	68
3.2	EXPERIMENTAL	74
3.2.1	Preparation of Cobaltates	74
3.2.2	Electrical and Magnetic Measurements	75
3.2.3	Mössbauer Studies	78

	<u>Page</u>
3.3 RESULTS AND DISCUSSION	79
3.3.1 System $\text{LaCo}_{1-x}\text{Ti}_x\text{O}_3$	79
3.3.2 System $\text{La}_{1-x}\text{Sr}_x\text{Co}_{1-x}\text{Ti}_x\text{O}_3$	99
3.4 SUMMARY	118
REFERENCES	120
CHAPTER 4 : MÖSSBAUER SPECTROSCOPIC STUDIES OF THE SYSTEM $\text{Y}_{3-x}\text{Gd}_x\text{Fe}_5\text{O}_{12}$ WITH $x = 0, 0.5$ AND 3	122
4.1 INTRODUCTION	122
4.2 EXPERIMENTAL METHODS	126
4.2.1 Sample Preparation	126
4.2.2 Mössbauer Measurements	128
4.2.3 Other Measurements	129
4.3 RESULTS AND DISCUSSION	129
4.3.1 $\text{Y}_{3-x}\text{Gd}_x\text{Fe}_5\text{O}_{12}$ System with $x = 0$	130
4.3.2 $\text{Y}_{3-x}\text{Gd}_x\text{Fe}_5\text{O}_{12}$ System with $x = 0.5$	143
4.3.3 $\text{Y}_{3-x}\text{Gd}_x\text{Fe}_5\text{O}_{12}$ System With $x = 3$	153
4.4 SUMMARY	164
REFERENCES	169
CHAPTER 5 MÖSSBAUER SPECTROSCOPIC STUDIES OF DILUTE ALUMINIUM-IRON ALLOYS	171
5.1 INTRODUCTION	171
5.2 EXPERIMENTAL	176

	<u>Page</u>
5.2.1 Sample Preparation	176
5.2.2 Mössbauer Measurements	176
5.3 RESULTS AND DISCUSSION	177
5.3.1 Mössbauer Studies on Isochronally Annealed Samples	177
5.3.2 Mössbauer Studies of Isothermally Treated Samples	189
5.3.3 <u>In-situ</u> Measurements	189
5.4 SUMMARY	202
REFERENCES	204

LIST OF TABLES

<u>Number</u>	<u>Caption</u>	<u>Page</u>
1.1	Relationship between variables measured using Mössbauer spectroscopy and various research fields (Ref. 1).	2
1.2	Parameters for the 14.4 keV Mössbauer transition in ^{57}Fe .	9
1.3	Approximate ranges of isomer shift observed in iron compounds at room temperature (300 K) with respect to ^{57}Fe [5].	15
3.1	(a) Lattice parameters of $\text{LaCo}_{1-x}\text{Ti}_x\text{O}_3$ and $\text{La}_{1-x}\text{Sr}_x\text{Co}_{1-x}\text{Ti}_x\text{O}_3$ at room temperature. (b) Temperature variation of lattice parameters of $\text{LaCo}_{0.5}\text{Ti}_{0.5}\text{O}_3$ and $\text{La}_{0.5}\text{Sr}_{0.5}\text{Ti}_{0.5}\text{O}_3$ measured using X-ray diffraction technique.	76 77
3.2	Mössbauer parameters for $\text{LaCo}_{1-x}\text{Ti}_x\text{O}_3$ at 295 K (room temperature) measured using PFC absorber.	83
3.3	Temperature variation of isomer shift (measured using ^{57}Fe absorber) for $\text{LaCo}_{1-x}\text{Ti}_x\text{O}_3$.	89
3.4	Observed peak width (FWHM) of resonance lines at various temperature in different compositions of $\text{LaCo}_{1-x}\text{Ti}_x\text{O}_3$.	91
3.5	Temperature variation of percent area of various resonance peaks and total area under resonance observed in $\text{LaCo}_{1-x}\text{Ti}_x\text{O}_3$.	91

<u>Number</u>	<u>Caption</u>	<u>Page</u>
3.6	Temperature variation of relative population of high-spin (Co^{3+} , Co^{2+}) and low-spin ($\text{Co}^{\text{III,II,IV}}$) cobalt ion for $\text{LaCo}_{1-x}\text{Ti}_x\text{O}_3$.	97
3.7	Mössbauer parameters for $\text{La}_{1-x}\text{Sr}_x\text{Co}_{1-x}\text{Ti}_x\text{O}_3$ at 295 K (room temperature) measured using PFC absorber.	103
3.8	Temperature variation of isomer shift in various compositions of $\text{La}_{1-x}\text{Sr}_x\text{Co}_{1-x}\text{Ti}_x\text{O}_3$ measured using ^{57}Fe absorber.	109
3.9	Observed peak width of the resonances at various temperature in different composition of $\text{La}_{1-x}\text{Sr}_x\text{Co}_{1-x}\text{Ti}_x\text{O}_3$.	111
3.10	Temperature variation of area ratio of high-velocity resonance to low-velocity resonance and total area under resonance observed in Mössbauer spectra of $\text{La}_{1-x}\text{Sr}_x\text{Co}_{1-x}\text{Ti}_x\text{O}_3$.	112
3.11	Comparison of properties of (a) LaCoO_3 , (b) $\text{La}_{0.5}\text{Sr}_{0.5}\text{CoO}_3$, (c) $\text{LaCo}_{0.5}\text{Ti}_{0.5}\text{O}_3$, and (d) $\text{La}_{0.5}\text{Sr}_{0.5}\text{Co}_{0.5}\text{Ti}_{0.5}\text{O}_3$ at 500 K.	116
4.1	Details of the $\text{Y}_{3-x}\text{Gd}_x\text{Fe}_5\text{O}_{12}$ samples studied by us.	127
4.2	X-ray data of $\text{Y}_{3-x}\text{Gd}_x\text{Fe}_5\text{O}_{12}$ ($x = 0$).	134
4.3	Mössbauer parameters of $\text{Y}_{3-x}\text{Gd}_x\text{Fe}_5\text{O}_{12}$ ($x = 0$) samples.	137

<u>Number</u>	<u>Caption</u>	<u>Page</u>
4.4	Magnetic moment of $Y_{3-x}Gd_xFe_5O_{12}$ ($x = 0$) samples.	141
4.5	EPR results for $Y_{3-x}Gd_xFe_5O_{12}$ ($x = 0$) samples.	141
4.6	X-ray data for sample $Y_{3-x}Gd_xFe_5O_{12}$ ($x = 0.5$) samples.	145
4.7(a)	Mössbauer parameter of $Y_{3-x}Gd_xFe_5O_{12}$ ($x = 0.5$) samples given heat-treatment as per schedule A.	151
(b)	Mössbauer parameters of $Y_{3-x}Gd_xFe_5O_{12}$ ($x = 0.5$) samples given heat-treatment as per schedule N.	152
4.8	EPR results for $Y_{3-x}Gd_xFe_5O_{12}$ ($x = 0.5$) samples.	156
4.9	X-ray diffraction data for $Y_{3-x}Gd_xFe_5O_{12}$ ($x = 3.0$) samples.	159
4.10	Mössbauer parameter of $Y_{3-x}Gd_xFe_5O_{12}$ ($x = 3$) samples.	161
4.11	EPR results for the $Y_{3-x}Gd_xFe_5O_{12}$ ($x = 3$) samples.	166
5.1	Parameters of defect states and phases of iron in aluminium [7].	174
5.2	Observed amount of various phases present in Al-Fe (5.8 wt %. Fe) as-received sample and in samples heat-treated at various temperature for 1 hour each. These results are based on our Mössbauer measurements.	181

<u>Number</u>	<u>Caption</u>	<u>Page</u>
5.3	Same as Table 5.2 (a) but for Al-Fe (9.94 wt % Fe) samples.	185
5.4 (a)	Observed amounts of various phases in Al-Fe (5.8 wt % Fe) samples annealed at 550 °C for various lengths of time. These results are based on our Mössbauer measurements.	191
(b)	Same as Table 5.3 (a) but for Al-Fe (9.94 wt % Fe) samples.	193
5.5 (a)	Different iron phases present at various temperatures in Al-Fe (5.8 wt % Fe) sample and Mössbauer parameters of $\text{Al}_{13}\text{Fe}_4$ obtained from the analysis of Mössbauer spectra measured in-situ.	196
(b)	Same as Table 5.4 (a) but for Al-Fe (9.94 wt % Fe) samples.	198

LIST OF FIGURES

<u>Number</u>	<u>Caption</u>	<u>Page</u>
1.1	Overlapping of the emission and absorption lines showing the relation between E_o , $E_{\gamma s}$, $E_{\gamma a}$ and for two cases : (a) optical case $E_R \ll \Gamma$ and (b) nuclear case $E_R \gg \Gamma$.	5
1.2	Decay scheme of ^{57}Co .	8
1.3	Mössbauer spectrum showing monopole interaction.	13
1.4	Approximate ranges of isomer shifts (w.r.t. $\alpha\text{-Fe}$) observed in iron compounds. More frequently met configurations are shadowed. S refers to spin quantum number [5].	14
1.5	Review of ^{57}Fe Mössbauer parameters (a) IS (isomer shift) and (b) ΔE (quadrupole splitting) for iron plotted against the coordination number for 'ionic' high spin and low spin compounds and minerals. Arrows indicate that the values outside the range of boxes have been observed [11].	16
1.6	Data for the ^{57}Fe isomer shift with respect to natural iron ($\alpha\text{-Fe}$) at room temperature. Units of the IS values are mm sec^{-1} and the signs of the velocity for the source are to be read from the top row while the signs of the velocity for the absorber are to be read from the bottom row [13].	18

<u>Number</u>	<u>Caption</u>	<u>Page</u>
1.7	Effect of the quadrupole interaction on the nuclear energy levels of source/absorber and the resulting Mössbauer spectrum showing the quadrupole splitting and isomer shift.	23
1.8	Effect of magnetic hyperfine interaction on energy levels of ^{57}Fe . Peak positions of the six-figure pattern are shown at the bottom.	27
1.9	Effect of weak quadrupole interaction and a strong magnetic interaction on the energy levels of ^{57}Fe . The numbers 1 to 6 refer to those in Fig. 1.8.	27
2.1	Schematic block diagram of Mössbauer spectrometer.	35
2.2	Functional block diagram of the Mössbauer spectrometer.	38
2.3	Schematic block diagram of the electromechanical transducer used in the Mössbauer spectrometer.	40
2.4	Pulse height spectrum of ^{57}Co in Rh matrix (Mössbauer source) measured using proportional counter.	42
2.5	Design of the cryostat used in the Mössbauer experiments carried out in temperature range 80–300 K.	44

<u>Number</u>	<u>Caption</u>	<u>Page</u>
2.6	Design of the furnace with resistance heating assembly.	46
2.7	EFG distribution in sodium nitroprusside (absorber) at room temperature. The top figure shows the $(p V)$ distribution while the bottom figure shows the fitted Mössbauer spectrum.	63
2.8	Hyperfine field distribution for α -Fe (absorber) at room temperature. The top figure shows the $p(H)$ distribution while the bottom figure shows the corresponding Mössbauer spectrum of α -Fe.	64
3.1	Plot of $X_g T$ versus temperature (T) for the system $\text{LaCo}_{1-x}\text{Ti}_x\text{O}_3$.	81
3.2	Mössbauer spectra of $\text{LaCo}_{1-x}\text{Ti}_x\text{O}_3$ system recorded at room temperature (295 K) using PFC absorber.	82
3.3	(a) Mössbauer spectra of $\text{LaCo}_{0.5}\text{Ti}_{0.5}\text{O}_3$ recorded at various temperature using 310 stainless steel absorber.	85
	(b) Mössbauer of $\text{LaCo}_{1-x}\text{Ti}_x\text{O}_3$ ($x = 0.3$) recorded at various temperatures using 310 stainless steel absorber.	86
	(c) Mössbauer spectra of $\text{LaCo}_{1-x}\text{Ti}_x\text{O}_3$ ($x = 0.15$) measured at various temperature using 310 stainless steel absorber.	87

<u>Number</u>	<u>Caption</u>	<u>Page</u>
3.3	(d) Mossbauer spectra of $\text{LaCo}_{0.95}\text{Ti}_{0.05}\text{O}_3$ recorded at various temperature using 310 stainless steel absorber.	88
3.4	Temperature variation of isomer shift (IS) observed in $\text{LaCo}_{1-x}\text{Ti}_x\text{O}_3$ using 310 stainless steel absorber.	90
3.5	Spin states of cobalt and consequent iron.	95
3.6	Plot of $\log \rho$ and α versus $1000/T$ for the system $\text{LaCo}_{1-x}\text{Ti}_x\text{O}_3$.	96
3.7	Plot of χ_T against temperature (T) for various compositions of $\text{La}_{1-x}\text{Sr}_x\text{Co}_{1-x}\text{Ti}_x\text{O}_3$.	101
3.8	Mössbauer spectra of $\text{La}_{1-x}\text{Sr}_x\text{Co}_{1-x}\text{Ti}_x\text{O}_3$ system recorded at room temperature (295 K) using PFC absorber.	102
3.9	(a) Mössbauer spectra at $\text{La}_{1-x}\text{Sr}_x\text{Co}_{1-x}\text{Ti}_x\text{O}_3$ ($x = 0.5$) recorded at various temperature using 310 stainless steel absorber.	105
	(b) Mössbauer spectra of $\text{La}_{1-x}\text{Sr}_x\text{Co}_{1-x}\text{Ti}_x\text{O}_3$ ($x = 0.3$) recorded at various temperatures using 310 stainless steel absorber.	106
	(c) Mössbauer spectra of $\text{La}_{1-x}\text{Sr}_x\text{Co}_{1-x}\text{Ti}_x\text{O}_3$ ($x = 0.15$) measured at various temperatures using 310 stainless steel absorber.	107

<u>Number</u>	<u>Caption</u>	<u>Page</u>
3.9	(d) Mössbauer spectra of $\text{La}_{1-x}\text{Sr}_x\text{Co}_{1-x}\text{Ti}_x\text{O}_3$ ($x = 0.05$) measured at various temperatures using 310 stainless steel absorber.	108
3.10	Temperature variation of isomer shift observed in $\text{La}_{1-x}\text{Sr}_x\text{Co}_{1-x}\text{Ti}_x\text{O}_3$ using 310 stainless steel absorber.	110
3.11	Room temperature Mössbauer spectra of (a) LaCoO_3 [7], (b) $\text{La}_{0.5}\text{Sr}_{0.5}\text{CoO}_3$ [15], (c) $\text{La}_{0.5}\text{Sr}_{0.5}\text{Co}_{0.5}\text{Ti}_{0.5}\text{O}_3$ and (d) $\text{LaCo}_{0.5}\text{Ti}_{0.5}\text{O}_3$ recorded using PFC absorber.	117
4.1	(a) X-ray diffractograms of $\text{Y}_{3-x}\text{Gd}_x\text{Fe}_5\text{O}_{12}$ ($x = 0$) samples recorded using CuK_α target with Ni filter.	131
	(b) X-ray diffractograms of $\text{Y}_{3-x}\text{Gd}_x\text{Fe}_5\text{O}_{12}$ ($x = 0$) samples and polycrystalline YIG recorded using CuK_α target with Ni filter.	132
4.2	Mössbauer spectra of $\text{Y}_{3-x}\text{Gd}_x\text{Fe}_5\text{O}_{12}$ ($x = 0$) samples recorded at room temperature (295 K). Peak positions observed for polycrystalline YIG and $\gamma\text{-Fe}_2\text{O}_3$ are also shown.	135
4.3	EFG distribution for $\text{Y}_{3-x}\text{Gd}_x\text{Fe}_5\text{O}_{12}$ ($x = 0$) samples.	136
4.4	Typical EPR spectra for $\text{Y}_{3-x}\text{Gd}_x\text{Fe}_5\text{O}_{12}$ ($x = 0$) samples recorded at RT (295 K) and LNT (78 K).	142

<u>Number</u>	<u>Caption</u>	<u>Page</u>
4.5	X-ray diffractograms of $Y_{3-x}Gd_xFe_5O_{12}$ ($x = 0.5$) samples recorded using CrK_α target.	144
4.6	(a) Mössbauer spectra of $Y_{3-x}Gd_xFe_5O_{12}$ ($x = 0.5$) samples heat treated as per schedule A. Peak positions observed for polycrystalline YIG and $\gamma-Fe_2O_3$ are also shown.	147
	(b) Same as Fig. 4.6 (a), but heat treatment schedule N samples.	148
4.7	EFG distribution for $Y_{3-x}Gd_xFe_5O_{12}$ ($x = 0.5$) samples.	150
4.8	Magnetic moment versus H for $Y_{3-x}Gd_xFe_5O_{12}$ ($x = 0.5$) samples heat treated at 650 and 700 °C.	154
4.9	Typical spectra of $Y_{3-x}Gd_xFe_5O_{12}$ ($x = 0.5$) samples measured at RT (295 K) and LNT (78 K).	155
4.10	X-ray diffractograms of $Y_{3-x}Gd_xFe_5O_{12}$ ($x = 3.0$) samples recorded using CrK_α target.	157
4.11	Mössbauer spectra of $Y_{3-x}Gd_xFe_5O_{12}$ ($x = 3$) samples recorded at room temperature. Peak positions observed for polycrystalline YIG and $\gamma-Fe_2O_3$ are shown at the bottom.	160
4.12	Mössbauer spectra of $Y_{3-x}Gd_xFe_5O_{12}$ ($x = 3$) recorded at liquid nitrogen temperature. Peak positions observed for polycrystalline YIG and $\gamma-Fe_2O_3$ are shown at the bottom.	163

<u>Number</u>	<u>Caption</u>	<u>Page</u>
4.13	Typical EPR spectra of $Y_{3-x}Gd_xFe_5O_{12}$ ($x = 3$) samples recorded at room temperature.	165
4.14	EPR resonance linewidth (ΔH) observed at RT and LNT versus heat-treatment temperature plot for $Y_{3-x}Gd_xFe_5O_{12}$ ($x = 3$) samples.	167
5.1	Aluminium-rich end of the Al-Fe binary phase diagram [7].	173
5.2	Variation of sample temperature with time during <u>in-situ</u> Mössbauer measurements. Mössbauer spectra were recorded in constant temperature regions marked 1-8.	178
5.3	Mössbauer spectra of as-received Al-Fe (5.8 wt %. Fe) sample and of samples annealed at various temperatures for one hour.	180
5.4	Variation of amount of various phases observed in Al-Fe (5.8 wt %. Fe) isochronal annealing as a function of temperature.	182
5.5	Same as Fig. 5.3 but for Al-Fe (9.94 wt %. Fe) samples.	184
5.6	Same as Fig. 5.4 but for Al-Fe (9.94 wt %. Fe) samples.	186

<u>Number</u>	<u>Caption</u>	<u>Page</u>
5.7	Mössbauer spectra of Al-Fe (9.94 wt % Fe) as-received sample and the samples annealed at various temperatures for one hour. The spectra were fitted for presence of various phases including cluster states.	188
5.8(a)	Room temperature Mössbauer spectra of Al-Fe (5.8 wt % Fe) samples annealed at 550 °C for various length of time.	190
(b)	Same as Fig. 5.8 (a) but for Al-Fe (9.94 wt % Fe) samples.	192
5.9(a)	Mossbauer spectra of Al-Fe (5.8 wt % Fe) sample recorded at 20 °C (RT), 100, 200, 300, 400, 500, 550 and 600 °C. The solid lines represents the fits for $Al_{13}Fe_4$ phase.	195
(b)	Same as Fig. 5.9 (a) but for Al-Fe (9.94 wt % Fe) samples.	197
5.10(a)	A typical transmission electron micrograph of as-received Al-Fe (9.94 wt % Fe) alloy.	200
(b)	A typical electron diffraction pattern of as-received Al-Fe (9.94 wt % Fe) alloy.	200
(c)	A single crystal spot pattern of an insoluble observed in as-received Al-Fe (9.94 wt % Fe) alloy.	200

SYNOPSIS

MÖSSBAUER SPECTROSCOPIC STUDIES OF SOME COBALTATES,
GARNETS AND DILUTE ALUMINIUM-IRON ALLOYS

by

VIRENDRA KUMAR

Ph.D.

Department of Physics
Indian Institute of Technology
Kanpur, INDIA

Mössbauer spectroscopy is a highly sensitive technique for studying hyperfine interactions in solids. It provides valuable information about the local environment of the probe atom and various phases present in the solid. Mössbauer spectroscopic techniques have been successfully applied to a wide variety of problems in physics, chemistry, biology, metallurgy and geological sciences etc. In the present work, valence fluctuations in cobaltates, crystallization kinetics of amorphous rare-earth garnets and phase transformation in rapidly solidified aluminium-iron alloys are studied using Mössbauer spectroscopy. Recently substituted garnets and cobaltates are the two classes of materials which have evoked considerable interest because of technological usefulness of these materials. The dilute Al-Fe system has been studied extensively because iron is an important impurity in commercial Al alloys and it has a considerable effect on the properties of Al alloys. The present thesis describes the studies of

substituted rare-earth transition metal cobaltates ($\text{LaCo}_{1-x}\text{Ti}_x\text{O}_3$ and $\text{La}_{1-x}\text{Sr}_x\text{Co}_{1-x}\text{Ti}_x\text{O}_3$ with $x = 0.5, 0.3, 0.15$ and 0.05), amorphous rare-earth garnets ($\text{Y}_{3-x}\text{Gd}_x\text{Fe}_5\text{O}_{12}$ with $x = 0, 0.5$ and 3) and dilute Al-Fe ($\text{Fe} \sim 5\text{-}10 \text{ wt } \%$) alloys.

The thesis is divided into five chapters. In Chapter 1 a brief introduction to Mössbauer effect and hyperfine interactions is given. The origin and usefulness of three important Mössbauer parameters : isomer shift, quadrupole splitting and magnetic hyperfine splitting are discussed. The topics like (a) Goldanskii-Karyagin effect, (b) asymmetric quadrupole doublet are also discussed briefly.

Chapter 2 provides the details of experimental techniques used in the present study. The different aspects of Mössbauer effect methodology like the radioactive source, Mössbauer spectrometer, detector and storage system are discussed in some detail. The experimental considerations for the good quality of Mössbauer spectra such as absorber thickness optimization and effect of geometry are discussed. In the present work the data obtained from Mössbauer spectroscopy were corroborated with the data obtained by other experimental techniques such as X-ray powder diffraction, electron paramagnetic resonance, magnetization and electrical measurement, and transmission electron microscopy. The brief working details of these techniques are given.

In Chapter 3, the experimental results of our studies of spin-state equilibria in substituted perovskite systems

$\text{LaCo}_{1-x}\text{Ti}_x\text{O}_3$ and $\text{La}_{1-x}\text{Sr}_x\text{Co}_{1-x}\text{Ti}_x\text{O}_3$ ($x = 0.5, 0.3, 0.15$ and 0.05) are presented and discussed. The studies were undertaken in the temperature range -195 to 630°C . None of the systems show itinerant electron ferromagnetism which was observed in the parent system $\text{La}_{1-x}\text{Sr}_x\text{CoO}_3$. Both the systems showed a change in behaviour above a critical value of x and temperature. The Co^{2+} state is found to exist in $\text{LaCo}_{1-x}\text{Ti}_x\text{O}_3$ system in addition to Co^{3+} and $\text{Co}^{\text{III,II,IV}}$ states found in both the systems. The results of Mössbauer spectroscopy are in agreement with electron transport and magnetic properties. The results obtained for the two systems are compared and discussed in the light of the known results of parent systems.

In Chapter 4, the results of our studies of crystallization kinetics of amorphous garnet system synthesized through citrate gel process are presented and discussed. The amorphous garnets are very useful because of their special electrical, magnetic and optical properties. In particular, the gadolinium substituted Yttrium Iron Garnet system is found to be very useful. Mössbauer spectroscopy is ideally suited to study various magnetic phases present in these systems. The amorphous garnet system $\text{Y}_{3-x}\text{Gd}_x\text{Fe}_5\text{O}_{12}$ ($x = 0, 0.5$ and 3) in which garnet phase can be crystallized by suitable heat-treatment has been studied by Mössbauer, EPR, X-ray and magnetization measurements. The measurements were made on samples heat-treated at various temperatures in atmosphere of nitrogen and/or air. The

crystallization temperature for $Y_{3-x}Gd_xFe_5O_{12}$ system has been found to be around 650, 600, 550 °C for $x = 0, 0.5$ and 3 respectively. The Mössbauer spectra of sample heat-treated below the crystallization temperature consist of broad quadrupole split peaks characteristic of amorphous paramagnetic nature of these samples. From IS and ΔE values it is inferred that Fe^{3+} exist in both octahedral and tetrahedral coordinations. The Mössbauer spectra of samples heated above the crystallization temperature consist of magnetically split components due to crystallization and magnetic ordering of $\alpha-Fe_2O_3$, $\gamma-Fe_2O_3$ and garnet phase. The volume fraction of garnet phase is found to increase in samples heat-treated at higher temperature and for longer duration. The heat-treatment in nitrogen atmosphere is more favourable than in air for development of garnet phase. In EPR spectra recorded at RT (20 °C) and at LNT (-195 °C) we observe resonance corresponding to $g = 2$ resonance which arises due to $Fe^{3+} - Fe^{3+}$ interaction. In some of the $x = 3$ sample resonance corresponding to $g = 4.3$ is also observed. EPR line-width also shows a different behaviour for these samples, indicative of some kind of transition in these samples. EPR line-width is found to decrease with higher heat-treatment temperature which indicates crystallization of magnetic phases. In $x = 3$ system, Mössbauer spectrum does not show the same amount of garnet phase as observed in X-ray data. The reason of this may be the presence

of large amount of $\alpha\text{-Fe}_2\text{O}_3$ and $\gamma\text{-Fe}_2\text{O}_3$ in this system which might smear out the hyperfine field due to garnet phase. Secondly the compensation temperature of GdIG is around room temperature therefore the garnet phase may be in a disordered state in this system. Both these reasons account for the observed behaviour.

In Chapter 5, the results of Mössbauer spectroscopic studies of rapidly solidified Al-Fe alloys ($\text{Fe} \sim 5\text{-}10 \text{ wt } \%$) are presented. The Al-Fe system especially the dilute one, has been the subject of great research interest. Mössbauer parameters for various phases established by earlier investigators form a good basis for the study of phase transformations in this system. The measurements were made on samples heat-treated at various temperatures for one hour and for different times at 550°C . In-situ measurements were also made in the temperature range, RT (20°C) to (600°C). The amount of various phases, present in the sample after the heat-treatment, is estimated from the analysis of Mössbauer spectra. The results obtained by Mössbauer spectroscopy are compared with those of transmission electron microscopy.

It is hoped that the present work has contributed to a better understanding of the valence fluctuations in cobaltates, crystallization kinetics of amorphous rare-earth garnets and phase transformation in dilute Al-Fe alloys.

CHAPTER 1

1.1 INTRODUCTION

Recoilless nuclear absorption and emission of gamma radiation is known as Mössbauer effect after its discoverer R.L. Mössbauer [1]. The great potential of Mössbauer spectroscopy for the study of hyperfine interactions in solids was immediately realised by scientists all over the world and Mössbauer was awarded Nobel prize in 1962 for this very useful discovery. Large number of excellent books and review articles have been published on Mössbauer effect [2-10]. Mössbauer spectroscopic techniques have been applied for investigation of wide variety of problems in solid state physics, chemistry, metallurgy, biology, geology etc., as shown in Table 1.1 [2].

In this chapter we shall briefly discuss the Mössbauer effect and describe how various types of hyperfine interactions are reflected in the Mössbauer spectrum and what useful information can be extracted from the study of hyperfine interactions.

1.2 NUCLEAR RESONANCE

Let us consider a free atomic or nuclear system of mass M which has two levels, A and B separated by an energy E_0 . If the system decays from the higher state B to the lower state A

Table 1.1 Relationship between Variables Measured Using Mössbauer Spectroscopy and Various Research Fields (Ref. 1).

Measured variable	Nuclear physics	Solid state physics	Chemistry	Metallurgy	Biology	Analytical
Isomer shift	Nuclear radius change	Electronic structure	Valence state and covalency	Electronic structure	Valence change	
Magnetic hyperfine structure		Magnetic structure, electronic configuration of magnetic ions	Electronic configuration of magnetic ions		Chemical or phase identification by comparison with spectra of known materials	
	Nuclear moments			Order-disorder, precipitate identification	Ligand conformation	
Electric quadrupole hyperfine structure		Electronic configuration	Ligand symmetry, bonding orbitals			Particle size information via superparamagnetism
Recoil-free fraction		Phonon spectrum anisotropic binding	Anisotropic binding	Force constants and anharmonic binding	Free or bound complex	

by emission of a photon of energy $E_{\gamma s}$, the momentum conservation demands that the momentum \vec{p} of the photon and the momentum \vec{P} of the recoiling system should be equal and opposite. Hence the recoiling system receives an energy E_R , given by

$$E_R = \frac{p^2}{2M} = \frac{P^2}{2M} = \frac{E_{\gamma s}^2}{2Mc^2} \quad (1.1)$$

where c is velocity of light.

In case $Mc^2 \gg E_0$ equation (1.1) reduces to

$$E_R = \frac{E_0^2}{2Mc^2} \quad (1.2)$$

The energy conservation gives

$$E_{\gamma s} = E_0 - E_R \quad (1.3)$$

Similarly in order to excite the absorber system from state A to state B the energy $E_{\gamma a}$ of incoming photon should be able to supply this recoil energy E_R over and above the transition energy E_0 i.e.

$$E_{\gamma a} = E_0 + E_R \quad (1.4)$$

It is known that the excited state is not characterised by a single energy E_0 but has a spectral lineshape $\omega(E)$ centered around E_0 , and is given by

$$\omega(E) = \frac{1}{1 + \frac{4(E - E_0)^2}{\Gamma^2}} \quad (1.5)$$

where Γ is the natural linewidth of the state and is restricted by Heisenberg's uncertainty relation

$$\Gamma \cdot \tau = \frac{h}{2\pi} \quad (1.6)$$

where τ is the mean lifetime of the state and h is Planck's constant.

As seen from (1.6) energy of stable ground state A is sharply defined as $\tau = \infty$. Hence a photon emitted in the transition from state B to state A, shows the natural line-shape similar to (1.5) but centered around $E_{\gamma s}$ given by (1.3). Similarly the energy of a photon which would induce transition from state A to state B also has a similar distribution centered around $E_{\gamma a}$ given by (1.4). The resonant absorption would take place when $E_{\gamma s} = E_{\gamma a}$ and therefore it is proportional to the amount of overlap of these two distributions $\omega_s(E)$ and $\omega_a(E)$ given by

$$\begin{aligned} \omega_s(E) &= \frac{1}{1 + \frac{4(E - E_{\gamma s})^2}{\Gamma^2}} \quad \text{and} \\ \omega_a(E) &= \frac{1}{1 + \frac{4(E - E_{\gamma a})^2}{\Gamma^2}} \end{aligned} \quad (1.7)$$

This overlap is schematically shown in Fig. 1.1(a) for atomic system (optical case) and in Fig. 1.1(b) for nuclear system (gamma-ray case). In the case of nuclear system the overlap is very small due to narrow linewidth and high recoil energy

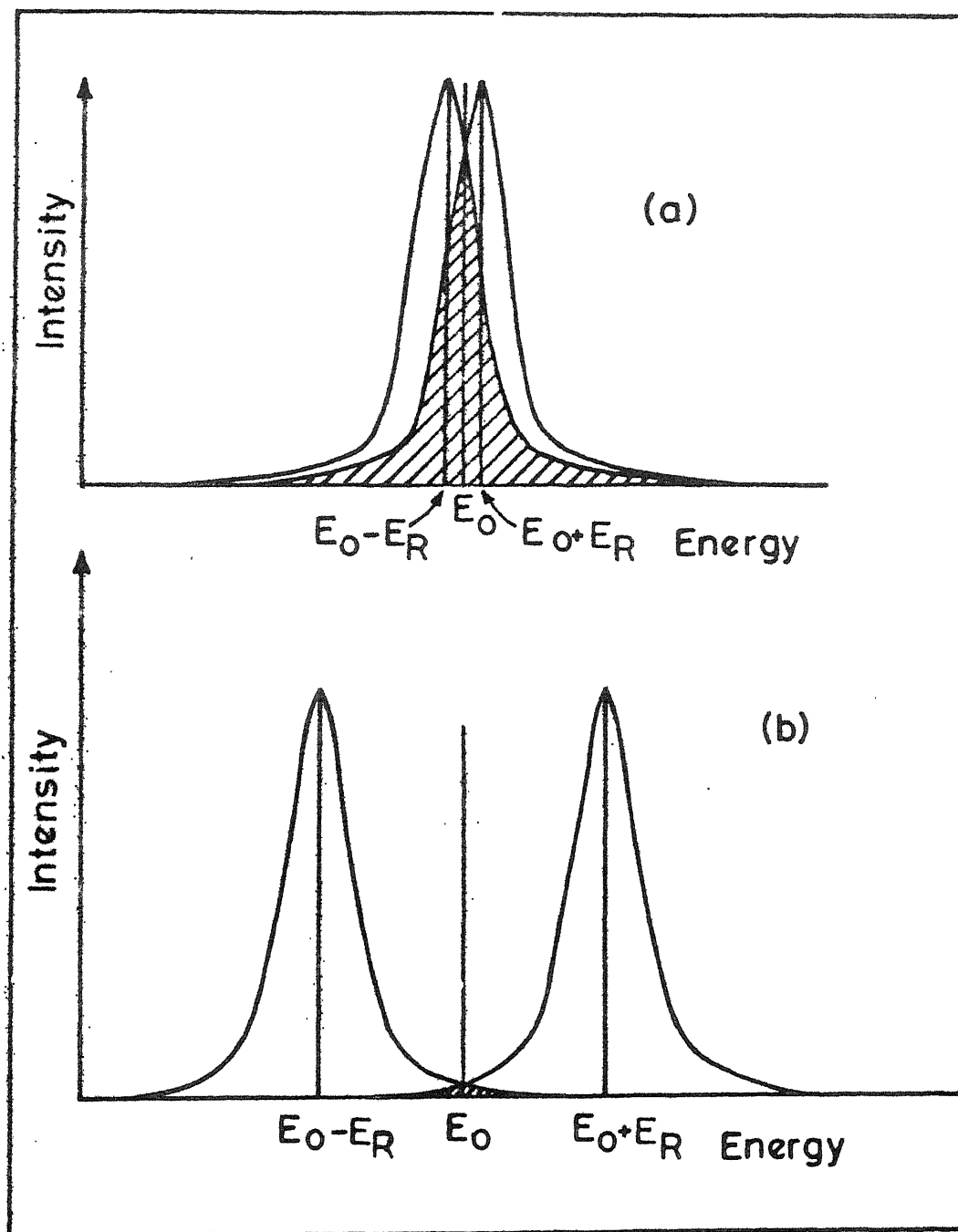


Fig. 1.1 Overlapping of the emission and absorption lines showing the relation between E_0 , E_{γ_s} , E_{γ_a} and for two cases: (a) optical case $E_R \ll \Gamma$ and (b) nuclear case $E_R \gg \Gamma$.

E_R . While in the optical case the overlap is quite large.

Mössbauer's principal discovery was that if the emitting and absorbing nuclei are bound tight enough into a solid lattice, the overlap of emission and absorption spectrum could be increased significantly, and hence the efficiency of resonant absorption could be appreciably increased. In classical terms this means that the recoil energy E_R given by equation (1.1) is decreased by a factor of $\sim 10^{21}$, as now mass M stands for the mass of the whole lattice. In quantum mechanical terms, it means that the probability for observing the zero-phonon events (i.e. where there is no transfer of energy to or from the lattice) has been increased over one-phonon, two-phonon and more-phonon events.

The probability of zero-phonon events, or more popularly known as recoil-free fraction f , is given by

$$f = \left| \int \Psi_n^*(\vec{r}) \Psi_n(\vec{r}) \exp(-i\vec{k}\cdot\vec{r}) d\vec{r} \right|^2 \quad (1.8)$$

where Ψ_n represents the vibrational state of the lattice, the initial and final state being same in case of recoilless emission and absorption, \vec{k} is the wave vector of the gamma ray and \vec{r} is the position vector of the centre of mass of the nucleus under investigation. Under the assumption of harmonic vibrations the probability f is given by

$$f = \exp[-k^2 \langle x^2 \rangle] \quad (1.9)$$

$$\text{or } f = \exp\left[-\frac{\hbar^2 k^2}{2M} \int_0^\infty \frac{g(\omega)}{\hbar\omega} \cot(\hbar\omega/2kT) d\omega\right] \quad (1.10)$$

where $\langle x^2 \rangle$ is the mean square displacement of the nucleus and $g(\omega)$ is the normalised density of photon state of angular frequency ω .

In Debye model the frequency distribution function is

$$\begin{aligned} g(\omega) &= \text{Constant} \cdot \omega^2 & \text{for } 0 \leq \omega \leq \omega_{\max} \\ &= 0 & \omega \geq \omega_{\max} \end{aligned} \quad (1.11)$$

and the expression (1.10) for recoil-free fraction reduces to

$$f = \exp\left[-\frac{6E_R}{K\theta_D} \left\{ \frac{1}{4} + \left(\frac{T}{\theta_D}\right)^2 \int_0^{\theta_D/T} \frac{x dx}{e^x - 1} \right\}\right] \quad (1.12)$$

for $T = 0 \text{ K}$

$$f = \exp(-3E_R/2K \theta_D) \quad (1.13)$$

For observation of Mössbauer effect, f must be large.

One nucleus in which Mössbauer effect is often observed is ^{57}Fe and in the present study we have used only ^{57}Fe Mössbauer transition. Decay scheme of ^{57}Co is shown in Fig. 1.2 and some useful data about this transition are shown in Table 1.2.

Nuclear resonance has been observed in several elements of periodic table. In Mössbauer experiment either the source or the absorber is subjected to a velocity programme to give an appropriate Doppler energy shift ($E_D = E_\gamma v/c$), so that one

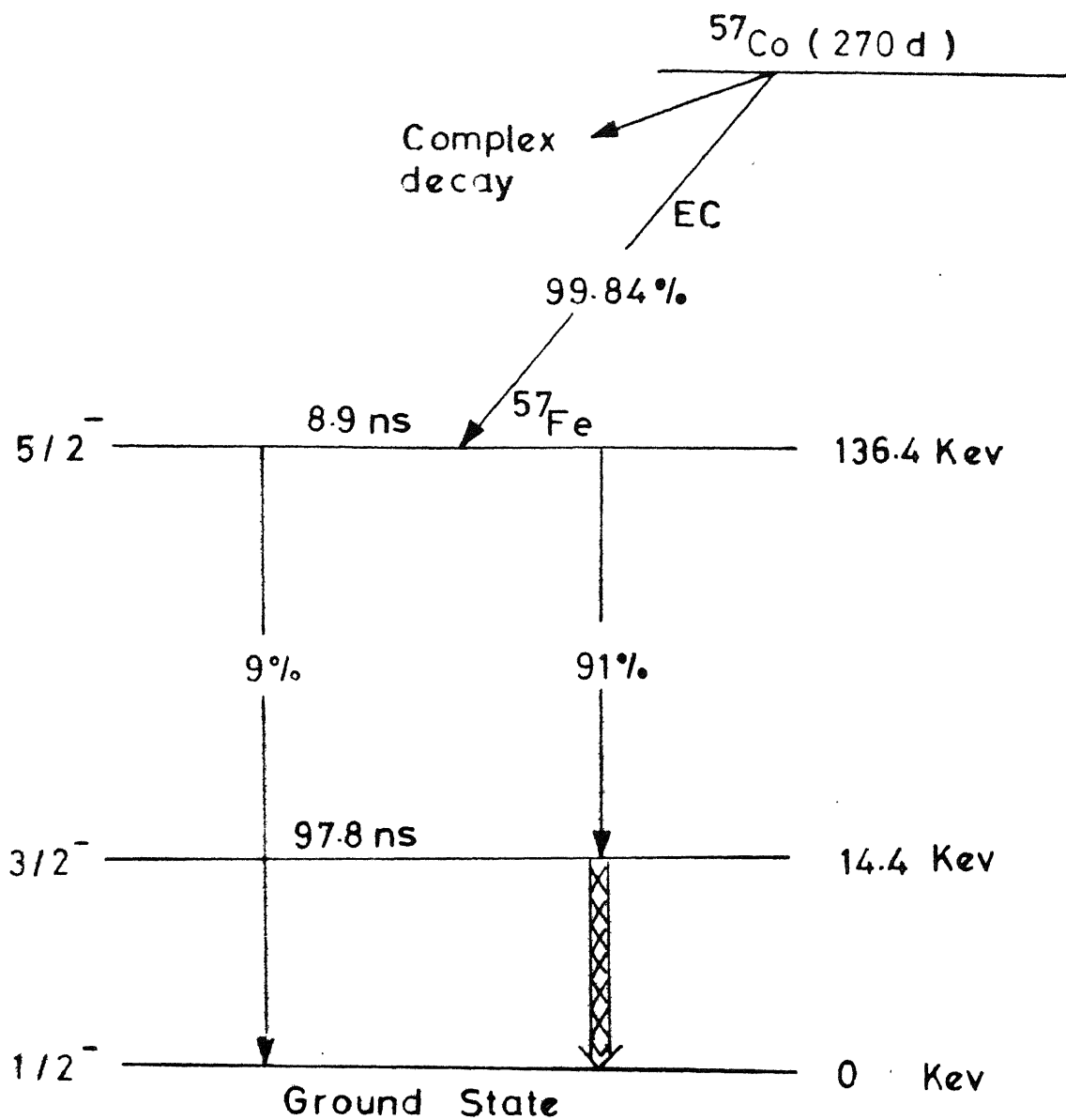


Fig.1.2 Decay scheme of ^{57}Co .

Table 1.2 Parameters for the 14.4 keV Mössbauer transition
in ^{57}Fe .

Sr. No.	Parameter		Value
1	Isotopic abundance		2.14%
2	Transition energy	E_{γ}	14.41303 keV
3	Half life	$t_{1/2}$	97.81 ns
4	Ratio of the excited and ground state nuclear magnetic moment	R_{μ}	-1.7145
5	Nuclear magnetic dipole moment of excited state	μ	-0.15534 nm
6	Nuclear electric quadrupole moment of the excited state	Q	0.209 barns
7	Total internal conversion coefficient	α_T	8.21
8	Debye temperature	θ_D	440 K
9	Mössbauer cross section	σ	$256 \times 10^{-20} \text{ cm}^{-2}$
10	Mössbauer line width (theoretical FWHM)	Γ	$0.1940 \text{ mm sec}^{-1}$
11	Recoil energy	E_R	$1.957 \times 10^{-3} \text{ eV}$
12	Conversion factor (mm/sec-Hz)		1 mm/sec = 11.6248 MHz

may obtain the resonance intensity as a function of energy (i.e. velocity).

The resolution of Mössbauer spectrum depends upon the natural linewidth Γ and strength of hyperfine interaction. In the following sections we shall discuss the hyperfine interactions.

1.3 HYPERFINE INTERACTIONS

Nuclei when embedded in a solid interact with electric and magnetic field produced by the surrounding charges and currents. These interactions, known as hyperfine interactions, perturb nuclear energy levels. The Hamiltonian of the system may be written as

$$\mathcal{H} = \mathcal{H}_0 + E_0 + M_1 + E_2 + \text{higher order terms} \quad (1.14)$$

where

- \mathcal{H}_0 : the Hamiltonian excluding hyperfine interactions
- E_0 : electric monopole interaction between the nucleus and surrounding electrons
- M_1 : magnetic dipole interaction between the nuclear magnetic dipole moment and the surrounding extra nuclear magnetic field
- E_2 : electric quadrupole interaction between the nuclear electric quadrupole moment and the electric field gradient of the surrounding electrons.

Interactions of higher order (M_3 , E_4 etc.) are negligible and **may** not be resolved in a Mössbauer spectrum. Electric monopole interaction changes the energy separation between ground and excited state of the nucleus (e.g. ^{57}Fe). Depending on the chemical state of compound containing ^{57}Fe , this change will be different for **absorber** and source causing a shift in the Mössbauer line commonly known as isomer shift or chemical shift.

The electric quadrupole and magnetic interactions give rise to multiple line Mössbauer spectra. The peak position and intensity of these lines provide valuable information about the sample under investigation.

1.4 ISOMER SHIFT

Isomer shift (IS) is one of the important Mössbauer parameters and it is a measure of difference between the Mössbauer transition energy in the source and that in the absorber when both of them are at the same temperature. It arises due to electric monopole interaction of the electrons with the finite-sized nucleus and is given by [4]

$$\delta = \frac{2\pi}{5} Z e^2 [|\Psi_s(0)|_A^2 - |\Psi_s(0)|_S^2] [\langle r_e^2 \rangle - \langle r_g^2 \rangle]$$

(1.15)

where suffixes A and S refer to the absorber and the source respectively, $\Psi_s(0)$ is the s-electron density at the site

of the nucleus and $\langle r_e^2 \rangle$ and $\langle r_g^2 \rangle$ are the mean-squared nuclear charge radii in the excited and ground state respectively (Fig. 1.3).

The shift δ given by (1.15) is known as isomer shift and has been discussed in several reviews [2-11]. Some important applications of isomer shift measurements are

- (i) Oxidation or valence state of iron in a solid can be determined from the examination of the measured isomer shift as it lies in a range depending upon the oxidation state of iron. The range of isomer shift for different valence state of iron is shown in Fig. 1.4 and in Table 1.3 [5].
- (ii) Co-ordination number of iron can also be determined from isomer shift data. Fig. 1.5(a) shows the plot of ^{57}Fe isomer shift against the iron co-ordination number for high spin and low spin compounds and minerals. The arrow marks on the boxes indicate that values outside the range shown (boxed areas) have also been observed. Similar data for quadrupole splitting are shown in Fig. 1.5(b) [12].
- (iii) Valuable information about structural or chemical phase transitions can also be obtained from the temperature dependence of isomer shift.

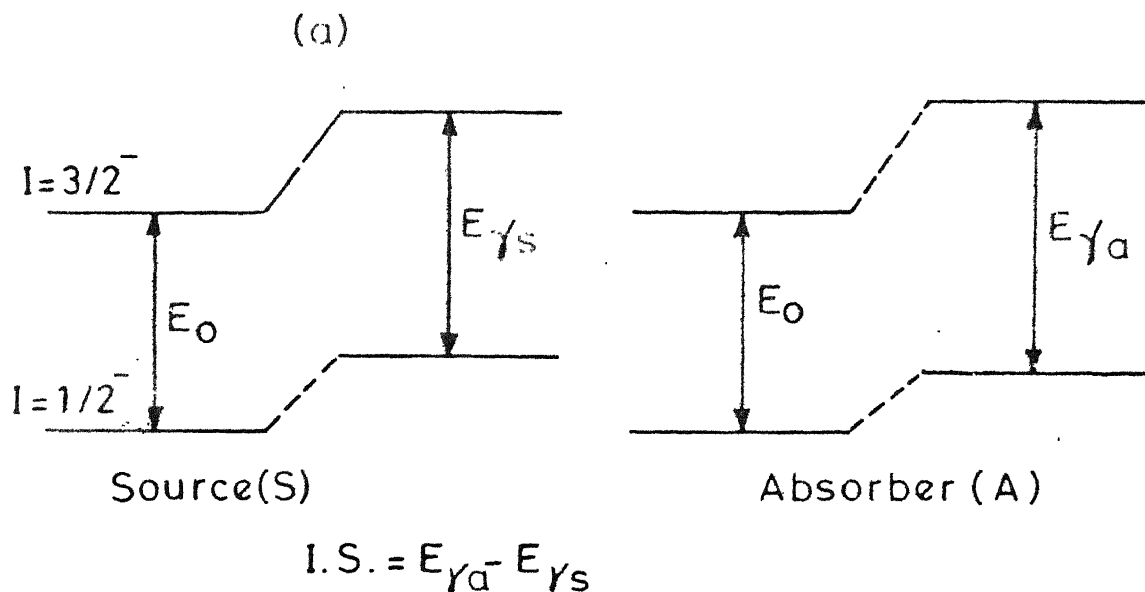


Fig.1.3 - Effect of monopole interaction on the energy levels of source and absorber.

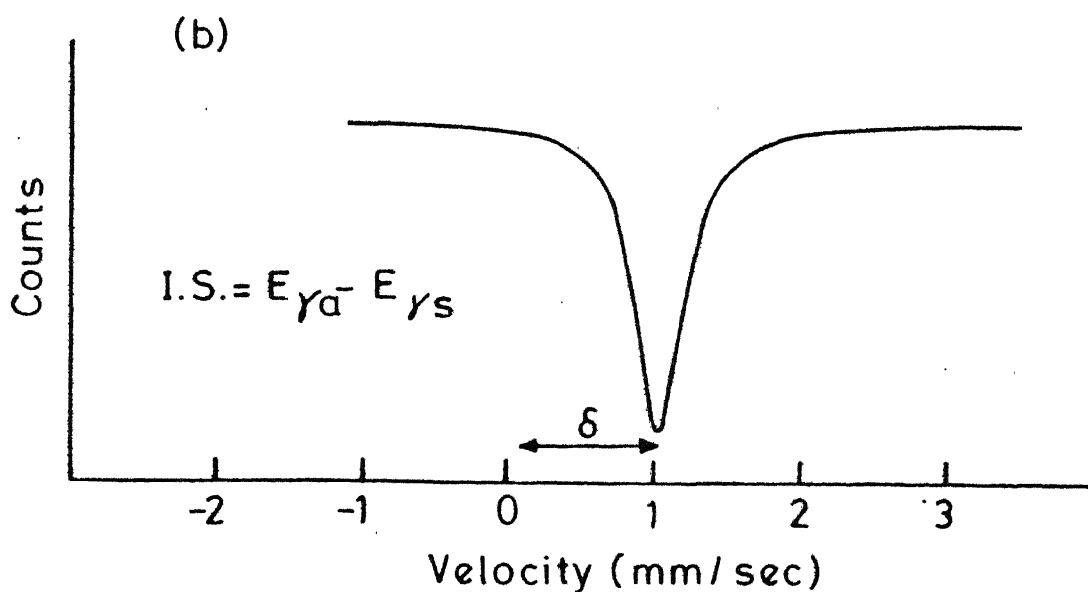


Fig.1.3 - Mössbauer spectrum showing monopole interaction.

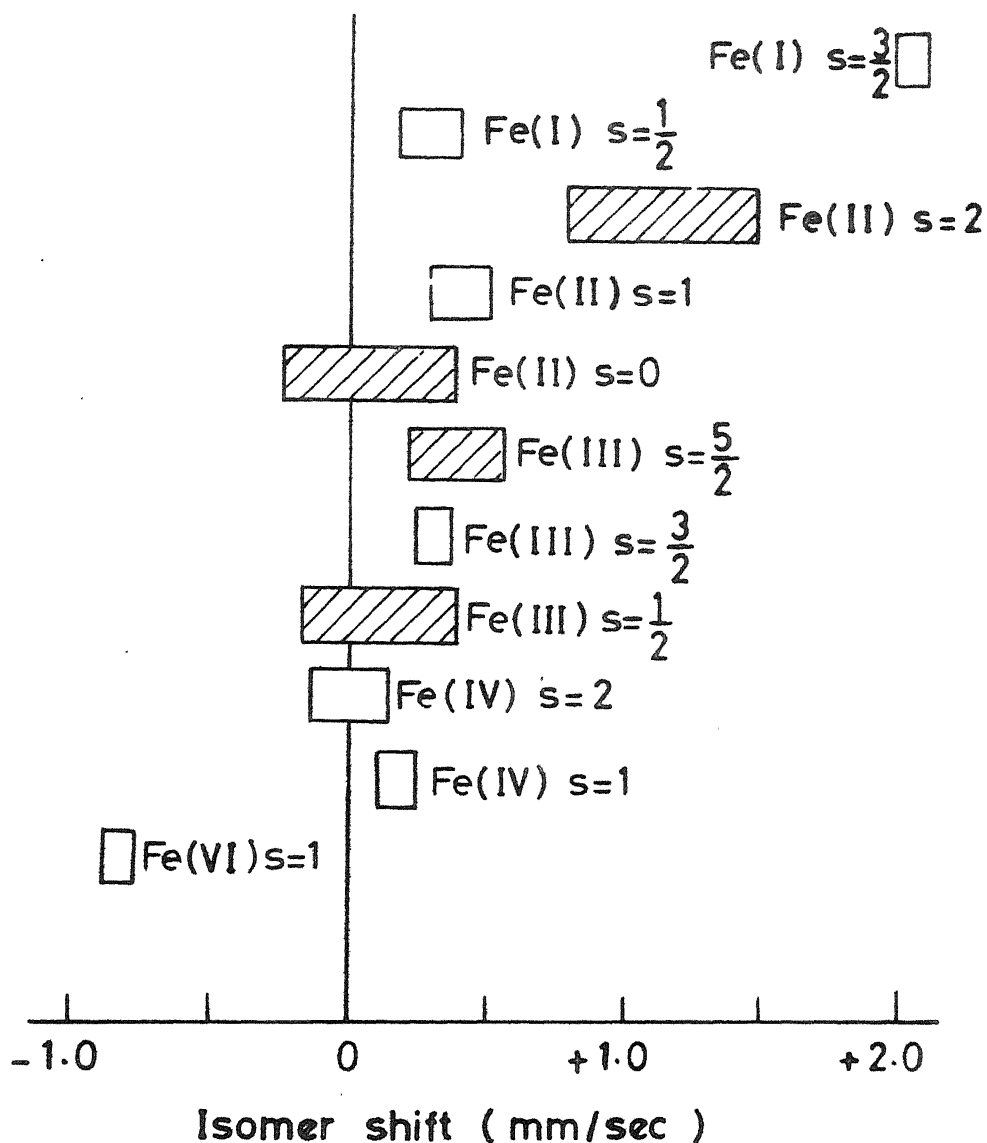


Fig.1.4 Approximate ranges of isomer shifts (w.r.t. α -Fe) observed in iron compounds. More frequently met configurations are shadowed. s refers to spin quantum number [5].

Table 1.3 Approximate ranges of isomer shift observed in iron compounds at room temperature (300 K) with respect to ^{57}Fe SS [5].

Iron state	Spin S	Isomer shift (mm/sec)
Fe^{1+}	3/2	1.90 - 2.02
Fe^{2+}	2	0.65 - 1.45
Fe^{3+}	5/2	0.10 - 0.51
Fe^{4+}	2	-0.23 - 0.07
Fe^{I}	1/2	0.04 - 0.27
Fe^{II}	1	0.21 - 0.43
Fe^{II}	0	-0.34 - 0.31
Fe^{III}	1/2	-0.26 - 0.27
Fe^{III}	3/2	0.12 - 0.26
Fe^{IV}	1	0.01 - 0.27
Fe^{VI}	1	-0.98 - -0.88

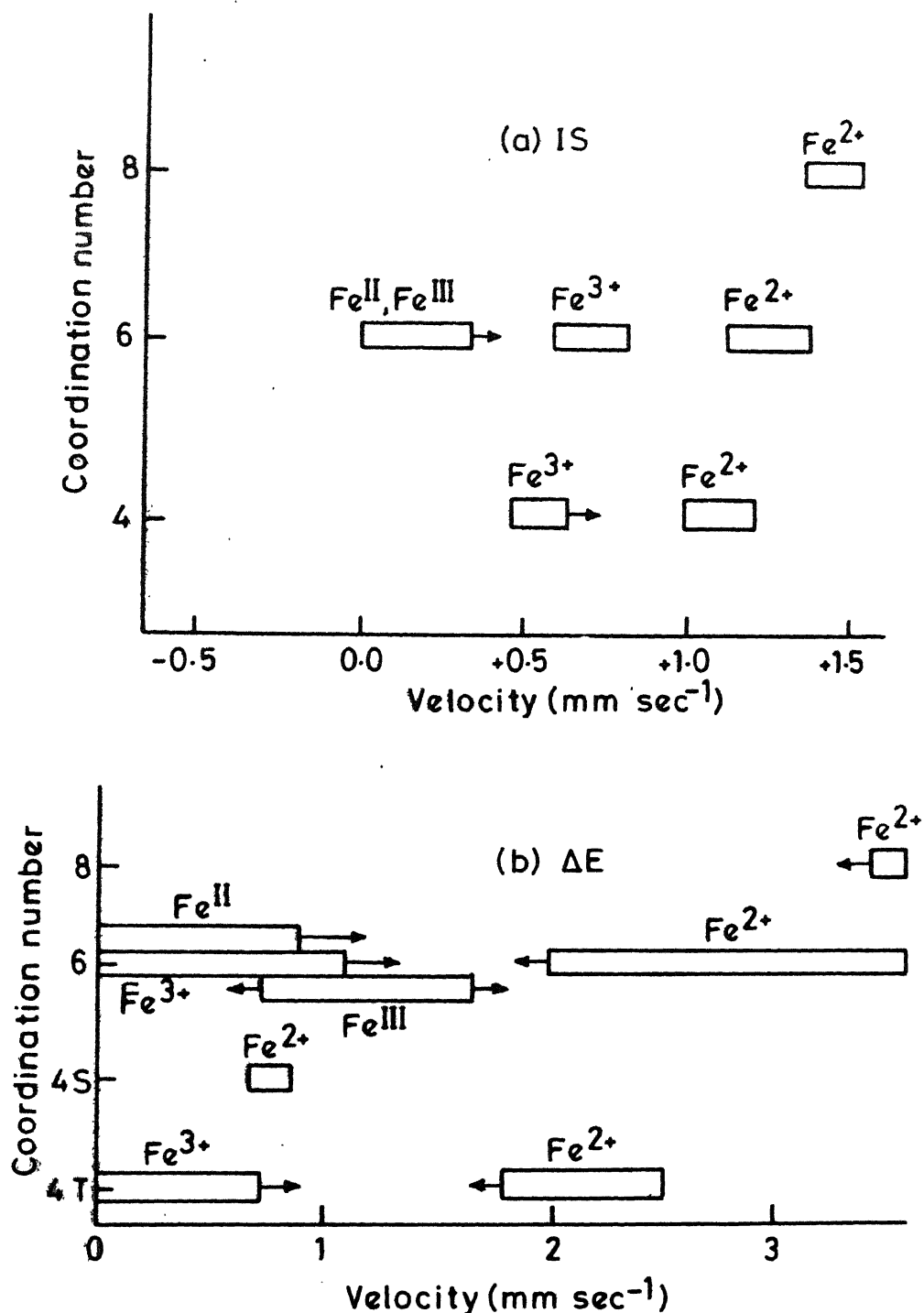


Fig.1.5 Review of ^{57}Fe Mössbauer parameters (a) IS (isomer shift) and (b) ΔE (quadrupole splitting) for iron plotted against the coordination number for 'ionic' high spin and low spin compounds and minerals. Arrows indicate that the values outside the range of boxes have been observed [12].

Different authors quote their results for the isomer shift relative to different sources or to different absorber. In order to have a universal comparison of isomer shift values obtained by different workers, it is necessary to have a ^{57}Fe isomer shift scale of sources and absorbers as shown in Fig. 1.6.

1.5 SECOND ORDER DOPPLER SHIFT

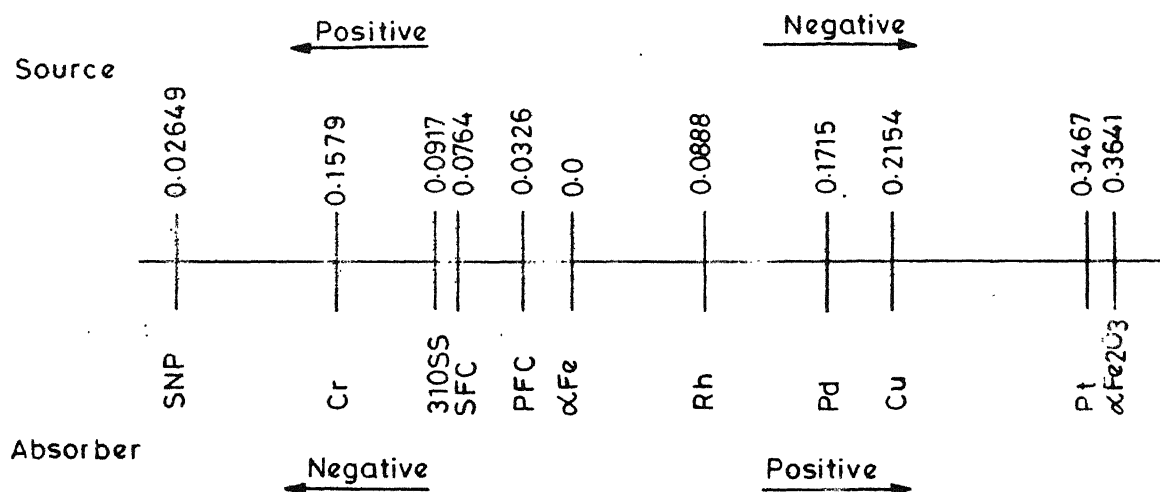
When there is a temperature difference between source and absorber then isomer shift has an additional contribution due to temperature shift known as second order Doppler (SOD) shift. The SOD shift should be separated from isomer shift to obtain true isomer shift.

$$\delta_{\text{total}} = \delta_{\text{IS}} + \delta_{\text{SODS}} \quad (1.16)$$

Isomer shift (δ_{IS}) has an explicit temperature dependence since the thermal expansion of solid affects the electronic charge density at the nucleus. In high temperature region isomer shift at temperature T can be expressed as

$$\delta_{\text{IS}}(T) = \delta_{\text{IS}}(0) + \alpha T \quad (1.17)$$

where $\delta_{\text{IS}}(T)$ is the isomer shift at T K. The coefficient α can be determined from the pressure dependence of isomer shift, the coefficient of thermal expansion and the bulk



SNP = $\text{Na}_2\text{Fe}(\text{CN})_5\text{NO} \cdot 2\text{H}_2\text{O}$

SFC = $\text{Na}_4\text{Fe}(\text{CN})_6 \cdot 10\text{H}_2\text{O}$

PFC = $\text{K}_4\text{Fe}(\text{CN})_6 \cdot 3\text{H}_2\text{O}$

SS = Stainless steel

Fig.1-6 Data for the ^{57}Fe isomer shift with respect to natural iron (α -Fe) at room temperature. Units of the IS values are mm sec^{-1} and the signs of the velocity for the source are to be read from the top row while the sign of the velocity for the absorber are to be read from the bottom row [13].

modules [14].

The second order Doppler shift results from relativistic effect of thermal vibrational velocity of the nuclei. The SOD shift is given by

$$\delta_{\text{SODS}} = -\frac{1}{2} (\langle v^2 \rangle / c^2) E_0 \quad (1.18)$$

where $\langle v^2 \rangle$ is the component of mean square velocity of the emitting or absorbing nuclei in the gamma-ray direction.

Using Debye model of solids SODS can be written as [16]

$$\delta_{\text{SODS}} = \frac{9}{2} \frac{kT}{Mc} \left[\frac{1}{8} + \left(\frac{T}{\theta_D} \right)^3 \int_0^{\theta_D/T} \frac{x^3}{e^x - 1} dx \right] \quad (1.19)$$

or

$$\delta_{\text{SODS}} = -\frac{3kT}{2Mc^2} \left[1 + \frac{1}{20} \left(\frac{\theta_D}{T} \right)^2 \right] \quad \text{for } T \gg \theta_D$$

and

$$\delta_{\text{SODS}} = -\frac{9}{16} \frac{k\theta_D}{Mc} \left[1 + \frac{8\pi^4}{15} \left(\frac{T}{\theta_D} \right)^4 \right] \quad \text{for } T \ll \theta_D \quad (1.20)$$

At temperature higher than Debye temperature (for ^{57}Fe $\theta_D = 440$ K) SODS is -0.073 mm/sec/100 K for ^{57}Fe . At temperature much lower than Debye temperature of lattice the shift becomes vanishingly small and depends on the relationship between temperature and the Debye temperature. Hence while interpreting temperature dependent isomer shift data, contribution due to SODS should be taken into account.

1.6 QUADRUPOLE INTERACTION

In section 1.4 we considered electrostatic interaction between nuclear and electronic charge distribution on the nuclear energy levels assuming nucleus to be spherical with uniform charge density. A nucleus with spin $> \frac{1}{2}$ has a non-spherical charge distribution, and it has a quadrupole moment Q , given by

$$Q = \frac{1}{e} \int \rho(\vec{r}) r^2 (3 \cos^2 \theta - 1) d\vec{r} \quad (1.21)$$

where e is the charge of the proton, $\rho(\vec{r})$ is the charge density in a volume element $d\vec{r}$, which is at a distance r from the centre of nucleus and making an angle θ to the nuclear spin quantization axis.

Electronic charge distribution surrounding the nucleus is generally non-spherical and can be represented in terms of electric field gradient (EFG), given by

$$\begin{aligned} \text{EFG} &= \vec{\nabla} E \\ &= - \vec{\nabla} (\vec{\nabla} V) \end{aligned} \quad (1.22)$$

i.e. EFG is a 3×3 second rank tensor. ij^{th} component of EFG can be written as

$$V_{ij} = - \frac{\partial^2 V}{\partial x_i \partial x_j} \quad (1.23)$$

where $x_i, x_j = x, y, z$ and V is the electrostatic potential.

In the principal axis system EFG is diagonal and can be completely specified by three diagonal terms, V_{XX} , V_{YY} and V_{ZZ} ordered as

$$|V_{ZZ}| \geq |V_{YY}| \geq |V_{XX}| \quad (1.24)$$

The diagonal terms are related by Laplace equation, i.e.

$$V_{ZZ} + V_{YY} + V_{XX} = 0 \quad (1.25)$$

Using relation (1.25), we can express EFG in principal axis system in terms of two independent parameters $V_{ZZ} = eq$, and asymmetry parameter η defined as

$$\eta = \frac{V_{YY} - V_{XX}}{V_{ZZ}} \quad (1.26)$$

whose value lies between zero and one i.e. $0 < \eta < 1$.

Nuclear quadrupole moment interacts with the EFG. The Hamiltonian describing the interaction can be written as

$$\mathcal{H}_{E_2} = \frac{e^2 q Q}{4I(2I-1)} [3I_z^2 - I(I+1) + \frac{\eta}{2} (I_+^2 + I_-^2)] \quad (1.27)$$

where I is the nuclear spin operator and $I_{\pm} = I_x \pm iI_y$ are ladder operators. If the separation of nuclear energy levels is much larger than the magnitude \mathcal{H}_{E_2} , then to a good approximation the quadrupole interaction can be treated as a perturbation. The perturbation calculations require only the matrix elements of the form $\langle \text{Im}_I | \mathcal{H}_{E_2} | \text{Im}_I \rangle$, which are diagonal in

all quantum numbers except m_I . Performing first order perturbation calculation, the eigenvalues of H_{E2} can be written as

$$E_{Q2} = \frac{eq V_{ZZ}}{4I(2I-1)} [3m_I^2 - I(I+1)] (1 + \frac{\eta^2}{3})^{1/2} \quad (1.28)$$

where $m_I = I, (I-1), \dots, -I$ and it is the magnetic quantum number.

In case of ^{57}Fe , Mössbauer transition is from $I_e = 3/2$ to $I_g = 1/2$ level. The higher level splits into two levels as a result of quadrupole interaction while the $I_g = 1/2$ level remains unsplit. Selection rule ($\Delta m_I = \pm 1, 0$) allows both the transitions. This results in a two-line Mössbauer spectrum as shown in Fig. 1.7 with quadrupole splitting

$$QS = \frac{1}{2} e^2 q Q (1 + \frac{\eta^2}{3})^{1/2} \quad (1.29)$$

For axially symmetric EFG (i.e. $\eta = 0$), the matrix of the Hamiltonian is diagonal in $|Im\rangle$ representation and energy shift in nuclear energy levels given by Eq. (1.28) reduces to

$$\frac{e^2 q Q}{4I(2I-1)} [3m_I^2 - I(I+1)] \quad (1.30)$$

For ^{57}Fe it is

$$\begin{aligned} &+ \frac{e^2 q Q}{4} && \text{for } m_I = \pm 3/2 \\ &- \frac{e^2 q Q}{4} && \text{for } m_I = \pm 1/2 \end{aligned}$$

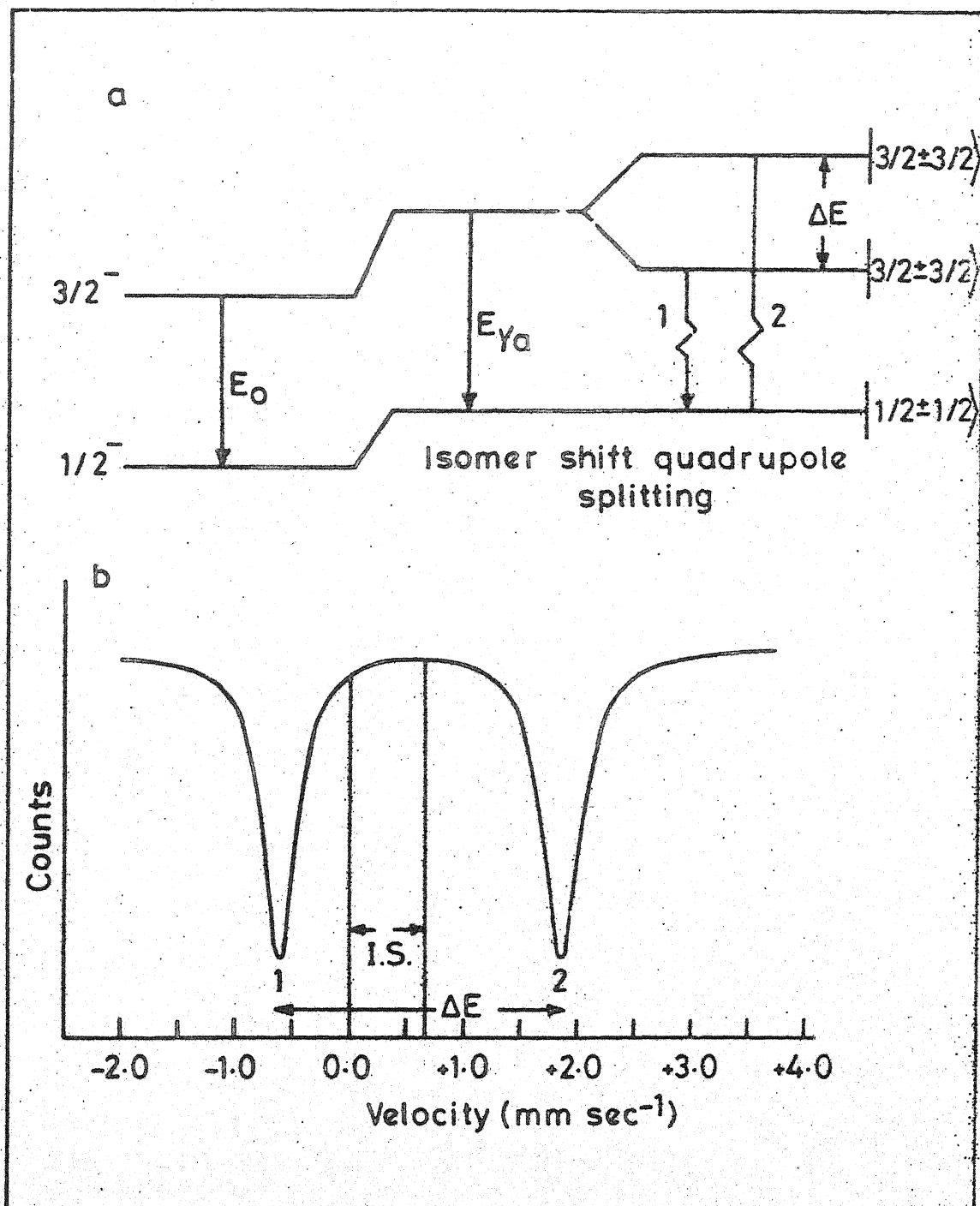


Fig.1.7 Effect of the quadrupole interaction on the nuclear energy levels of source/absorber and the resulting Mössbauer spectrum showing the quadrupole splitting and isomer shift.

Thus the Mössbauer spectrum results in a symmetric doublet with a separation $e^2_q Q/2$.

In case of asymmetric EFG (i.e. $\eta \neq 0$) the matrix of Hamiltonian also contains off-diagonal terms with $\Delta m_I = \pm 2$. The secular equation is generally not solvable exactly and is solved using numerical approximation methods.

Analysis of quadrupole splitting values determine from Mössbauer spectrum can provide useful information about the sample under investigation. One can determine valence state of Mössbauer atom, its coordination number etc. in the solids. A study of temperature variation of quadrupole splitting can be used to investigate temperature induced structural or chemical phase changes.

1.7 MAGNETIC HYPERFINE INTERACTION

A nucleus with nuclear spin $I > 0$ has a magnetic dipole moment $\vec{\mu}$, given by

$$\vec{\mu} = g_N \beta_N \vec{I} \quad (1.31)$$

where g_N is nuclear Landau splitting factor and $\beta_N = \frac{eh}{2M_N C}$ is nuclear Bohr magneton.

The magnetic dipole moment can interact with a magnetic field \vec{H} present at the nuclear site. The interaction Hamiltonian ($H_{MI} = -\vec{\mu} \cdot \vec{H}$) is diagonal in $|I m_I\rangle$ representation. As the magnitude of interaction Hamiltonian

H_{MI} is small compared to separation of nuclear energy levels, it can be treated as a perturbation. Using first order perturbation, the change in the energy of state $|Im_I\rangle$ is given by

$$E_{MI} = - \frac{\mu_B}{I} m_I \quad (1.32)$$

Thus the magnetic dipole interaction splits a nuclear state $|Im_I\rangle$ into $(2I+1)$ equally spaced sub-states having magnetic spin quantum number $m_I = I, (I-1), \dots, -I$. The m_I degeneracy is completely lifted in magnetic dipole interaction while electric quadrupole interaction removes the m_I degeneracy only partially.

For ^{57}Fe $I_e = 3/2 \rightarrow I_g = 1/2$ transition the line splits into six lines as a result of magnetic dipole interaction. Relative intensity of each of the transition lines is decided by the m_I values involved and the relative angle θ between the quantization axis and the gamma-ray direction. For ^{57}Fe relative intensities of six lines are in the ratio [4]

$$\left(\frac{3}{2} \frac{3}{2} \rightarrow \frac{1}{2} \frac{1}{2}\right) : \left(\frac{3}{2} \frac{1}{2} \rightarrow \frac{1}{2} \frac{1}{2}\right) : \left(\frac{3}{2} \frac{1}{2} \rightarrow \frac{1}{2} -\frac{1}{2}\right) : \left(\frac{3}{2} -\frac{1}{2} \rightarrow \frac{1}{2} \frac{1}{2}\right) : \left(\frac{3}{2} -\frac{1}{2} \rightarrow \frac{1}{2} -\frac{1}{2}\right) : \left(\frac{3}{2} -\frac{3}{2} \rightarrow \frac{1}{2} -\frac{1}{2}\right) = 3:2:1:1:2:3 \quad (1.33)$$

$$\text{where} \quad Z = \frac{4}{1 + \cos^2 \theta} \quad (1.34)$$

For polycrystalline sample all orientations are equally probable so averaging over θ gives $Z = 2$.

One of the important application of Mössbauer hyperfine splitting is for the calibration of the Mössbauer spectrometer. Mössbauer spectrum of natural iron (α -Fe) recorded at room temperature consists of six lines (as shown in Fig. 1.8) at positions -5.328, -3.083, -0.838, +0.838, +3.083, +5.328 (mm/sec) with respect to ^{57}Fe source.

Effective magnetic field H_{int} for a given sample can be determined by Mössbauer spectroscopy using following equations [4]

$$E_{\left(\frac{3}{2} \frac{1}{2} \rightarrow \frac{1}{2} \frac{1}{2}\right)} - E_{\left(\frac{3}{2} \frac{1}{2} \rightarrow \frac{1}{2} -\frac{1}{2}\right)} = \frac{E_0}{c} [V_{\left(\frac{3}{2} \frac{1}{2} \rightarrow \frac{1}{2} \frac{1}{2}\right)} - V_{\left(\frac{3}{2} \frac{1}{2} \rightarrow \frac{1}{2} -\frac{1}{2}\right)}] = \mu_g^H (3/2) \quad (1.35)$$

and

$$E_{\left(\frac{3}{2} \frac{3}{2} \rightarrow \frac{1}{2} \frac{1}{2}\right)} - E_{\left(\frac{3}{2} \frac{1}{2} \rightarrow \frac{1}{2} \frac{1}{2}\right)} = \frac{E_0}{c} [V_{\left(\frac{3}{2} \frac{3}{2} \rightarrow \frac{1}{2} \frac{1}{2}\right)} - V_{\left(\frac{3}{2} \frac{1}{2} \rightarrow \frac{1}{2} \frac{1}{2}\right)}] = \mu_e^H (3/2) \quad (1.36)$$

where E_0 represents the energy state of corresponding level.

The value of H from Eq. (1.35) and Eq. (1.36) can be obtained if the values of nuclear magnetic moment in ground state μ_g and excited state μ_e are known.

The value of μ_g obtained by Ludwig and Woodbury [14] by NMR technique is 0.0903 ± 0.0007 nm. Using value of μ_g and

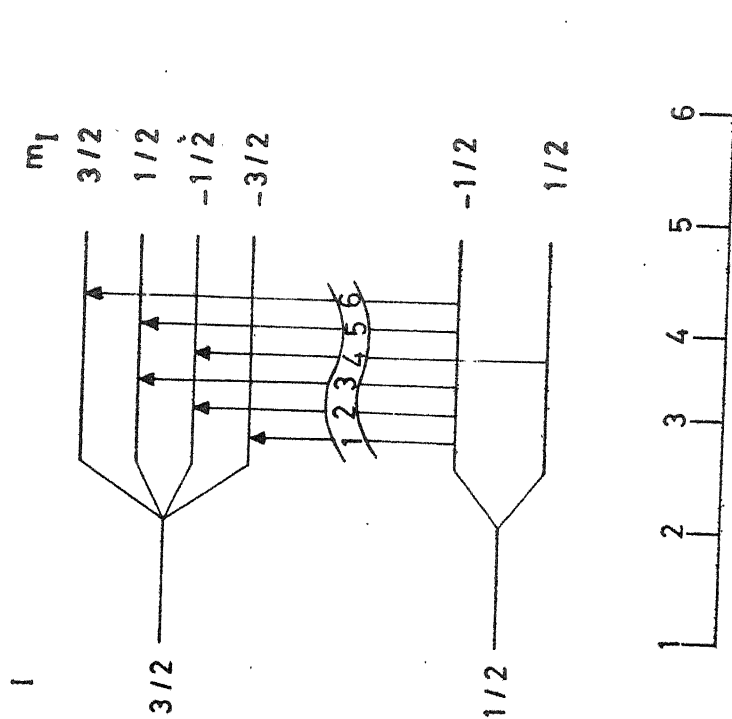


Fig.1.8 Effect of magnetic hyperfine interaction on energy levels of ^{57}Fe . Peak positions of the six-figure pattern are shown at the bottom.

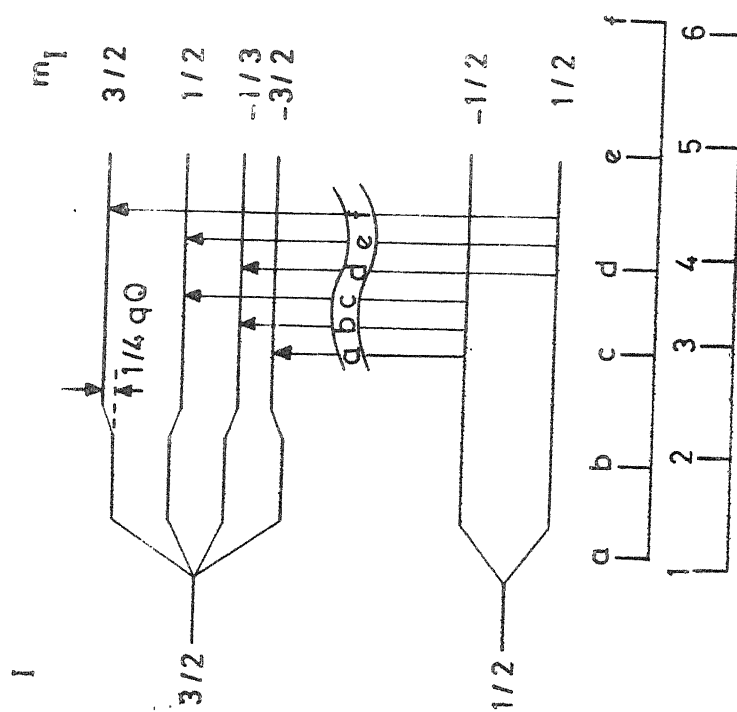


Fig.1.9 Effect of weak quadrupole interaction and a strong magnetic interaction on the energy levels of ^{57}Fe . The numbers 1 to 6 refer to those in Fig.1.8.

$E_0 = 14.4$ keV the magnetic hyperfine field H_{int} is given by

$$H_{int} = 0.843 \times 10^5 \left[V_{\left(\frac{3}{2} \frac{1}{2} \rightarrow \frac{1}{2} \frac{1}{2}\right)} - V_{\left(\frac{3}{2} \frac{1}{2} \rightarrow \frac{1}{2} \frac{1}{2}\right)} \right] \text{ Oersted}$$

$$= 0.843 \times 10^5 [L_5 - L_3] \times \text{Calibration constant Oersted}$$

where L_3 and L_5 represent the position of third and fifth line. Using this value of H_{int} in Eq. (1.36) we can determine μ_e . Hence Mössbauer spectroscopy can be used to measure hyperfine field at the nuclear site and the nuclear moment of nuclei in their excited state.

1.8 COMBINED QUADRUPOLE AND MAGNETIC DIPOLE INTERACTION

In many magnetic substances both electric quadrupole and magnetic dipole interactions are present. If one of the interactions is small compared to other, it can be treated as a perturbation term in the Hamiltonian. For example small quadrupole interaction shifts the position of magnetically split lines as shown in Fig. 1.9.

In case both interactions are comparable in strength i.e. none of them is negligible compared to other, the spectrum becomes quite complicated and such situations are appropriately treated in literature [4,7].

1.9 GOLDANSKII-KARYAGIN EFFECT

The intensity of Mössbauer line directly depends on the recoil-free fraction

$$f = \exp[-\langle (\vec{k} \cdot \vec{x})^2 \rangle]$$

where \vec{k} is the wave vector of the incident gamma ray and \vec{x} is the amplitude of vibration of the Mössbauer nucleus. If the gamma ray direction \vec{k} is characterised by polar coordinates θ and ϕ with respect to EFG axes, we can write

$$\langle (\vec{k} \cdot \vec{x})^2 \rangle = k^2 [(\langle x_x^2 \rangle \cos^2 \phi + \langle x_y^2 \rangle \sin^2 \phi) \sin^2 \theta + \langle x_z^2 \rangle \cos^2 \theta]$$

If the amplitudes of vibration are not equal in all directions, the recoil-free fraction becomes a function of (θ, ϕ) . Thus, for ^{57}Fe quadrupole doublet and for a polycrystalline sample the intensities of the two lines have the ratio

$$\frac{I_\pi}{I_\sigma} = \frac{\int_0^{2\pi} \int_0^\pi f(\theta, \phi) (1 + \cos^2 \theta) \sin \theta \, d\theta \, d\phi}{\int_0^{2\pi} \int_0^\pi f(\theta, \phi) (\frac{5}{3} - \cos^2 \theta) \sin \theta \, d\theta \, d\phi}$$

For axially symmetric vibrations where

$$\langle x_x^2 \rangle = \langle x_y^2 \rangle = \langle x_\perp^2 \rangle \neq \langle x_z^2 \rangle = \langle x_\parallel^2 \rangle$$

$$f(\theta, \phi) = \exp[-k^2 \langle x_\perp^2 \rangle] \exp[k^2 (\langle x_\perp^2 \rangle - \langle x_\parallel^2 \rangle) \cos^2 \theta]$$

above equation reduces to

$$\frac{I_{\pi}}{I_{\sigma}} = \frac{\int_0^{\pi} \exp[-k^2(\langle X_{||}^2 \rangle - \langle X_{\perp}^2 \rangle) \cos^2 \theta] (1 + \cos^2 \theta) \sin \theta \, d\theta}{\int_0^{\pi} \exp[-k^2(\langle X_{||}^2 \rangle - \langle X_{\perp}^2 \rangle) \cos^2 \theta] (5/3 - \cos^2 \theta) \sin \theta \, d\theta}$$

Thus even for a perfectly random orientation of crystallites the intensities of two lines may be different. The intensity of magnetically split lines are also modified for the same reason i.e. the anisotropy of Debye-Waller factor. This effect is known as Goldanskii-Karyagin (G-K) effect. As the vibrational anisotropy is an increasing function of temperature, the asymmetry in intensities related to G-K effect also increases with temperature.

1.10 ASYMMETRIC QUADRUPOLE DOUBLET

The quadrupole doublet in Mössbauer spectra may sometimes be asymmetric. The asymmetry may arise due to following reasons:

- (1) Lack of randomness of crystallites
- (2) Anisotropy of Debye-Waller factor (G-K effect)
- (5) Relaxation effects

The intensity ratio of two lines strongly depends upon the angle between the gamma ray direction and the sample surface. Hence lack of randomness of crystallites orientations in absorber will result in asymmetrical doublet.

Anisotropy of Debye-Waller factor, as explained in Sec. 1.9, also results in an asymmetric doublet. The intensity ratio is ≈ 1 at low temperatures and increases with temperature.

The asymmetry ratio will strongly depend upon the relaxation mechanism. If the fluctuations in the magnetic field are due to spin-lattice relaxation, relaxation time will decrease with increasing temperature. Thus temperature rise will decrease the asymmetry, an effect opposite to G-K effect. But if the fluctuations are due to spin-spin relaxation, the asymmetry will depend on the concentration of the paramagnetic ions.

REFERENCES

1. R.L. Mössbauer, Z. Physik 151, 124 (1958); Z. Naturforsch. 14a, 211 (1959)
2. R.L. Cohen, (Ed), Application of Mössbauer Spectroscopy, Vol I, Academic Press, New York (1976)
3. H. Frauenfelder, The Mössbauer effect, W.A. Benjamin, New York (1962)
4. V.I. Goldanskii and R.H. Herber, (Eds), Chemical Applications of Mössbauer Spectroscopy, Academic Press, New York and London (1968)
5. H.N. Greenwood and T.C. Gibb, Mössbauer Spectroscopy, Plenum Press, New York - London (1971)
6. L. May, (Ed), An Introduction to Mössbauer Spectroscopy, Plenum Press, New York - London (1971)
7. V.G. Bhide, Mössbauer Effect and its Applications, Tata McGraw-Hill Publishing Co. Ltd. New Delhi (1973)
8. J.G. Stevens and L.H. Bowen, Analy. Chemistry 48, 232R (1976)
9. U. Gonser, (Ed), Mössbauer Spectroscopy, Springer-Verlag - Berlin (1975), p. 7.
10. G.K. Shenoy, F.E. Wagner, (Eds), Mössbauer Isomer Shifts, North-Holland - Amsterdam (1978)
11. G.K. Wertheim, Mössbauer Effect : Principle and Applications of Mössbauer Spectroscopy, Academic Press, New York and London (1964)

12. G.M. Brancroft, Mössbauer Spectroscopy, McGraw-Hill Book Co. England (1973)
13. J.G. Stevens and W.L. Gettys, "'Int. Conf. on the Application of Mössbauer Effect'", Jaipur, India Dec. 14-18, (1981)
14. R.V. Pound, G.B. Benedek and R. Drever, Phys. Rev. Letters 7, 405 (1961)
15. G.W. Ludwig and H.H. Woodbury, Phys. Rev. 117, 1286 (1960)
16. P.K. Tseng and S.L. Ruby, Phys. Rev. 172, 249 (1968).

CHAPTER 2

INSTRUMENTATION AND EXPERIMENTAL METHODS

This chapter presents the basic aspects of experimental techniques used in the present study. These include the description of Mössbauer spectrometer, cryogenic and high temperature arrangements, radioactive sources, absorbers, absorber thickness optimization, geometry effects, details of Mössbauer data analysis and other measurement methods.

2.1 INTRODUCTION

The quality of Mössbauer spectra depends on the specific experimental conditions. The signal-to-noise ratio depends on the radioactive strength of the Mössbauer source, the efficiency and resolution of gamma-ray detection and amplification system, the thickness of absorber, the geometry of the experiment and the ambient temperature of source and absorber.

A Mössbauer spectrometer shown schematically in Fig. 2.1 consists of following units:

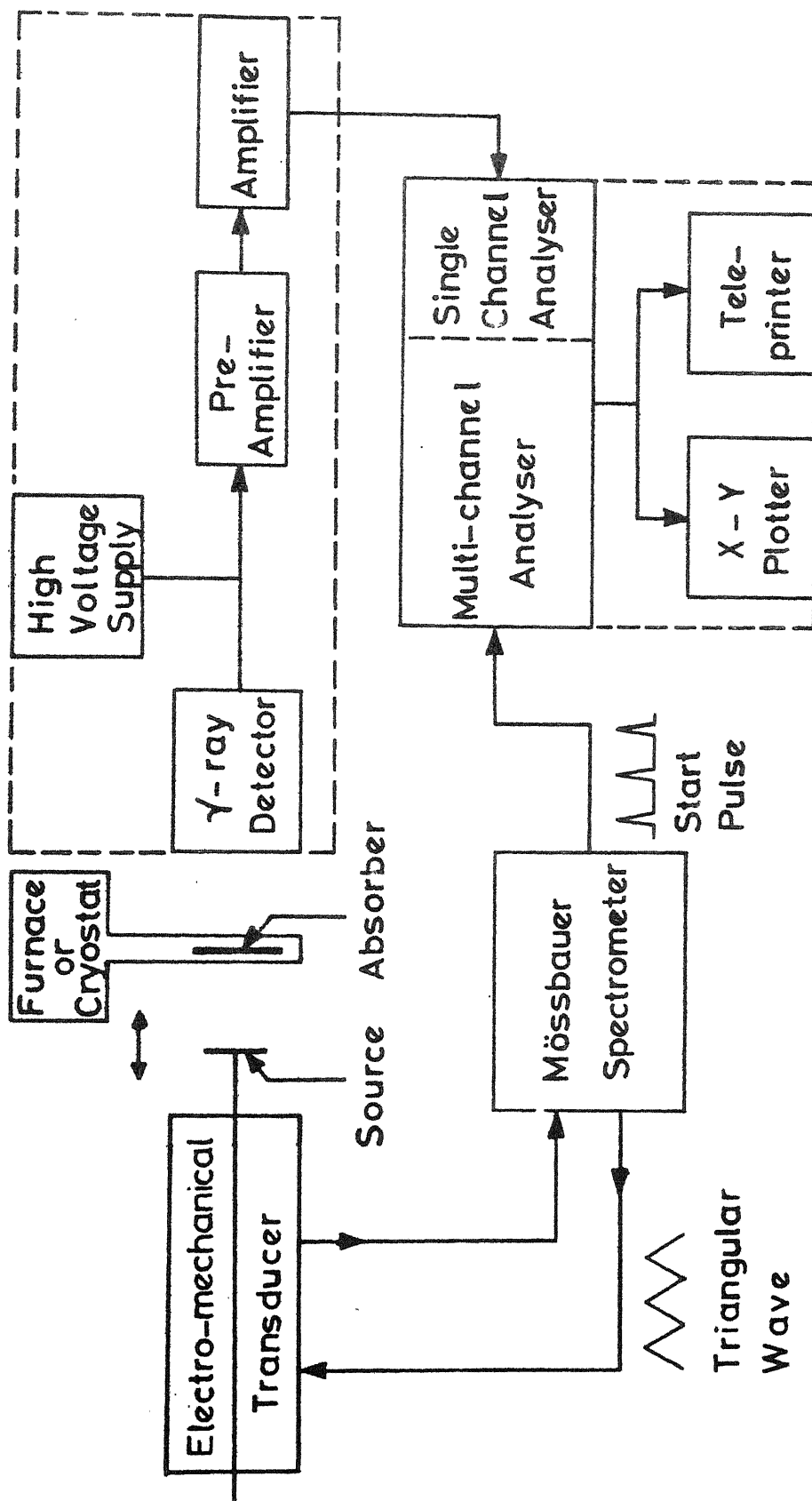


Fig. 2.1 Schematic block diagram of Mössbauer spectrometer.

- (i) Mössbauer spectrometer or drive unit for waveform generation and synchronization,
- (ii) Electro-mechanical velocity transducer,
- (iii) Gamma-ray detection and amplification system,
- (iv) Multichannel analyser (MCA) for data storage and reduction,
- (v) Cryostat or furnace for temperature-dependent measurements,
- (vi) Mössbauer source and absorber.

In following sections we shall briefly discuss the above units of the Mössbauer set-up used in the present work. The detailed description and general methodology of Mössbauer effect has been reported in literature [1-8] and these will not be discussed here.

2.2 MÖSSBAUER SPECTROMETER

The Mössbauer spectrometer used in the present work was designed and developed in this Institute [9] and built by M/s Encardiorite, Lucknow, India. This spectrometer could be run in three modes i.e. (a) constant velocity, (b) constant acceleration and (c) sinusoidal velocity.

In the present work we have run the spectrometer in constant acceleration mode throughout. In the spectrometer a precision velocity drive is realised, by generating a signal

with highly stable amplitude, frequency and phase and placing the transducer in a feedback loop. The block diagram of the spectrometer is shown in Fig. 2.2. A highly stable temperature compensated crystal controlled oscillator produces 100 kHz drive signals which are scaled down to 20 Hz square wave using JK-flip flops. The reference triangular wave for constant acceleration mode is generated by integrating the square wave by an integrator consisting of IC 741.

The transducer described in Sec. 2.2 consists of a conventional double speaker arrangement having a drive coil and a pick up coil. The velocity is monitored by comparing the pick up signal with the reference signal in an error amplifier. The difference between the two signals, called the error signal is a measure of deviation from the designed velocity. Error amplifier output is fed to the power amplifier which drives the transducer (Fig. 2.2). There is a synchronization between the transducer velocity and reference signal in amplitude as well as in phase.

The start pulse for resetting the multichannel analyser is obtained by scaling down the complementary output of penultimate $\div 2$ stage by a factor of 2 which is again applied to monostable multivibrator (IC 74121) through a level shifter to get a narrow pulse of 10 μ sec width. The start pulse synchronises the opening of the first channel of the MCA with the negative maxima of velocity reference signal.

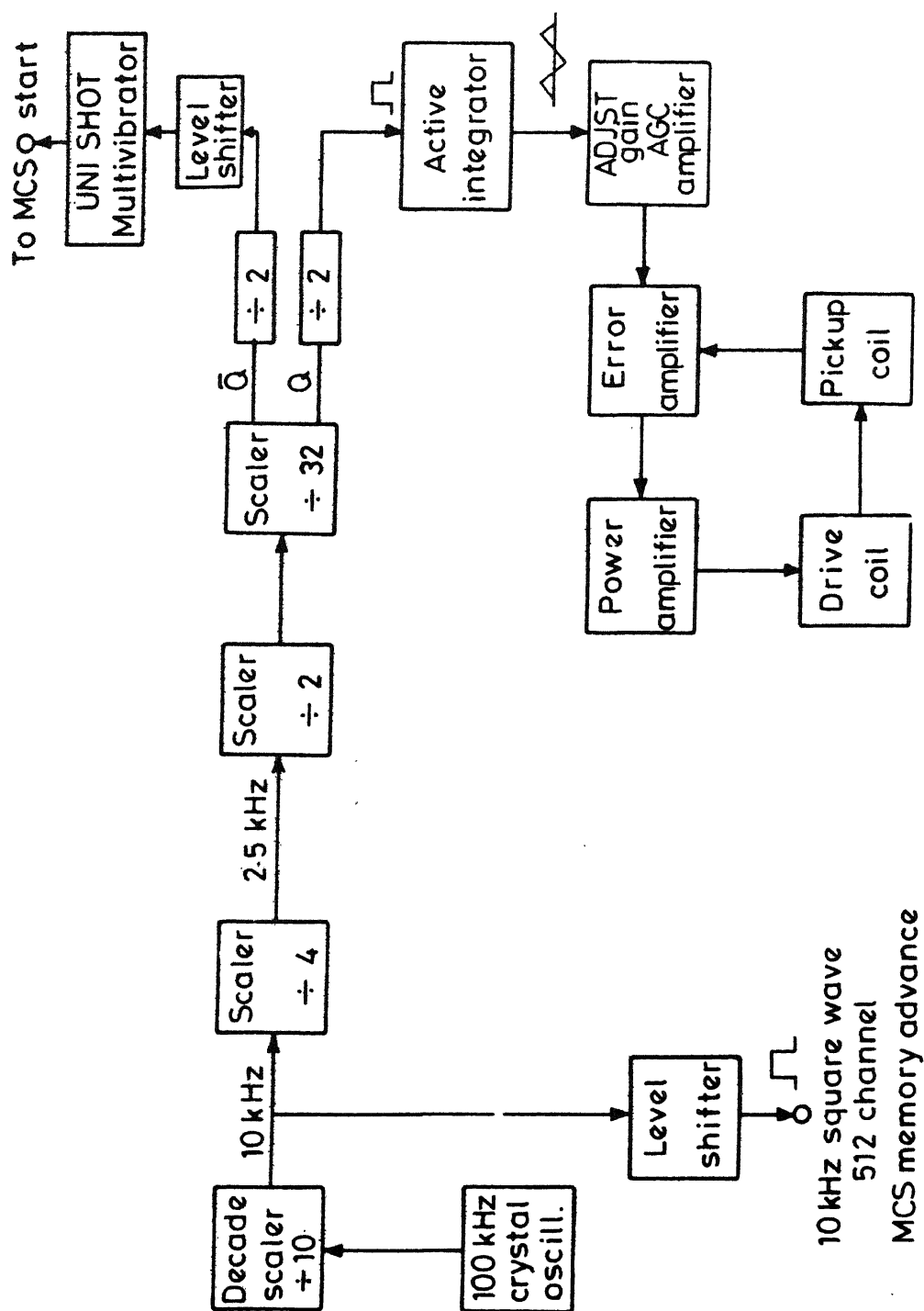


Fig. 2-2 Functional block diagram of the Mössbauer spectrometer.

2.3 ELECTRO-MECHANICAL VELOCITY TRANSDUCER

The construction of the transducer used is shown in Fig. 2.3. It consists of a dual coil speaker, where one coil (the drive coil) is used to drive the movable shaft which carries the source or absorber, and the second coil (the pick-up coil) is used as a velocity sensing coil. The drive coil impedance is matched with the output impedance of power amplifier. The magnetic field and number of turns on the coil are chosen to get efficient conversion of electrical energy to mechanical energy.

The mechanical design of the transducer is such that the frequency of external vibrations is far away from the basic resonance frequency. The drive coil and pick-up coil are wound in grooves, at the two ends of a common holder, having diameter of 38 mm which is made out of perspex. Each coil has a length 7.8 mm which is subdivided into three coils of length 2.6 mm each. The three pick-up coils are connected in series and the drive coils are in parallel in the normal operation for impedance matching of the drive coil and to improve linearity.

2.4 GAMMA-RAY DETECTION AND AMPLIFICATION SYSTEM

We used argon gas-filled proportional counter with aluminised mylar window, supplied by the Electronic Corporation of India, for detection of gamma rays. We have chosen proportional counter as it has good energy resolution (~ 2 keV at

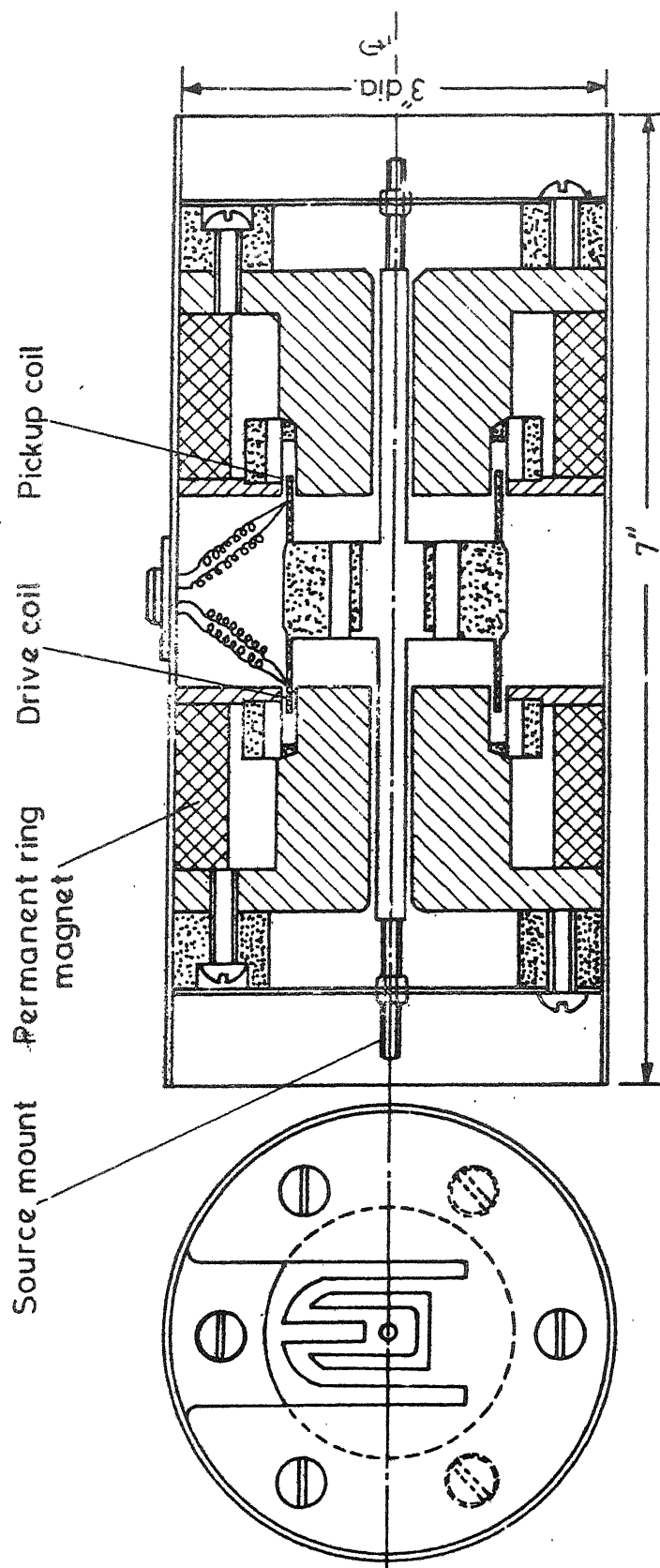


Fig. 2.3 Schematic block diagram of the electromechanical transducer used in the Mössbauer spectrometer.

14.4 keV gamma ray) and high detection efficiency for low-energy gamma-rays. The unwanted X-rays are satisfactorily discriminated from the 14.4 keV Mössbauer gamma ray. Pulse height spectrum of ^{57}Co in a Rh-matrix obtained using proportional counter is shown in Fig. 2.4. The bias voltage +1500 VDC for the proportional counter is supplied by high voltage power supply (Baird Atomic Model 318 A). Proportional counter was connected to a low-noise preamplifier and a linear amplifier (ECIL model PA 521). The output of the linear amplifier is fed to the multichannel analyser (Nuclear Data model ND-60).

2.5 MULTICHANNEL ANALYSER

The model ND-60 (microprocessor based 2048 (2K) channel) multichannel analyser was used in the present work. The ^{57}Fe Mössbauer gamma-ray (14.4 keV) line was selected by the in-built single channel analyser and by running the MCA in PHA mode. The MCS external mode with a dwell time 100 μsec (for 512 channel operation) and 50 μsec (for 1024 channel operation) was used for recording the Mössbauer spectrum. The counting efficiency was very high in the analyser. The start pulse supplied by Mössbauer spectrometer is used for triggering the MCS sweep. The data in subsequent sweeps are added continuously to the data stored in preceding sweeps. Four (in case of 512 channel operation) Mössbauer spectra could be kept

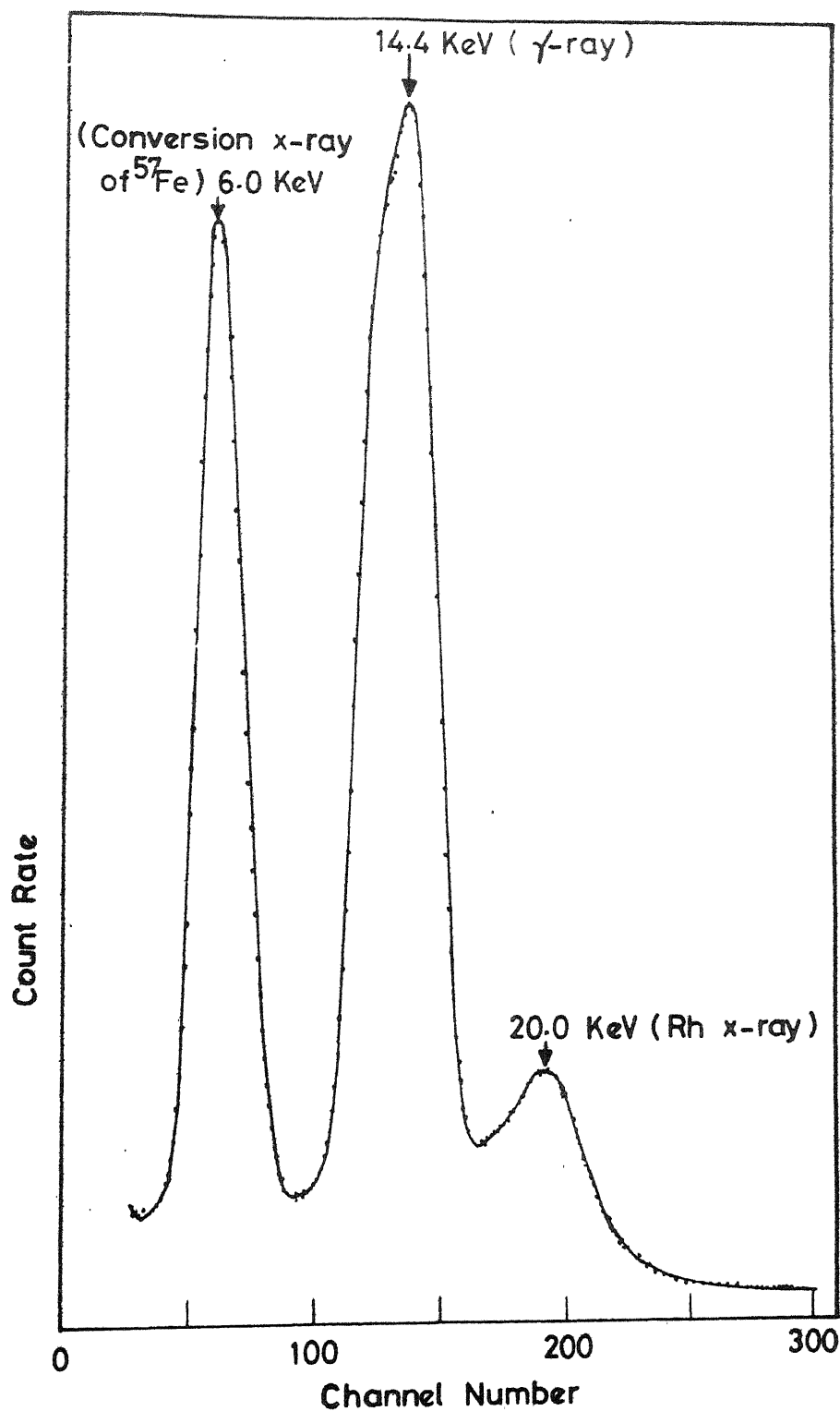


Fig.2.4 Pulse height spectrum of ^{57}Co in Rh matrix (Mössbauer source) measured using proportional counter.

stored in MCA memory for critical comparison. The data stored in the MCA memory are printed/plotted using a series line printer (Teletype model 33 TBP)/X-Y recorder (Hewlett Packard model 7015 A).

2.6 CRYOSTAT AND FURNACE

For the study of problems like phase transition, valence fluctuation, magnetic ordering, kinetics of crystallization process, etc. one needs to study the temperature variation of Mossbauer parameters. Hence one requires a suitable cryostat/furnace to regulate the temperature of absorber and/or source. We used a cryostat and a furnace to cover the temperature range from 80 K to 800 K.

2.6.1 Cryostat

A liquid nitrogen cryostat designed for measurements in the temperature range 80-300 K (room temperature) was fabricated by us in the laboratory. The design is shown in Fig. 2.5. Two concentric cylindrical brass vessels are connected by a thin-walled stainless steel tube. This tube is used for filling liquid nitrogen in the inner vessel. Prior to liquid nitrogen filling, space between the inner and outer vessels is evacuated with the help of an oil diffusion pump used in conjunction with a rotary pump. A demountable copper cold finger is attached to the inner vessel. The sample is kept pressed on the cold finger with

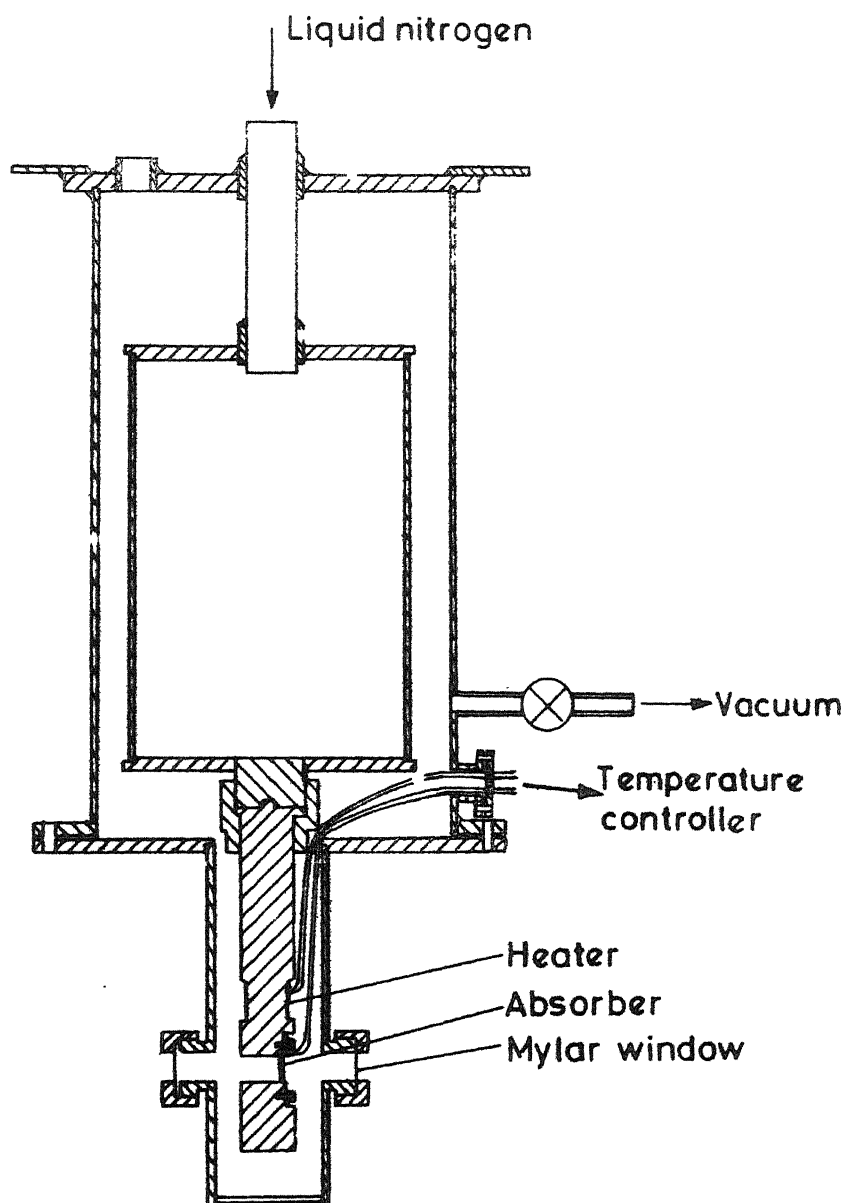


Fig.2.5 Design of the cryostat used in the Mössbauer experiments carried out in temperature range 80-300 K.

the help of a flat copper plate. This ensures uniform sample temperature. Flat nicrome wire is wound on the cold finger for raising the temperature of the sample. The sample temperature is measured with the help of a copper-constantan thermocouple. Outer surface of cryostat is nickel plated to prevent heating by radiation.

The sample can be easily changed by opening the bottom flange. A temperature controller fabricated by us was used for controlling the temperature of the sample. The temperature controller provided an accuracy of the order of $\pm 0.4^{\circ}\text{C}$.

2.6.2 Furnace

For Mössbauer spectroscopic study of the sample above room temperature a vacuum furnace, which has variable temperature (upto 800 K) facility, has been used. The furnace shown in Fig. 2.6 is fabricated by using a design developed in our laboratory [10]. The advantages of this design are :

- (i) A very good vacuum can be achieved within a short time.
- (ii) The separation between counter and source can be kept very small, i.e. Mössbauer experiment can be performed even with very weak source.
- (iii) The furnace is easy to handle.
- (iv) Power consumption is very small.

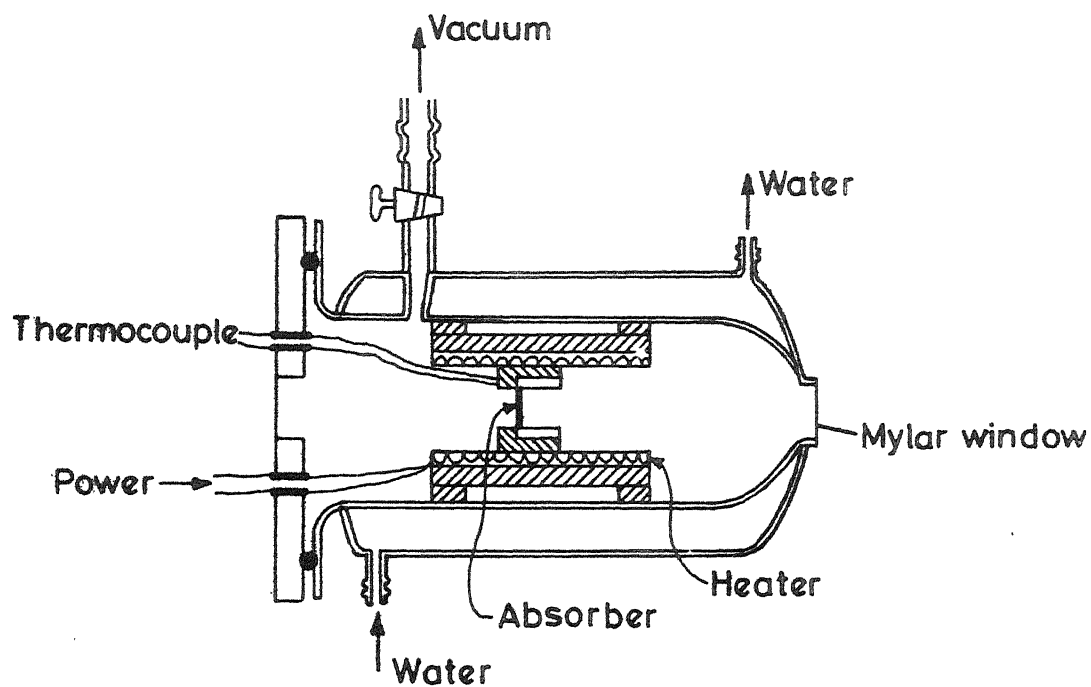


Fig.2.6 Design of the furnace with resistance heating assembly.

The furnace is made of two quartz tubes joined concentrically having diameters 4 cm and 5 cm and length 6 cm. One end is tapered to a diameter of about 1.5 cm. This end is permanently sealed with the help of a beryllium window. A flange is made at the other end on which a brass or perspex flange is connected keeping an 'O' ring in between. Thermocouple and the heater connections are made through the brass/perspex flange. A stop-cock has been connected for evacuating the inner chamber. Cooled water is flown continuously for keeping the temperature outside the furnace low.

Heating assembly consists of a 3.5 cm long quartz tube of diameter 2.5 cm and about 3.5 cm long with nicrome wire wound on it non-inductively. The coil is kept in position by high temperature cement. Remaining space between quartz tube (furnace) and the heating assembly is filled with refractory brick. The sample is put in the heating assembly by the help of a copper disc of 2.3 cm diameter and 1.5 cm thickness having an axial hole of diameter 1.2 cm for gamma-ray transmission. The sample is sandwiched between two iron-free mica or aluminium sheets and is fixed in the copper sample holder with the help of grooves. The sample temperature is controlled using the same temperature controller.

2.7 MÖSSBAUER SOURCE AND ABSORBER

For observing Mössbauer effect one must have Mössbauer atom in excited state embeded in a suitable host matrix, and an absorber having Mössbauer atom in ground state. Mössbauer effect has been observed in many elements but iron-57 has been the most extensively used isotope because of the ease of operation. In the present work we have used ^{57}Fe throughout, hence our discussion will be limited to the case in which ^{57}Co (a precussor of $^{57}\text{Fe}^*$) is the source and ^{57}Fe is the absorber.

2.7.1 Sources

A good Mössbauer source should have the following properties :

- (i) Host matrix should be chemically stable.
- (ii) The Mössbauer gamma rays should be single line free from any hyperfine interaction in the source.
- (iii) Line broadening caused by self-absorption, thickness effects etc. should be minimum.
- (iv) Recoil-free fraction should be large.
- (v) Radiations not contributing to the Mössbauer effect such as characteristic X-rays, gamma-rays and X-rays arising out of Compton scattering should have low intensity. The energy of interfering radiations should be such that they can be clearly separated from the

resonant gamma rays (14.4 keV) in the energy spectrum.

The Mössbauer source used in the present studies can be classified as :

- (a) Standard Mössbauer source.
- (b) Mössbauer source made of sample under study.

Standard Mössbauer Source

The standard source of ^{57}Co deposited in Rh-matrix with initial strength of 24 mCi, supplied by Amersham International Ltd., Amersham, UK was used in the present studies. The recoil-free fraction of this source as specified by the supplier was 0.76. The characteristic X-rays have energies in the range 22-23.3 keV (which is quite high compared to 14.4 keV, the energy of the Mössbauer gamma ray) and could be filtered out easily.

Sample Source

All the ^{57}Co Mössbauer sources of cobaltates $\text{LaCo}_{1-x}\text{Ti}_x\text{O}_3$ and $\text{La}_{1-x}\text{Sr}_x\text{Co}_{1-x}\text{Ti}_x\text{O}_3$ (for $x = 0.5, 0.3, 0.15, 0.05$) were prepared as follows.

Few drops of carrier-free aqueous solution of radioactive $^{57}\text{CoCl}_2$ were dropped on the well-sintered 1-15 mm thick pellets of the cobaltate sample. The drops were dried with the help of an IR lamp. The samples were then heated in air at about 1200 °C for 4 hours to diffuse the ^{57}Co in the sample. The samples were then slowly cooled to room

temperature. The sample surface was polished to remove any undiffused radioactivity.

2.7.2 Absorbers

In the present work we have used (i) standard absorbers for calibration of Mössbauer set up and (ii) absorber made of sample under investigation for specific studies.

Standard Absorbers

In the present work we have used following standard absorbers for calibration:

- (a) Natural iron foil 25 μm thick ($\alpha\text{-Fe}$)
- (b) 310 stainless steel foil (310 SS)
- (c) Enriched $\text{K}_4\text{Fe}(\text{CN})_6 \cdot 3\text{H}_2\text{O}$ single crystal (PFC)
- (d) Sodium nitroprusside (5 mg/cm^2 of iron) (SNP).

All the above absorbers were supplied by Amersham International Ltd., Amersham, U.K.

Sample Absorbers

In some cases sample under investigation was used as Mössbauer absorber. The method used for absorber preparation is described separately for each case in the following chapters at appropriate places.

2.7.3 Absorber Thickness Optimization

The quality of Mössbauer spectrum depends on thickness of absorber and source. The Mössbauer line is broadened out due to thickness of both absorber and source. A number of studies made to analyse the effect of absorber thickness on Mössbauer spectrum has been reported [11-14]. The area as well as peak-width of Mössbauer line is affected by the thickness of the absorber. The area of the Lorentzian or Gaussian shaped line is given by

$$A = \frac{\pi}{2} \Gamma f_s L(t) \quad (2.1)$$

or

$$A = \frac{1}{2} f_s \Gamma [\pi/\ln 2]^{1/2} G(t) \quad (2.2)$$

where f_s is the recoilless fraction of the gamma ray source and Γ is the natural line width of the absorption spectrum and $L(t)$ and $G(t)$ are the respective Lorentzian and Gaussian functions dependent on t , thickness of the absorber.

The thickness t is defined by the relation

$$t = \sigma n f_a \quad (2.3)$$

where σ is the resonance cross section of the absorber nuclei and is given by

$$\sigma = 2\pi \lambda^2 \frac{2I_e + 1}{2I_g + 1} \frac{1}{1+\alpha}$$

where

I_e, I_g : nuclear spin quantum number of excited and ground state respectively.

α : internal conversion coefficient of γ -rays.

λ : wavelength of gamma rays.

and n is the number of the absorbing nuclei in unit area in the path of gamma rays and f_a is the recoil-free fraction of the gamma ray in the absorber.

The number of transmitted gamma rays at the resonance dip as a function of thickness, t , is given by the equation [15]

$$N(t, V_0) = (1 - f)N + N_f \exp(-t/2) J_0(i t/2) \quad (2.4)$$

where t is the thickness of absorber, N and V_0 are the number of gamma rays emitted and the Doppler velocity respectively. The intensity of Mössbauer line is given by

$$N - N(t, V_0) = f_s N [1 - \exp(t/2) J_0(i t/2)] \quad (2.5)$$

where $J_0(x)$ is the zeroth order Bessel function of an imaginary argument.

It is clear from equation (2.5) that peak intensity (i.e. resonance absorption amplitude) is a function of Doppler velocity V_0 and thickness of the absorber t . It suggests that the resonance absorption will increase

monotonically with thickness as the number of active nuclei in the path of γ -ray will increase. However too thick an absorber will increase non-resonant damping of all gamma rays and background noise. As a result of it Mössbauer spectrum will be distorted. On the other hand too thin ~~an~~ absorber will have very small number of active particles contributing to resonance absorption. It will result in poor absorption peak intensity in the Mössbauer spectrum. Hence in order to get a good Mössbauer spectrum an intermediate thickness which gives maximum absorption has to be selected.

The equation (2.5) does not take into account the non-resonant absorption. The amplitude, when non-resonant absorption [13] is considered, is given by

$$N-N(d, V_0) = f_s N [1 - \exp(-\mu_r d/2) J_0(i\mu_r d/2)] \exp(-\mu_a d) \quad (2.6)$$

where μ_a and μ_r are maximum non-resonant and resonant absorption coefficients respectively. The resonant and non-resonant absorption coefficients are related by

$$\mu_r = (n/d) \sigma f_a \quad (2.7)$$

where d is the actual thickness of absorber and n/d is the density of active nuclei.

The optimum thickness to get maximum peak amplitude for a given N is given by Shimony [16]

$$\frac{\mu_r}{2\mu_a} = \frac{\exp(\mu_r d_o/2) - J_0(i\mu_r d_o/2)}{\exp(i\mu_r d_o/2) - J_1(i\mu_r d_o/2)} \quad (2.8)$$

where $J_1(x)$ is the first order Bessel function related to $J_0(x)$ by the identity

$$J_1(x) = - \frac{d J_0(x)}{dx}$$

Another consideration for choosing a thickness is the ratio of the amplitude of peak and the statistical uncertainty in the counts and is defined by α

$$\alpha = \frac{\text{Amplitude of absorption spectrum}}{\text{Statistical uncertainty in the counts}}$$

The count at velocity which is very high compared to V_o is given by

$$N(d, \mu_a) = N \exp(-\mu_a d) \quad (2.9)$$

If the absorption is not too large, the statistical uncertainty is given by

$$\begin{aligned} N &= [N(d, \mu_a)]^{1/2} \\ &= [N \exp(-\mu_a d)]^{1/2} \end{aligned} \quad (2.10)$$

$$\therefore \alpha(d) = f\sqrt{N} [1 - \exp(-\mu_r d/2) J_0(i\mu_r d/2)] \exp(-\mu_a d/2) \quad (2.11)$$

For a good spectrum α should be maximum. For maximum $\alpha(d)$ we find,

$$\frac{\mu_r}{2\mu_a} = \frac{\exp(\mu_r d_o/2) - J_0(i\mu_r d_o/2)}{J_0(i\mu_r d_o/2) + J_1(i\mu_r d_o/2)} \quad (2.12)$$

Using eq. (2.12) we can evaluate d_o if μ_a and μ_r are known.

The optimum thickness of Mössbauer absorber, in order to get in a given experimental time a good Mössbauer spectrum (i.e. having the maximum value of the ratio (α) of the peak intensity to the statistical error in the background count) was selected using the above equation.

2.8 GEOMETRY EFFECTS

The geometry of source-absorber-detector system in a Mössbauer experiment considerably affects the Mössbauer spectrum. There are mainly two types of effects which give rise to distortions in the Mössbauer spectrum. These are :

- (1) Source-detector distance variation effect
- (2) Cosine effect.

2.8.1 Source-Detector Distance Variation Effect

In a Mössbauer experiment source is made to move back and forth from the counter. As a result distance between the source and detector changes continuously. The counting rate of gamma ray is inversely proportional to the square of source detector distance (say r). This variation in count-rate results in non-flat base line.

In constant acceleration mode velocity $V(t)$ at any instant t , can be expressed as

$$V(t) = -V_o + \frac{4V_o}{T} t \quad \text{for } 0 \leq t \leq T/2 \quad (2.13)$$

$$= 3V_o - \frac{4V_o}{T} t \quad \text{for } T/2 \leq t \leq T \quad (2.14)$$

where V_o is the amplitude of velocity and T , its time period. The distance between source and detector can be obtained by integrating eq. (2.13) and eq. (2.14) and is given by

$$X(t) = -V_o t + \frac{2V_o}{T} t^2 + X_o \quad 0 \leq t \leq T/2 \quad (2.15)$$

$$= 3V_o - \frac{2V_o}{T} t^2 + X_o \quad T/2 \leq t \leq T \quad (2.16)$$

where X_o is the distance between source and absorber at $t = 0$. The two equations for different time periods will be same for $t = T/2$. This gives

$$x_o = X_o - V_o T \quad (2.17)$$

Writing $X(t) = X_o + \Delta X(t)$.

The variation in distance $\Delta X(t)$ due to the motion of source is given by

$$\Delta X(t) = -V_o(t) + \frac{2V_o}{T} t^2 \quad 0 \leq t \leq T/2 \quad (2.18)$$

$$= 2V_o(t) - \frac{2V_o}{T} t^2 \quad T/2 \leq t \leq T \quad (2.19)$$

The count rate in the absence of any absorber is given by

$$C(t) = \frac{K}{[X_0 + \Delta X(t)]^2} \quad (2.20)$$

where K is a constant. At the turning points (i.e. when the velocity of the source is zero) at $t = T/4$ and $3T/4$ the displacement is maximum and is given by

$$X(t)_{\max} = \frac{V_0 T}{8} \quad (2.21)$$

In our experiment the time period of oscillation $T = 50$ milliseconds and velocity amplitude $V_0 = 10$ mm/sec. For $X_0 = 5$ cm, $\frac{\Delta X}{X_0}$ is nearly 0.001. The count rate $C(t)$ (eq. 2.20) expressed by the help of binomial theorem is

$$C(t) = \frac{K}{X_0^2} \left[1 - \frac{2\Delta X}{X_0} + \dots \right] \quad (2.22)$$

neglecting higher
order terms

The first term of equation (2.22) results in 0.1 % shift in the base line. The other terms are small and can be neglected. The shift in the base line is very small and has no effect on the spectrum if the percentage absorption is large. If the absorption is small, the effect can be nullified by folding the spectrum about the maximum velocity point [17]. The folding is possible when the linearity of the velocity cycle is good in both halves, otherwise folding of spectrum may result in bad quality and poor resolution.

2.3.2 Cosine Smearing Effect

The cosine smearing effect, caused by the finite size of source absorber and detector window, results in broadening of absorption peaks with a slight shift in peak positions. The gamma rays reaching the detector have different angles with respect to direction of relative motion. The energy of the gamma rays which enter the detector is given by

$$E(\theta) = E_0 (1 - (v/c)) \cos \theta$$

where θ is the angle between the gamma ray and the direction of relative motion. The possible value of θ for a particular geometry varies between 0 and θ_{\max} and hence it is not possible to consider an effective velocity. If θ is large (when source - detector separation is small) this effect will be pronounced resulting in broad distorted spectrum.

If we increase detector-source separation cosine smearing effect will decrease. But at large source-detector separation count rate will be low, requiring longer time for spectrum recording. Hence an intermediate value of source-detector separation should be selected keeping in mind the other experimental considerations.

2.4 DATA ANALYSIS

The Mössbauer data are analysed by the help of a digital computer. In writing the computer program, the

Mössbauer peaks are assumed to be Lorentzian as suggested by Margulies and Ehrman [11]. The approximation is reasonably good, when the source and absorber line width are equal and relaxation effects are small. A number of computer programs are available for the analysis of Mössbauer data. In all the programs the basic concept is almost similar. Our program is based upon the method developed by Law and Bailey [18,19]. The program finds the value of adjustable parameters (guess values) to get closest agreement between experimental data and the value predicted by assumed function.

Let the function $\phi_i = \phi_i(B_1, B_2, \dots, B_n)$ be the functional form chosen to fit the experimental data points Y_i . The condition for getting the set of parameters such as

$$S^2 = \sum_{i=1}^N S_i^2 = \sum_{i=1}^N (Y_i - \phi_i)^2 \quad (2.23)$$

is minimum. Here N is the number of experimental data points. The condition for minimum of the above equation is

$$\frac{\partial S^2}{\partial B_k} = 0$$

This condition gives n simultaneous equations. These equations are solved to get correction in approximate value ΔB_k . The new parameters

$$B_k^{i+1} = B_k^i + \Delta B_k$$

are then selected for $(i+1)^{\text{th}}$ iteration. The new parameters are examined to ensure that S^2 is minimum. These iterations are carried on till minimum is reached.

Better and faster results are obtained if the increment of the parameters is restricted, i.e.

$$B_k^{i+1} = B_k^i + \alpha \Delta B_k \quad (2.24)$$

where α is less than one. Program converges if the successive values of S^2 differ by an amount less than the pre-assigned tolerance. The goodness of fit is tested by the calculation of the Chi-square.

Standard error in the fitted parameters B_k , is also calculated with the help of inversion matrix [20].

2.9.1 Hyperfine Field Distribution

The broadening of the Mössbauer line as explained earlier may be due to thickness effects, cosine smearing effect etc. If there is a distribution of hyperfine parameters as observed in amorphous systems, then it will also contribute to broadening of Mössbauer lines. One can calculate the hyperfine field distribution from broadening Mössbauer spectrum when other effects contributing to broadening of Mössbauer spectra are small. Many attempts **have** been made to calculate hyperfine field distribution from Mössbauer spectra. However we have used Window method [21] illustrated below.

2.9.2 Computation Method

The basic principle for the two distribution (EFG and hyperfine distributions) is same. If we denote the hyperfine distribution as $p(H)$, the ^{57}Fe Mössbauer spectrum can be written as

$$Y(E) = \sum_{i=1}^N \frac{A_i p(H)}{1 + 4[(E-E_0)/W]^2} dH \quad (2.25)$$

where A_i is the intensity of i^{th} peak, W is the peak width and

$E_0 = V_{ZZ}$ = Principal component of electric field distribution for EFG distribution

$E_0 = a_i H$ = Position of the peak for magnetic field distribution.

The value a_i is given as [23]

$$a_6 = -a_1 = 16.15 \times 10^{-3} \text{ mm/KOe}$$

$$a_5 = -a_2 = 9.34 \times 10^{-3} \text{ mm/KOe}$$

$$a_4 = -a_3 = 2.54 \times 10^{-3} \text{ mm/KOe}$$

and W is the peak width.

The $p(H)$ can be Fourier expanded in terms of a trigonometric series

$$p(H) = \sum_{n=1}^N b_n \left[\cos \frac{n\pi H}{H_{\max}} - (-1)^n \right] \quad (2.26)$$

with the boundary conditions

$$\left(\frac{d p(H)}{dH} \right)_{H=H_{\min}} = 0 = \left(\frac{d p(H)}{dH} \right)_{H=H_{\max}}$$

The H_{\max} is far away from the real value of H such that $p(H_{\max}) = 0$. The Fourier coefficients b_n are calculated by usual least square fit to the experimental data. If $N \rightarrow \infty$ any hyperfine distribution $p(H)$ can be expressed by eq. (2.26). The coefficients b_n are determined by solving $(N+1)$ simultaneous equations. The largest value of N , one can use is limited due to finite memory space available in the computer.

The computer program for hyperfine field distribution was tested for the standard sample such as sodium nitroprusside and α -Fe. The results are shown in Fig. 2.7 and Fig. 2.8.

2.10 OTHER MEASUREMENTS

To corroborate the results obtained for various samples with Mössbauer measurements, we have also carried out other measurements using various other methods such as X-ray powder diffraction, electron microscopy, electron paramagnetic resonance, magnetization and electron transport

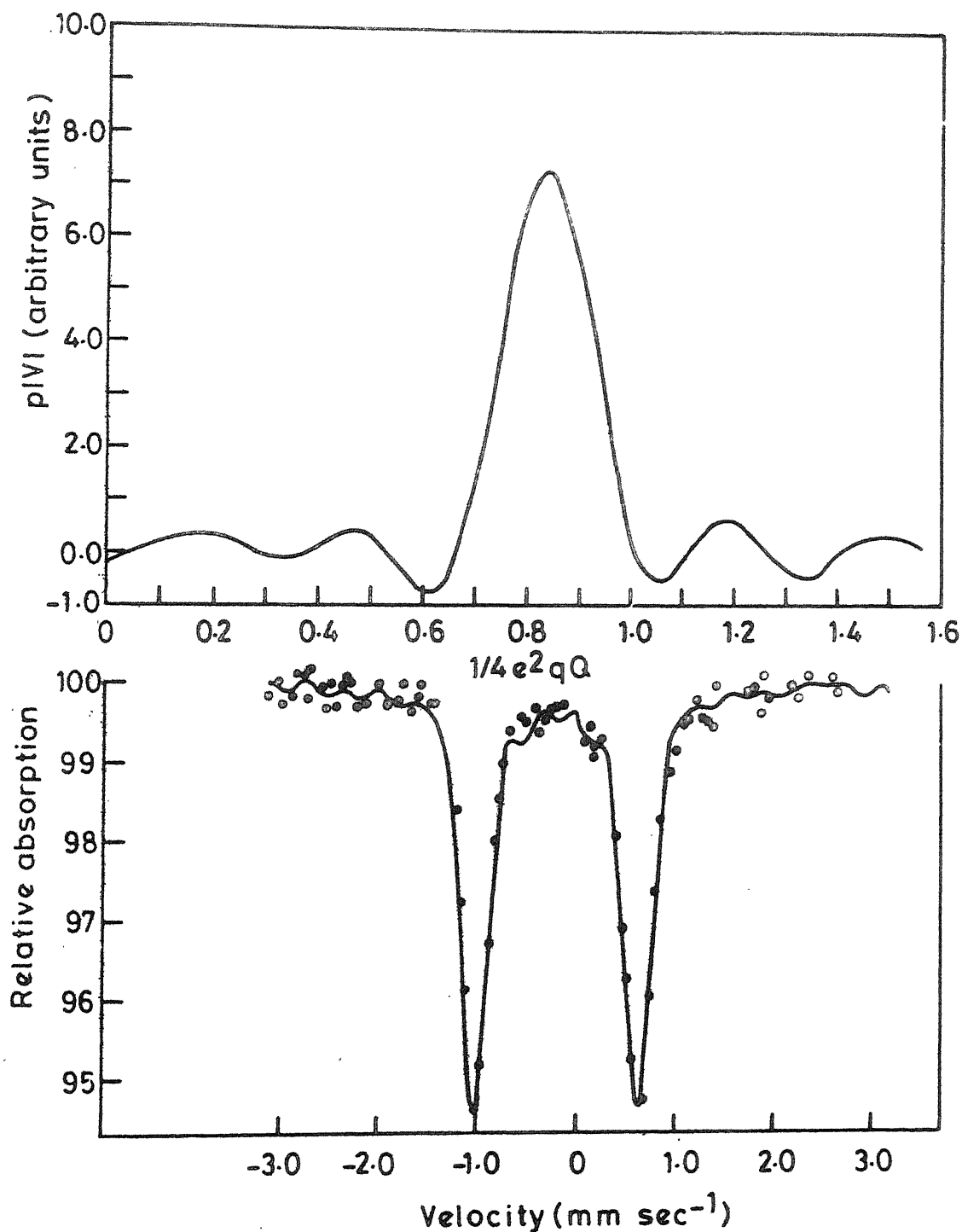


Fig.2.7 EFG distribution in sodium nitroprusside (absorber) at room temperature. The top figure shows the ($p|V|$) distribution while the bottom figure shows the fitted Mössbauer spectrum.

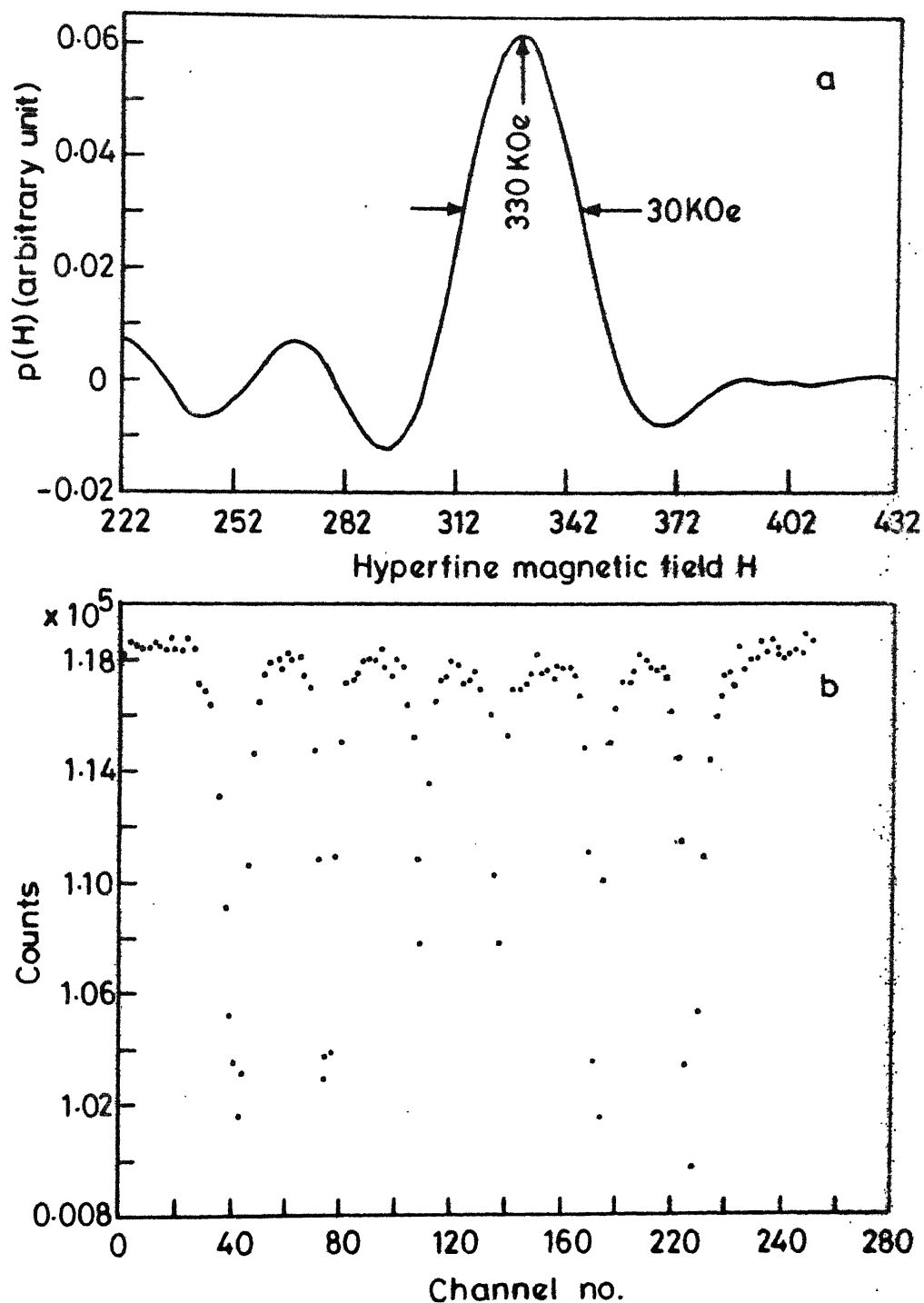


Fig.2.8 Hyperfine field distribution for α -Fe (absorber) at room temperature. The top figure shows the $p(H)$ distribution while the bottom figure shows the corresponding Mössbauer spectrum of α -Fe.

measurements.

The X-ray powder diffraction patterns of the samples were recorded by using Rich Seifert ISO-Debye flux 2002 diffractometer with CuK_α target and Ni filter. The diffraction patterns were recorded at various temperatures in the temperature range room temperature (25 °C) to 700 °C.

The EPR measurements were made using Varian Associates Spectrometer (model V4502-12) in the X-band frequency and with a 100 KHz field modulation. The EPR spectra were recorded at room temperature (295 K) and at liquid nitrogen temperature (78 K).

The magnetization measurements were made by using Varian Associates PAR vibrating sample magnetometer (model 150A) and using a field up to 8 KG. All these measurements were made at room temperature.

Electrical conductivity (ρ) was measured by using four probe sample cell fabricated locally. The Seebeck coefficients α were measured with respect to platinum in the temperature range RT to 700 K.

The transmission electron micrograph were recorded using Philips EM 301 electron microscope.

REFERENCES

1. N. Benezer-Koller and R.H. Herber in Chemical Applications of Mössbauer Spectroscopy, edited by V.I. Goldanskii and R.H. Herber, Academic Press, New York (1968)
2. U. Gonser in Mössbauer Spectroscopy, edited by U. Gonser, Springer-Verlag, Berlin - Heidelberg, New York (1975)
3. N.N. Greenwood and T.C. Gibb, Mössbauer Spectroscopy, Chapman and Hall Ltd., London (1971)
4. G.M. Bancraft, Mössbauer Spectroscopy, An Introduction for Inorganic Chemist and Geochemists, McGraw-Hill, London (1973)
5. A. Vertes, L. Korecz and K. Burger, Mössbauer Spectroscopy, Elsevier Scientific Publishing Co., Amsterdam (1979)
6. V.G. Bhide, Mössbauer Effect and its Applications, Tata McGraw-Hill Publishing Co. Ltd., New Delhi (1973)
7. Mössbauer Effect Methodology, Vol. 1-9 edited by I.J. Gruverman, Plenum Press, New York (1965-74)
8. J.J. Spijkerman in An Introduction to Mössbauer Spectroscopy, edited by L. May, Plenum Press, New York (1971)

9. A.W. Gupta, H.R. Sharma, J.J. Huntzicker and G.N. Rao, Rev. Sci. Instrum. 45, 1423 (1974)
10. N.V. Nair, Ph.D. Thesis, Indian Institute of Technology, Kanpur, India (1981) (Unpublished)
11. S. Margulies and J.R. Ehrman, Nucl. Inst. and Methods, 12, 131 (1961)
12. D.A. Shirley, M. Kaplan and P. Axel, Phys. Rev. 123, 816 (1961)
13. D.A. O'Connor, Nucl. Inst. and Method. 21, 318 (1963)
14. A.J. Stone, Nucl. Inst. and Method. 107, 285 (1973)
15. R.M. Housley, W.E. Brickson and J.G. Dash, Nucl. Inst. and Method. 27, 29 (1964)
16. V. Shimony, Nucl. Inst. and Method. 37, 348 (1965)
17. Takayuki Kobayashi and Kazuko Fukumura, Nucl. Inst. and Method. 173, 363 (1980)
18. V.J. Law and R.V. Bailey, Chem. Eng. Sci. 18, 189 (1963)
19. H.C. Verma, Ph.D. Thesis, Indian Institute of Technology, Kanpur, India (1980) (Unpublished)
20. J.R. Wolberg, Prediction Analysis, D. Van Nostrand Company Inc., Princeton (1967)
21. B. Window, J. Physics E4, 401 (1971).

CHAPTER 3

MÖSSBAUER SPECTROSCOPIC STUDIES OF $\text{LaCo}_{1-x}\text{Ti}_x\text{O}_3$ AND $\text{La}_{1-x}\text{Sr}_x\text{Co}_{1-x}\text{Ti}_x\text{O}_3$ SYSTEMS

3.1 INTRODUCTION

In recent years perovskite oxides ABO_3 (where A is an ion like La^{3+} and B is a transition metal ion) have been a subject of extensive research. Among these perovskite oxides LaCoO_3 has received maximum attention [1-7] because of its interesting electrical and magnetic properties. Many new technological applications of LaCoO_3 and its derivatives (solid solution with other perovskites) have evoked considerable interest in these perovskites.

It is now established that the oxides with low cationic spin ($S \leq 1/2$) exhibit metallic conductivity and Pauli paramagnetism. It is further shown that the d-electrons in such transition metal oxides behave collectively and are well described by band theory (e.g. LaTiO_3 , LaNiO_3). In the case of compounds having high cationic spin ($S \geq 2$) the atomic moment can be described by crystal field theory with the

d-electrons showing localized behaviour [8-10] (e.g. LaCrO_3 , LaMnO_3 , LaFeO_3). In those cases where $S = 2$, the compounds exhibit Jahn-Teller distributions. In a given system the crystal field splitting, Δ_{cf} and the exchange energy, Δ_{ex} are the two factors which determine the spin state of transition metal ion. If $\Delta_{\text{cf}} > \Delta_{\text{ex}}$, the low-spin state becomes the stable state as in WO_3 , LaTiO_3 , CaVO_3 and ZnCo_2O_4 [8,10]. The high-spin state becomes energetically more stable when $\Delta_{\text{cf}} < \Delta_{\text{ex}}$ as in LaCrO_3 , LaMnO_3 etc. Both the states can coexist if $\Delta_{\text{cf}} = \Delta_{\text{ex}}$ as in the case of LaCoO_3 . LaCoO_3 for which $\Delta_{\text{cf}} \simeq \Delta_{\text{ex}}$ is known to exhibit unique electrical and magnetic properties [2,3,5]. The system LaCoO_3 is one of the few oxide materials where localized electron \rightarrow collective electron transition has been observed [2,7].

The system LaCoO_3 has been studied by Raccach and Goodenough [2] in great detail. The observed plateau in the inverse magnetic susceptibility versus temperature curve in the 400-650 K range has been identified [2] with (i) the variation of relative population of the low- and high-spin cobalt ions, (ii) the establishment of short range order. Experimental evidence supporting such ordering was obtained from the differential thermal analysis (DTA) and other measurements. Symmetry of LaCoO_3 changes from R_{3c}^- to R_3^- following the short range ordering. These authors [2] observed a first order transition at 1210 K arising out of the delocalization

of the e_g electrons (localized at lower temperature at high-spin Co^{3+} ions) to form σ^* band electrons. LaCoO_3 becomes metallic beyond the transition where the bonding electrons form a σ^* band.

Goodenough [2] interpreted the electron transport and other properties of LaCoO_3 in terms of temperature variation of the spin and valence state equilibria of cobalt ion. It was further interpreted that the $e_g \rightarrow \sigma^*$ transition could indicate that the crystal field and band limits of d-electrons are distinct thermodynamic states. The mechanism suggested by Goodenough for electrical conduction in LaCoO_3 presumed the formation of high-spin divalent and low-spin tetravalent cobalt ion pairs.

Bhide et al. [7] have performed an extensive investigation of LaCoO_3 using a variety of techniques including Mössbauer spectroscopy. In particular, the Mössbauer spectroscopic studies employing $\text{La}^{57}\text{CoO}_3$ as the radioactive source not only served as a diagnostic tool [11] for determining the valence and spin states but it also gave information about the degree of covalency and therefore about the variation of overlap integral Δ_{cac} . In addition, the temperature variation of Lamb-Mössbauer factor provides valuable information about the phase transition. The results of these extensive studies of LaCoO_3 have helped to establish that cobalt ions exist predominantly in the low-spin ($t_{2g}^6 e_g^0$)

Co^{III} state at low temperature which transforms partially to high-spin ($t_{2g}^4 e_g^2$) Co³⁺ state upto 200 K. It is observed from Mössbauer spectroscopic studies that there is electron transfer from Co³⁺ to Co^{III} above 200 K producing divalent and tetravalent cobalt ions with an accompanying decrease in the resultant population of Co³⁺ ions. Studies of magnetic properties indicate a continuous increase in the $\chi_g T$ throughout the temperature range studied. Since the divalent and tetravalent cobalt ions are paramagnetic, the population of Co³⁺ decreases significantly at high temperature and completely disappears at the localized - collective electron transition temperature (1210 K). These changes in the physical properties are also reflected in the electron transport properties of LaCoO₃.

We have described above the studies of LaCoO₃ in some details because it forms a basis for the studies of substituted systems. Several studies of substituted LaCoO₃ systems (i.e. La_{1-x}M_xCoO₃ and LaCo_{1-x}M_xO₃) have been made [4,6,12-18] in order to understand the electronic and magnetic properties of these compounds. Among these substituted systems La_{1-x}Sr_xCoO₃ has received more attention than others [6,16-19] owing to its interesting properties. Mössbauer spectroscopic and magnetic studies showed [15] that the system La_{1-x}Sr_xCoO₃ is ferromagnetic for $x > 0.125$ at low temperature and metallic

ferromagnet with $T_c = 232$ K for $x = 0.5$. In $\text{La}_{1-x}\text{Sr}_x\text{CoO}_3$ the ferromagnetically rich clusters coexist with the paramagnetic La^{3+} regions in the same crystallographic phase. The ferromagnetic component increases with x and decreases with temperature. These authors [15] have assigned the origin of observed ferromagnetism to itinerant electron ferromagnetism originally suggested by Goodenough [19,20]. According to Goodenough's model [19], the 3d holes generated by the substitution of Sr^{2+} are not localized at a single cobalt ion, but are shared by the eight cobalt ions nearest to strontium forming an acceptor level. With increase in x , the acceptor complex grows in size to form an impurity band giving rise to itinerant ferromagnetism.

LaCoO_3 system substituted at Co site by another transition metal ion has been studied by several workers [6,17,18]. Substitution of an ion of valency other than 3 may result in non-stoichiometric compound. The system $\text{LaCo}_{1-x}\text{Ti}_x\text{O}_3$ has been studied [17,18] for its electrical and magnetic properties. The expected n-type semiconductor behaviour is found only for low values of x (about 0.05) and at higher values of x it shows p-type behaviour [17]. The electrical and magnetic properties of this system show a change in behaviour above a critical value of x which was also confirmed by the studies of Bahadur et al. [18]. In order to have a better understanding of this non-stoichiometric system, we

have carried out detailed Mössbauer spectroscopic studies of this system. The investigation by means of Mössbauer spectroscopy of non-stoichiometry in single phase perovskite is useful, because the existence of mixed valence state of Mössbauer cation can be determined [11].

The system $\text{La}_{1-x}\text{Sr}_x\text{Co}_{1-x}\text{Ti}_x\text{O}_3$ have been found to have interesting electrical and magnetic properties. Simultaneous substitution of divalent ion at La site and a tetravalent ion at Co site results in a stoichiometric compound. Like $\text{LaCo}_{1-x}\text{Ti}_x\text{O}_3$ a change in electronic behaviour above a critical value of x is observed [18]. Cobalt exists only in trivalent state in this system. Hence this system consists of only one paramagnetic ion Co^{3+} as in LaCoO_3 . Thus, in principle, this system should behave similar to LaCoO_3 . However as x increases the distortion from cubic symmetry decreases and so does crystal field splitting. This should bring out some changes in the spin state equilibria. To study these changes we have carried out detailed Mössbauer spectroscopic investigation of this system. The Mössbauer results are correlated with other data.

The results obtained for $\text{LaCo}_{1-x}\text{Ti}_x\text{O}_3$ and $\text{La}_{1-x}\text{Sr}_x\text{Co}_{1-x}\text{Ti}_x\text{O}_3$ are compared with the known results of parent systems LaCoO_3 and $\text{La}_{1-x}\text{Sr}_x\text{CoO}_3$.

3.2 EXPERIMENTAL

In this chapter we report our studies of substituted perovskite systems (a) $\text{LaCo}_{1-x}\text{Ti}_x\text{O}_3$ and (b) $\text{La}_{1-x}\text{Sr}_x\text{Co}_{1-x}\text{Ti}_x\text{O}_3$ with $x = 0.50, 0.30, 0.15$ and 0.05 . Various experimental techniques such as X-ray diffraction, magnetic susceptibility measurements, electrical conductivity and transport properties, and Mössbauer spectroscopy have been used to investigate the above substituted perovskite systems. Mössbauer spectroscopic studies are particularly useful as they provide a direct insight into the spin- and valence-state equilibrium in these solids.

3.2.1 Preparation of Cobaltates

All the samples of the system $\text{LaCo}_{1-x}\text{Ti}_x\text{O}_3$ and $\text{La}_{1-x}\text{Sr}_x\text{Co}_{1-x}\text{Ti}_x\text{O}_3$ were prepared by decomposition of appropriate mixtures of oxalates or oxides having high purity of constituent elements. The resulting solids were repeatedly ground, in a ball mill, pressed as pellets and fired at 1475 K for several hours. X-ray diffraction patterns were taken at each stage to monitor the completion of the reaction.

Chemical analysis of $\text{LaCo}_{1-x}\text{Ti}_x\text{O}_{3+\delta}$ showed that for $x = 0.05$ the sample is nearly stoichiometric. However, for other values of x the samples are non-stoichiometric with excess oxygen being $0.006, 0.016$ and 0.168 atoms per molecule for

$x = 0.15, 0.30, 0.50$ respectively. Hereafter we shall represent this system as $\text{LaCo}_{1-x}\text{Ti}_x\text{O}_3$ for convenience. The system $\text{La}_{1-x}\text{Sr}_x\text{Co}_{1-x}\text{Ti}_x\text{O}_3$ is stoichiometric for all values of x as expected.

X-ray diffraction measurements were made using Rich-Seifert X-ray diffractometer to determine lattice parameters of the two systems at room temperature. Lattice parameters are given in Table 3.1(a). Temperature variation of lattice parameters of the $\text{LaCo}_{0.5}\text{Ti}_{0.5}\text{O}_3$ and $\text{La}_{0.5}\text{Sr}_{0.5}\text{Co}_{0.5}\text{Ti}_{0.5}\text{O}_3$ was studied using high temperature X-ray diffraction in the temperature range from 300 to 1000 K. The results are given in Table 3.1(b). No significant change beyond a slight increase in lattice parameters due to thermal expansion was observed.

In view of these observations high temperature X-ray diffraction measurements for other compositions were not carried out.

3.2.2 Electrical and Magnetic Measurements

DC electrical resistivity measurements were performed in the temperature range 300-1000 K by the two probe method for high resistivity samples and by the four probe method for low-resistivity samples. Seebeck coefficients were measured relative to platinum in the temperature range 400-1000 K. Magnetic susceptibility measurements were made using

Table 3.1(a) Lattice parameters of $\text{LaCo}_{1-x}\text{Ti}_x\text{O}_3$ and $\text{La}_{1-x}\text{Sr}_x\text{Co}_{1-x}\text{Ti}_x\text{O}_3$ at room temperature.

System	Composition x	a (Å)	α (degrees)	Structure
LaCoO_3	-	5.380	60.87	Perovskite with rhombohedral distortion
$\text{LaCo}_{1-x}\text{Ti}_x\text{O}_3$	0.05	5.388	60.78	--do--
	0.15	5.420	60.49	--do--
	0.30	5.500	-	Cubic
	0.50	5.560	-	Cubic
$\text{La}_{1-x}\text{Sr}_x\text{Co}_{1-x}\text{Ti}_x\text{O}_3$	0.05	5.381	60.71	Perovskite with rhombohedral distortion
	0.15			
	0.30	5.420	60.48	--do--
	0.50	5.460	-	Cubic

Table 3.1(b) Temperature variation of lattice parameters of $\text{LaCo}_{0.5}\text{Ti}_{0.5}\text{O}_3$ and $\text{La}_{0.5}\text{Sr}_{0.5}\text{Co}_{0.5}\text{Ti}_{0.5}\text{O}_3$ measured using X-ray diffraction technique.

Sample	Lattice Constant (a) (in Angstrom)							
	20°C	100°C	200°C	300°C	400°C	500°C	600°C	700°C
$\text{LaCo}_{0.5}\text{Ti}_{0.5}\text{O}_3$	5.456	5.452	5.455	5.456	5.451	5.451	5.458	5.467
$\text{La}_{0.5}\text{Sr}_{0.5}\text{Co}_{0.5}\text{Ti}_{0.5}\text{O}_3$	5.477	-	5.472	5.479	5.478	5.476	5.467	5.482

PAR vibrating sample magnetometer (model 150) between 300-700 K.

3.2.3 Mössbauer Studies

^{57}Fe Mössbauer studies were carried out using $\text{La}^{57}\text{Co}_{1-x}\text{Ti}_x\text{O}_3$ and $\text{La}_{1-x}\text{Sr}_x^{57}\text{Co}_{1-x}\text{Ti}_x\text{O}_3$ as radioactive Mössbauer source with 310 stainless steel (310SS) or enriched potassium ferrocyanide (PFC : $\text{K}_4\text{Fe}(\text{CN})_6 \cdot 3\text{H}_2\text{O}$) single crystal absorber. For the preparation of sample source, 1.0-1.5 mm thick pellets were made. Few drops of an aqueous solution of $^{57}\text{CoCl}_2$ were added to the sample and were dried using Philips 150 watt infrared lamp. The samples were next heated in air at 1500 K for 4 hours to allow the ^{57}Co activity to diffuse in the sample and then slowly cooled to room temperature. The sample surface was polished to remove any undiffused radioactivity.

Mössbauer spectra were recorded using electromechanical drive spectrometer (described in Chapter 2) in constant acceleration mode in conjunction with 512 channel analyser. The spectra were recorded at 78, 295, 400, 500, 600, and 800 K by mounting the sample source in cryostat or furnace. Standard 310SS absorber was used in these studies. Room temperature Mössbauer spectra were also recorded using enriched PFC single crystal absorber to get better resolution. High temperature Mössbauer spectra were however recorded using 310SS absorber alone. The choice of 310SS absorber

was based on its larger recoil-free fraction $f = 0.28$ as compared to $f = 0.08$ for PFC absorber. Larger value of f was desirable during the high temperature measurements because of the larger source-to-detector distance involved in the high temperature furnace.

3.3 RESULTS AND DISCUSSION

3.3.1 System $\text{LaCo}_{1-x}\text{Ti}_x\text{O}_3$

The spin-state equilibrium and nature of ordering of cobalt ions can be understood by an examination of the variation of magnetic susceptibility (χ_g) with temperature. Ordinarily, for a paramagnetic substance $\chi_g T$ does not vary with temperature, because

$$\chi_g T = \frac{N^2 \mu^2}{3R} = \text{Constant} \quad (3.1)$$

However, when the population of paramagnetic species varies with temperature $\chi_g T$ would not remain constant with temperature variation but would obey the relation

$$\chi_g T = \frac{N^2 \mu^2}{3R} \frac{n}{n+m} \quad (3.2)$$

where n and m represent the proportion of paramagnetic and diamagnetic ions respectively. Equation (3.2) can be rewritten as

$$\frac{n}{m} = \frac{1}{\left(\frac{N \mu^2}{3R X_g T} - 1 \right)} \quad (3.3)$$

where μ is the effective spin-only magnetic moment of paramagnetic ions. Thus the variation of $X_g T$ with temperature would provide information on the transformation of spin states. The plots of $X_g T$ versus T for $\text{LaCo}_{1-x}\text{Ti}_x\text{O}_3$ system are given in Fig. 3.1. These plots indicate that the proportion n/m remains constant for $x = 0.05$ and 0.15 upto 350 K. There is a change in slope in the 350 - 550 K range for all the four compositions studied. Similar behaviour was observed in the parent system LaCoO_3 [2]. For all the compositions $X_g T$ decrease rather sharply after 500 K indicating a rapid decrease of paramagnetic ions population. Similar changes have also been observed in the Mössbauer data (discussed below) of these compounds.

We have studied the variation in the spin state equilibrium in these compounds by means of ^{57}Fe Mössbauer spectroscopy. Room temperature Mössbauer spectra measured for various compositions of $\text{LaCo}_{1-x}\text{Ti}_x\text{O}_3$ (i.e. $x = 0.50, 0.30, 0.15$ and 0.05) with the help of enriched PFC single crystal absorber are shown in Fig. 3.2. Mössbauer spectra for various compositions of $\text{LaCo}_{1-x}\text{Ti}_x\text{O}_3$ recorded at various temperatures ($78, 295, 400, 500, 600$ and 800 K) using ^{57}Fe absorber are

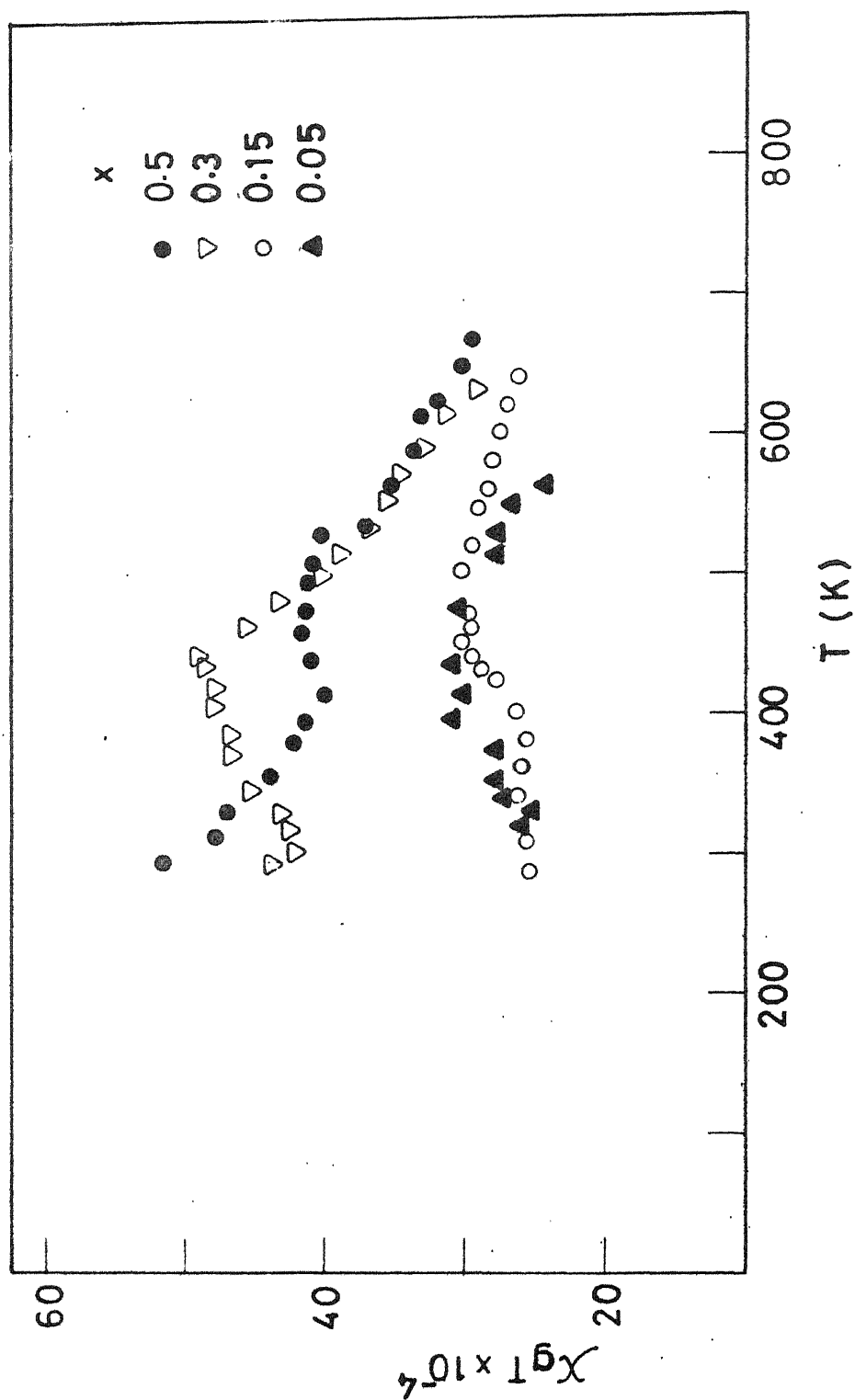


Fig.3.1 Plot of $\chi_g T$ versus temperature (T) for the system $\text{La Co}_{1-x}\text{Ti}_x\text{O}_3$.

Fig. 3.2 Mossbauer spectra of $\text{LaCo}_{1-x}\text{Ti}_x\text{O}_3$ system recorded at room temperature (295K) using PFC absorber.

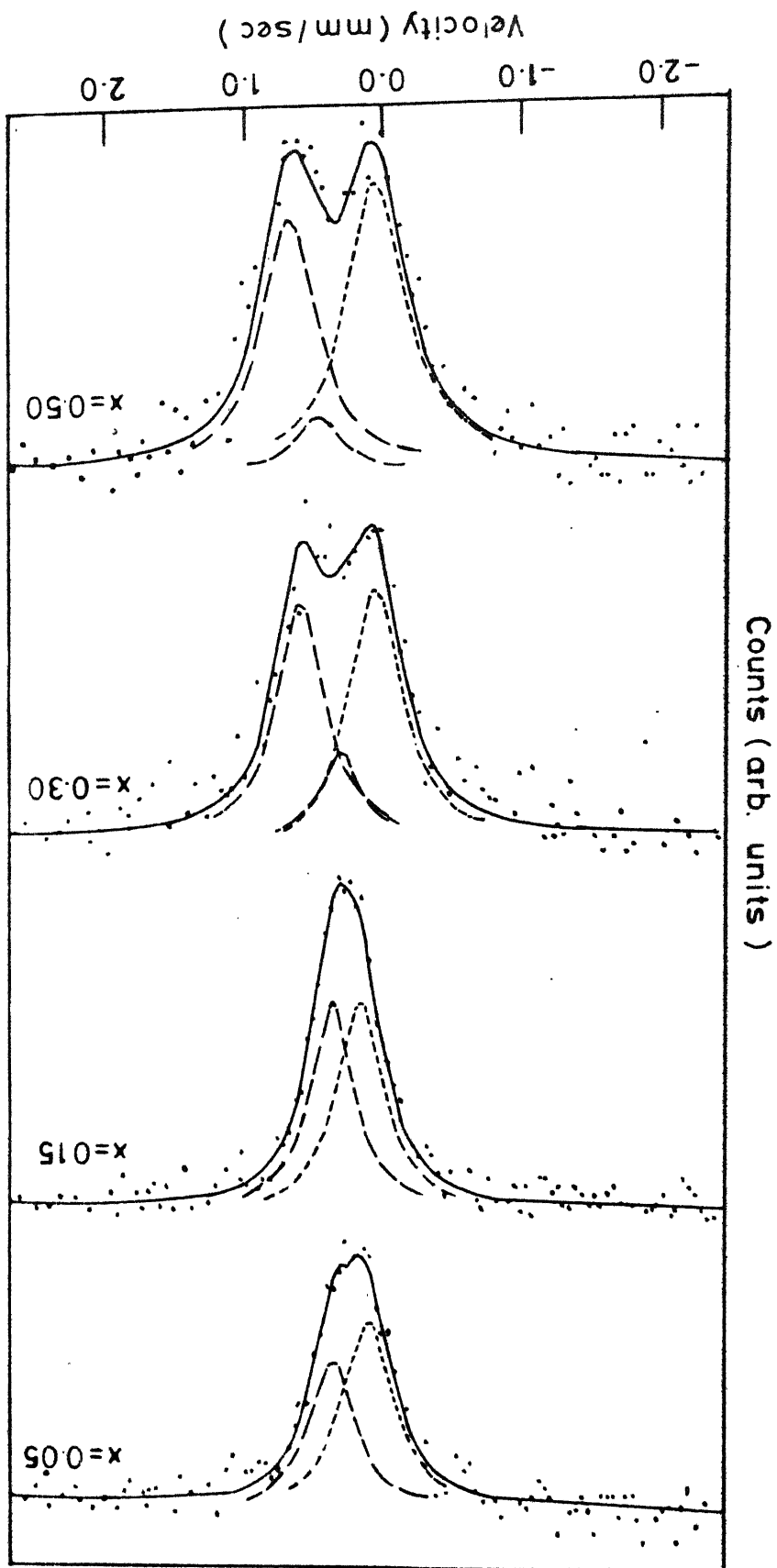


Table 3.2 Mossbauer parameters for $\text{LaCo}_{1-x}\text{Ti}_x\text{O}_3$ at 295 K (room temperature) measured using PFC absorber.

Composition x	First resonance		Second resonance		Third resonance		Total area under resonance %
	IS [#] (mm/sec)	Peak width (mm/sec)	Area %	IS [#] (mm/sec)	Peak width (mm/sec)	Area %	
0.50	0.05(1)	0.52(3)	51.2	0.47(1)	0.39(6)	7.4	0.91
0.30	0.06(1)	0.45(1)	45.9	0.32(2)	0.38(5)	13.2	0.62
0.15	0.19(1)	0.42(2)	52.3	0.39(1)	0.38(1)	47.7	0.93
0.05	0.12(5)	0.45(4)	58.1	0.38(1)	0.40(1)	41.9	0.88

[#] Zero of velocity scale refers to the peak position obtained using standard ^{57}Co source in Rh matrix.

[#] Error in the least significant digit are given in adjacent paranthesis.

shown in Fig. 3.3(a) for $x = 0.50$, (b) $x = 0.30$, (c) $x = 0.15$ (d) $x = 0.05$. None of these spectra show presence of magnetic Zeeman splitting. All the spectra show the presence of two or three resonance lines. The resolution between these resonance lines appears better in the case of those spectra which are recorded using PFC absorber.

The room temperature Mössbauer parameters for different compositions of $\text{LaCo}_{1-x}\text{Ti}_x\text{O}_3$ evaluated from the Mössbauer spectra (Fig. 3.2), recorded using enriched PFC absorber, are summarised in Table 3.2. The observed temperature variation of isomer shift (IS) for various compositions of $\text{LaCo}_{1-x}\text{Ti}_x\text{O}_3$ is given in Table 3.3 and plotted in Fig. 3.4(a) for $x = 0.50$, (b) $x = 0.30$, (c) $x = 0.15$ and (d) $x = 0.05$. These IS values were determined using 310SS absorber and the zero of velocity scale refers to the position of resonance line observed using standard ^{57}Co source in Rh matrix. The observed peak-width (FWHM) of resonance lines at various temperatures in the Mössbauer spectra of $\text{LaCo}_{1-x}\text{Ti}_x\text{O}_3$ are given in Table 3.4. Also shown, are temperature variation of percent area of the peaks and of total area under resonance in Table 3.5.

Three resonance peaks are observed in Mössbauer spectra of $\text{LaCo}_{1-x}\text{Ti}_x\text{O}_3$ with $x = 0.50$ and 0.30 . At room temperature these resonance peaks are observed at 0.19 ± 0.01 , 0.44 ± 0.02 and 0.75 ± 0.01 mm/sec for $x = 0.50$ and at 0.08 ± 0.01 ,

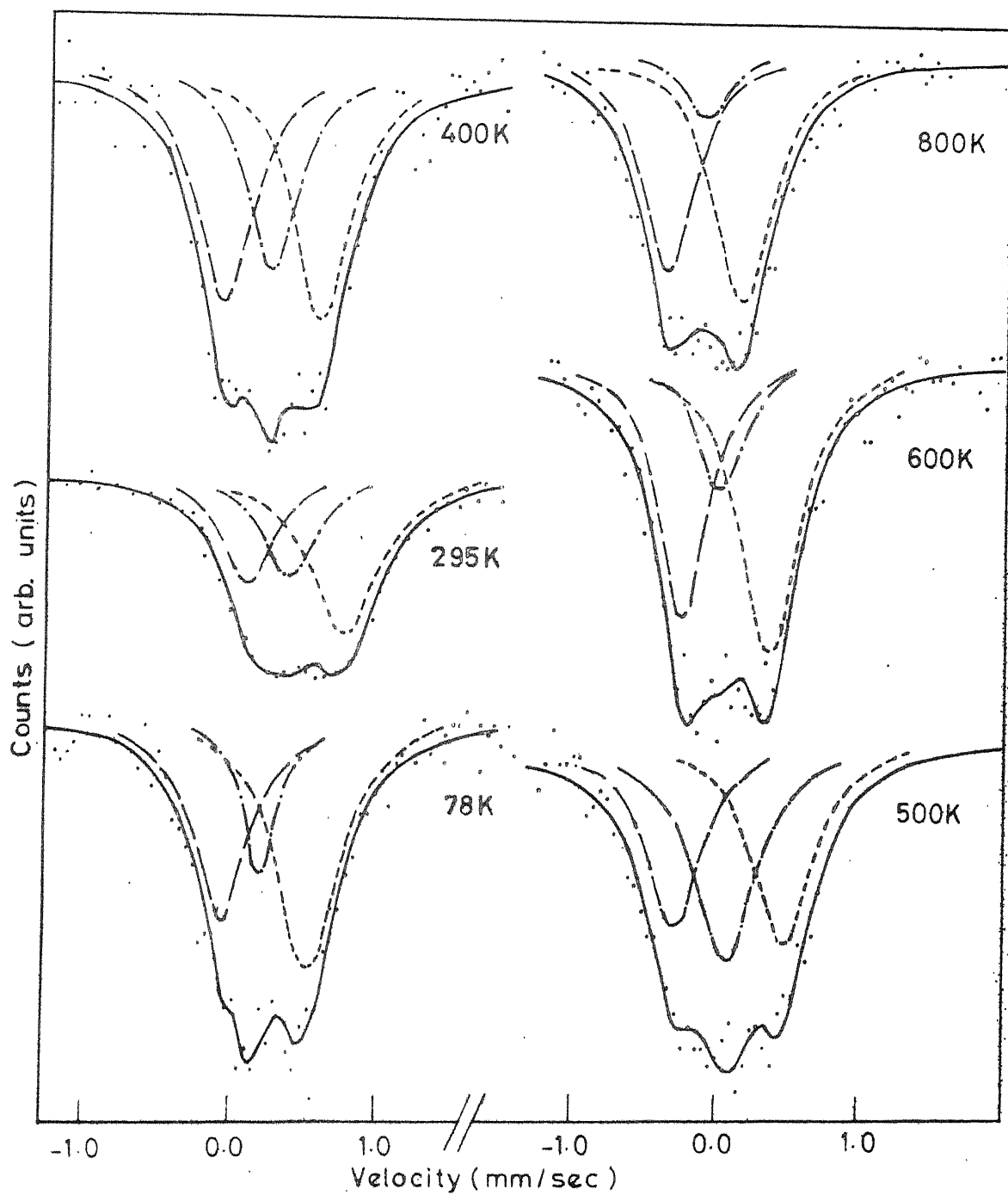


Fig. 33(a) Mossbauer spectra of $\text{LaCo}_{0.5}\text{Ti}_{0.5}\text{O}_3$ recorded at various temperature using 310 stainless steel absorber.

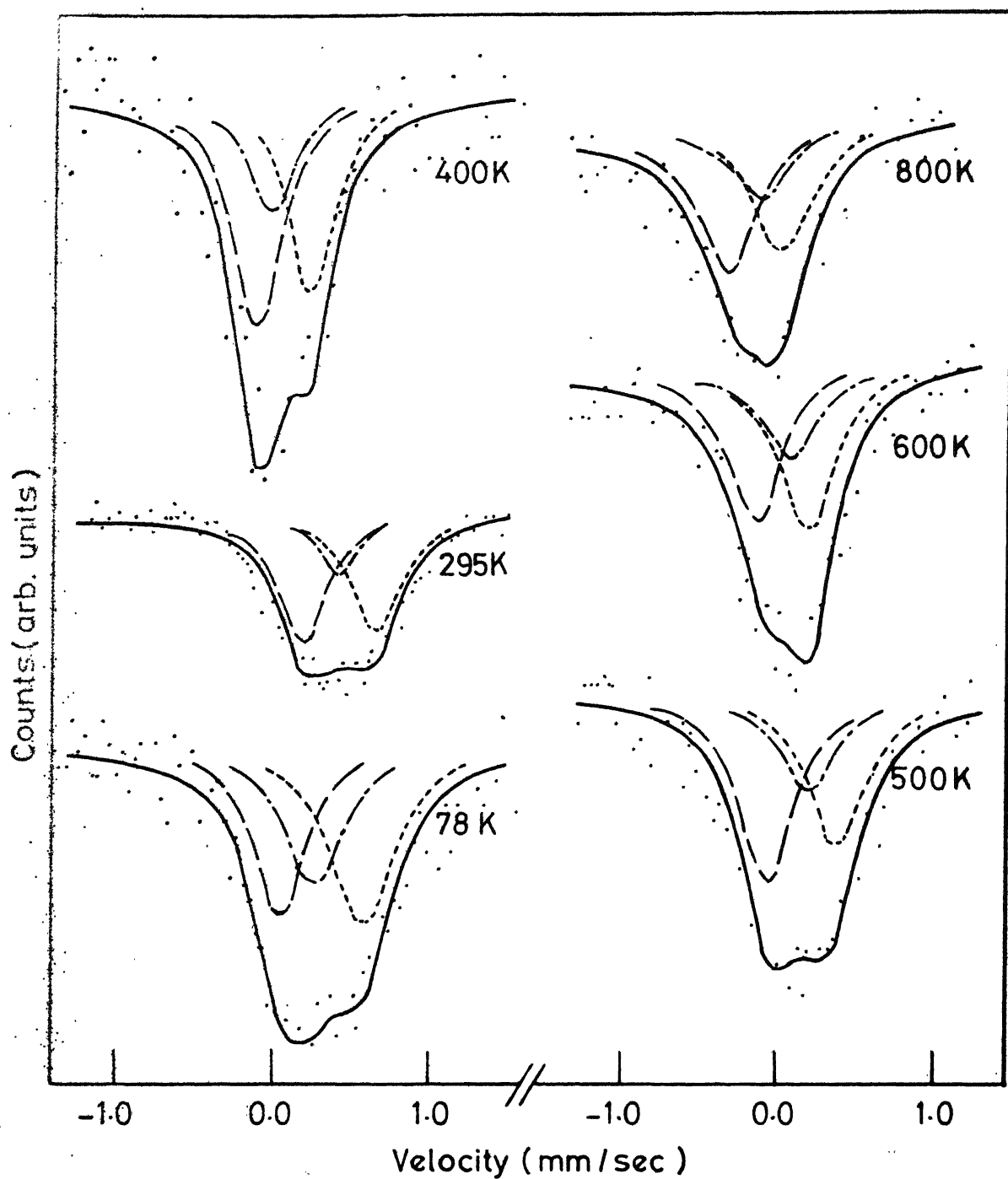


Fig.3.3(b) Mossbauer of $\text{LaCo}_{1-x}\text{Ti}_x\text{O}_3$ ($x=0.3$) recorded at various temperatures using 310 stainless steel absorber.

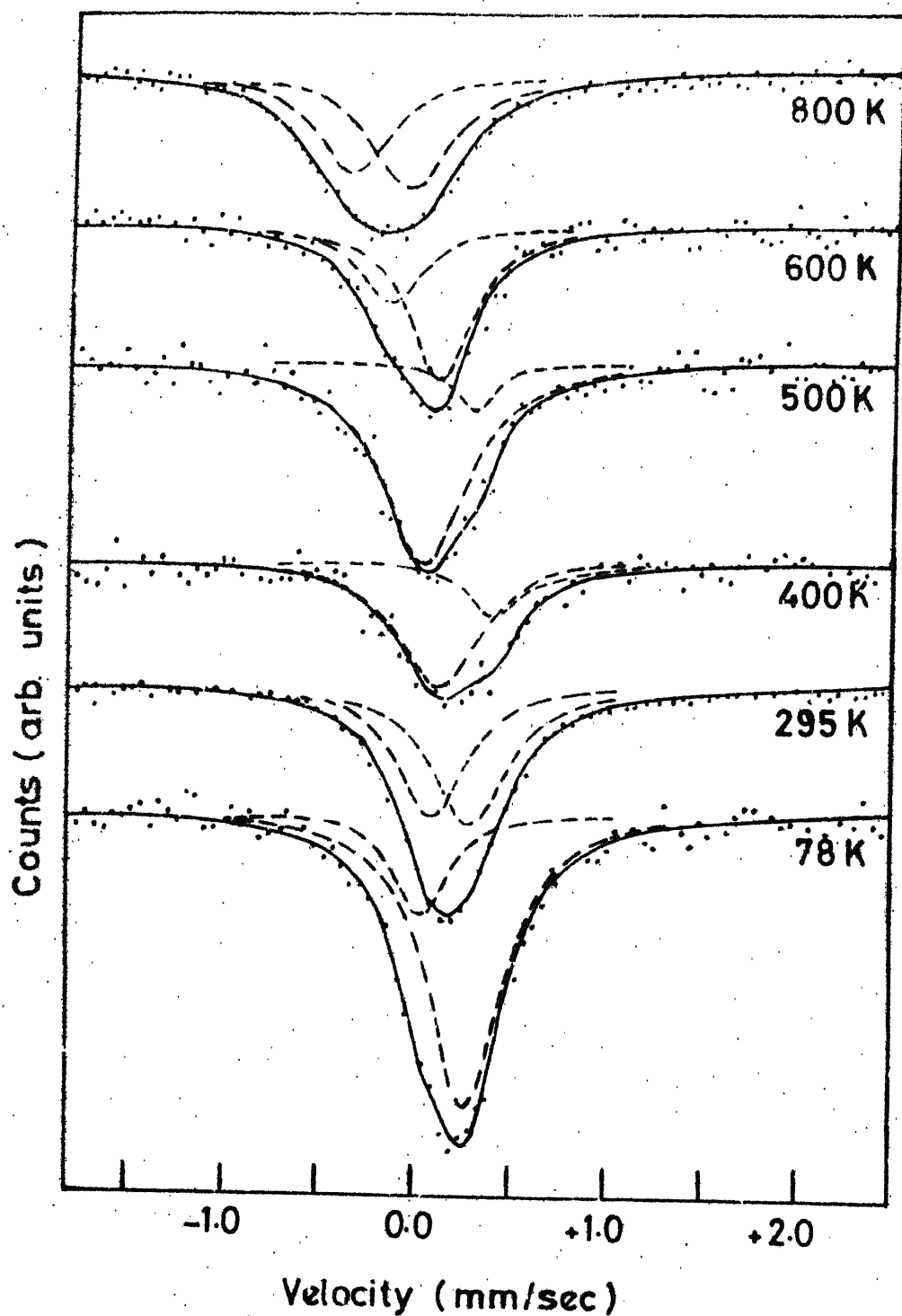


Fig3.3(c) Mössbauer spectra of $\text{LaCo}_{1-x}\text{Ti}_x\text{O}_3$ ($x=0.15$) measured at various temperature using 310 stainless steel absorber.

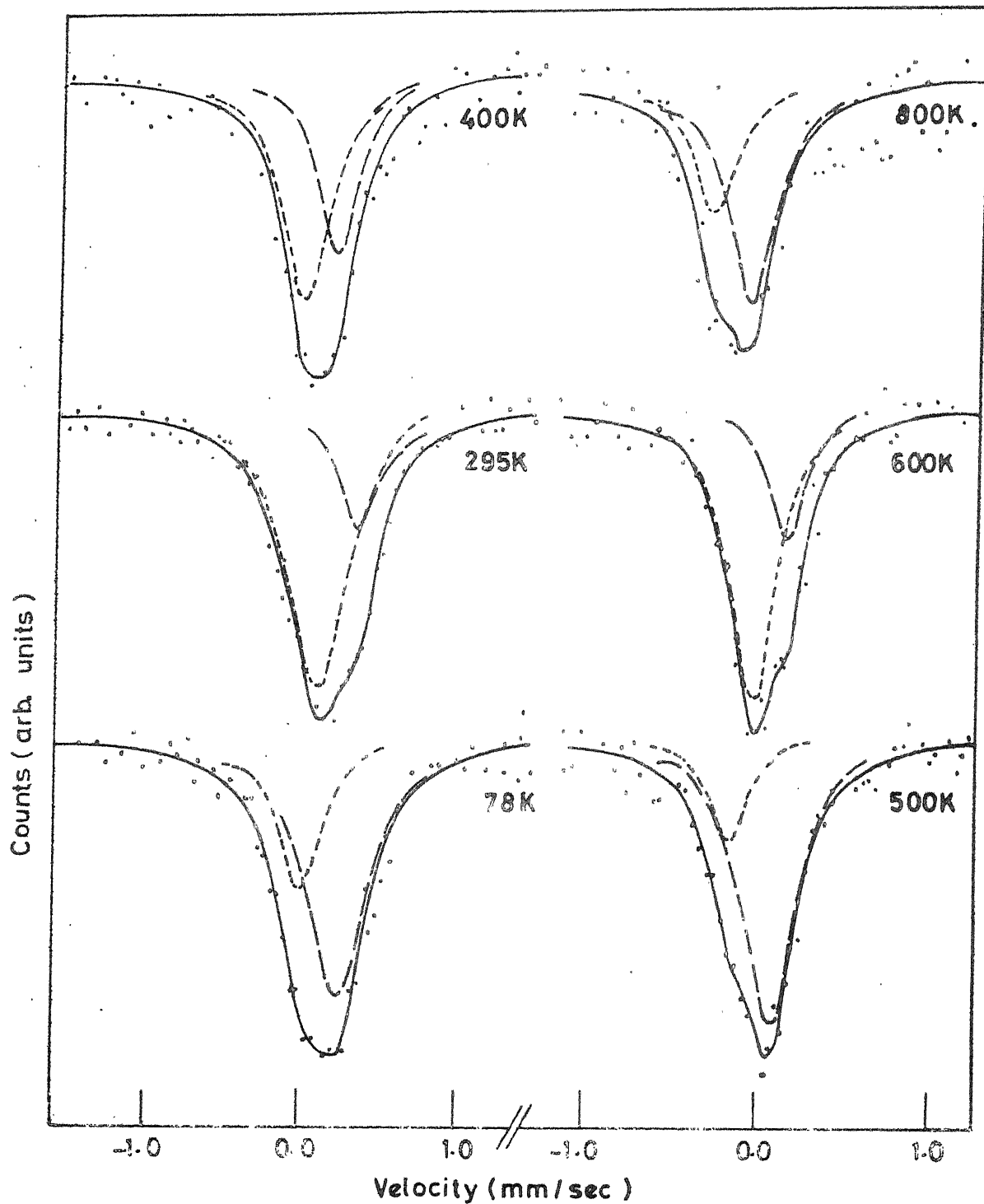


Fig. 3.3(d) Mössbauer spectra of $\text{LaCo}_{0.95}\text{Ti}_{0.05}\text{O}_3$ recorded at various temperature using 310 stainless steel absorber.

Table 3.3 Temperature variation of isomer shift[‡] (measured using 210SS absorber) for $\text{LaCo}_{1-x}\text{Ti}_x\text{O}_3$.

Compo- sition x	First resonance ($\text{Co}^{\text{III,II,IV}}$)			Second resonance (Co^{3+})			Third resonance (Co^{2+})		
	78K	295K	400K 500K 600K 800K	78K	295K	400K 500K 600K 800K	78K	295K	400K 500K 600K 800K
0.50	-0.04	0.08	-0.20 -0.31 -0.21 -0.34	0.19	0.36	0.12 0.06 0.05 -0.08	0.51	0.75	0.46 0.45 0.38 0.20
0.30	0.04	0.09	-0.12 -0.05 -0.11 -0.22	0.27	0.34	-0.02 0.20 0.14 0.00	0.59	0.58	0.25 0.38 0.23 0.14
0.15	0.05	0.13	0.20 0.02 -0.16 -0.44	0.28	0.34	0.48 0.28 0.09 -0.07			
0.05	0.03	0.13	0.05 -0.14 -0.01 -0.20	0.27	0.38	0.26 0.11 0.23 0.01			

[‡] IS values are in mm/sec and zero velocity refers to the peak position observed using standard ^{57}Co source in Rh matrix.

^{‡‡} Average error in IS values is ± 0.02 mm/sec (maximum error is ± 0.04 and minimum is ± 0.01 mm/sec).

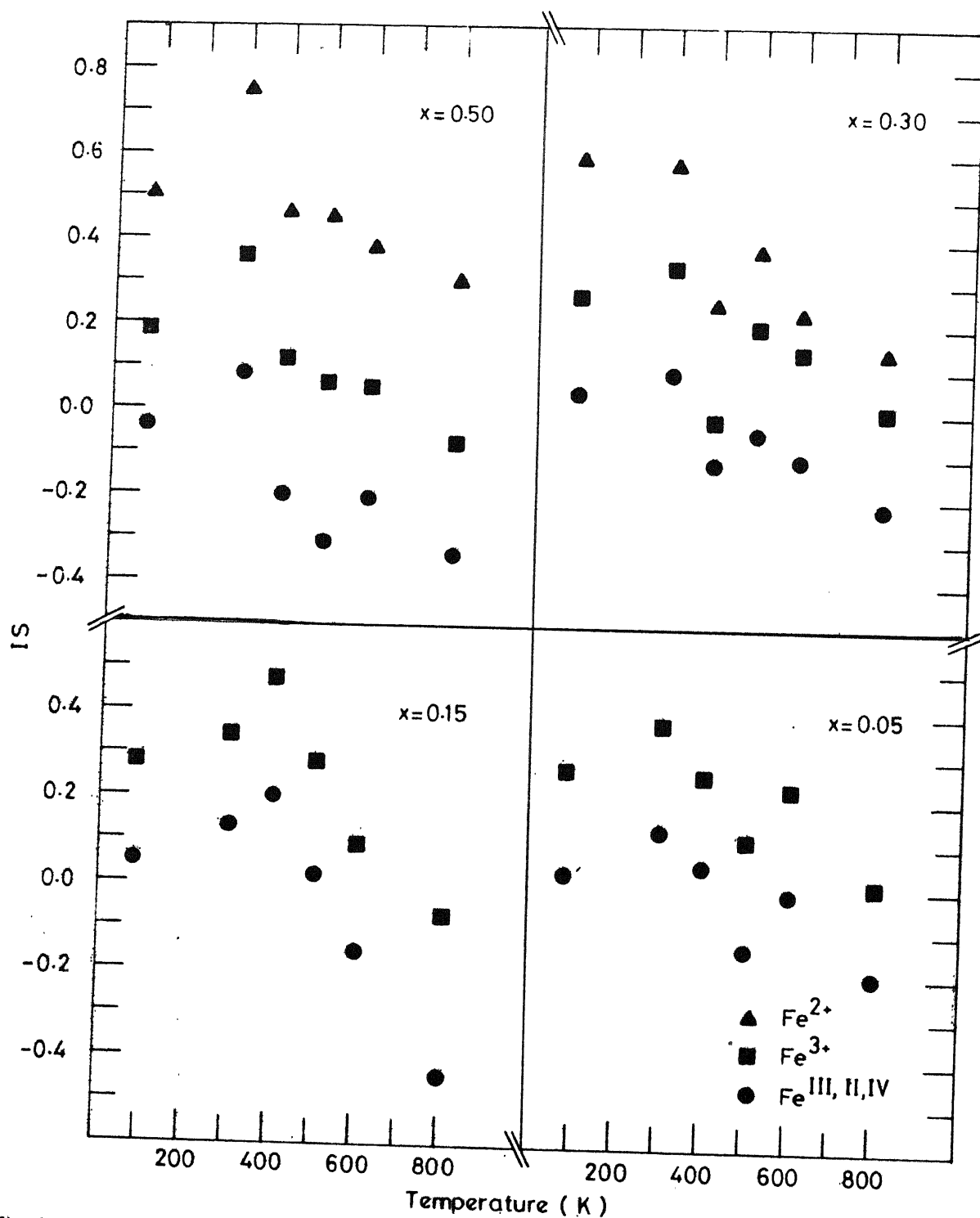


Fig.3.4 Temperature variation of isomer shift (IS) observed in $\text{LaCo}_{1-x}\text{Ti}_x\text{O}_3$ using 310 stainless steel absorber.

Table 3.4 Observed peak width^a (FWHM) of resonance lines at various temperature in different compositions of $\text{LaCo}_{1-x}\text{Ti}_x\text{O}_3$.

Com- posi- tion x	First resonance (Co ^{III,II,IV})				Second resonance (Co ³⁺)				Third resonance (Co ²⁺)			
	78 K	295 K	400 K	500 K	600 K	800 K	78 K	295 K	400 K	500 K	600 K	800 K
0.50	0.49(1)	0.45(1)	0.47(1)	0.47(1)	0.41(1)	0.47(3)	0.39(2)	0.49(1)	0.42(1)	0.52(2)	0.40(9)	0.41(2)
0.30	0.43(2)	0.40(6)	0.39(4)	0.42(6)	0.42(1)	0.45(2)	0.50(10)	0.32(5)	0.37(1)	0.47(1)	0.49(4)	0.49(5)
0.15	0.34(10)	0.50(4)	0.51(8)	0.52(5)	0.41(13)	0.55(6)	0.47(3)	0.60(3)	0.31(15)	0.25(17)	0.39(7)	0.61(5)
0.05	0.37(8)	0.47(3)	0.38(3)	0.30(4)	0.33(4)	0.30(1)	0.48(3)	0.30(6)	0.32(7)	0.42(3)	0.25(8)	0.37(3)

^aPeak width are given in mm/sec.^bError in the least significant digit are given in brackets.Table 3.5 Temperature variation of percent area of various resonance peaks and total area under resonance observed in $\text{LaCo}_{1-x}\text{Ti}_x\text{O}_3$.

Temperature resonance	Percent area of various resonances																		Total Area Under Resonance																																			
	Temperature																																																					
	78 K						295 K						400 K						500 K						600 K						800 K																							
Com- posi- tion x	Resonance Peak																		78K						295K						400K						500K						600K						800K					
	I	II	III	I	II	III	I	II	III	I	II	III	I	II	III	I	II	III																																				
0.50	37.2	18.4	44.4	25.6	26.1	48.3	34.5	27.3	38.2	30.6	38.3	31.1	35.8	17.5	46.7	40.3	10.3	49.4	0.85	3.60	1.30	1.46	1.28	1.41	1.12	0.96	0.57	0.86	0.68	0.66	1.72	1.17	0.86	0.96	0.76	1.53	1.44	1.57	0.86	0.85	0.62	0.66												
0.30	32.1	29.2	38.7	43.7	16.2	40.1	43.3	20.8	35.9	42.7	22.9	34.4	35.3	23.8	40.9	41.9	19.5	38.6																																				
0.15	19.6	80.4	40.4	40.4	59.6	78.3	21.7	89.2	10.8	33.9	66.1	44.2	55.8																																									
0.05	32.9	67.1	77.8	22.2	60.3	39.7	20.7	79.3	72.0	28.0	34.3	65.7																																										

0.34 ± 0.03 and 0.68 ± 0.01 mm/sec for $x = 0.30$. Only two resonance peaks are observed in samples with $x = 0.05$ and 0.15 . At room temperature the peak positions are 0.13 ± 0.01 , 0.34 ± 0.02 mm/sec for $x = 0.15$ and 0.13 ± 0.01 , 0.38 ± 0.01 mm/sec for $x = 0.05$. Using the systematics of IS values reported by Greenwood and Gibbs [19] (also shown in Fig. 1.4 of Chapter 1) the resonances can be assigned to $\text{Co}^{\text{III,II,IV}}$, Co^{3+} and Co^{2+} states respectively which are known to exist in $\text{LaCo}_{1-x}\text{Ti}_x\text{O}_3$ [18]. Other possibilities must be excluded before assigning these resonances due to different valence states of cobalt. One such possibility is that the two peaks out of the observed peaks may be the quadrupole split partners of a single valence state. This seems most unlikely since the intensity of three peaks are unequal and are uneven. Furthermore, the observed temperature variation of percent area of three peaks (see Table 3.5) excludes the possibility of any two peaks being partners of a quadrupole split spectrum. Hence the assignment, of the observed three peaks to $\text{Co}^{\text{III,II,IV}}$, Co^{3+} and Co^{2+} in increasing velocity order is justified. The sample with low value of x (i.e. $x = 0.15$ and 0.05) does not show the presence of third peak (Co^{2+}) which is present in samples with large x (i.e. $x = 0.30$ and 0.50). It indicates that divalent cobalt generated by substitution of Ti^{4+} in samples with low value of x (i.e. 0.15 and 0.05) are in low-spin (Co^{II}) state.

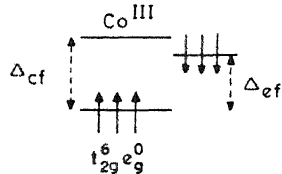
The other possibility is that cobalt might also be present in divalent high-spin (Co^{2+}) state but probably due to small concentration of these Co^{2+} ions, they are not detectable in Mössbauer spectra of these compounds. In sample with larger x (i.e. $x = 0.30$ and 0.50) divalent cobalt generated by substitution of Ti^{4+} exists in high-spin Co^{2+} state which give the third resonance peak in Mössbauer spectra of these compounds. The above behaviour could be explained as in $\text{LaCo}_{1-x}\text{Ti}_x\text{O}_3$ distortion from cubic symmetry decreases as x increases. The crystal field splitting also decreases as x increases, making low-spin state (Co^{II}) energetically favourable for low value of x and high-spin (Co^{2+}) state for high value of x .

Assuming that the three resonances are due to $\text{Co}^{\text{III,II,IV}}$, Co^{3+} and Co^{2+} , we have tabulated in Table 3.5 the percent intensities of these resonances at various temperatures to obtain the relative populations of $\text{Co}^{\text{III,II,IV}}$, Co^{3+} and Co^{2+} states. The intensity of these resonances was determined from the area under the respective Lorentzian, after they were resolved (see Fig. 3.3). In this analysis we have assumed that the Debye-Waller factor for the three states of cobalt in $\text{LaCo}_{1-x}\text{Ti}_x\text{O}_3$ is about the same. This assumption is justified to some extent because all the cobalt sites in $\text{LaCo}_{1-x}\text{Ti}_x\text{O}_3$ may be occupied by any of the cobalt species. Bhide et al. [7] have

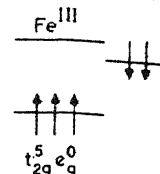
established that following the electron capture decay of $^{57}\text{Co} \rightarrow ^{57}\text{Fe}$, the low-spin cobalt ion leads to respective low-spin iron ion and the high-spin cobalt gives rise to respective high-spin iron. The schematic energy level diagram [7] relevant for this decay is shown in Fig. 3.5. We have extended these results and have assumed that in $\text{LaCo}_{1-x}\text{Ti}_x\text{O}_3$ population of $\text{Fe}^{\text{III,II,IV}}$, Fe^{3+} and Fe^{2+} observed in its Mössbauer spectra reflects the population of $\text{Co}^{\text{III,II,IV}}$, Co^{3+} and Co^{2+} respectively. The relative population of high-spin (Co^{3+} , Co^{2+}) and low-spin ($\text{Co}^{\text{III,II,IV}}$) states evaluated from Mössbauer spectra of $\text{LaCo}_{1-x}\text{Ti}_x\text{O}_3$ system is given in Table 3.6. The area ratio of high-spin (Co^{3+} , Co^{2+}) and low-spin ($\text{Co}^{\text{III,II,IV}}$) for each composition (see Table 3.6) shows a change at about 500 K, which is consistent with earlier magnetic susceptibility and electron transport studies [18]. Except the change around 500 K, there is no systematic trend in the area ratio. It is interesting that the plot of electrical resistivity [18] and thermo-electric power versus inverse of temperature (Fig. 3.6) also shows changes around 500 K for all the compositions. The change is more obvious in samples with small x (i.e. $x = 0.05$ and 0.15).

The temperature variations of isomer shift (IS) of various resonances observed in $\text{LaCo}_{1-x}\text{Ti}_x\text{O}_3$ system are

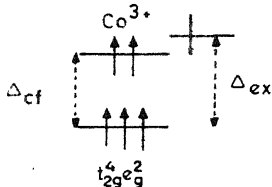
TRIVALENT LOW-SPIN COBALT

ELECTRON
CAPTURE

TRIVALENT LOW-SPIN IRON



TRIVALENT HIGH-SPIN COBALT

ELECTRON
CAPTURE

TRIVALENT HIGH-SPIN IRON

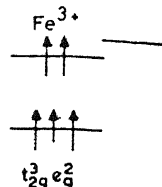
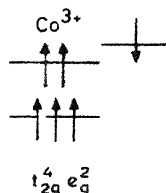
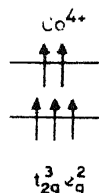
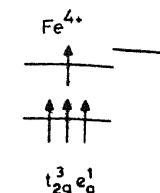
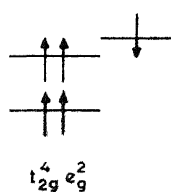
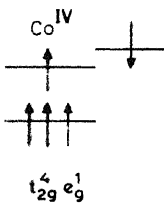
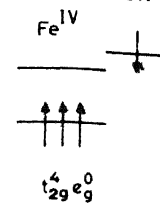
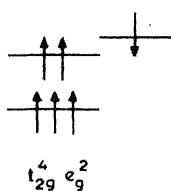
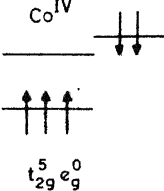
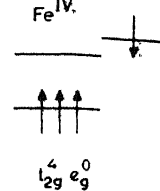
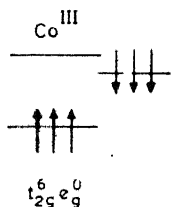
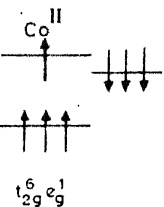
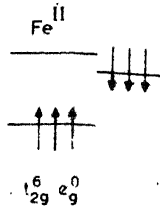
HIGH-SPIN
TRIVALENT COBALTTRANSFER OF
AN ELECTRONHIGH-SPIN
TRIVALENT COBALTELECTRON
CAPTUREHIGH-SPIN
TRIVALENT IRONINTERMEDIATE
TETRAVALENT COBALTTRANSFER OF
AN ELECTRONELECTRON
CAPTURELOW-SPIN
TETRAVALENT IRONLOW-SPIN
TETRAVALENT COBALTTRANSFER OF
AN ELECTRONELECTRON
CAPTURELOW-SPIN
TETRAVALENT IRONLOW-SPIN
TETRAVALENT COBALTADDITION OF
AN ELECTRONLOW-SPIN
DIVALENT COBALTELECTRON
CAPTURELOW-SPIN
DIVALENT IRON

Fig 3.5 Spin states of cobalt and consequent iron

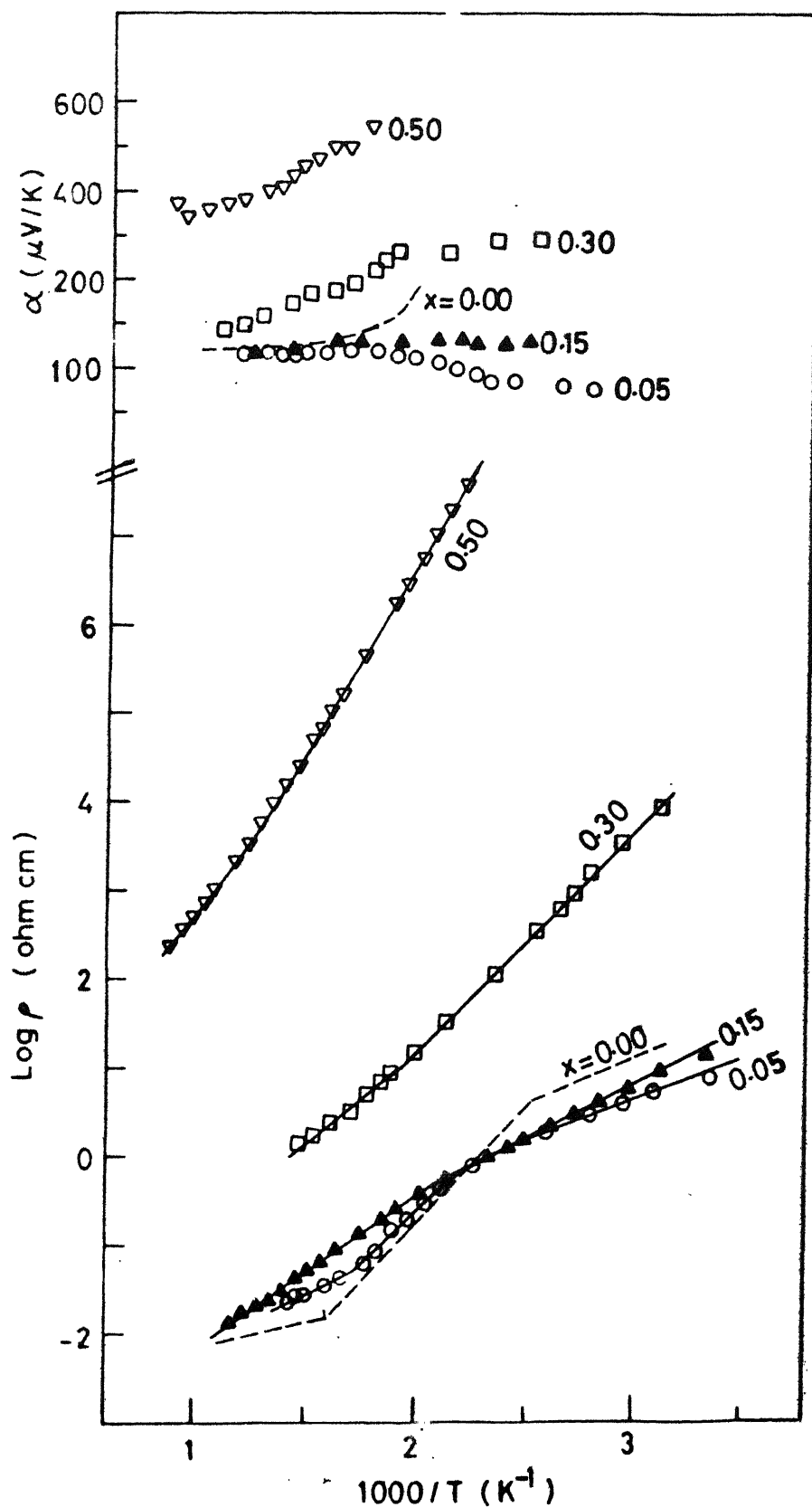


Fig.3.6 Plot of $\log \rho$ and α versus $1000/T$ for the system $\text{LaCo}_{1-x}\text{Ti}_x\text{O}$

Table 3.6 Temperature variation of relative population of high-spin (Co^{3+} , Co^{2+}) and low-spin ($\text{Co}^{\text{III,II,IV}}$) cobalt ions for $\text{LaCo}_{1-x}\text{Ti}_x\text{O}_3$.

Composition x	78 K	295 K	400 K	500 K	600 K	800 K
0.50	1.69	2.91	1.90	2.28	1.79	1.48
0.30	2.25	1.29	1.30	1.34	1.83	1.39
0.15	4.10	1.48	0.28	0.12	1.95	1.26
0.05	2.04	0.28	0.66	3.83	0.38	1.91

shown in Fig. 3.4 and Table 3.3. The IS for all the compositions decreases rather substantially with the increase in temperature. The decrease in IS may occur due to following possibilities.

- (i) Change in mean square velocity, $\langle v^2 \rangle$ giving rise to changes in the second order Doppler shift [20].
- (ii) Change in IS arising because of thermal displacement of neighbouring atoms.
- (iii) Generation of cobalt species which have lower IS values.

The observed changes in IS values (Fig. 3.4) cannot be fully accounted for as due to second order Doppler shift (δ_{SOD}) because the observed changes are $\delta_{\text{SOD}} > -0.073 \times 10^{-2}$ mm/sec-K [21] (the maximum theoretical value of second order Doppler shift in case of ^{57}Fe 14.4 keV gamma-ray). If the observed changes are attributed to ionic vibrations, the decrease in IS would imply greater covalency and increase in the overlap integrals [10].

It is known that divalent cobalt ions are generated when Ti^{4+} is substituted in LaCoO_3 to form $\text{LaCo}_{1-x}\text{Ti}_x\text{O}_3$ [18]. Mossbauer spectra of $\text{LaCo}_{1-x}\text{Ti}_x\text{O}_3$ recorded at room temperature using PFC absorber (Fig. 3.2) show presence of a broad resonance peak at 0.65 ± 0.02 mm/sec for $x = 0.50$ and at 0.55 ± 0.03 mm/sec for $x = 0.30$ when fitted for two resonances.

The larger peak width 0.62 ± 0.05 mm/sec for $x = 0.50$ and 0.58 ± 0.08 mm/sec for $x = 0.30$ suggest the presence of more than two resonance peaks in these Mössbauer spectra. Hence we have fitted these spectra for three peaks (Fig. 3.2). The Mössbauer parameters obtained from these spectra are given in Table 3.2. The samples with $x = 0.05$ and $x = 0.15$, however, show only two resonance peaks at about 0.04 mm/sec ($\text{Co}^{\text{III,II,IV}}$) and 0.19 mm/sec (Co^{3+}). These results indicate the presence of $\text{Co}^{\text{III,II,IV}}$, Co^{3+} in all the samples. In addition, Co^{2+} is present in samples with $x = 0.50$ and 0.30 . Similar behaviour has been observed in the Mössbauer spectra recorded using ^{57}Fe absorber.

3.3.2 System $\text{La}_{1-x}\text{Sr}_x\text{Co}_{1-x}\text{Ti}_x\text{O}_3$

This system is stoichiometric for all values of x . The charge compensation takes place due to simultaneous substitution of Sr^{2+} at La^{3+} site and Ti^{4+} at Co^{3+} site. By using electrical and magnetic measurements, Bahadur et al. [18] have confirmed that in this system cobalt exists only in trivalent state.

Thus, in this system the transformation is mainly between paramagnetic Co^{3+} ion and diamagnetic Co^{III} ion. Hence for this system equation (3.4) can be written as

$$\frac{n}{m} = \frac{Co^{3+}}{Co^{III}} = \frac{1}{\left(\frac{N\mu^2}{3R \times_g T} - 1 \right)} = \frac{\text{Paramagnetic ions}}{\text{Diamagnetic ions}} \quad (3.5)$$

where μ is the spin only magnetic moment of paramagnetic ion. Plots of $\chi_g T$ versus temperature for $La_{1-x}Sr_xCo_{1-x}Ti_xO_3$ system are given in Fig. 3.7. These plots indicate that proportion n/m remains constant up to about 450 K for all compositions of $La_{1-x}Sr_xCo_{1-x}Ti_xO_3$. For $x = 0.50$ and 0.30 $\chi_g T$ increases continuously in 450-650 K range and thereafter it remains constant. The increase in $\chi_g T$ indicates increase in the population of paramagnetic ions (Co^{3+}). For $x = 0.05$ and 0.15 a sharp change has been observed in $\chi_g T$ vs. T plot at 480 K for $x = 0.05$ and at 560 K for $x = 0.15$. The $\chi_g T$ decreases rapidly after $T = 560$ K for both the compositions. This decrease in $\chi_g T$ value implies decrease in the population of paramagnetic ions after $T = 560$ K.

We sought to confirm the above variation in the spin state equilibria by means of ^{57}Fe temperature dependent Mossbauer spectroscopy of $La_{1-x}Sr_xCo_{1-x}Ti_xO_3$ system. Room temperature Mossbauer spectra of $La_{1-x}Sr_xCo_{1-x}Ti_xO_3$ measured using enriched PFC absorber are shown in Fig. 3.8. Mössbauer parameters evaluated from the spectra (Fig. 3.8) are given in Table 3.7. Mössbauer spectra of the

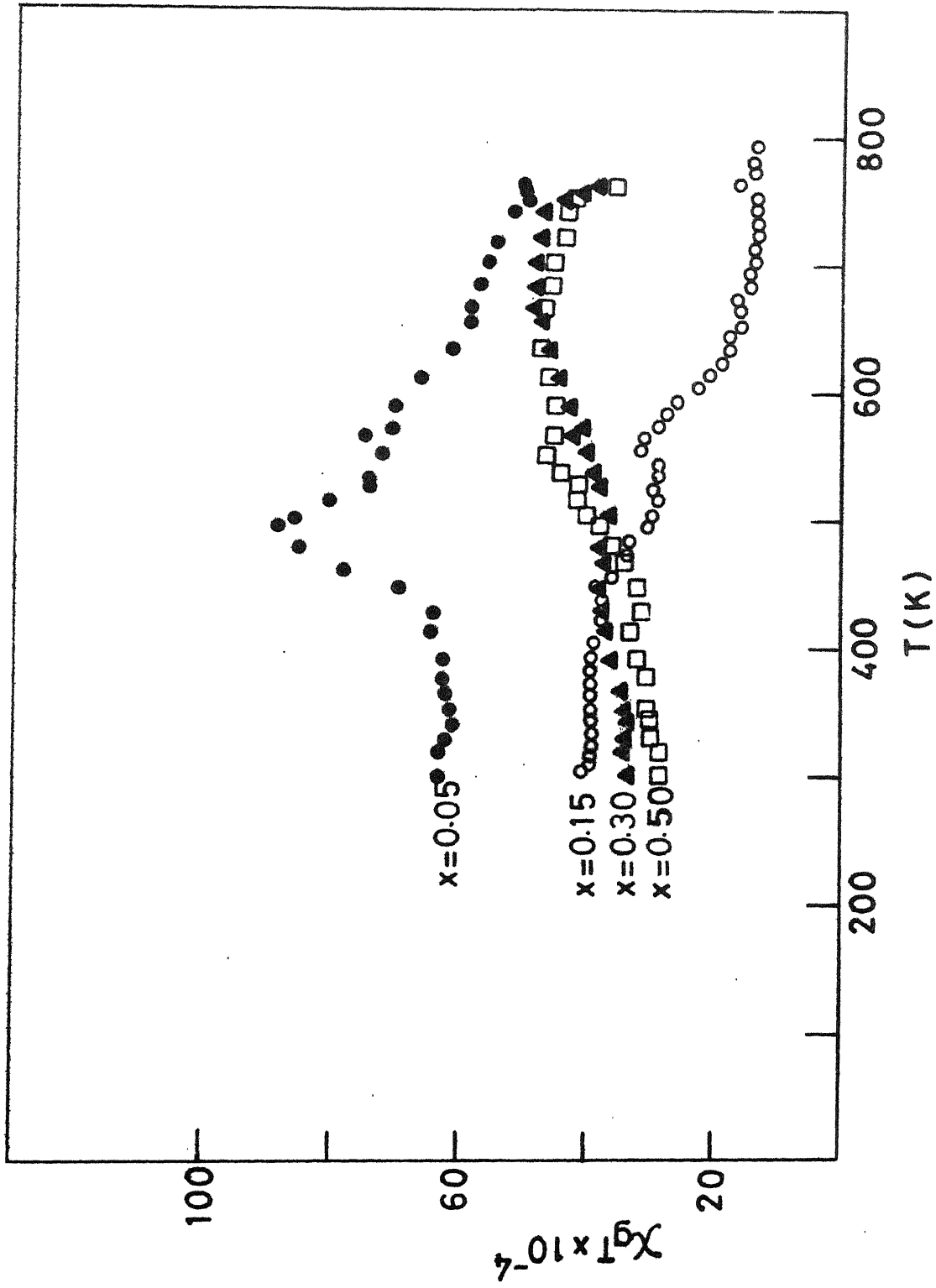


Fig.3.7 Plot of $\chi_g T$ against temperature (T) for various compositions of $\text{La}_{1-x}\text{Sr}_x\text{Co}_{1-x}\text{Ti}_x\text{O}_3$

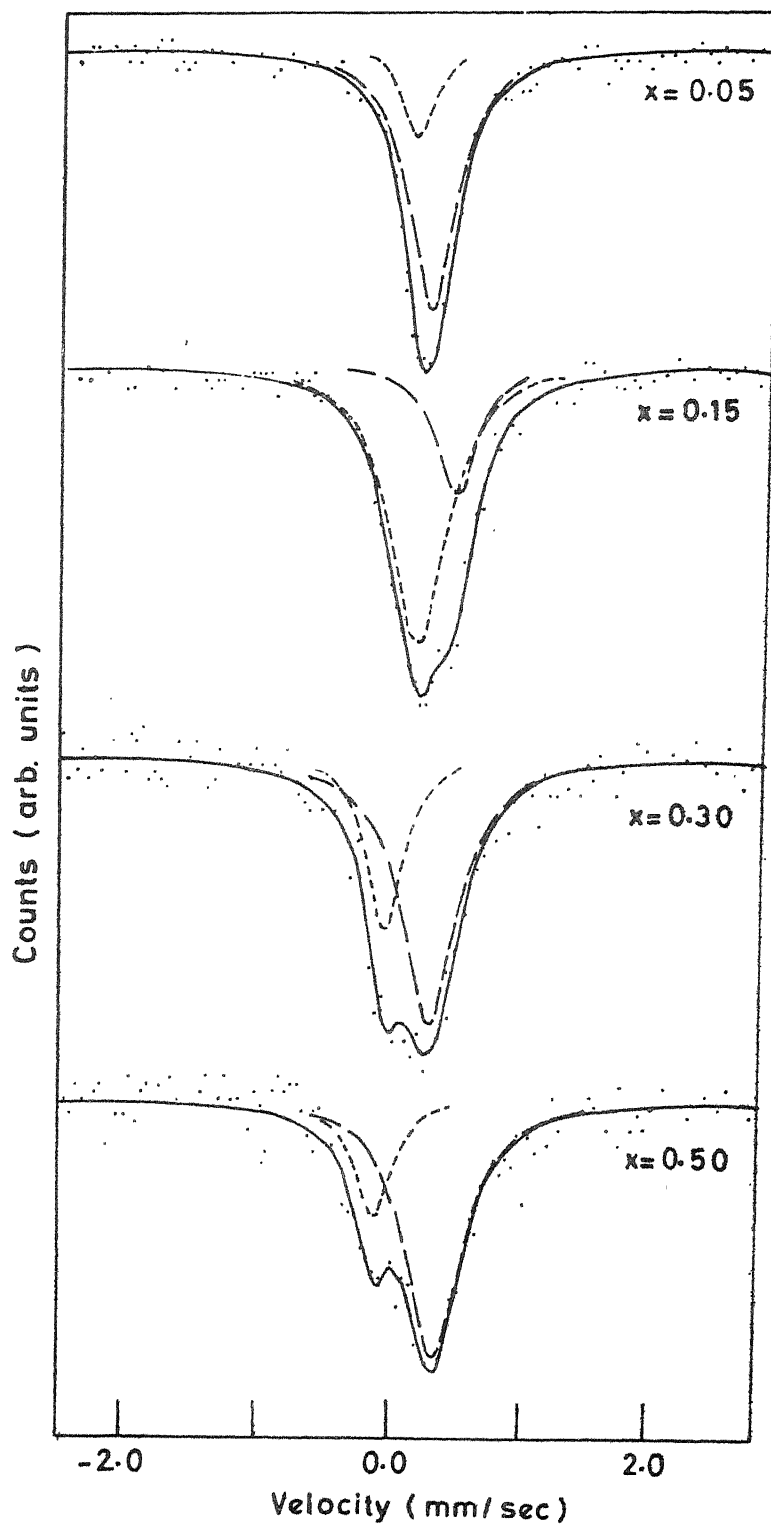


Fig. 3.8 Mössbauer spectra of $\text{La}_{1-x}\text{Sr}_x\text{Co}_{1-x}\text{Ti}_x\text{O}_3$ system recorded at room temperature (295K) using PFC absorber.

Table 3.7 Mössbauer parameters for $\text{La}_{1-x}\text{Sr}_x\text{Co}_{1-x}\text{Ti}_x\text{O}_3$ at 295 K (room temperature) measured using PFC absorber.

Composition x	Low-velocity resonance			High-velocity resonance			Total area under resonance %
	IS [‡] (mm/sec)	Peak width (mm/sec)	Area %	IS [‡] (mm/sec)	Peak width (mm/sec)	Area %	
0.50	-0.08±.02	0.36±.04	24.1	0.39±.01	0.52±.11	75.9	0.53
0.30	-0.01±.01	0.34±.03	29.6	0.34±.01	0.53±.06	70.4	0.97
0.15	0.21±.01	0.54±.01	74.4	0.50±.01	0.38±.01	25.6	1.12
0.05	0.18±.02	0.30±.10	18.8	0.30±.01	0.44±.01	81.2	1.18

*Zero of velocity scale refers to peak position obtained using standard ^{57}Co source in Rh matrix.

$\text{La}_{1-x}\text{Sr}_x\text{Co}_{1-x}\text{Ti}_x\text{O}_3$ recorded at various temperatures using 310SS absorber are shown in Fig. 3.9 for (a) $x = 0.50$, (b) $x = 0.30$, (c) $x = 0.15$ and (d) $x = 0.05$. All these spectra (Fig. 3.9) consist of a broad asymmetric peak which is resolved into two Lorentzians. The IS values obtained from the analysis of these spectra are given in Table 3.8 and plotted in Fig. 3.10. The isomer shift values are comparable to that for LaCoO_3 reported by Bhide et al. [7]. The peak widths of the two resonances observed in $\text{La}_{1-x}\text{Sr}_x\text{Co}_{1-x}\text{Ti}_x\text{O}_3$ are given in Table 3.9. The percent areas of the two resonances, their ratio and total area under resonance observed in Mössbauer spectra of $\text{La}_{1-x}\text{Sr}_x\text{Co}_{1-x}\text{Ti}_x\text{O}_3$ are given in Table 3.10.

It may be mentioned that none of the Mössbauer spectra show the presence of magnetic hyperfine splitting, even at liquid nitrogen temperature. This could be explained by assuming that Ti^{4+} substitution restricts the generation of Co^{4+} ions which are responsible for ferromagnetic interaction observed in $\text{La}_{1-x}\text{Sr}_x\text{CoO}_3$ [19]. This type of behaviour has also been observed for the system $\text{LaCo}_{1-x}\text{Ti}_x\text{O}_3$.

Two resonance peaks have been observed in all the spectra of system $\text{La}_{1-x}\text{Sr}_x\text{Co}_{1-x}\text{Ti}_x\text{O}_3$ recorded at various temperatures. The two resonances are clearly resolved in the Mössbauer spectra recorded at room temperature using PFC absorber (Fig. 3.8). At room temperature the high

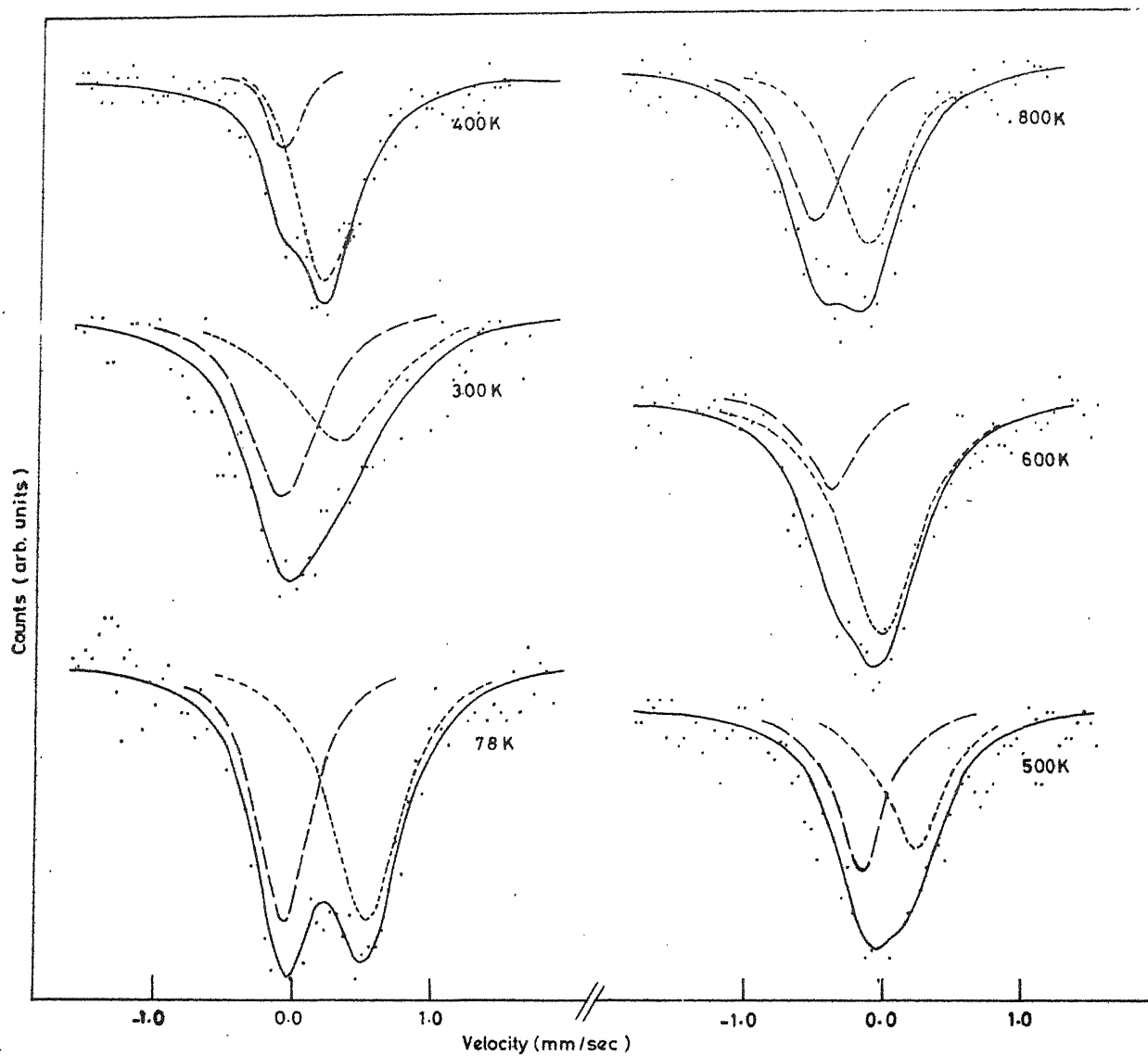


Fig.3.9(a) Mössbauer spectra of $\text{La}_{1-x}\text{Sr}_x\text{Co}_{1-x}\text{Ti}_x\text{O}_3$ ($x=0.5$) recorded at various temperature using 310 stainless steel absorber.

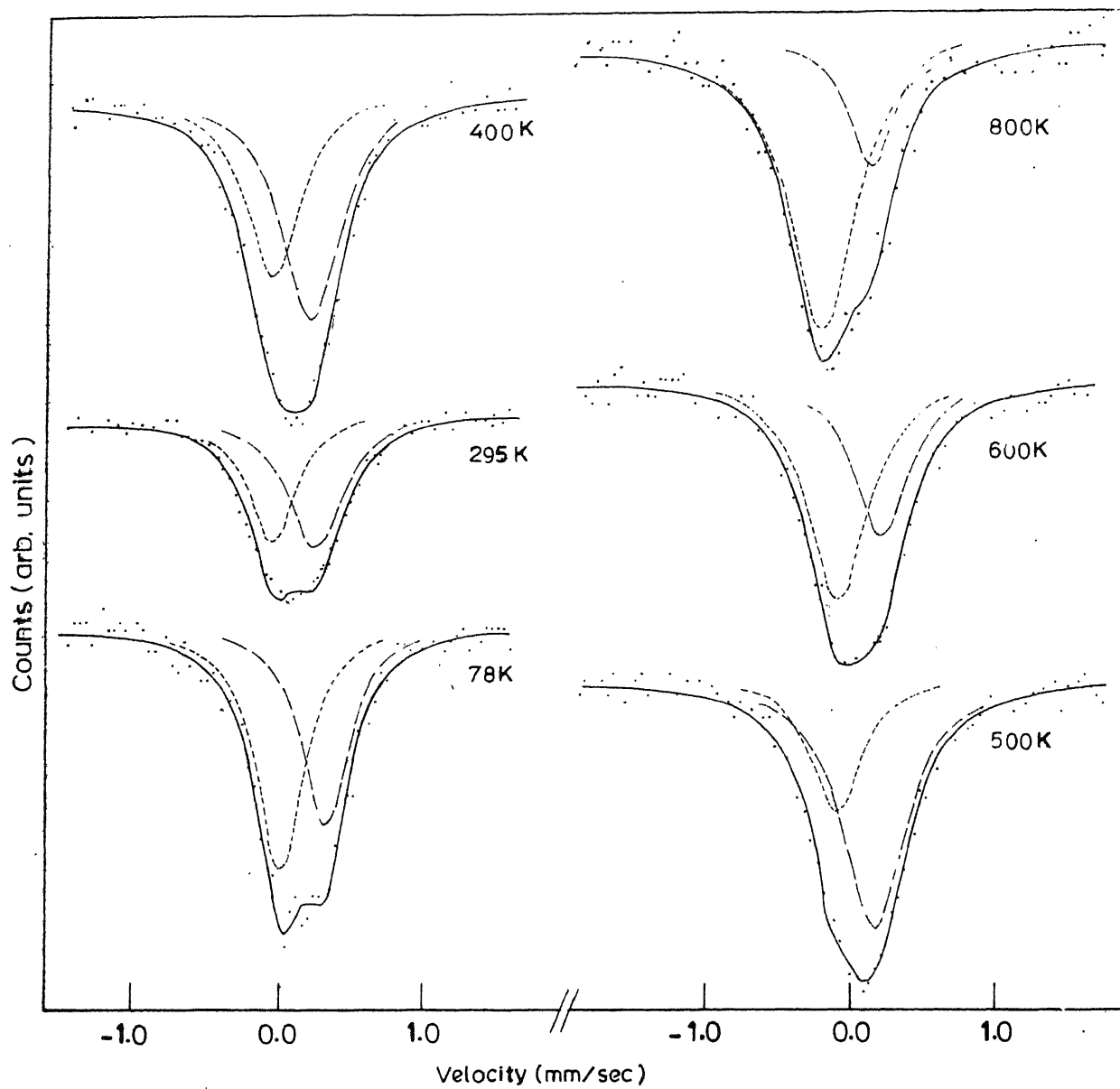


Fig. 3.9(b) Mössbauer spectra of $\text{La}_{1-x}\text{Sr}_x\text{Co}_{1-x}\text{Ti}_x\text{O}_3$ ($x=0.3$) recorded at various temperatures using 310 stainless steel absorber.

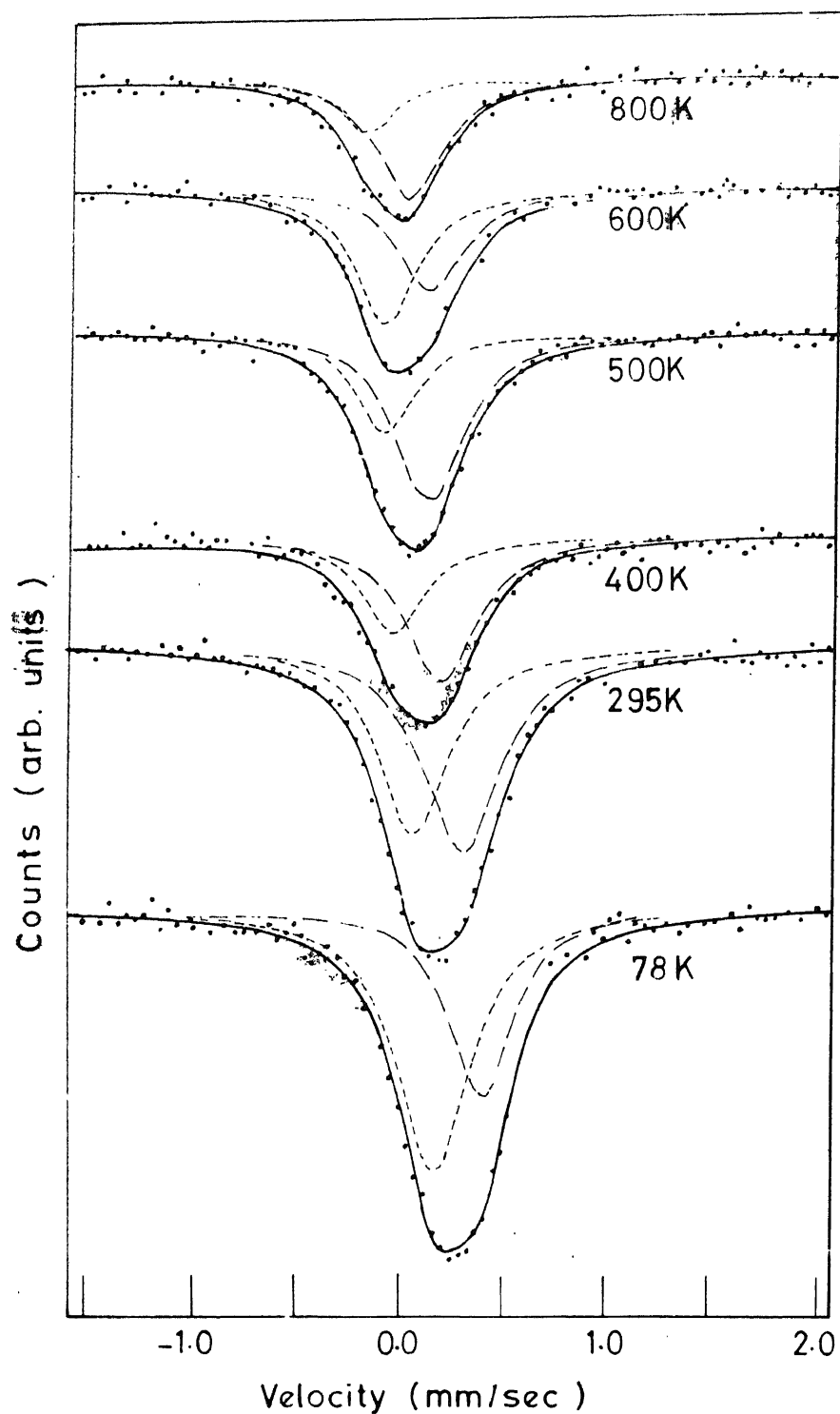


Fig. 3.9(c) Mössbauer spectra of $\text{La}_{1-x}\text{Sr}_x\text{Co}_{1-x}\text{Ti}_x\text{O}_3$ ($x=0.15$) measured at various temperatures using 310 stainless steel absorber.

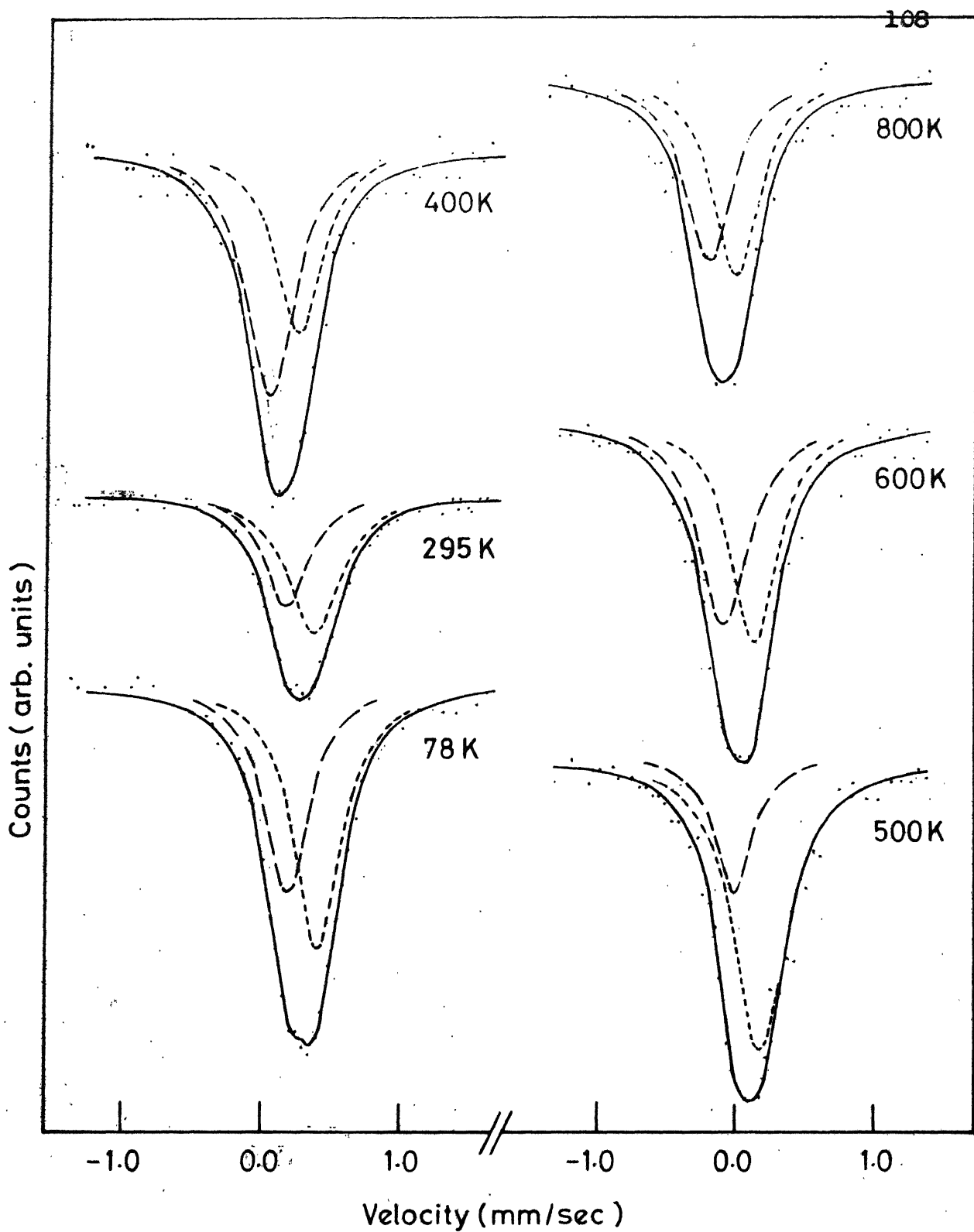


Fig. 3.9(d) Mössbauer spectra of $\text{La}_{1-x}\text{Sr}_x\text{Co}_{1-x}\text{Ti}_x\text{O}_3$ ($x = 0.05$) measured at various temperature using 310 stainless

Table 3.8 Temperature variation of isomer shift² in various compositions of $\text{La}_{1-x}\text{Sr}_x\text{Co}_{1-x}\text{Ti}_x\text{O}_3$ measured using 31058 absorber.

Com- posi- tion x	Low-velocity resonance (Co III, II, IV)				High-velocity resonance (Co ²⁺)			
	78 K	295 K	400 K	500 K	500 K	600 K	600 K	800 K
0.50	-0.06(2)	-0.03(3)	-0.09(3)	-0.28(2)	-0.36(11)	-0.46(3)	0.56(2)	0.41(3)
0.30	0.05(2)	0.01(4)	0.02(3)	-0.10(3)	-0.08(3)	-0.19(3)	0.42(2)	0.35(2)
0.15	0.19(2)	0.18(2)	0.06(3)	0.02(3)	0.01(2)	-0.09(3)	0.40(2)	0.41(2)
0.05	0.20(1)	0.12(2)	0.05(3)	-0.02(4)	-0.10(4)	-0.21(5)	0.43(1)	0.31(2)

²IS values are given in mm/sec.

³The zero of velocity scale refers to the peak position obtained using standard source ^{57}Co in Rh matrix.

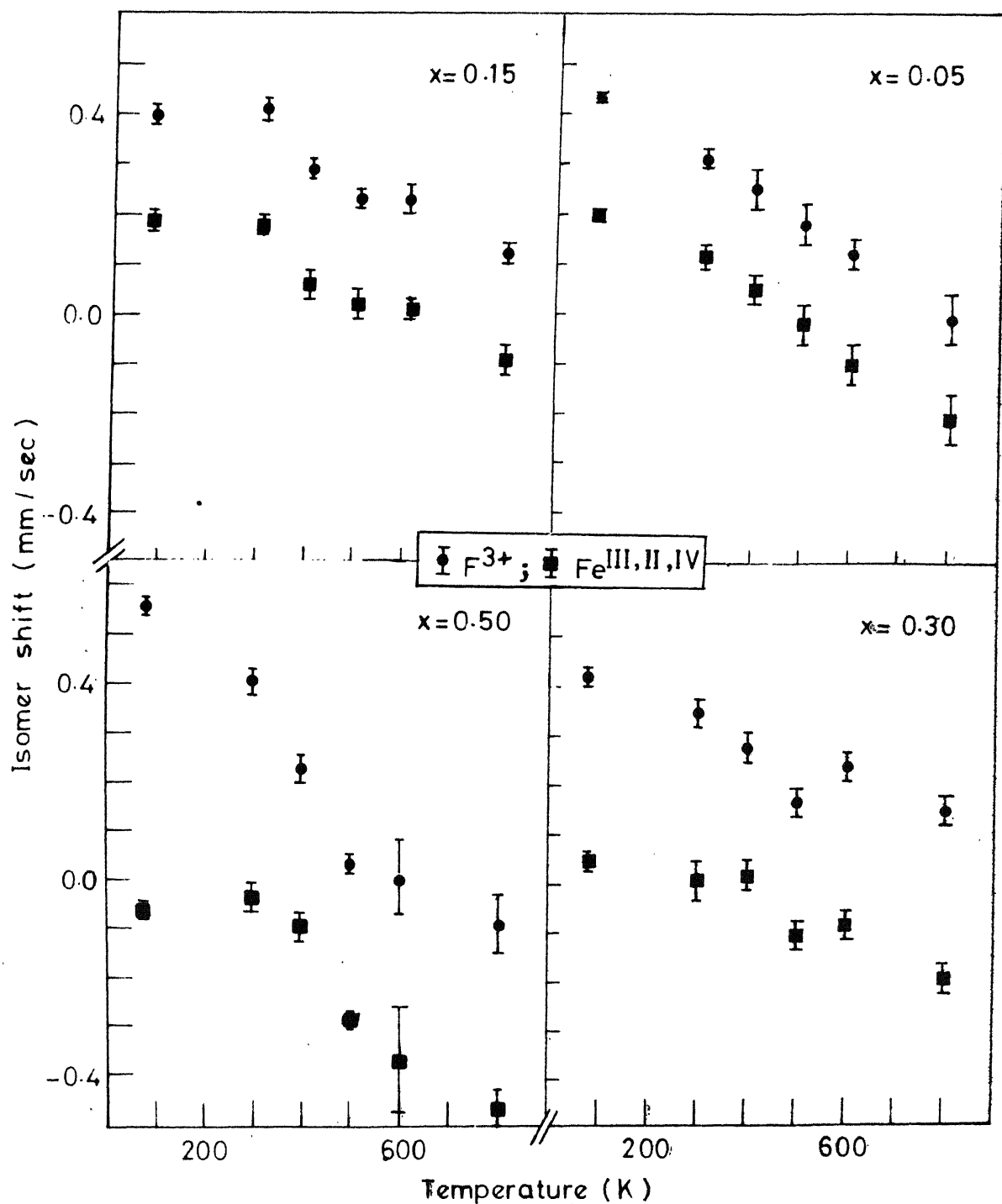
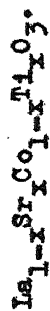


Fig. 3 10 Temperature variation of isomer shift observed in $\text{La}_{1-x}\text{Sr}_x\text{Co}_{1-x}\text{Ti}_x\text{O}_3$ using 310 stainless steel absorber.

Table 3.9 Observed peak width^a of the resonances at various temperature in different composition of

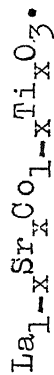


Composition	Low-velocity resonance (Co ^{III} , II, IV)						High-velocity resonance (Co ³⁺)					
	78 K	295 K	400 K	500 K	600 K	800 K	78 K	295 K	400 K	500 K	600 K	800 K
0.50	0.50(6)	0.42(15)	0.38(2)	0.51(8)	0.49(19)	0.56(14)	0.63(7)	0.62(21)	0.47(9)	0.78(5)	0.69(13)	0.60(13)
0.30	0.48(4)	0.51(4)	0.47(5)	0.44(6)	0.55(4)	0.57(4)	0.46(4)	0.70(4)	0.51(4)	0.57(3)	0.50(5)	0.38(4)
0.15	0.39(3)	0.40(3)	0.37(5)	0.38(5)	0.38(3)	0.31(7)	0.34(4)	0.44(3)	0.41(3)	0.42(3)	0.40(4)	0.38(5)
0.05	0.39(2)	0.38(3)	0.40(5)	0.30(10)	0.45(6)	0.43(7)	0.41(1)	0.48(2)	0.39(4)	0.47(4)	0.41(6)	0.42(7)

^aPeak width are given in mm/sec.

^bErrors in the least significant digit are given in brackets.

Table 3.10 Temperature variation of area ratio of high-velocity resonance to low-velocity resonance and total area under resonance observed in Mössbauer spectra of



Composition x	Area ratio of high-velocity to low-velocity resonance ($\text{Co}^{3+}/\text{Co}^{\text{III,II,IV}}$)						Total area under resonance (in %.)					
	78 K	295 K	400 K	500 K	600 K	800 K	78 K	295 K	400 K	500 K	600 K	800 K
0.50	1.27	1.01	3.34	0.88	3.51	1.24	1.28	0.69	0.59	1.54	0.61	0.53
0.30	0.69	1.24	1.34	2.33	0.67	0.30	1.77	2.39	2.15	2.20	1.98	1.54
0.15	0.62	1.18	1.69	1.84	0.78	2.58	1.68	2.34	1.36	1.82	1.49	1.05
0.05	1.35	1.48	0.71	3.31	0.99	1.05	3.21	4.05	1.32	1.33	1.37	0.90

velocity resonance lies between 0.30 ± 0.02 mm/sec and 0.45 ± 0.03 mm/sec and the low velocity resonance is near the zero velocity position (zero of velocity scale refers to the peak position obtained using standard ^{57}Co source in Rh matrix and NiO absorber). From the systematics of IS reported by Greenwood and Gibbs [23] the high velocity resonance is assigned to Co^{3+} state and low velocity resonance may be due to $\text{Co}^{\text{III,II,IV}}$ states. Before assigning these resonances to different valence states of cobalt we must exclude other possibilities; one such possibility is that the two resonances may be quadrupole split partners of a single valence state. This possibility can be ruled out by arguing on lines similar to the system $\text{LaCo}_{1-x}\text{Ti}_x\text{O}_3$.

Hence it is justified to assign the two resonances to Co^{3+} and $\text{Co}^{\text{III,II,IV}}$ which are known to exist in parent system LaCoO_3 [7]. The comparable values of IS obtained for the system $\text{La}_{1-x}\text{Sr}_x\text{Co}_{1-x}\text{Ti}_x\text{O}_3$ to that of LaCoO_3 [7] (Fig. 3.10) also indicate the presence of similar kind of cobalt species in two systems. The observed temperature variation of IS values in this system is also similar to that of LaCoO_3 (Fig. 3.10). A change in slope, in the IS versus temperature plots in the temperature range 450–600 K has been observed for all the compositions. In the $x_g T$ versus temperature plots (Fig. 3.7) a sharp change has been observed for $x = 0.05$ and 0.15 in this temperature range. While for $x = 0.50$ and

0.30 a change in slope has been observed (see Fig. 3.7). Similar changes have been observed in the temperature range 400-600 K for the system LaCoO_3 [7].

The IS values for low-velocity resonance measured at 78 K (Table 3.8) increase as we go from $x = 0.05$ to $x = 0.15$ and then the IS values decrease with further increase in x . The IS values at 78 K for high-velocity resonance first decrease upto $x = 0.15$ and then they increase for $x = 0.30$ and 0.50 . The changes are, however, small in magnitude. These changes in IS values indicate that upto certain concentration of x , the low-spin states are more favourable. It is also possible that because of change in crystal field splitting due to increase in x , some intermediate spin states (e.g. $t_{2g}^5 e_g^1$) are formed. The IS values for these intermediate spin states lie between that of low-spin and high-spin resonance. However, with further increase in x the distortion further decreases and as a result of this decrease, high-spin state may become more favourable.

The total area under resonance and area **ratio** of high-velocity resonance to low-velocity resonance for the system $\text{La}_{1-x}\text{Sr}_x\text{Co}_{1-x}\text{Ti}_x\text{O}_3$ are given in Table 3.10. No systematic trend is observed in the total area under resonance values. However, the observed changes are indicative of ionic vibrations and transitions which are

also reflected in other data. For all the compositions studied, the area ratio of high-velocity resonance to low-velocity resonance changes sharply at about 500 K (Table 3.10). A similar observation has been made for the previous system $\text{LaCo}_{1-x}\text{Ti}_x\text{O}_3$. These results indicate significant change in population of spin states around this temperature.

All above observations suggest that the spin state equilibrium in $\text{La}_{1-x}\text{Sr}_x\text{Co}_{1-x}\text{Ti}_x\text{O}_3$ is similar to that in LaCoO_3 . Both the systems also show similar magnetic behaviour because the only magnetic ion Co^{3+} is common in the systems.

It would be interesting to compare the perovskite system (a) LaCoO_3 , (b) $\text{La}_{1-x}\text{Sr}_x\text{CoO}_3$, (c) $\text{La}_{1-x}\text{Sr}_x\text{Co}_{1-x}\text{Ti}_x\text{O}_3$ and (d) $\text{LaCo}_{1-x}\text{Ti}_x\text{O}_3$, where there is a considerable change in the valence state of cobalt. In these systems cobalt ions exist in (a) trivalent state only, in (b) trivalent and tetravalent states, in (c) trivalent state only and in (d) divalent and trivalent states respectively. In $\text{La}_{1-x}\text{Sr}_x\text{CoO}_3$, the Co^{4+} forms the itinerant band which is mainly responsible for itinerant electron ferromagnetism. In the present two systems the formation of Co^{4+} is restricted because of the substitution of Ti^{4+} . This is the reason for the localized behaviour and absence of ferromagnetic interaction in these systems ((c) and (d)).

Table 3.11 Comparison of properties of (a) LaCoO_3 , (b) $\text{La}_{0.5}\text{Sr}_{0.5}\text{CoO}_3$, (c) $\text{LaCo}_{0.5}\text{Ti}_{0.5}\text{O}_3$, and (d) $\text{La}_{0.5}\text{Sr}_{0.5}\text{Co}_{0.5}\text{Ti}_{0.5}\text{O}_3$

500 K.

System	Electrical			Seebeck coefficient ($\mu\text{V/K}$)	Magnetic susceptibility χ_g	Electrical behaviour	Mössbauer Data					
	resistivity (Ωcm)	ρ		α			Low spin resonance ($\text{Co}^{\text{II,III,IV}}$)	High spin resonance (Co^{3+})	Area (mm/sec)	Area (mm/sec)	IS (mm/sec)	Area (mm/sec)
(a) LaCoO_3	0.15			10	9.1×10^{-6}	p-type semiconductor	-0.04	50	0.34	50	-	-
(b) $\text{La}_{0.5}\text{Sr}_{0.5}\text{CoO}_3$	5.2×10^{-4}			10		p-type metallic	-	-	0.42	-	-	-
(c) $\text{LaCo}_{0.5}\text{Ti}_{0.5}\text{O}_3$	3.98×10^6			550	8.4×10^{-6}	p-type insulator	-0.31	31	0.06	38	0.45	31
(d) $\text{La}_{0.5}\text{Sr}_{0.5}\text{Co}_{0.5}\text{Ti}_{0.5}\text{O}_3$	3.16×10^{-1}			180	7.7×10^{-6}	p-type semiconductor (n-type below 500 K)	-0.28	53	0.04	47	-	0.88

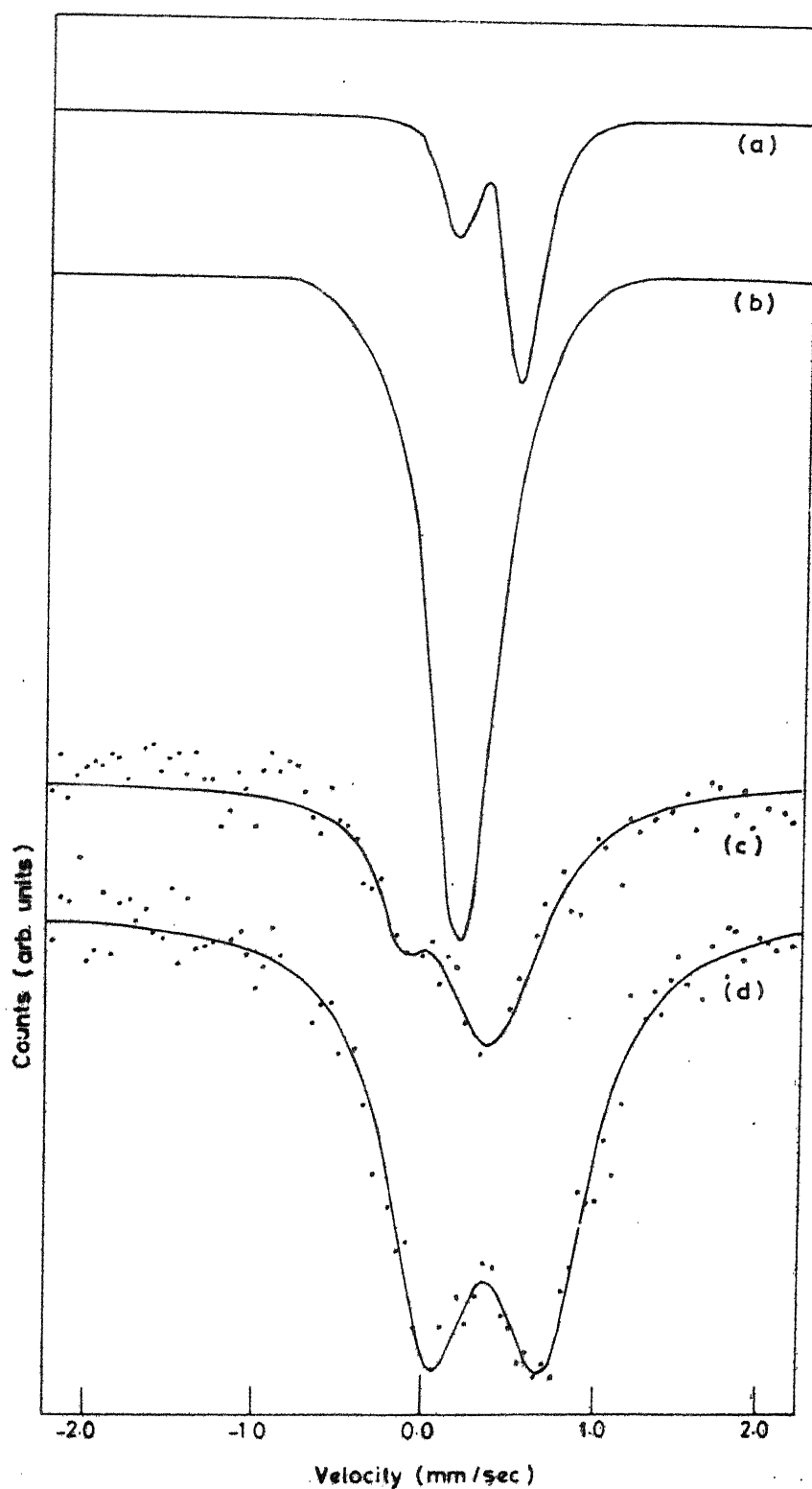


Fig.3.11 Room temperature Mössbauer spectra of (a) LaCoO_3 [7]
 (b) $\text{La}_{0.5}\text{Sr}_{0.5}\text{CoO}_3$ [19], (c) $\text{La}_{0.5}\text{Sr}_{0.5}\text{Co}_{0.5}\text{Ti}_{0.5}\text{O}_3$ and
 (d) $\text{LaCo}_{0.5}\text{Ti}_{0.5}\text{O}_3$, recorded using PFC absorber.

In Table 3.11 we have compared the properties of the above four systems for $x = 0.50$ and at $T = 500$ K. The data for LaCoO_3 have been taken from [7] and those for $\text{La}_{0.5}\text{Sr}_{0.5}\text{CoO}_3$ from [15]. There is a wide variation in the electrical properties of these systems. Although at 500 K holes are majority carriers in all the four systems but electrical nature of the four systems are different; system (a) and (c) are semiconductor, (b) is metallic and (d) is an insulator at $T = 500$ °K for $x = 0.5$.

In Fig. 3.12, we have shown the room temperature Mössbauer spectra of the four systems measured using PFC absorber. The Mössbauer parameters of these spectra are given in Table 3.11. The Mössbauer spectra of LaCoO_3 are taken from [7] and of $\text{La}_{0.5}\text{Sr}_{0.5}\text{CoO}_3$ from [15].

3.4 SUMMARY

Substituted perovskite systems $\text{LaCo}_{1-x}\text{Ti}_x\text{O}_3$ and $\text{La}_{1-x}\text{Sr}_x\text{Co}_{1-x}\text{Ti}_x\text{O}_3$ with $x = 0.50, 0.30, 0.15$ and 0.05 have been studied by Mössbauer spectroscopy, X-ray diffraction and magnetization measurements. The Mössbauer measurements were made at temperatures, 78, 295, 400, 500, 600 and 800 K. Both systems show a change in behaviour above a critical value of x and temperature. Itinerant electron ferromagnetism is not observed in these systems. Co^{2+} is found in $\text{LaCo}_{1-x}\text{Ti}_x\text{O}_3$

for larger x (i.e. $x = 0.50$ and 0.30), in addition to Co^{3+} and $\text{Co}^{\text{III,II,IV}}$ observed in both the systems. The results of Mössbauer spectroscopy are in agreement with electron transport and magnetic properties. The results obtained for the two systems are compared and discussed with the known results of the parent systems.

16. S.B. Patil, D. Chakrabarty, M.V. Babu and S.N. Shringi, Phys. Stat. Sol. (a) 65, 65 (1981)
17. N. Ramdass, J. Gopalkrishnan and M.V.C. Sastri, J. Less. Common. Met. 65, 129 (1979)
18. D. Bahadur and Om Prakash, J. Solid State Chem. 46, 197 (1983)
19. N.N. Greenwood and T.C. Gibb, Mössbauer Spectroscopy, Plenum Press, New York (1971)
20. A.A. Maraduddin, P.A. Flinn and S.L. Ruby, Proceedings of the second International Conference on the Mössbauer Effect, Saclay, France, 1961 Wiley, New York (1962), p. 97; Phy. Rev. 126, 9 (1962)
21. R.L. Cohen, Editors, Applications of Mössbauer Spectroscopy, Vol. I, Academic Press, New York (1976).

CHAPTER 4

MÖSSBAUER SPECTROSCOPIC STUDIES^{*} OF THE SYSTEM $Y_{3-x}Gd_xFe_5O_{12}$ WITH $x = 0, 0.5$ AND 3

4.1 INTRODUCTION

Rare earth garnet (RIG) $R_3Fe_5O_{12}$ (where R is a rare earth ion or yttrium ion) have been studied extensively in view of their interesting electrical and magnetic properties. Many new exciting technological applications of these garnets have also evoked considerable interest in these materials. Some of these important technological applications are [1-2]:

- (i) Tunable filters, circulators and gyrators for microwave region,
- (ii) magnetic bubble domain-type digital memory devices,
- (iii) magneto-optical device,
- (iv) acoustic devices.

For each application, RIG with specific characteristic properties are required. The properties of RIG are basically determined by the method of their preparation. The micro-structure, grain size and related properties can be suitably

^{*}The results of these studies shall be presented at Int. Conf. Ferrites, San-Fransisco, U.S.A., Nov. (1984).

controlled using specialized techniques mentioned below. The garnets in amorphous state are relatively less known [3-9]. The amorphous garnets may be prepared by some of these techniques. We can make garnets with requisite properties by giving suitable heat-treatment to amorphous samples. The methods used to prepare non-crystalline RIG samples are :

- (a) melt quenching [3],
- (b) spray pyrolysis [4],
- (c) d-c or R-F sputtering [5,6],
- (d) freeze drying [7],
- (e) amorphous citrate gel process [8,9].

Among the above method, amorphous citrate process has distinct advantages over the other. Some of the advantages of the citrate gel process are that the growth of various phases and the grain size can be suitably controlled. The amorphous citrate process is a promising technique for preparation of RIG with wide range of characteristic properties. Suitability of RIG for various applications is determined by various standard characterization techniques such as X-ray diffraction, differential thermal analysis (DTA), electron paramagnetic resonance (EPR), transmission electron and optical microscopy, magnetization measurements and Mössbauer spectroscopy. In particular Mössbauer spectroscopy is very useful as it provides valuable information about the various magnetic phases in the sample.

In this Institute mixed yttrium-gadolinium garnet system $Y_{3-x}Gd_xFe_5O_{12}$ with $x = 0, 0.5$ and 3 has been prepared by amorphous citrate process [9]. The first member with $x = 0$ is the novel garnet system YIG. This system is ideally suited for studies of fundamental relaxation process, spin wave excitations etc. [2]. Its small g-factor (≈ 2.0), narrow line-width and small anisotropic field make it especially suitable for low-frequency applications. In many devices such as ferromagnetic amplifiers, resonance filters, harmonic generators and passive limiters, which exploit the high-power non-linearities of ferromagnets; YIG has been widely used because of its small resonance line-width.

The last member $x = 3$, is the pure gadolinium garnet (GdIG) which has received great attention because of its very interesting properties. Firstly, the Gd^{3+} ion (like Y^{3+} and Lu^{3+} ions) has no orbital angular momentum and, consequently does not interact strongly with the crystal fields of the lattice as most of the other rare earth ions do. The fact that Gd^{3+} interacts weakly with the crystal fields is reflected in both magnetization and resonance properties of GdIG. Gadolinium has non-zero spin angular momentum and GdIG has a compensation temperature ($T_{comp} \approx 290$ K) where the net magnetization vanishes. Its coercive field H_c is very sensitive to temperature and it is therefore, ideally suited for thermo-magnetic writing and magneto-optical readout memory devices.

The middle member $x = 0.5$ is mixed yttrium-gadolinium garnet $Y_{2.5}Gd_{0.5}Fe_5O_{12}$. The substitution of gadolinium in YIG reduces the magnetization without changing the Curie temperature T_c , which results in a stabilization of saturation magnetization (M_s) with temperature. Harrisson and Hodges [10] suggested that composition $Y_{1.2}Gd_{1.8}Fe_5O_{12}$ to be a good temperature stable garnet over a wide temperature range centred around $50^\circ C$. Garnets with compensation temperature anywhere between room temperature and absolute zero can be made by appropriate substitution of Gd^{3+} in YIG. The Gadolinium being an S-ion ($L = 0$) does not exhibit spin-orbit coupling which affects the gyromagnetic movement (rapid relaxation) resulting in increased line-widths, ΔH_k , ΔH_{eff} and ΔH . The RIG with large line-widths are unsuitable for various microwave applications. Thus the Gd^{3+} in one of the magnetic rare earth ion which on substitution in YIG gives useful garnet systems.

In the following sections we shall describe the results of our Mössbauer studies of the garnet system $Y_{3-x}Gd_xFe_5O_{12}$ with $x = 0, 0.5$ and 3 . To corroborate the results obtained by Mössbauer studies we have also studied this garnet system using X-ray diffraction, electron paramagnetic resonance (EPR), and magnetization measurements. The Mössbauer spectroscopy is ideally suited to provide information about the various magnetic phases present in the sample. The usefulness of Mössbauer spectroscopy in characterization

of magnetic phase, in particular, YIG phase in different glass systems has been illustrated earlier [11-12].

4.2 EXPERIMENTAL METHODS

In this section we will briefly outline the sample preparation and various experimental techniques used in the present investigation.

4.2.1 Sample Preparation

The amorphous $Y_{3-x}Gd_xFe_5O_{12}$ garnet samples were prepared by the citrate gel process [9]. The stoichiometric amount of Y_2O_3 and Gd_2O_3 were dissolved in concentrated nitric acid. The required amount of ferric citrate and citric acid solution in water was added. Citric acid was added in excess. The mixture was refluxed for about six hours and then heated upto $120^\circ C$ and kept at this temperature till it dried. The dried precursors were subjected to two different heat schedules. In the first schedule, the obtained product was heated at $400^\circ C$ for 24 hours in an atmosphere of 95 % nitrogen and 5 % oxygen and again for 24 hours at $400^\circ C$ in air. This was followed by heating in air at different temperatures for 4 hours each. In the other heating schedule the initial heat treatment at $400^\circ C$ was only given in air instead of a mixture of nitrogen and oxygen. The above two heating schedules shall be referred to as A and N schedules respectively. All the samples obtained by different heat-treatment are listed in Table 4.1. The

Table 4.1 Details of the $Y_{3-x}Ga_1Fe_{50}O_{12}$ samples studied by us.

System	Samples given heating schedule A									Samples given heating schedule B			
	as prepared	400	500	550	600	650	700	800	900	600	650	700	800
$x = 0$	YAO	YA4	-	-	YA6	YA6.5	YA7	YA8	YA9	YN6	-	YN7	YN8
$x = 0.5$	-	YGA4	-	-	YGA6	YGA6.5	YGA7	YGA8		YGN6	YGN6.5	YGN7	YGN8
$x = 3$	GAO	GA4	GA5	GA5.5	GA6	GA6.5	GA7	-		-	-	-	-
				GA5.5 [≡]									

* Samples marked asterisk '*' are heat-treated for 40 hours instead of 4 hours.

All other samples are heat-treated for 4 hours.

Heat-treatment temperature are in degree centigrade.

samples are denoted by Y, YG and G for $x = 0, 0.5$ and 3 system respectively. The heat-treatment schedule A or N with heat-treatment temperature in units of 100°C are added next to these symbols. For example YGA8 stands for $\text{Y}_{3-x}\text{Gd}_x\text{Fe}_5\text{O}_{12}$ ($x = 0.5$) sample heat-treated for 4 hours at 800°C as per schedule A. The samples marked by asterisk (*) are heat-treated for 40 hours instead of 4 hours. The heated samples were allowed to cool down slowly to room temperatures before studying them by various techniques.

4.2.2 Mössbauer Measurements

For Mössbauer spectroscopic studies, approximately 50 gm of powdered sample were layered on a circular area of about 1 cm diameter and sandwiched using two layers of cello tape. The Mössbauer spectra of these samples were recorded using the constant acceleration Mössbauer spectrometer described in Chapter 2. Mössbauer spectra of all the samples were recorded at room temperature (295 K). For some of the samples Mössbauer spectra were also recorded at liquid nitrogen temperature (78 K). The source used in these measurements was a 10 mCi ^{57}Co in Rh matrix obtained from New England Nuclear Inc., USA. The spectrometer was calibrated using $\alpha\text{-Fe}$ absorber. Mössbauer spectra of polycrystalline YIG and $\gamma\text{-Fe}_2\text{O}_3$ were recorded for identification of various magnetic phases. Mössbauer spectra were analysed

with the help of DEC 1090 digital computer using least square fitting programme as discussed in Chapter 2. The EFG and magnetic field distributions are also computed using computer programmes based on Window's method [13].

4.2.3 Other Measurements

Magnetization measurements of all the samples were made using Varian Associates PAR vibrating sample magnetometer (Model 150A) at room temperature (295 K) using magnetic field upto 10 KG.

X-ray diffraction patterns were recorded after each heat-treatment schedule to monitor the crystallization kinetics of various (garnet and spinel) phases. The Rich Seifert ISO-Debyeflex-2002 diffractometer with CrK_α (with V filter) or CuK_α (with Ni filter) was used to record the diffraction patterns.

EPR spectra of all the samples were recorded at room temperature (295 K) and at liquid nitrogen temperature (78 K) using Varian Associates spectrometer (Model V-4502-12) in the x-band frequency using 100 MHz field modulation. The magnetic field was set at 3.3 KG and scanning range used was 5 KG.

4.3 RESULTS AND DISCUSSION

The system $\text{Y}_{3-x}\text{Gd}_x\text{Fe}_5\text{O}_{12}$ is amorphous when heated below 650, 600 and 500 °C for $x = 0$, 0.5 and 3 respectively.

The Mössbauer spectra of amorphous samples consist of two quadrupole-split broad peaks characteristic of paramagnetic amorphous nature of the sample. The Mössbauer spectra of samples heat-treated above crystallization temperature consist of magnetically split six-finger patterns characteristic of magnetic nature of the sample. The intensity of magnetically split spectrum increases with higher heat-treatment indicating growth of the magnetic phases. We shall first discuss the system $x = 0$ in detail and follow it up with $x = 0.5$ and 3 systems.

4.3.1 $\text{Y}_{3-x}\text{Gd}_x\text{Fe}_5\text{O}_{12}$ System with $x = 0$

The X-ray diffraction patterns of the as prepared precursor sample and of samples heat-treated at $T = 400, 600, 650, 700, 800, 900^\circ\text{C}$ are shown in Fig. 4.1(a) and (b). Samples heat-treated below 650°C are X-ray amorphous [5]. The lines corresponding to YIG and spinel $\gamma\text{-Fe}_2\text{O}_3$ and hexagonal $\alpha\text{-Fe}_2\text{O}_3$ phase are observed in samples heat-treated at or above 650°C . The intensity of peaks corresponding to YIG increases with higher heat-treatment temperature and longer heat-treatment time indicating growth of garnet phase.

The d -values for observed diffraction lines in the X-ray spectrum are evaluated and are assigned to various diffraction planes with the help of values reported for

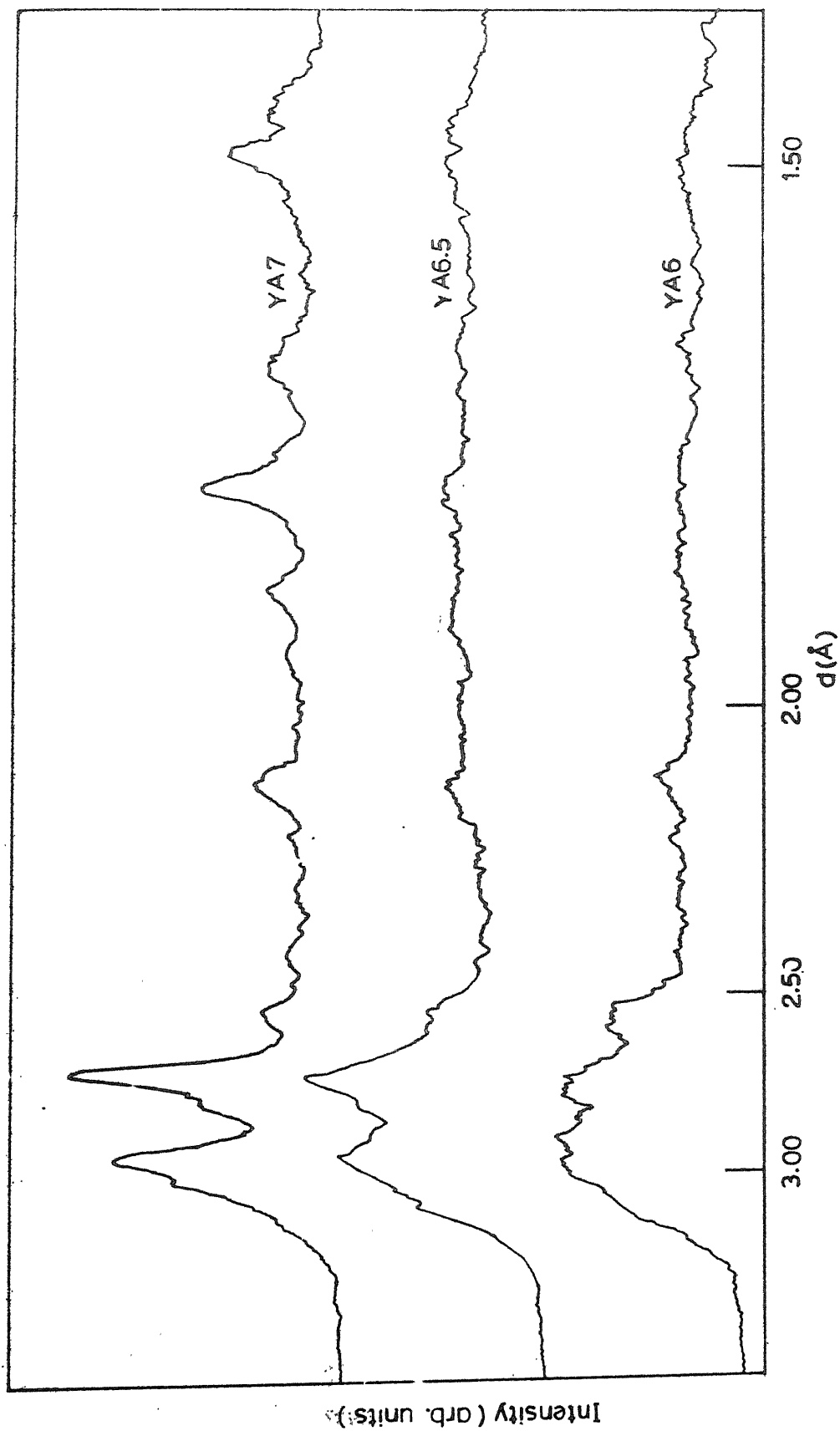


Fig.4.1(a) X-ray diffractograms of $\text{Y}_{3-x}\text{Gd}_x\text{Fe}_5\text{O}_{12}$ ($x=0$) samples, recorded using $\text{Cr K}\alpha$ target.

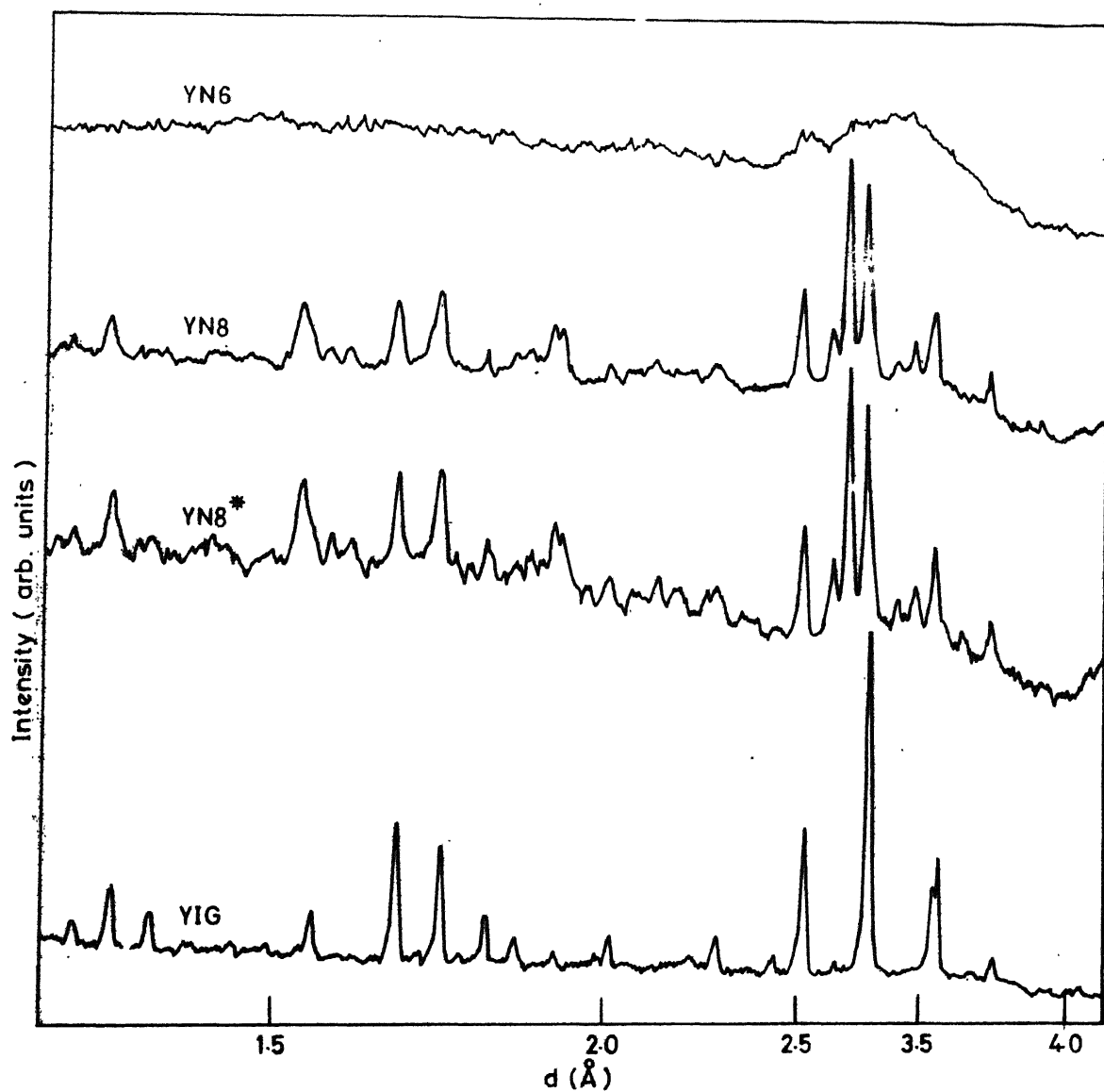


Fig.4.1(b) X-ray diffractograms of $\text{Y}_{3-x}\text{Gd}_x\text{Fe}_5\text{O}_{12}$ ($x=0$) samples and polycrystalline YIG recorded using $\text{Cu K}\alpha$ target with Ni filter.

YIG [14], $\gamma\text{-Fe}_2\text{O}_3$ [15] and $\alpha\text{-Fe}_2\text{O}_3$ [16]. The d-values and relative intensity of various diffraction lines are given in Table 4.2 for ready reference.

Mössbauer spectra of amorphous $\text{Y}_{3-x}\text{Gd}_x\text{Fe}_5\text{O}_{12}$ ($x = 0$) samples heat-treated for 4 hours at temperature $T = 400, 600, 650, 700, 800, 900^\circ\text{C}$ are shown in Fig. 4.2. The Mössbauer spectra are analysed by conventional least square fitting and EFG distribution are calculated using Window's [10] method. The calculated EFG distributions for these samples are shown in Fig. 4.3. The Mössbauer parameters of these spectra (Fig. 4.2) are given in Table 4.3. The volume fraction of garnet phase is calculated by the area of magnetically split peaks due to garnet phase. Two sets of quadrupole splitting values are given in Table 4.3. The values marked (a) are obtained by conventional least square fitting and marked (b) by EFG distribution method (Table 4.3). The quadrupole splitting values obtained by the two methods differ. This behaviour is common and has also been observed earlier [17]. The Mössbauer spectra of YA4 and YA6 consist of two broad (width ≈ 0.78 mm/sec) quadrupole split peaks characteristic of amorphous paramagnetic nature of the samples. The large quadrupole splitting (≈ 1.18 mm/sec) observed for YA4 and YA6 can be ascribed to amorphous nature of these samples because in amorphous systems a large number of non-identical sites with a substantial departure from

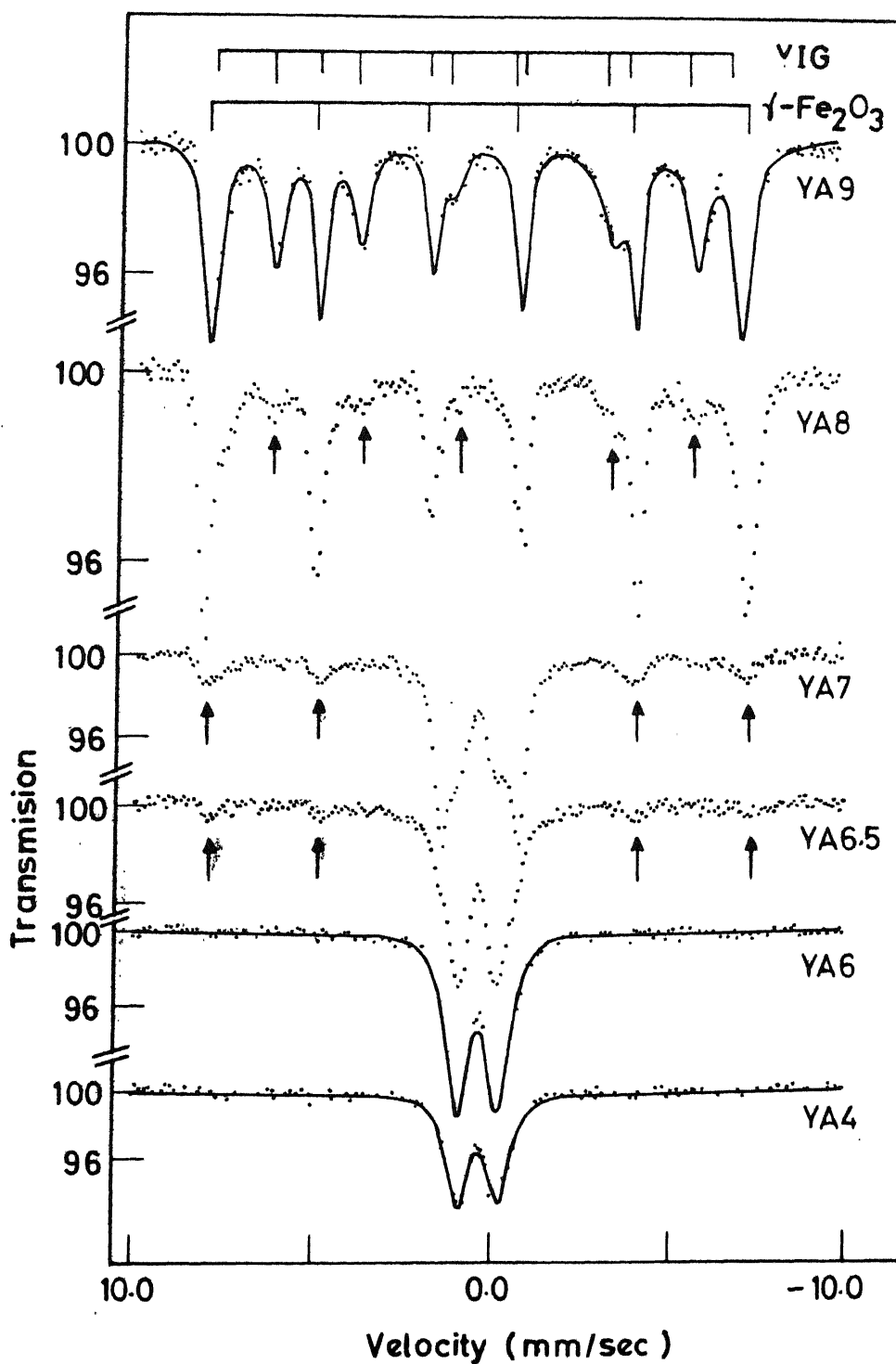


Fig.4.2 Mössbauer spectra of $Y_{3-x}Gd_xFe_5O_{12}$ ($x=0$) samples recorded at room temperature (295K). Peak positions observed for polycrystalline YIG and γ -Fe₂O₃ are also shown.

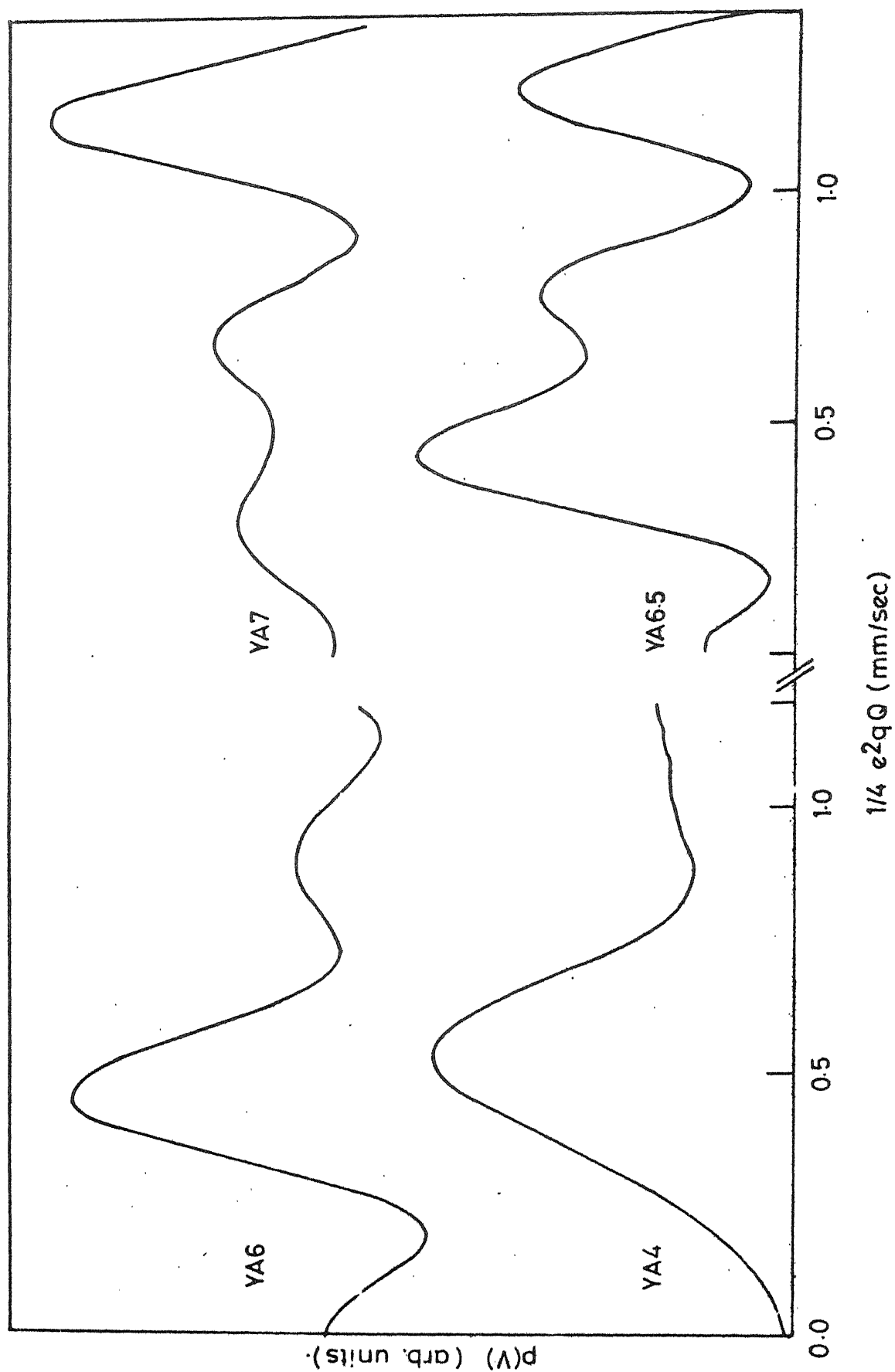


Fig.4.3 EFG distribution for $Y_{3-x}Gd_xFe_5O_{12}$ ($x=0$) samples.

Table 4.2 Mössbauer parameters of $Y_{3-x}Ga_xFe_5O_{12}$ ($x = 0$) samples.

Sample	Quadrupole split component(s)				Magnetic Zeeman split component(s)			
	IS (w.r.t. α -Fe) mm/sec	Peak width mm/sec	$\frac{\Delta E}{(a)}$ mm/sec	$\frac{\Delta E}{(b)}$ mm/sec	FWHM of $p(\nu)$ distribution mm/sec	IS (w.r.t. α -Fe) mm/sec	Assignment (phase)	Volume fraction of garnet phase %
YA4	0.36(2)	0.78(3)	1.18(2)	0.94	0.46			
YA6	0.38(2)	0.77(3)	1.19(2)	1.06	0.66	*	S,H	
YA6.5	0.39(3)	0.80(3)	1.24(2)	0.86	0.48	*	S,H	
				1.56	0.32			
				2.44	0.33			
YA7	0.44(2)	0.67(4)	1.19(2)	0.46	0.38	0.41(2)	476(16)	S,H
	0.37(2)	0.45(2)	2.25(2)	1.36	0.36			Traces
YA8			2.32		0.40	0.41(2)	483(3)	S,H
						*	G	10
YA9						0.40(5)	479(5)	S,H,G(0)
						0.13(4)	376(3)	G(t)
								65

* Indicate presence of the phase but Mössbauer parameter could not be evaluated due to very low intensity of resonance lines.

S = Srinel γ - Fe_2O_3 ; H = Hexagonal α - Fe_2O_3 ; G = Garnet (YIG).

cubic symmetry exists [18] which gives rise to large quadrupole splitting. The IS values with respect to α -Fe observed for YA4 and YA6 are 0.36 and 0.38 mm/sec respectively and are in between to the corresponding values for octahedral and tetrahedral coordinated Fe^{3+} . This indicates that Fe^{3+} exists in both coordinations but the spectra due to these sites are not resolved because of the amorphous nature of the samples. The Mössbauer spectra of YA6.5 consists of a quadrupole component and a weak magnetic component. The parameters of magnetic component could not be evaluated due to its very low intensity. In Fig. 4.2 we have also shown the observed Mössbauer peak positions for polycrystalline YIG and $\gamma\text{-Fe}_2\text{O}_3$ for easy identification of observed magnetic phases. The magnetic component further grows in sample heat-treated at 700 and 800 °C (YA7 and YA8). From IS (≈ 0.41 mm/sec) and internal magnetic field (483 ± 15 kOe) this magnetic component appears to be a combination of $\gamma\text{-Fe}_2\text{O}_3$ and $\alpha\text{-Fe}_2\text{O}_3$. In the X-ray data of these samples we have observed diffraction lines due to these phases and garnet YIG phase. In YA6.5 and YA7 we observe two sets of quadrupole splits pairs. The first one with $\Delta E = 1.19$ mm/sec is characteristic of amorphous state and this component reduces in intensity when we go from YA6.5 to YA7. The other pair with higher $\Delta E = 2.25$ mm/sec value may be characteristic of magnetic phases. In YA8 the quadrupole component completely

disappears indicating magnetic ordering of the present phases. In Mössbauer spectra of YA6.5 and YA7 the garnet phase is not visible but in YA8 we observe the presence of YIG phase. The volume fraction of garnet phase present in YA6.5 and YA7 and YA8 seemsto be small compared to other phases. Secondly, the garnet phase is not magnetically ordered in YA6.5 and YA7. In YA8 two six-line patterns are observed, the intense one can be due to a combination of $\gamma\text{-Fe}_2\text{O}_3$, $\alpha\text{-Fe}_2\text{O}_3$ and octahedral site of YIG. Since the internal magnetic field strength for these phases are adjacent and are not resolved in the Mössbauer spectra. The X-ray data of these samples also provide evidence of the coexistence of these phases. The weak six-finger component is due to tetrahedral site of YIG. The magnetic split component due to YIG octahedral site is submerged in the peak due to $\gamma\text{-Fe}_2\text{O}_3$ and $\alpha\text{-Fe}_2\text{O}_3$. The percentage area of YIG component is estimated to be 10 %. while the remaining 90 % is due to other phases. The YIG component grows from 10 % in YA8 to 65 % in YA9. A similar behaviour is observed in X-ray data where. the relative intensity of diffraction lines due to spinel and hexagonal phases decreases approximately by a factor of 3 in YA9 compared to YA8 (see Table 4.2). Thus heat-treatment at higher temperature is more favourable for development of garnet phase. From the X-ray data heat-treatment schedule A

seems to be more favourable than schedule N. Similar behaviour is observed for $x = 0.5$ system discussed in Sec.4.3.2.

As observed from the X-ray and Mössbauer data the crystallization temperature is around 600°C . To support this conclusion we present magnetization data of these samples given in Table 4.4. Saturation or spontaneous magnetic moment increases sharply in sample heat-treated at 600°C (YA6) or above 600°C indicating crystallization of magnetic phase as the heat-treatment temperature increases.

We have carried out EPR measurements of these samples to study the coordination and symmetry of iron ion. Typical EPR spectra of $\text{Y}_{3-x}\text{Gd}_x\text{Fe}_5\text{O}_{12}$ ($x = 0$) samples recorded at room temperature (295 K) and at liquid nitrogen temperature (78 K) are shown in Fig. 4.4. The Landau g factor and linewidth ΔH for $\text{Y}_{3-x}\text{Gd}_x\text{Fe}_5\text{O}_{12}$ ($x = 0$) samples are given in Table 4.5. The EPR spectra of all these samples show only one resonance with g value $\simeq 2.1$ at room temperature and g value lies between 2.13 to 2.37 at liquid nitrogen temperature. This resonance is due to $\text{Fe}^{3+} - \text{Fe}^{3+}$ interaction ($g = 2$) in these samples [18]. The observed g values (Table 4.5) differ from the g value observed for crystalline YIG [2]. This difference may be due to amorphous nature of these samples. It may be mentioned that resonance corresponding to $g = 4.3$ which usually occurs for paramagnetic Fe^{3+}

Table 4.4 Magnetic moment of $Y_{3-x}Gd_xFe_5O_{12}$ ($x = 0$) samples.

Sample	YA4	YA6	YA7	YA8	YN6.5	YN7
Magnetic moment at 6 KG M (emu/gm)	0.50	8.3	10.8	9.4	5.0	4.9

Table 4.5 EPR results for $Y_{3-x}Gd_xFe_5O_{12}$ ($x = 0$) samples.

Sample	Room temperature (295 K)		Liquid nitrogen temperature (78 K)	
	ΔH (gauss)	g	ΔH (gauss)	g
YA4	700	2.08	1350	2.22
YA6.5	725	2.09	1375	2.22
YA7	550	2.09	575	2.37
YA8	538	2.08	825	2.13
YA9	475	2.08	750	2.22

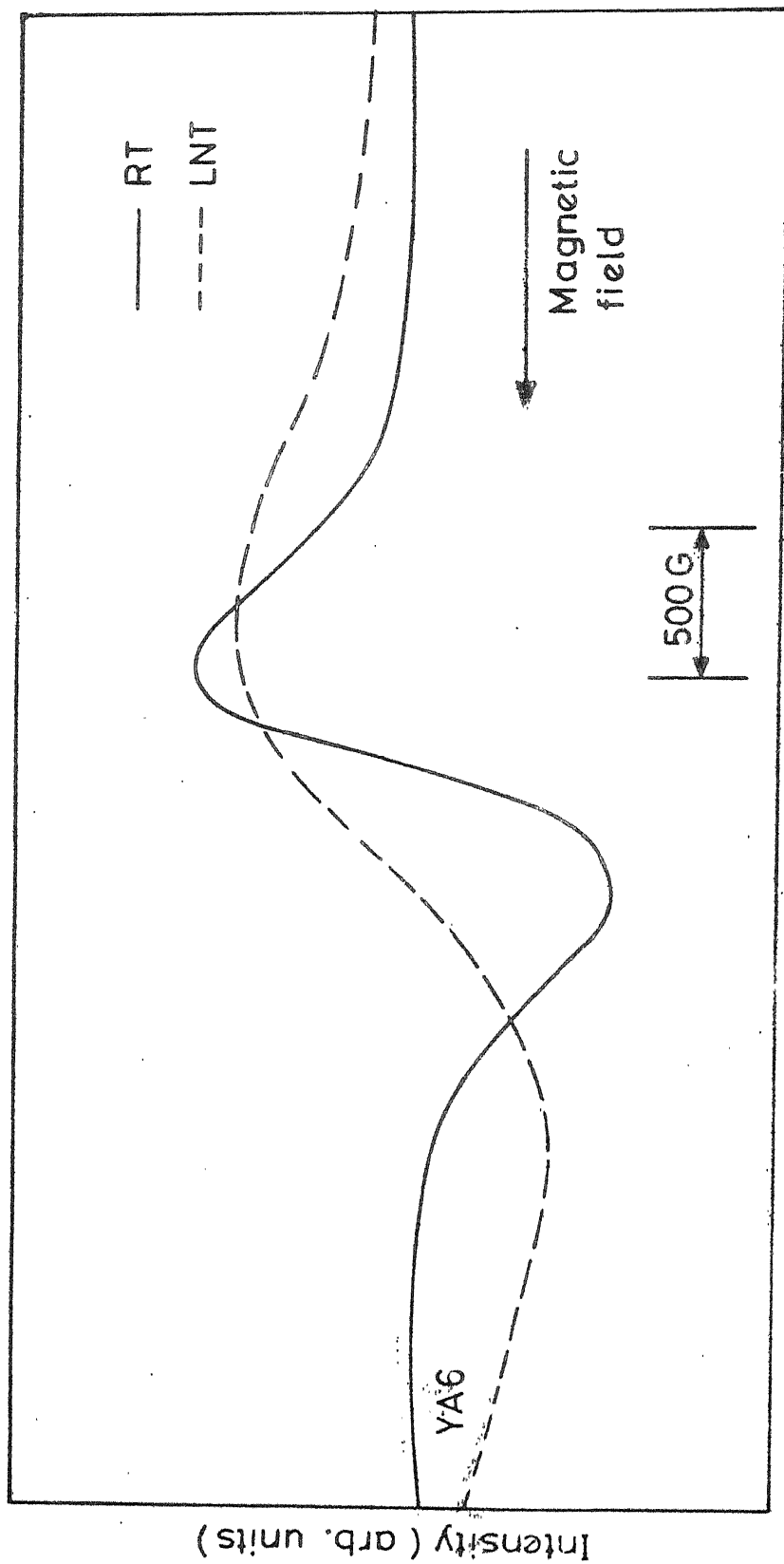


Fig.4.4 Typical EPR spectra for $Y_{3-x}Gd_xFe_5O_{12}$ ($x=0$) samples recorded at RT (295K) and LNT (78K).

ions [19] is not observed in any of the samples. This behaviour indicates the presence of some super-exchange interaction in all the samples. It is observed that line-width for YA4 and YA6.5 are nearly same. However, a sharp decrease is observed in case of YA7. The line-width further decreases for YA8 and YA9 in EPR spectra recorded at room temperature. The decrease in line-width as a function of heat-treatment temperature is indicative of crystallization of magnetic phases which enhances super-exchange interaction.

4.3.2 $\text{Y}_{3-x}\text{Gd}_x\text{Fe}_5\text{O}_{12}$ System With $x = 0.5$

The X-ray diffraction patterns of the as prepared precursor and heat-treated $\text{Y}_{3-x}\text{Gd}_x\text{Fe}_5\text{O}_{12}$ ($x = 0.5$) samples are shown in Fig. 4.5. The d values, relative intensity and assignment of observed diffraction lines are given in Table 4.6. The samples heat-treated below 600°C are X-ray amorphous. The samples given heat-treatment above 600°C show presence of garnet phases. Some other phases such as $\alpha\text{-Fe}_2\text{O}_3$ and $\gamma\text{-Fe}_2\text{O}_3$ are also present. The ratio of garnet phase increases in samples heat-treated at higher temperature. The heat-treatment schedule A compared to N is more favourable for development of garnet phase.

Mössbauer spectra of $\text{Y}_{3-x}\text{Gd}_x\text{Fe}_5\text{O}_{12}$ ($x = 0.5$) precursor samples heat-treated at temperatures, $T = 400, 600, 650, 700, 800^\circ\text{C}$ are shown in Fig. 4.6(a) for heat-treatment schedule A

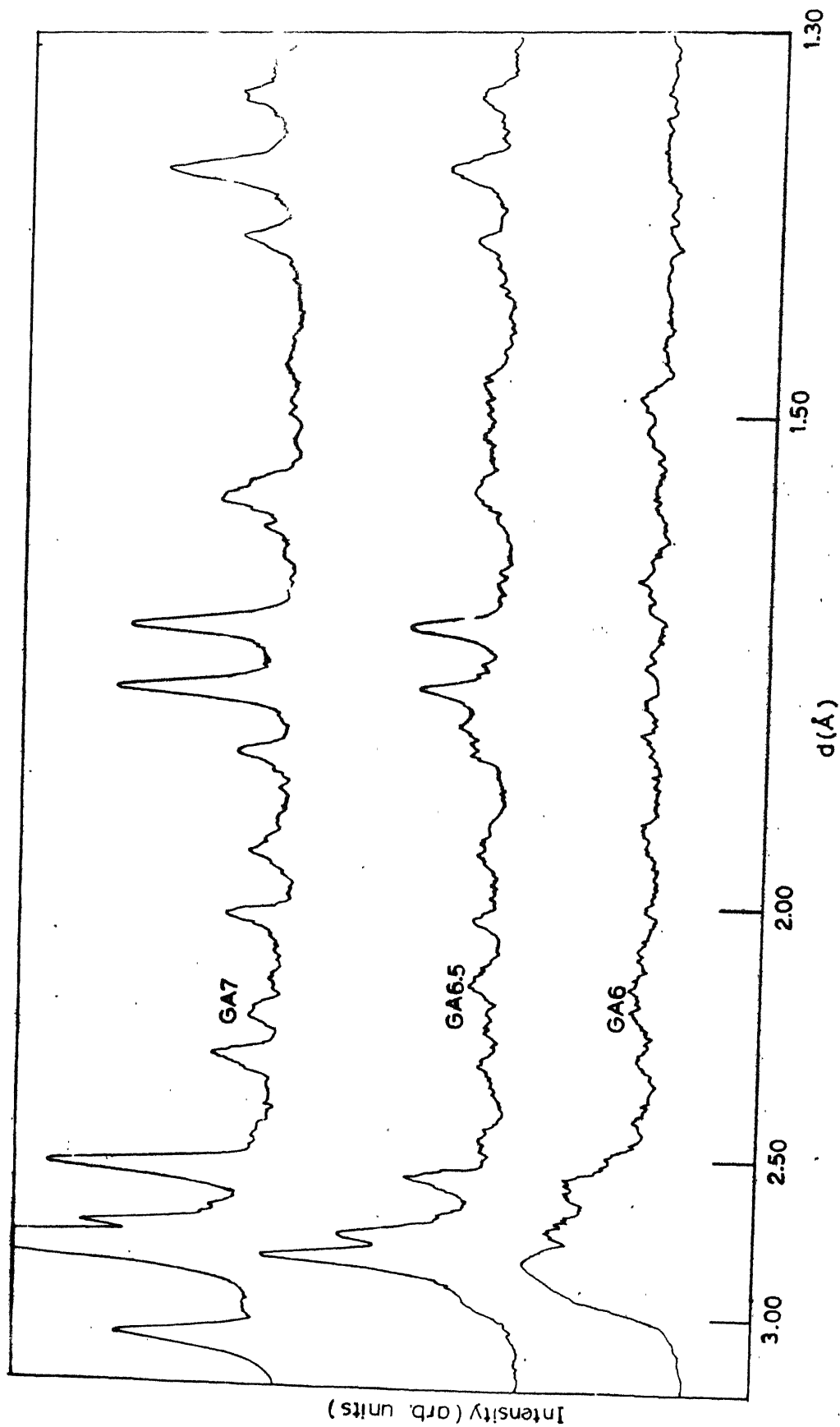


Fig 4.5 X-ray diffractograms of $Y_{3-x}Gd_xFe_5O_{12}$ ($x=0.5$) samples recorded using $CrK\alpha$ target.

Table 4.6 X-ray data for sample $Y_{3-x}Gd_xFe_5O_{12}$ ($x = 0.5$) samples.

YGA6.5		YGN7		YGA7		YGA8		Assignment, phase (hkl)
d (Å)	I/I ₀ %	d (Å)	I/I ₀ %	d (Å)	I/I ₀ %	d (Å)	I/I ₀ %	
2.8036	100	3.1306	39	3.1236	40	3.1306	50	G(400)
2.7190	73	2.7874	100	2.78	100	2.7981	100	G(420)
2.5524	45	2.7190	52	2.7190	46			S(100)
		2.5434	55	2.5524	51	2.5524	61	S(100), G(422)
				2.5348				
2.4466	22	2.4466	21					G(431)
2.2828	24	2.2724	45	2.2759		2.2793	37	G(521)
				2.2724	24			
				2.1973	19			H(113)
				2.1817				
2.1307	28							S(400)
2.0212	27	2.0212	25	2.0212	18	2.0212	37	G(611), 532
1.9201	26			1.9289	19			S(420)
1.7979	29	1.7979	30	1.7998	22	1.7960	41	G(444)
1.7663	34							
1.7243	49	1.7243	48	1.7243	43	1.7260	55	G(640)
1.6647	52	1.6616	54	1.6662	39	1.6555	55	S(422), H(116)
				1.6631				
1.5503	29	1.5540	30	1.5565	25			G(642)
				1.5528				
1.3916	27			1.3891	21	1.5552	41	G(800)
1.3559	39			1.3559	34	1.3891	37	G(410)
				1.3551				
1.3266	27			1.3233	21	1.3551	48	G(842), H(202)
						1.3239	37	G(654), S(620)

G - Garnet (Y₃GdFe₅O₁₂) ; S = spinel (Y-Fe₂O₃) ; H = Hexagonal (α-Fe₂O₃)

and in Fig. 4.6(b) for schedule H. The Mössbauer spectra of these samples ($x = 0.5$) show essentially the similar behaviour as that observed for $x = 0$ samples. The Mössbauer spectra are analysed as explained for $x = 0.0$ samples. The Mössbauer parameters obtained from the analysis of these spectra (Fig. 4.6(a) and (b)) are given in Table 4.7(a) for schedule A samples and in Table 4.7(b) for schedule N samples. The Mössbauer spectra of samples heat treated at various temperature show essentially the similar behaviour as that of $x = 0$ system except the volume fraction of garnet phase observed in $x = 0.5$ samples is more than that observed in $x = 0$ sample (see Tables 4.3 and 4.7). Our main interest in this study was to determine the optimum heat-treatment schedule suitable for development of garnet phase. We have studied this $x = 0.5$ system in detail by giving various heat-treatments. We have selected this system for extensive study because the volume fraction of garnet phase is found to be more in this system compared to other systems studied.

Mössbauer spectra of samples heat-treated below 600°C (YGA4, YGA6, YGN6) consist of two broad ($\text{FWHM} = 0.70$ mm/sec) quadrupole split peaks characteristic of amorphous paramagnetic nature. The quadrupole splitting $\Delta E = 1.10$, 1.11 and 1.05 mm/sec obtained for YGA4, YGA6 and YGN6 respectively by conventional least square fitting differ from the ΔE values obtained by EFG distribution (values

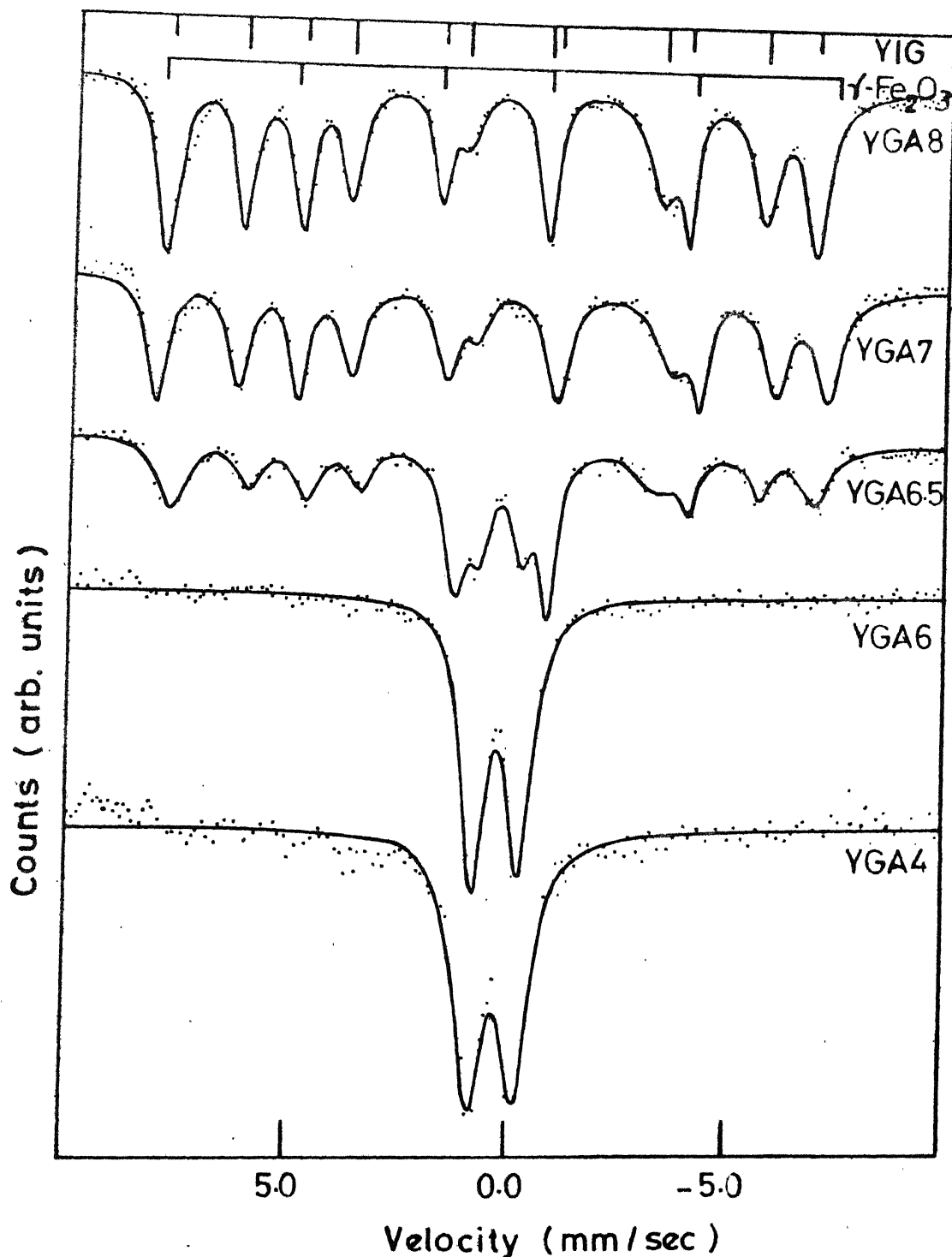


Fig.4.6(a) Mössbauer spectra of $Y_{3-x}Gd_xFe_5O_{12}$ ($x=0.5$) samples heat treated as per schedule A. Peak positions observed for polycrystalline YIG and γ -Fe₂O₃ are also shown.

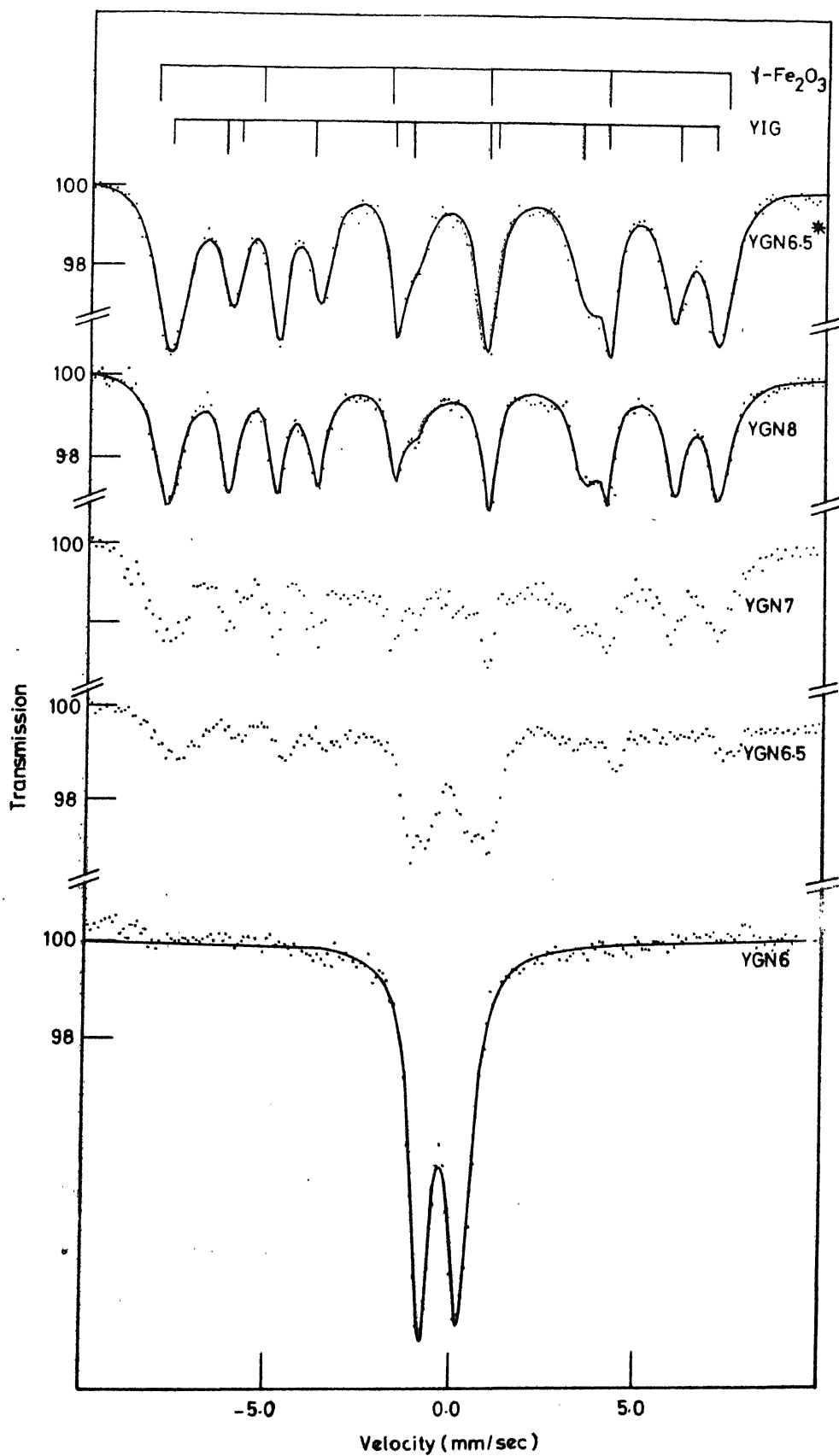


Fig.4-6(b) is same as Fig.4-6(a), but heat treatment schedule N samples.

marked (b)) in a consistent manner. The calculated EFG distributions for these samples ($x = 0.5$) are shown in Fig. 4.7. IS values in these samples are intermediate to those for octahedral and tetrahedral coordinated Fe^{3+} . It indicates that both coordinations do exist in these samples but are not resolved due to amorphous nature of these samples. Similar behaviour was also observed in $x = 0$ system for sample heat-treated at 600°C .

The Mössbauer spectra of samples heat-treated at 650°C for 4 hours (YGA6.5 and YGN6.5) consist of two quadrupole split peaks and magnetically split (six-finger) components, while in sample heat-treated at 650°C for 40 hours (YGN6.5^{*}) only magnetically split (six-finger) components are observed. One quadrupole pair with ΔE 1.05 mm/sec is due to amorphous state. The other quadrupole split pair with $\Delta E = 2.00$ mm/sec is characteristic of growth of magnetic phases. The quadrupole split component vanishes in sample heat-treated above 650°C indicating magnetic ordering. From IS and H_{int} values, the magnetic components are identified to be due to $\gamma\text{-Fe}_2\text{O}_3$, $\alpha\text{-Fe}_2\text{O}_3$ and the garnet phase. The volume fraction of garnet phase in YGN6.5, YGA6.5 and YGN6.5^{*} is 10 %, 59 % and 50 % (see Table 4.7) respectively. This shows that heat-schedule A and longer heat-treatment time is more suitable for development of garnet phase. Magnetic moment versus magnetising

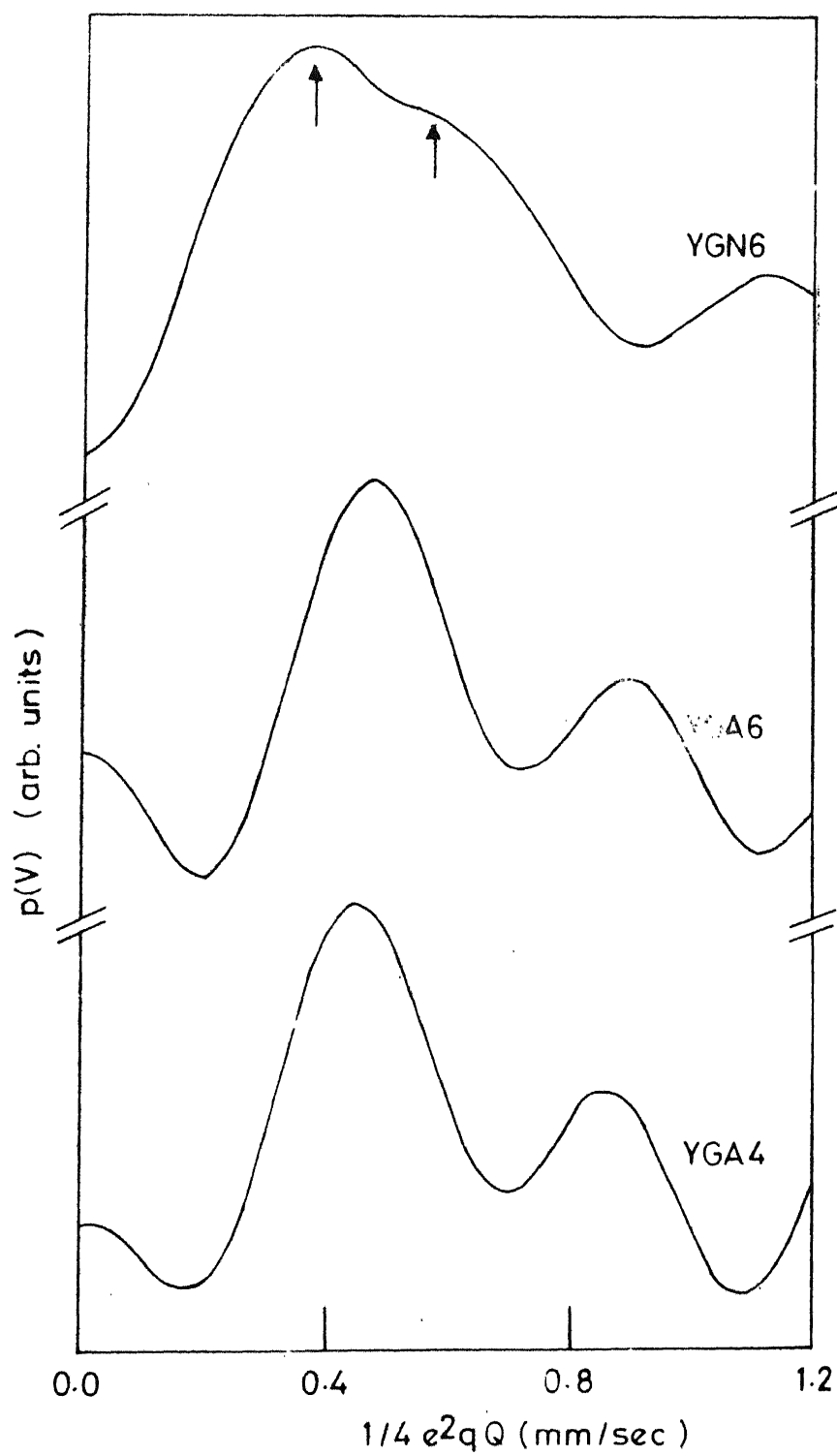


Fig.4.7 EFG distribution for $Y_{3-x}Gd_xFe_5O_{12}$ ($x=0$) samples.

Table 4.7(a) Mössbauer parameter of $Y_{3-x}Gd_xFe_5O_{12}$ ($x = 0.5$) samples given heat-treatment as per schedule A.

Sample	Quadrupole split components					Magnetic Zeeman split components			
	IS (w.r.t. α -Fe) mm/sec	peak width mm/sec	E		FWHM of p(V) distribution mm/sec	IS (w.r.t. α -Fe) mm/sec	H_{int} Koe	Assignment (phase)	Volume fraction of garnet phase %
			(a)	(b)					
YGA4	0.38(2)	0.85(5)	1.10(3)	0.88	0.54				
				0.77	0.32				
YGA6	0.35(1)	0.70(2)	1.11(4)	0.92	0.48				
				1.76	0.34				
YA6.5	0.33(2)	0.61(8)	1.02(4)			0.45(2)	471(7)	S,H,G(O)	59
	0.31(2)	0.56(4)	1.99(2)			0.21(2)	386(9)	G(t)	
YGA7						0.50(8)	472(4)	S,H,G(O)	80
						0.18(1)	393(5)	G(t)	
YGA8						0.58(1)	472(4)	G(O),S,H	69
						0.27(2)	373(4)	G(t)	

S = Spinel γ -Fe₂O₃; H = Hexagonal α -Fe₂O₃; G = Garnet (YGG).

field plots for samples heat-treated at 650 and 700 °C are shown in Fig. 4.8. The higher magnetic moment observed for YGN6.5* compared to YGA6.5 indicates larger amount of magnetic phases in this sample. The Mössbauer spectra of sample heat-treated at 700 °C (YGA7 and YGN7) and 800 °C (YGA8 and YGN8) show only magnetically split components. The volume fraction of garnet phase increases with higher heat-treatment temperature. The volume fraction of garnet phase is more in samples given heat-schedule A compared to samples given heat-schedule N.

Typical EPR spectra for $Y_{3-x}Gd_xFe_5O_{12}$ ($x = 0.5$) samples are shown in Fig. 4.9 and the EPR results are given in Table 4.8. The g value is around 2.1 at room temperature and lies in the range 2.48 - 2.13. The line-width remains almost similar in samples heat-treated at 400 and 600 °C. The line-width decreases sharply in sample heat-treated at 650 °C which is indicative of crystallization of magnetic phases at this temperature. The resonance corresponding to $g = 4.3$ is also not observed in any of these samples. This may be explained due to super-exchange interaction as done in case of $x = 0$ system.

4.3.3 $Y_{3-x}Gd_xFe_5O_{12}$ System With $x = 3$

The X-ray diffraction patterns of $Y_{3-x}Gd_xFe_5O_{12}$ ($x = 3$) samples are shown in Fig. 4.10. The sample heat-treated

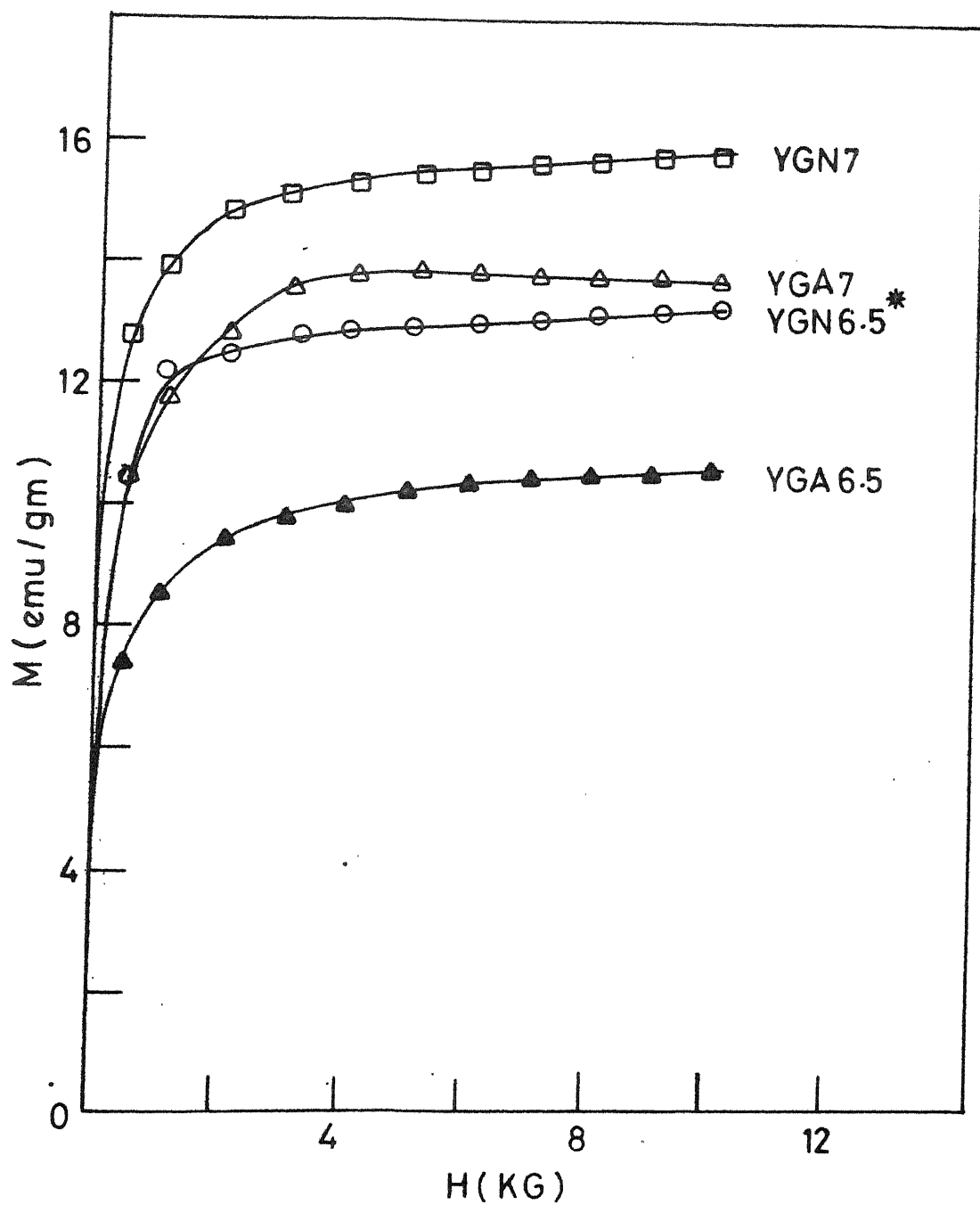


Fig.4.8 Magnetic moment versus H for $Y_{3-x}Gd_xFe_5O_{12}$ ($x=0.5$) samples heat treated at 650 and 700°C.

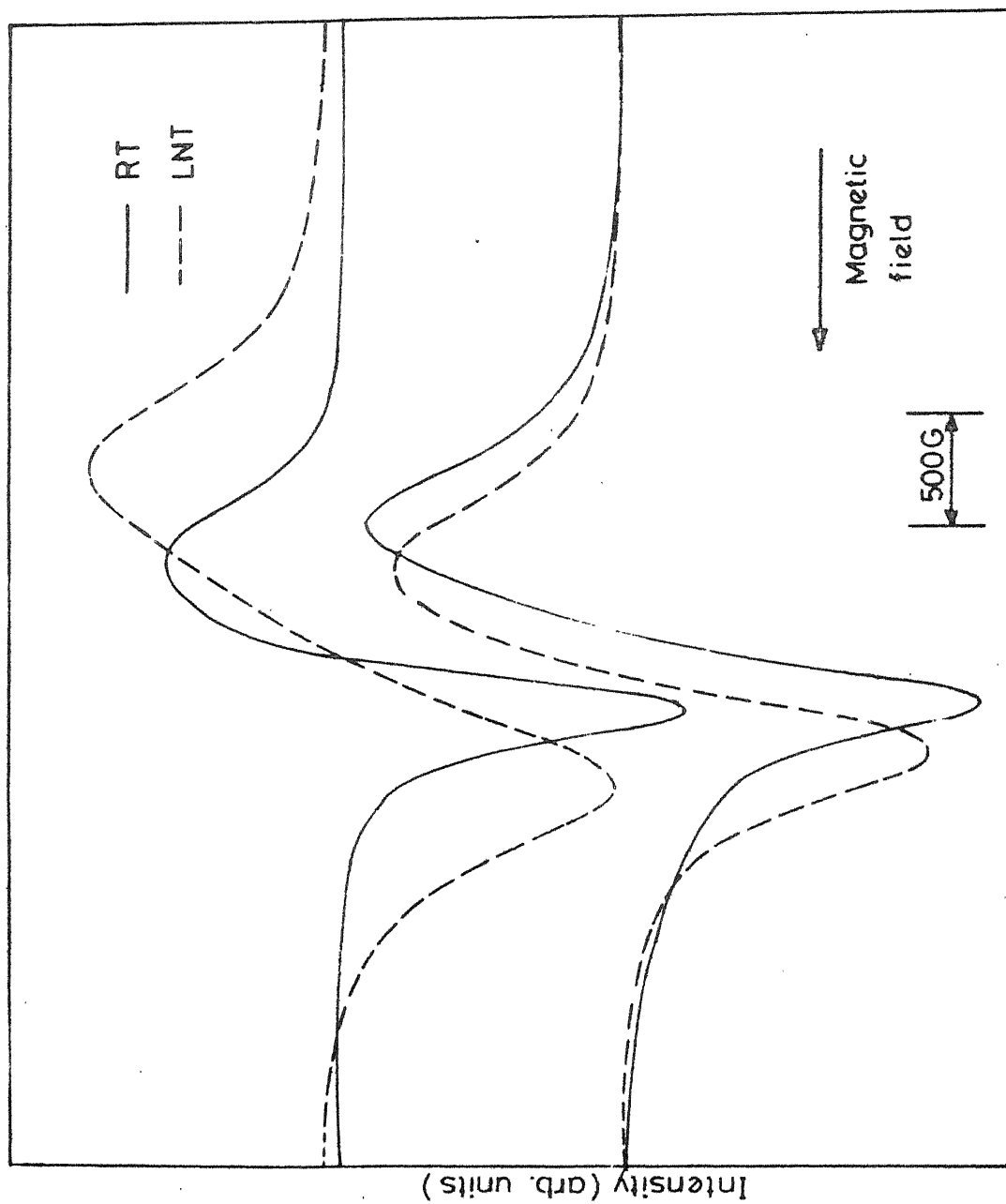


Fig.4.9 Typical spec spectra of $Y_{3-x}Gd_xFe_5O_{12}$ ($x=0.5$) samples measured at RT (295K) and LNT (78K).

Table 4.8 EPR results for $Y_{3-x}Gd_xFe_5O_{12}$ ($x = 0.5$) samples.

	Room temperature (295 K)		Liquid nitrogen temperature (78 K)	
	ΔH (gauss)	g	ΔH (gauss)	g
YGA4	875	2.14		
YGA6	725	2.09	1500	2.46
YGA6.5	375	2.11	475	2.22
YGA6.5*	263	2.10	562	2.18
YGAC	363	2.14	650	2.13
YGN6	850	2.09	1425	2.48
YGN8	387	2.12	450	2.26

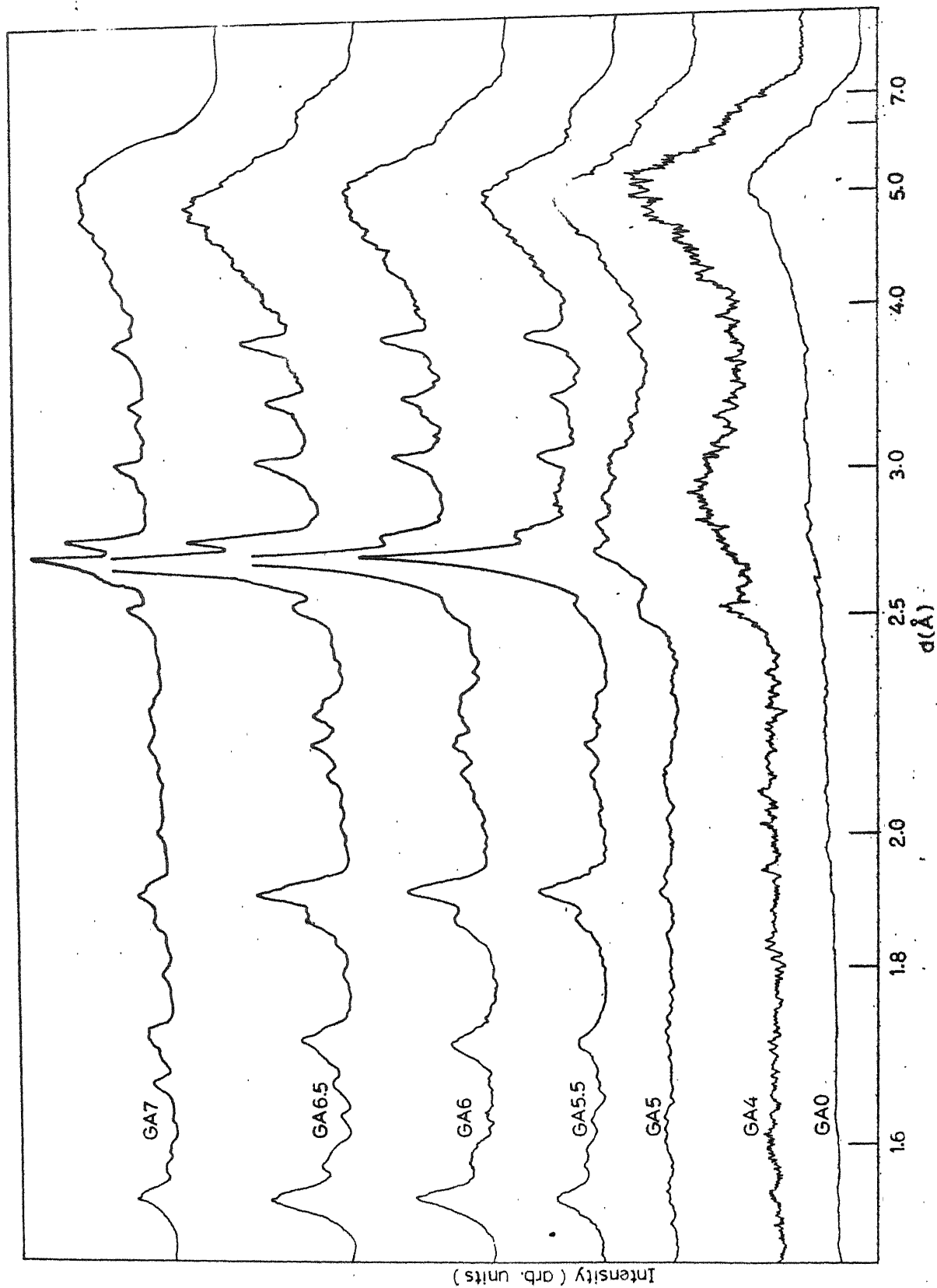


Fig.4.10 X-ray diffractograms of $Y_{3-x}Gd_xFe_5O_{12}$ ($x=3.0$) samples recorded using CrK target.

upto 500 °C are X-ray amorphous. The samples heat-treated above 500 °C show diffraction lines due to garnet (GdIG), Hexagonal (α -Fe₂O₃) and Spinel (γ -Fe₂O₃) phases. The d values, relative intensity and assignment of observed diffraction lines are given in Table 4.9. It is interesting that the X-ray diffraction lines observed for this system are nearly the same as observed for the earlier $x = 0$ and $x = 0.5$ samples. The volume fraction of hexagonal α -Fe₂O₃ phase is found to be more than that in $x = 0$ and $x = 0.5$ systems. Because the substitution of Gd³⁺ ion for Y³⁺ results in ~~ex~~solution of spinel and hexagonal phases [8]. The volume fraction of garnet phase increases with higher heat-treatment temperature (it increase by about a factor of 2 in YA7 as compared to YA5.5).

Mössbauer spectra of Y_{3-x}Gd_xFe₅O₁₂ ($x = 3$) samples heat-treated at temperatures $T = 500, 550, 600, 650, 700$ °C are shown in Fig. 4.11. The Mössbauer parameters evaluated from these spectra are given in Table 4.10. The Mössbauer spectrum of GA5 consists of two broad (FWHM = 0.80 mm/sec) quadrupole split peaks characteristic of amorphous paramagnetic nature of the sample. The isomer shift with respect to α -Fe (0.59(3) mm/sec) and quadrupole splitting ($\Delta E = 1.17(2)$ mm/sec) suggest that the Fe³⁺ exist mainly in tetrahedral coordination in YA5 and YA5.5. While YA5.5 shows a quadrupole split component and a magnetically split

Table 4.9 X-ray diffraction data for $Y_{3-x}Gd_xFeO_{5+12}$ ($x = 3.0$) Samples.

GA5.5			GA6			GA6.5			GA7			Assignment, phase (hkl)
d (Å)	I/I ₀ %	d (Å)	I/I ₀ %	d (Å)	I/I ₀ %	d (Å)	I/I ₀ %	d (Å)	I/I ₀ %	d (Å)	I/I ₀ %	
4.4668		5.2073	56.0	5.2073	45.6							G(211)
3.8071	57.0	4.7322	51.7									S(111)
3.4128	43.0	4.4522	45.6									G(220)
3.1030	34.5	3.8176	46.9	3.8282	53.7	3.8071	53.2					G(321)
2.7785	39.0	3.4128	40.9	3.4212	39.2	3.4212	45.9					G(400)
2.6937	47.0	3.10	43.3	3.11	31.2	5.1030	54.0					G(420), S(291)
2.5434	100.0	2.78	47.4	2.776	45.9	2.7819	83.0					H(104)
	35.0	2.6937	100.0	2.6937	100.0	2.7088	100.0					G(422), S(311)
		2.5434	30.1	2.5348	23.1	2.5391	45.1					G(521), H(321)
				2.2457	18.1							G(440)
2.1787	22.5	2.1756	26.7	2.1817	18.7	2.1817	33.8					G(611, 532), H(400)
1.9089	38.5	2.1190	24.5	2.1219	15.6							G(611, 531, 631)
1.8679	25.5	1.9111	40.0	1.9089	30.9	1.9089	39.5					G(631), H(024), S(420)
1.7027	25.0			1.8679	20.3							G(633, 552, 640), H(116), S(422)
				1.7125	21.5	1.7158	36.3					G(800), S(432)
				1.7026	16.5	1.7243						H(300)
				1.5809								H(208)
1.5441	31.0	1.5466	37.0	1.5454	27.8	1.5478	41.1					H(220), S(533)
1.5478						1.5540						
1.3574	20.0	1.4430	18.5	1.4469	15.0							
		1.3566	21.1	1.3581	22.5							
				1.2673	14.6							

G = Garnet phase (GdIG); H = Hexagonal phase ($CaFe_2O_3$); S = Spinel phase ($\gamma-Fe_2O_3$).

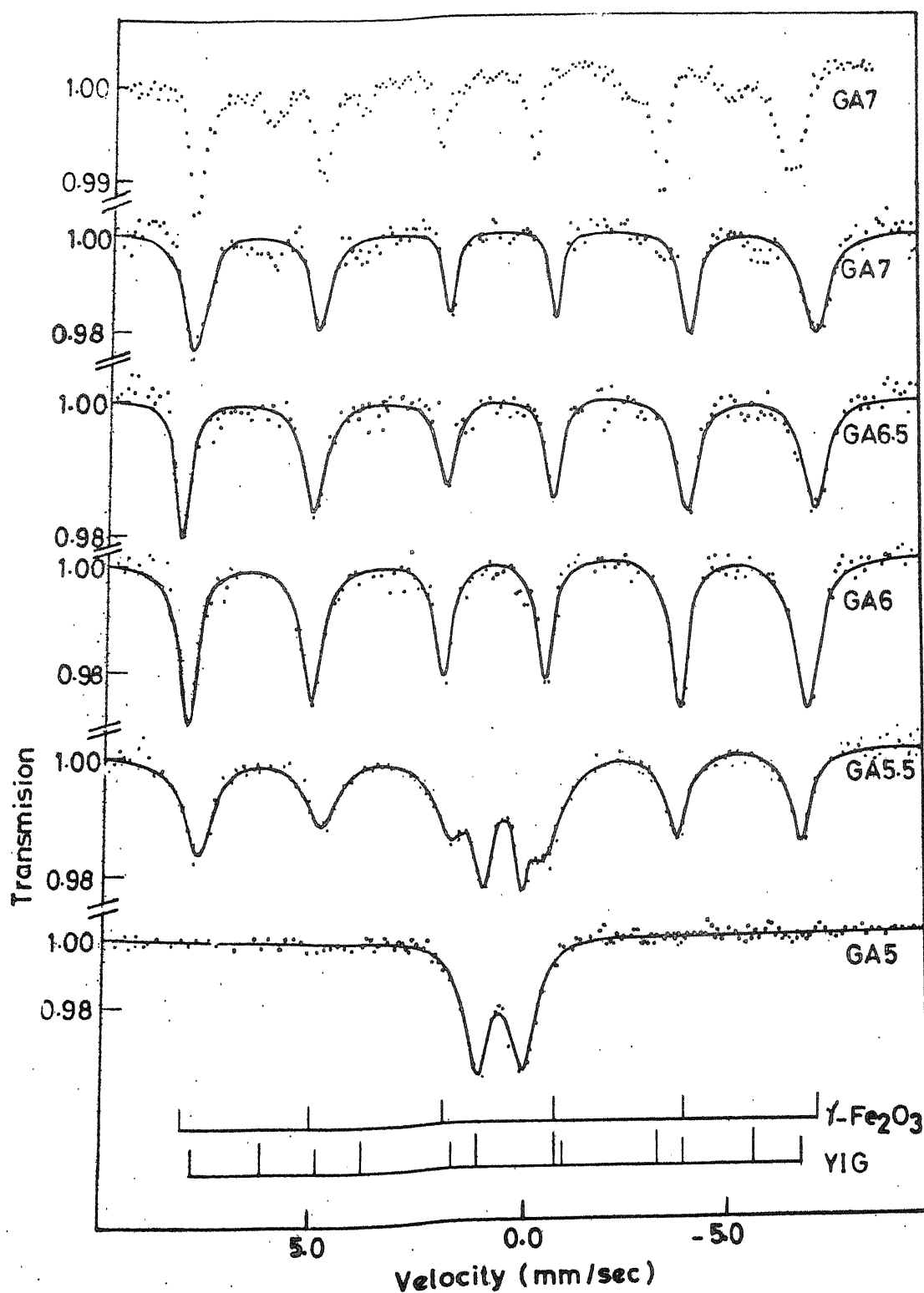


Fig. 4.11 Mössbauer spectra of $\text{Y}_{3-x}\text{Gd}_x\text{Fe}_5\text{O}_{12}$ ($x=3$) samples recorded at room temperature. Peak positions observed for polycrystalline YIG and $\gamma\text{-Fe}_2\text{O}_3$ are shown at the bottom.

Table 4.10 Mössbauer parameter of $Y_{3-x}Gd_xFe_5O_{12}$ ($x = 3$) samples.

	Quadrupole split components					Magnetic Zeeman split components				
	IS (w.r.t. α -Fe) mm/sec	peak width mm/sec	ΔE		area of distribution billion mm/sec	IS (w.r.t. α -Fe) mm/sec	Average peak width mm/sec	Hint Koe	Assignment (phase)	Volume fraction of garnet phase %.
			(a)	(b)						
GA5	0.59(3)	0.80(4)	1.17(2)	1.16	0.44	0.50(3)	0.88(11)	466(9)	S,H	
GA5.5	0.48(5)	0.48(11)	0.96(5)	-	-	0.58(3)	0.60(11)	472(4)	S,H	
GA6						0.46	0.57	490(5)	S,H,G(O)	Very small
GA6.5									G(t)	
GA7						0.37	0.54	482(6)	S,H,G(O)	Very small
									G(t)	

Indicate presence of the phase but Mössbauer parameters could not be evaluated due to very low intensity of resonance lines.

S = Spinel $Y-Fe_2O_3$, H = Hexagonal $\alpha-Fe_2O_3$, G = Garnet (GdIG)

component.

The Mössbauer spectra of GA6, GA6.5 and GA7 consist of only magnetically split components (six-finger spectra). The magnetic component found in GA5.5, GA6, GA6.5 and GA7 is identified to be mainly due to $\alpha\text{-Fe}_2\text{O}_3$ and $\gamma\text{-Fe}_2\text{O}_3$. The spectra of GA6.5 and GA7 show presence of garnet phase. The Mössbauer spectrum of GA7 was recorded for larger counts (\approx twice the value usually taken) to confirm the presence of garnet phase (see Fig. 4.11). Although the X-ray data reveal garnet phase (GdIG) the Mössbauer spectra do not show the same amount of garnet phase. The reason for this behaviour may be two-fold.

1. The volume fraction of garnet phase is small and the hyperfine-field corresponding to it is smeared out due to presence of large amounts of $\alpha\text{-Fe}_2\text{O}_3$ and $\gamma\text{-Fe}_2\text{O}_3$.
2. The compensation temperature of GdIG is near room temperature (275 K) [2]. Therefore GdIG remains in magnetically disordered state at room temperature. To check this point we recorded the Mössbauer spectra of these samples at liquid nitrogen temperature (78 K). These spectra are shown in Fig. 4.12. But even in spectra recorded at LNT the volume fraction of garnet phase has not changed.

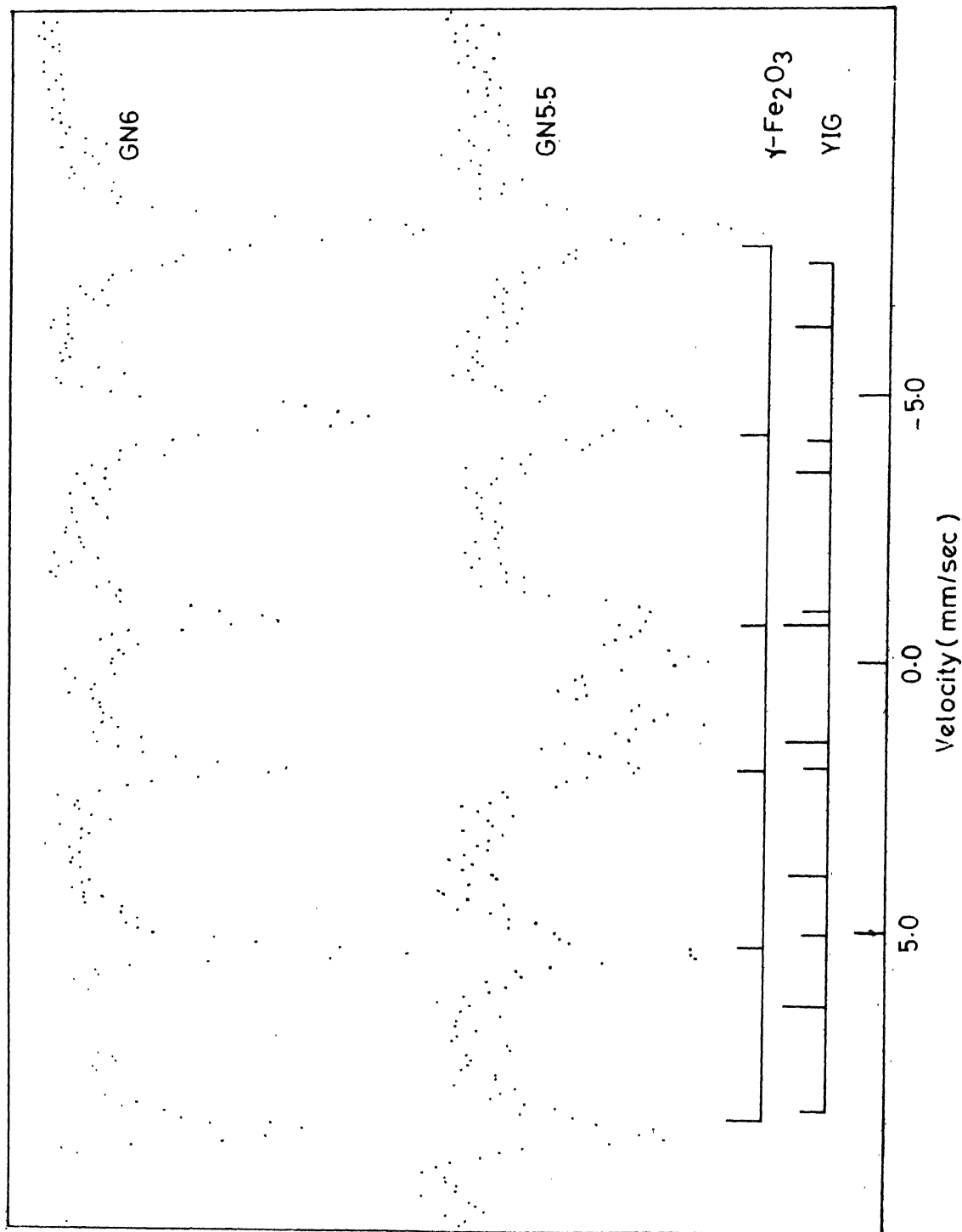


Fig.4.12 Mössbauer spectra of $\text{Y}_{3-x}\text{Gd}_x\text{Fe}_5\text{O}_{12}$ ($x=3$) recorded at liquid nitrogen temperature.

Peak positions observed for polycrystalline YIG and $\gamma\text{-Fe}_2\text{O}_3$ are shown at the bottom.

The above two effects may account for the observed volume fraction of GdIG phase. But in Mössbauer spectra of GA7 recorded for extended time we clearly see that garnet phase is present and in GA6.5 and GA6 also there is an indication of garnet phase (Fig. 4.11).

EPR spectra of these samples were recorded at RT and LNT. Some typical EPR spectra are shown in Fig. 4.12. EPR line-width for $g \simeq 2$ resonance versus heat-treatment temperature is plotted in Fig. 4.14. The EPR results are given in Table 4.11. We observe $g \simeq 2.00$ resonance as observed in earlier $x = 0$ and $x = 0.5$ system. In addition we observed another resonance with $g = 5.15$ in GA5.5 and $g = 5.70$ in GA6 at room temperature which correspond to $g = 4.3$ resonance observed for paramagnetic Fe^{3+} [19]. The EPR line-width ΔH versus heat-treatment temperature plot (Fig. 4.14) also shows a change at $T = 550^\circ\text{C}$. This indicates some kind of transition around this temperature. The g value for $g = 2$ resonance increases continuously for room temperature spectra and decreases for LNT spectra.

4.4 SUMMARY

Amorphous garnet system $\text{Y}_{3-x}\text{Gd}_x\text{Fe}_5\text{O}_{12}$ ($x = 0, 0.5$ and 3) in which garnet phase can be crystallized by suitable heat-treatment have been studied by Mössbauer spectroscopy, X-ray diffraction, electron paramagnetic resonance (EPR) and

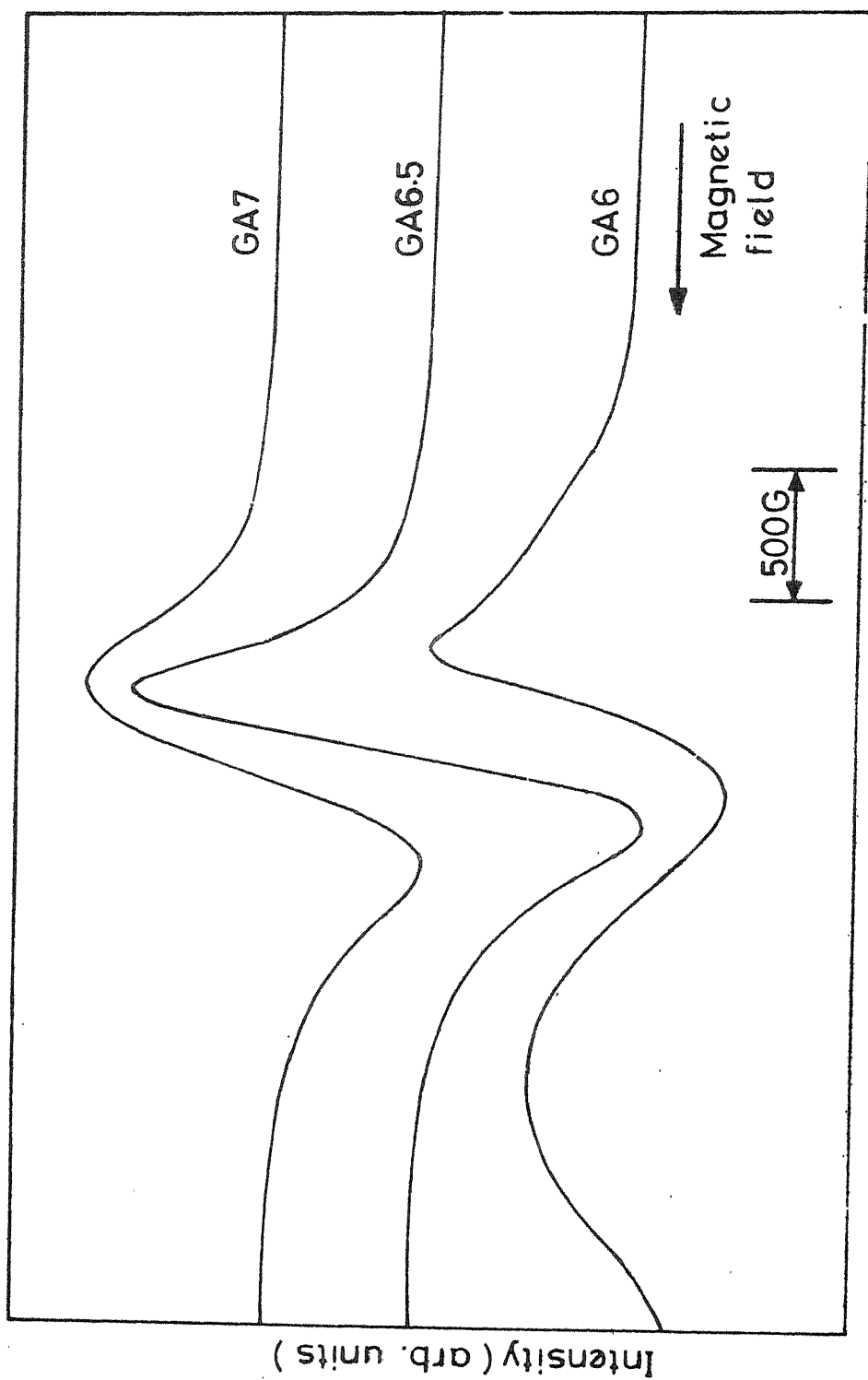


Fig.4.13 Typical EPR spectra of $Y_{3-x}Gd_xFe_5O_{12}$ ($x=3$) samples recorded at room temperature.

Table 4.11 EPR results for the $Y_{3-x}Gd_xFe_5O_{12}$ ($x = 3$) samples.

Sample	Room temperature (295 K)		Liquid nitrogen temperature (78 K)	
	g	$\Delta H(G)$	g	$\Delta H(G)$
YGA5	2.01	700	2.86	750
GA5.5	2.11	650	2.74	600
GA5.5 [±]	2.16	450	2.18	500
	5.15	825		
GA6	2.15	500	2.15	750
	5.70	900		
GA6.5	2.29	475	2.18	900
GA7	2.33	575	2.25	825

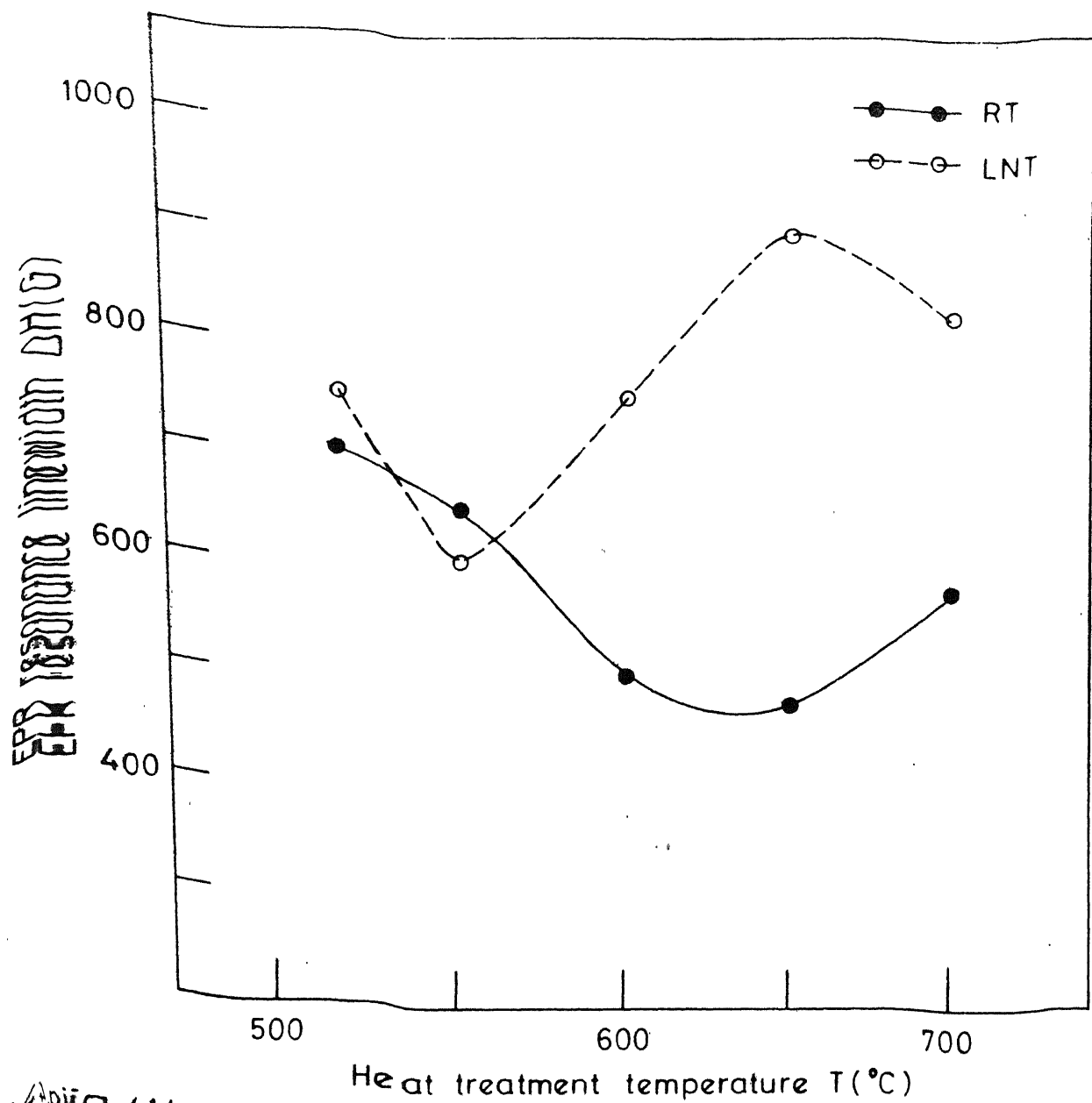


Fig. 4.14 EPR resonance linewidth (ΔH) observed at RT and LNT versus heat treatment temperature plot for $Y_{3-x}Gd_xFe_5O_{12}$ ($x=3$) samples.

magnetization measurements. The measurements have been made on sample given various heat-treatments (see Table 4.1 for details of these samples). The crystallization temperature for the $Y_{3-x}Gd_xFe_5O_{12}$ system has been found to be around 650, 600, 550 °C for $x = 0, 0.5$ and 3 respectively. The Mössbauer spectra of samples heat-treated below crystallization temperature consist of broad quadrupole split peaks characteristic of amorphous paramagnetic nature of samples. From IS and ΔE values it is inferred that Fe^{3+} exists in both octahedral and tetrahedral coordinations. The Mössbauer spectra of samples heat-treated above the crystallization temperature consist of magnetically split components due to crystallization and magnetic ordering of $\alpha-Fe_2O_3$, $\gamma-Fe_2O_3$ and garnet phase. The volume fraction of garnet phase is found to increase in sample heat-treated at higher temperature and for longer duration. The heat-treatment schedule A is found to be more favourable than schedule M for development of garnet phase. Mössbauer spectroscopic data are correlated with X-ray and magnetization data. In EPR resonance corresponding to $g = 2$ has been observed in all the samples, in addition $g = 4.3$ resonance has been observed in some $x = 3$ samples. The EPR line-width decreases with higher heat-treatment temperature indicative of crystallization of magnetic phases. These studies are found to be very useful for identification of various magnetic phases present in amorphous $Y_{3-x}Gd_xFe_5O_{12}$ garnet system.

REFERENCES

1. E.P. Wohlfarth, Ferromagnetic Materials, Vol. II, North-Holland, Amsterdam (1980)
2. W.H. Von Anlock, Handbook of Microwave Ferrite Materials, Academic press, New York (1965)
3. R. Schultes, H. Schieder, F.J. Literstand and G.M. Kolvius, Nucl. Inst. and Methods 199, 343 (1982)
4. D. Bahadur and D. Roy, accepted for presentation at the International Conference of Ferrites, San-fransisco U.S.A., Nov. (1984)
5. M. Eibschutz, M.E. Lines and K. Nasu, Phys. Rev. B22, 3767 (1980)
6. E. Sawatzky and E. Kay, J. Appl. Phys. 39, 4700 (1968)
7. D.W. Johnson and F.J. Schnettler, J. Amer. Cer. Soc. 53, 440 (1970)
8. Th. J.A. Popma and A.M. Von Dispen, Mater. Res. Bull. 9, 1119 (1974)
9. D. Roy, R. Bhatnagar and D. Bahadur, J. of Mater. Sci., (accepted) (1984)
10. G.R. Harrison and L.R. Hodges Jr., J. Appl. Phys. Suppl. to Vol. 33, 1375 (1962)
11. Akhilesh Prasad, D. Bahadur, R.M. Singru and D. Chakravorty, J. Mater. Sci. 17, 2687 (1982)
12. Akhilesh Prasad, R.M. Singru, D. Bahadur and D. Chakravorty, J. Mater. Sci., to be published (1983)

13. B. Window, J. Phys. B4, 401 (1971)
14. B. Greenberg, J. Phys. Chem. Solids 3, 30 (1957)
15. Von R. Schrader and G. Büttner, Z. Anorg. Allagem. Chemie. 320, 205 (1963)
16. V. Kastalsky and M.F. Westcott, Aust. J. Chem. 21, 1061 (1968)
17. M.V. Nair, Ph.D. thesis, Indian Institute of Technology, Kanpur (1981) unpublished.
18. C.R. Murjian and E.A. Sigety, Phys. Chem. Glasses 5, 63 (1964)
19. A.K. Bandopadhyaya, J. Zarzycki, P. Aurie and J. Chappert, J. Non Cryst. Solids 40, 253 (1980).

CHAPTER 5

MÖSSBAUER SPECTROSCOPIC STUDIES OF DILUTE ALUMINIUM-IRON ALLOYS

5.1 INTRODUCTION

Iron is always present as an impurity in commercial aluminium and aluminium alloys to the extent of 0.5 to 1.0 wt. %. They form a variety of intermetallic compounds such as Al_6Fe , $\text{Al}_{13}\text{Fe}_4$, Al_9Fe_2 , Al_5Fe_2 etc. which have well defined geometrical shapes. These compounds are formed when the molten aluminium and alloys are cooled to form ingots or castings. It is difficult to redissolve them by heat-treatment in the solid state and hence they are referred to as 'insolubles'. These insolubles are strongly electro-positive with respect to aluminium, leading to enhanced corrosive attack on these alloys. They have a profound effect on the mechanical properties; they are normally brittle and affect adversely the ductility of aluminium alloys. It is interesting to study the precipitation characteristics of various iron containing phases as a function of heat-treatment.

The solid solubility of iron in aluminium is extremely small (only 0.05 wt % iron at 655 °C [1] and dropping rapidly to almost zero solubility at lower temperatures). It is well known that a large super-saturation

of Fe in Al can be achieved by rapid solidification techniques such as melt, spinning, splat quenching etc. [2]. For example, Tonejc et al. have prepared super-saturated Al-Fe alloy (Fe 2.18 wt %) [3]. The extension of solid solubility results in constitutional changes in the retained phases. Non-equilibrium phases can form as a result of being favoured kinetically over equilibrium phases [2]. For example, by controlling the solidification front velocity (via steady withdrawal of a sufficiently thin sample through a high temperature gradient) the primary equilibrium phase $\text{Al}_{13}\text{Fe}_4$ can be suppressed in favour of the non-equilibrium Al-Al₆Fe eutectic with or without α -Al dendrites [4]. The other non-equilibrium phases Al_mFe or Al_xFe are also identified to be formed [5]. Further extension of solubility of Fe in α -Al, eventually results in partitionless solidification to form featureless single phase α -Al solid solution with the same composition as the parent melt [6]. The aluminium-rich end on the Al-Fe binary phase diagram is shown in Fig. 5.1 [7]. Under equilibrium condition, the solid solution and $\text{Al}_{13}\text{Fe}_4$ are the only phases present in alloys containing < 30 wt % Fe. However, as pointed out earlier a variety of metastable phase can be formed by rapid solidification.

A variety of experimental techniques such as X-ray diffraction and scattering [5,8] transmission electron microscopy [9-10], neutron diffraction [11] and Mössbauer

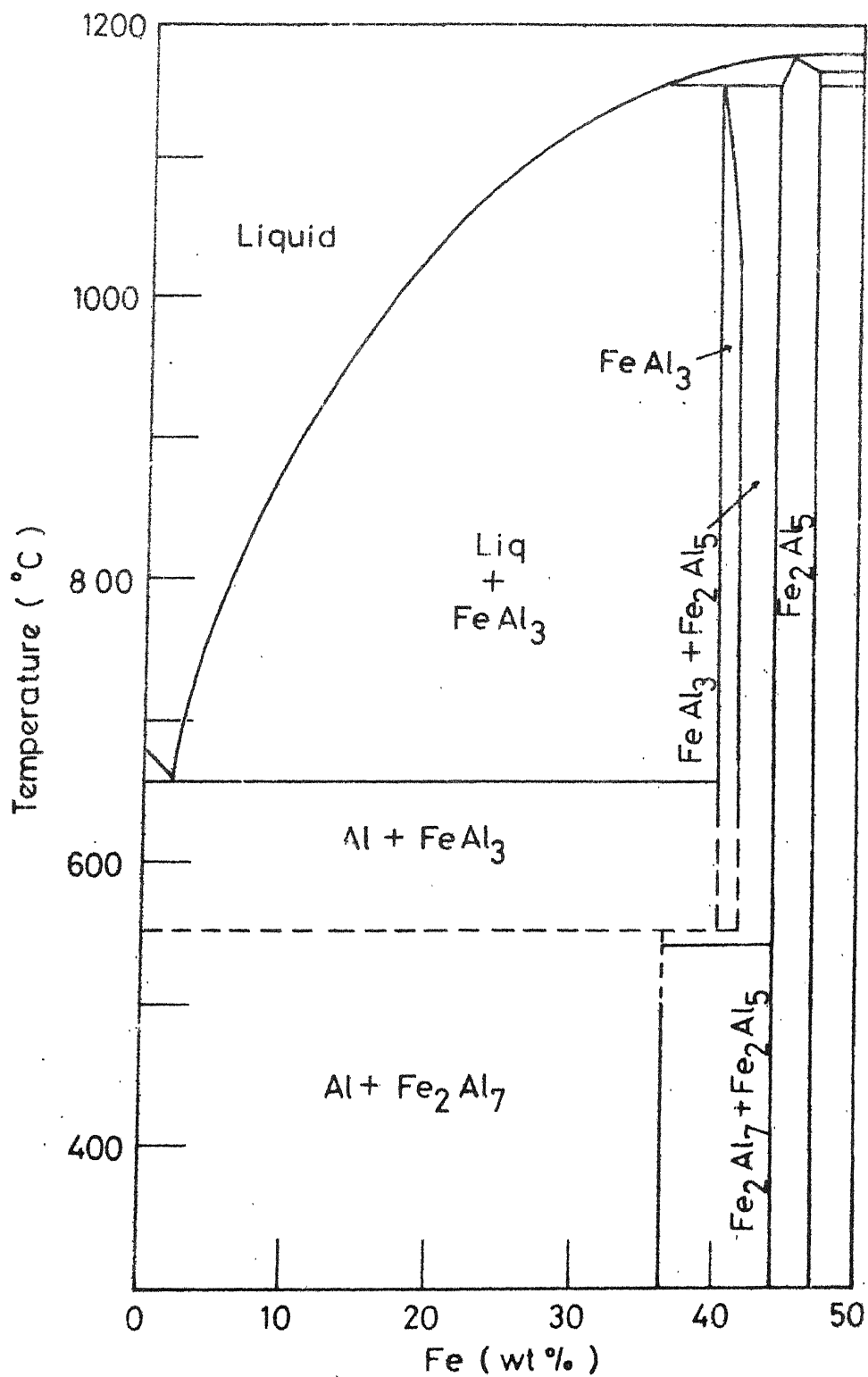


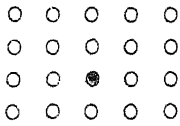
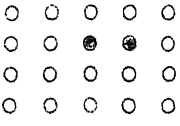
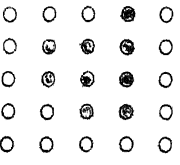
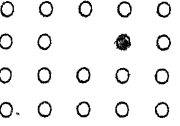
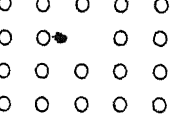
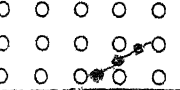
Fig.5.1. Aluminium-rich end of Al-Fe binary phase diagram [7].

spectroscopy have been used to study the structural defects (e.g. interstitial, vacancies and their agglomerates) their immediate neighbourhood on a quasi-microscopic scale and the nature of phases present. Mössbauer spectroscopy has been found to be very useful because it provides valuable information about the local environment of probe (Fe) atom and various phases present in the sample.

A large number of Mössbauer spectroscopic studies of Al-Fe alloys has been reported. These studies can be classified into two groups, one which is related to concentrated (>10.0 wt % Fe) and the other corresponding to dilute (<10.0 wt % Fe) Al-Fe alloys. Mössbauer studies on the concentrated alloys are mainly concerned with order-disorder transformation and the effect of cold working on these alloys [12-14]. A relatively large number of Mössbauer spectroscopic studies have been carried out on dilute Al-Fe alloys [15-20]. Mössbauer parameters of isolated iron atoms (monomer, dimer and clusters), intermetallic compounds ($\text{Al}_{13}\text{Fe}_4$, Al_6Fe , Al_5Fe_2 , AlFe) and structural defect states (vacancy, interstitials, grain boundary etc.) are established [15]. These results, given in Table 5.1 for ready reference, form an excellent basis for the study of various phases of iron in aluminium matrix.

In this chapter we report the results of Mössbauer spectroscopic studies of rapidly solidified Al-Fe alloys.

Table 5.1 Parameters of defect states and phases of iron in aluminium [15].

	Iron state or phase	Crystal structure	Lattice Parameters (Å)	Mössbauer Parameters	
				Isomer shift (w.r.t. α -Fe) mm/sec	Quadrupole splitting mm/sec
Intermetallic compounds	Al_6Fe	Orthorhombic	$a = 6.49$ $b = 7.44$ $c = 8.79$	0.22 ± 0.01	0.26 ± 0.01
	$\text{Al}_{13}\text{Fe}_4$	Monoclinic	$a = 15.49$ $b = 8.08$ $c = 12.48$	0.20	0.40
	Al_5Fe_2	Orthorhombic	$a = 7.67$ $b = 6.40$ $c = 4.20$	0.23 ± 0.01	0.46
Isolated iron states	Monomer		FCC $a = 4.05$	0.42 ± 0.002	
	Dimer			0.11 ± 0.02	0.37 ± 0.02
	Cluster			0.15 ± 0.01	0.32 ± 0.01
Structural defect states	Vacancy			$0.25 \pm 0.01^*$	
	Interstitial			$0.15 \pm 0.01^{**}$	0.17
	Grain- boundary			0.03 ± 0.01	0.32 ± 0.01

* at LNT (78 K), ** at Liquid He Temperature (4.2 K).

The samples were subjected to various heat-treatments and transformation of various phases was studied using Mössbauer spectroscopy.

5.2 EXPERIMENTAL

5.2.1 Sample Preparation

Two sets of samples, one with 5.8 wt % Fe and 0.85 % misch metal and other with 9.94 wt % Fe and 1.25 wt % misch metal were prepared by melt spinning technique. The misch metal composition is 51.7 % Ce, 20-25 % La, 10-15 % Nd, 4-6 % Pr and 0.1 % Fe. The samples have been supplied through the kind courtesy of Dr. J.A. Sekhar of Defence Metallurgical Research Laboratory, Hyderabad.

5.2.2 Mössbauer Measurements

The Mössbauer spectra of as-received samples were recorded at room temperature. The samples were annealed using two different schemes..

- (1) In order to study the effect of temperature on growth-decay of various phases, the samples were annealed at temperatures of 200, 300, 400, 450, 500, 550 and 600 °C for one hour each. Fresh samples were used for each temperature.

- (2) To study effect of annealing time the samples were annealed at 550 °C for 0.5, 1, 2, 5, 20 and 100 hours. Fresh samples were used **each time**.

For the above heat-treatments, furnace temperature was controlled within ± 5 °C of set value. The samples were cooled slowly to room temperature. ^{57}Fe Mössbauer spectra were recorded at room temperature using constant acceleration spectrometer described in Chapter 2.

To study the variation of the Mössbauer parameters of equilibrium phase $\text{Al}_{13}\text{Fe}_4$ and ~~monomer~~ as a function of temperature, the Mössbauer spectra were recorded in-situ at RT, 100, 200, 300, 400, 500, 550 and 600 °C by mounting the sample in a furnace. The sample temperature was controlled with ± 1 °C. A single sample of each concentration was used to record all these spectra. The variation of sample temperature with time is shown schematically in Fig. 5.2. The Mössbauer spectra were recorded in the constant temperature regions marked 1-8 of the Fig. 5.2.

5.3 RESULTS AND DISCUSSION

5.3.1 Mössbauer studies on isochronally annealed samples

As pointed out earlier Mössbauer spectroscopic studies on isochronally annealed Al-Fe alloys (5.8 and 9.94 wt % Fe) heat-treated in the temperature range 20 to 600 °C for an

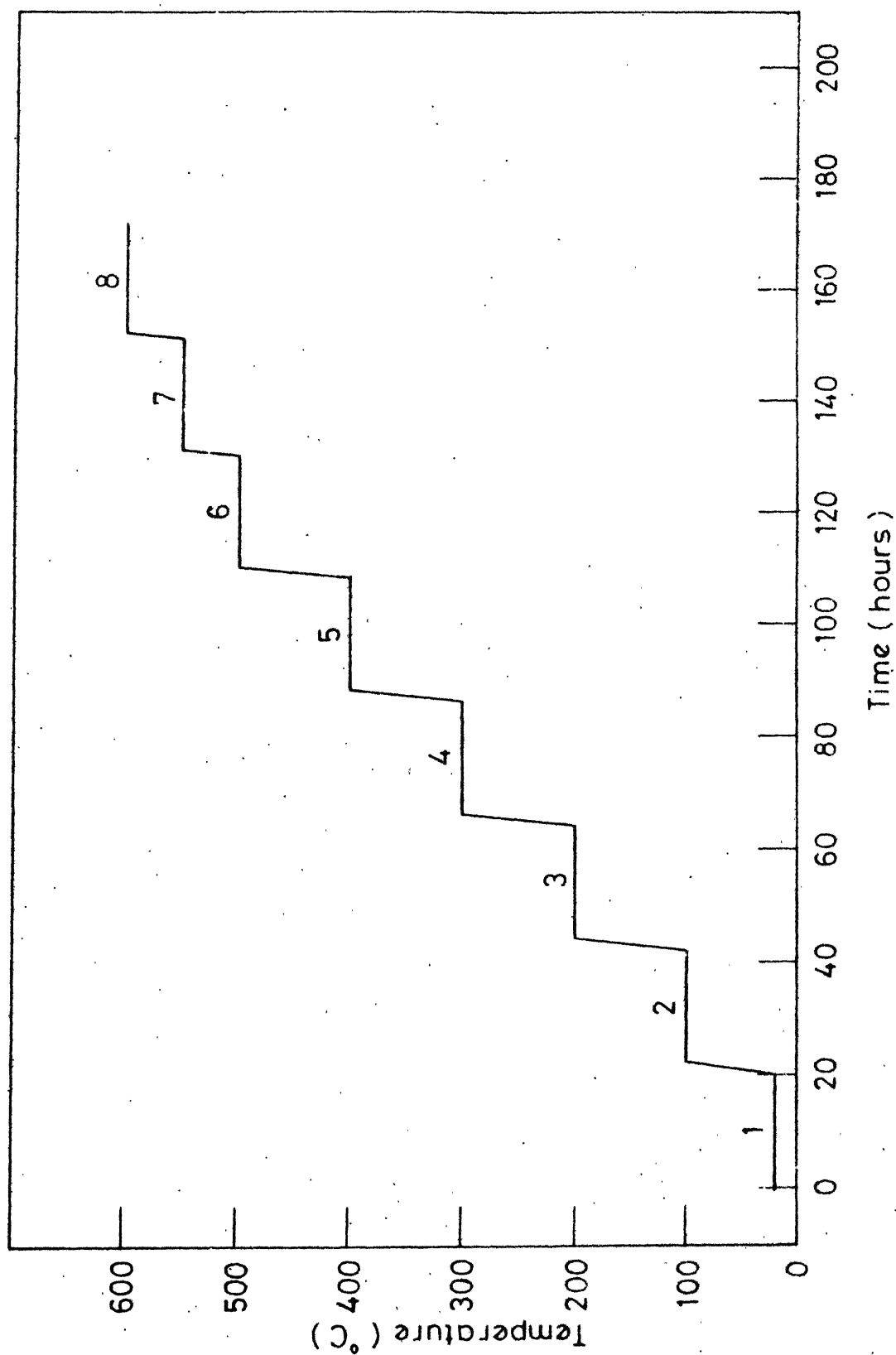


Fig.5.2 Variation of sample temperature with time during the in-situ Mössbauer measurements. Mössbauer spectra were recorded in constant temperature regions marked [1-8].

annealing time of 1 hour were carried out at room temperature. The results of these studies are presented in this section.

(a) Al-Fe alloy with 5.8 wt % Fe

The room temperature Mössbauer spectra of the samples in the as-received condition and after annealing at temperature of 200, 300, 400, 500, 550 and 600 °C are shown in Fig. 5.3. The spectra were analysed to estimate the amount of various phases using the computer program described in Chapter 2. The peak positions for various phases were taken from Table 5.1 and were kept fixed during the fitting. The peak width for various phases were constrained to be same. Thus width and intensities of peaks corresponding to various phases were the only adjustable parameters. Attempts have been made to fit the Mössbauer spectra of the as-received sample to a combination of a number (between 2-6) of phases using the parameters listed in Table 5.1. The best fit was obtained for a combination of the metastable phase Al_5Fe_2 , the equilibrium phase $\text{Al}_{13}\text{Fe}_4$ and isolated iron states (monomer and dimers). Using the same procedure, we tried to fit the Mössbauer spectra of samples heat-treated at various temperatures in terms of same phases as those found in as-received sample. In some cases, complications (i.e. computer program not converging and giving negative intensity for some phase(s)) arose and in such cases those particular phase(s) were excluded and other possibilities were tried. The results of this analysis

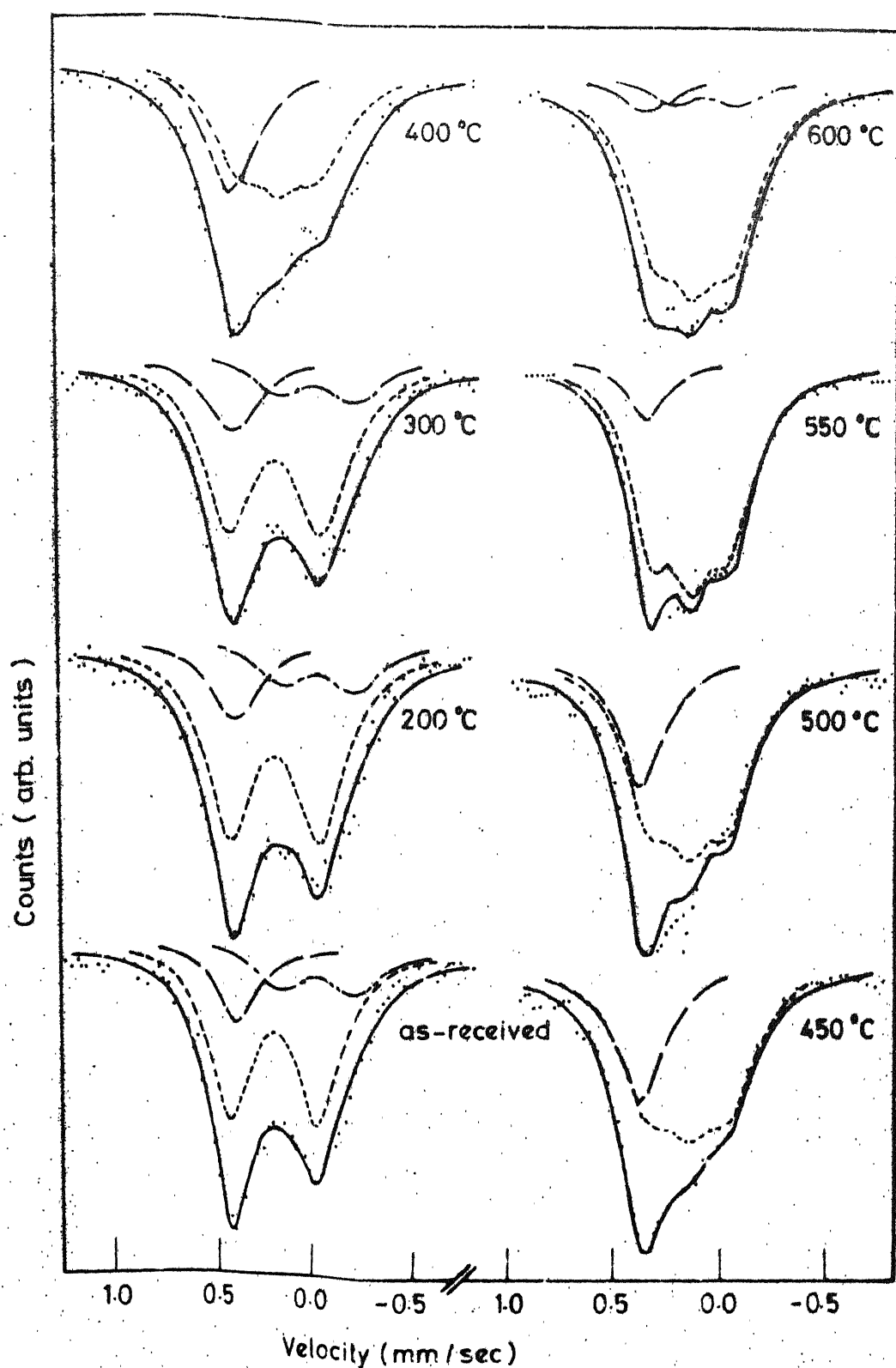


Fig.5.3: Mössbauer spectra of as-received Al-Fe (58 wt % Fe) sample and of samples annealed at various temperatures for one hour

Table 5.2(a) Observed amount of various phases present in Al-Fe (5.8 wt % Fe) as-received sample and in samples heat-treated at various temperature for 1 hour each. These results are based on our Mössbauer measurements.

Annealing Temperature °C	Peak width mm/sec	Amount of various phases present			
		Al_5Fe_2	$\text{Al}_{13}\text{Fe}_4$	Monomer	Dimer
As-received	$0.29 \pm .01$	61.7	8.1	14.4	15.8
200	$0.32 \pm .01$	66.9	3.6	14.6	14.9
300	$0.33 \pm .01$	67.3	2.4	15.7	14.6
400	$0.32 \pm .01$	9.0	48.0	28.8	14.2
450	$0.30 \pm .01$		71.1	29.9	
500	$0.27 \pm .02$		73.6	26.4	
550	$0.26 \pm .01$		88.1	11.5	
600	$0.30 \pm .01$		82.7	7.4	

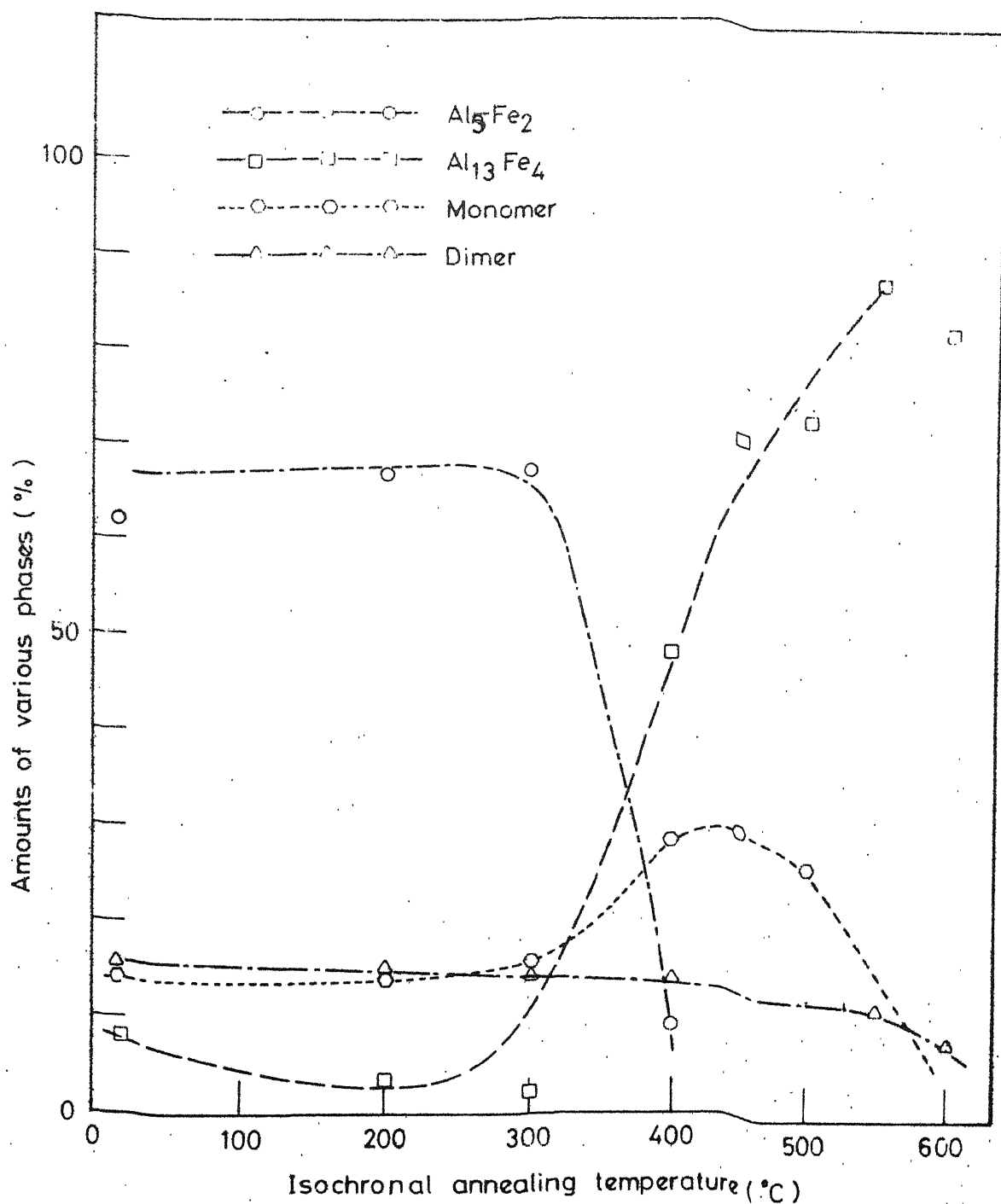


Fig.5.4 Variation of amounts of various phases observed in Al-Fe (5.8 wt % Fe) samples as a function of isochronal annealing temperature.

are given in Table 5.2. In Fig. 5.3 the component spectra due to various phases are shown along with the composite fitted spectra.

If the recoil-free fraction is assumed to be same for iron atoms in various phases, then the peak-area due to various phases would give the fraction of iron atoms present in the respective phases. The area under the resonance due to various phases is given in Table 5.2 and is also plotted in Fig. 5.4, to facilitate the discussion. The metastable phases Al_5Fe_2 remains almost constant in samples heat-treated at 200 and 300 °C. The amount of Al_5Fe_2 phase decreases rapidly above 300 °C and vanishes completely in sample heat-treated at 450 °C. The equilibrium phase $\text{Al}_{13}\text{Fe}_4$ and monomer are present in samples heat-treated at 550 °C. The amount of equilibrium phase is found to increase continuously in samples heat-treated at higher temperatures, while the total amount of isolated iron atom state (monomer and dimer) decreases with higher heat-treatment (see Table 5.2).

(b) Al-Fe alloy with 9.94 wt % Fe

The Mössbauer spectra of the as-received sample and samples heat-treated at various temperatures are shown in Fig. 5.5. The analysis of these spectra is similar to that of 5.8 % Fe samples (for details see Section (a)) and the results obtained are given in Table 5.3 and plotted in Fig. 5.6.

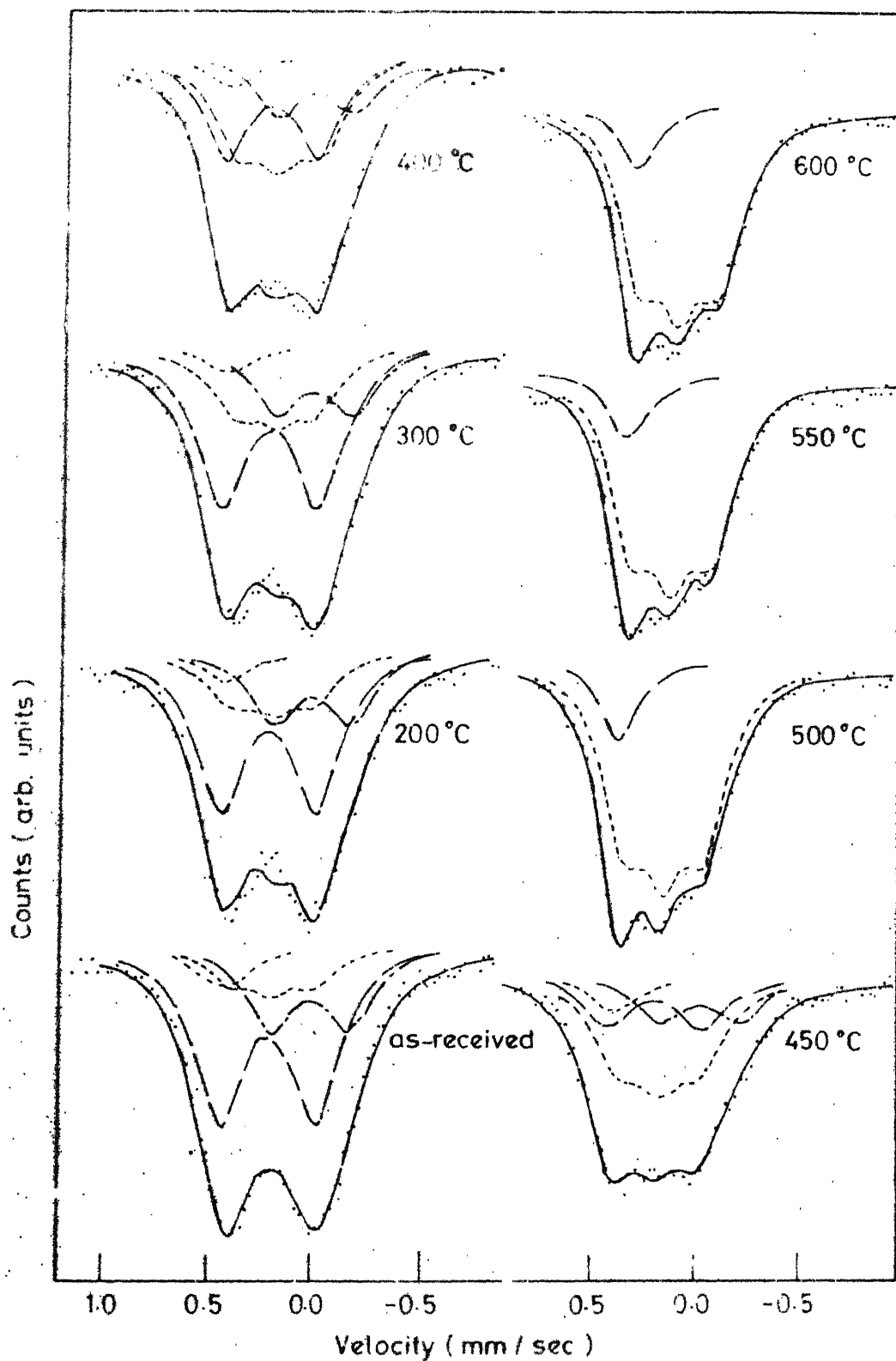


Fig.55 Same as Fig.53 but for Al-Fe (9.94 wt % Fe) samples.

Table 5.3 Same as Table 5.2 but for Al-Fe (9.94 wt % Fe) samples.

Annealing temperature °C	Peak ⁺ width mm/sec	Amount of various phases			
		Al ₅ Fe ₂	Al ₁₃ Fe ₄	Monomer	Dimer Cluster
As-received	0.29	53.6	14.6	6.8	24.8
	0.29*	49.9*	-	9.0*	17.8*
200	0.28	52.4	20.4	4.7	22.5
	0.29*	48.0*	-	8.0*	21.1*
300	0.30	50.1	25.1	4.0	24.8
	0.30*	46.1*	-	7.8*	19.1*
400	0.28	40.2	44.7	6.4	8.7
450	0.29	23.0	50.7	8.2	18.1
500	0.25		80.9	14.1	5.0
550	0.25		86.1	13.9	
600			86.9	13.1	

Second set of values marked * were obtained from a fitting which included cluster states (see Fig. 5.).

⁺Errors in peak width values are less than 0.01 mm/sec.

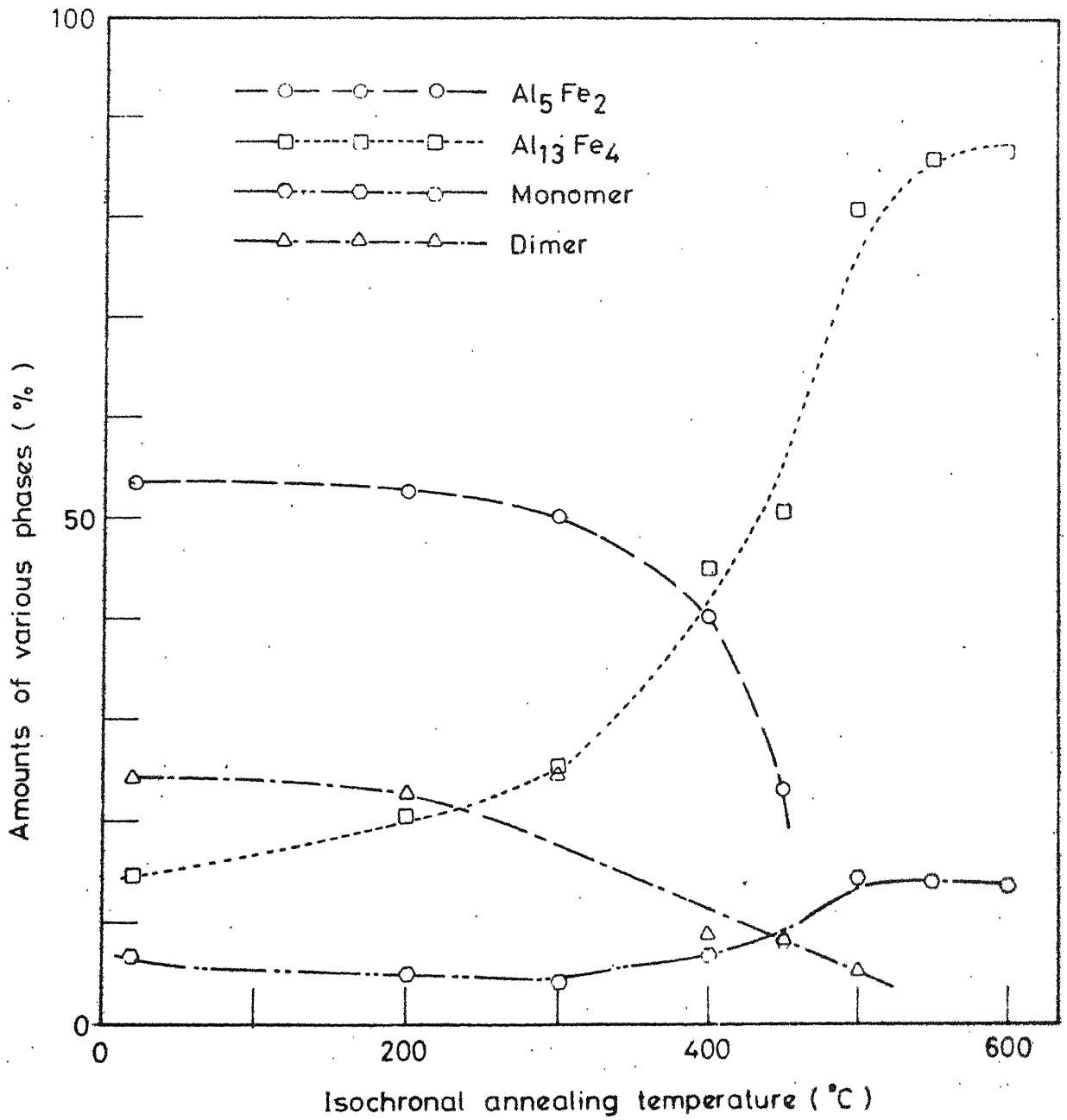


Fig.5.6 same as Fig.5.4 but for Al-Fe (9.94 wt % Fe) samples.

In the as-received sample we find metastable phase Al_5Fe_2 , equilibrium phase $\text{Al}_{13}\text{Fe}_4$ and isolated iron states (monomer, dimer and clusters). The amount of metastable phase decreases in samples heat-treated at higher temperature. The decrease is slow upto 300°C and rapid afterwards. The equilibrium phase $\text{Al}_{13}\text{Fe}_4$ is found to increase with heat-treatment at higher temperature. This behaviour is similar to that observed in the samples containing 5.8 wt % Fe.

In the Al-Fe alloy containing 5.8 and 9.94 wt % of Fe one expects iron clusters to be present. However in the case of 5.8 wt % Fe sample we obtained a good quality of fit without involving the cluster states. This observation indicates that clusters may not be present in these samples (5.8 wt % Fe).

In the case of 9.94 wt % Fe sample, one expects reasonable amount of cluster states to be present. We have, therefore, tried to include the cluster states while fitting the observed Mössbauer spectra. The results obtained with such fitting are shown in Fig. 5.7 and in Table 5.3. The peak position for $\text{Al}_{13}\text{Fe}_4$ and iron cluster states are very close to each other. Hence the inclusion of the cluster states in our fitting affects of the concentration of $\text{Al}_{13}\text{Fe}_4$ considerably. We could not fit our spectra to both $\text{Al}_{13}\text{Fe}_4$ and cluster states satisfactorily because such attempts resulted in negative intensity for $\text{Al}_{13}\text{Fe}_4$. We however feel that both $\text{Al}_{13}\text{Fe}_4$ and cluster states are present in the sample having 9.94 wt % Fe.

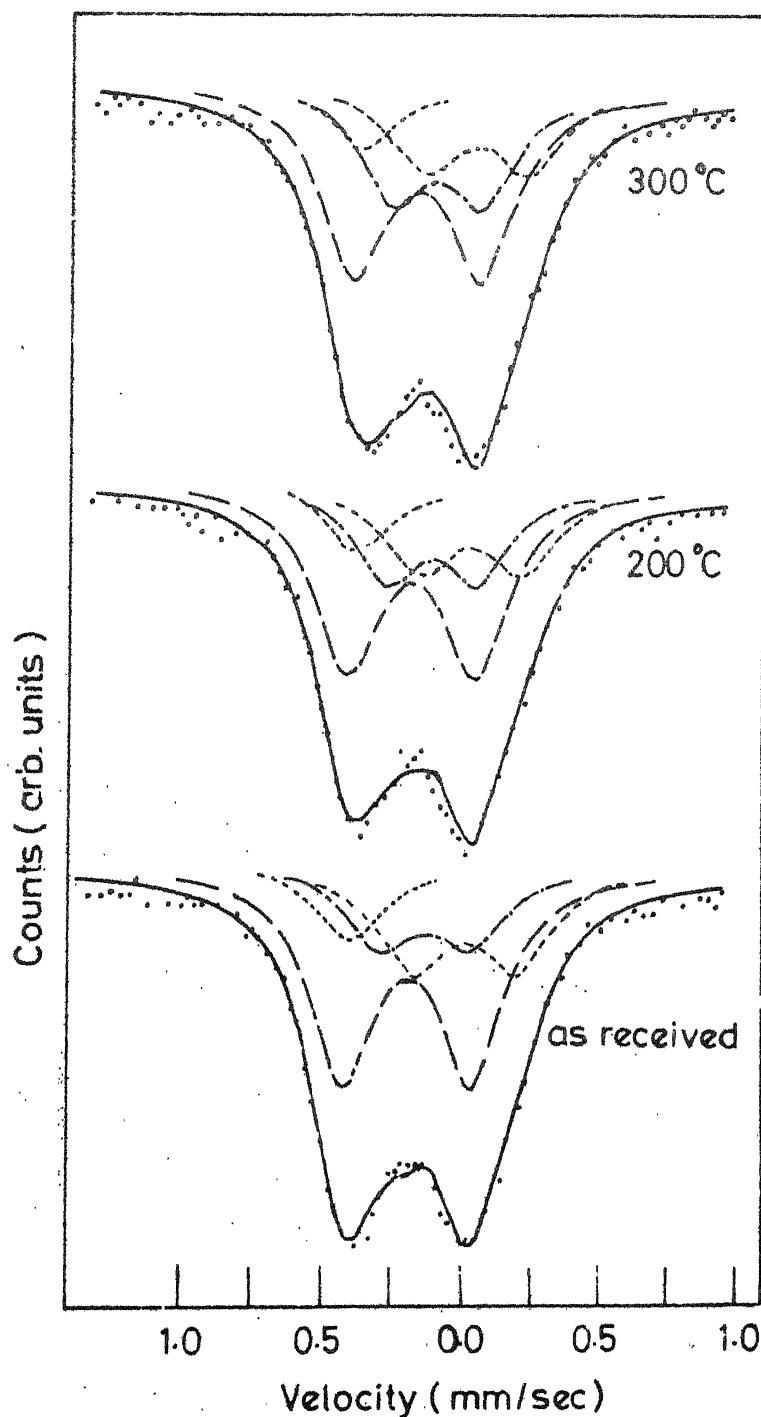


Fig.5.7 Mössbauer spectra of Al-Fe (9.94 wt % Fe) as-received sample and the samples annealed at various temperatures for one hour. The spectra were fitted for presence of various phases including cluster states.

5.3.2 Mössbauer studies of isothermally treated samples

Isothermal annealing of the Al-Fe alloy samples has been carried out at 550 °C for lengths of time varying from 0.5 to 100 hours. The results of Mössbauer studies of these samples are presented in this section.

The Mössbauer spectra (recorded at room temperature) of samples heat-treated at 550 °C for 0.5, 1, 2, 5, 20 and 100 hours are shown in Fig. 5.8 (a) and (b) for samples with 5.8 and 9.94 wt % Fe respectively. From our isochronal annealing studies at 550 °C of these samples we know that $\text{Al}_{13}\text{Fe}_4$ and monomer are the two phases present. Therefore we have fitted all the spectra to a combination of $\text{Al}_{13}\text{Fe}_4$ and monomer. The good quality of fit (see Fig. 5. (a) and (b)) confirms that these are the two phases present in large amount. The peak-area values for the two phases are given in Table 5.4 (a) and (b) for samples with 5.8 and 9.94 wt % Fe respectively. The intensity values do not show any systematic trend and remain constant (within $\pm 5\%$). In view of these observations we are not in a position to offer a definite comment about the effect of annealing time on phase transformation monomer $\text{Al}_{13}\text{Fe}_4$.

5.3.3 In-situ Measurements

(a) Al-5.8 wt % Fe alloy

Mössbauer spectra of Al-Fe (5.8 wt % Fe) sample

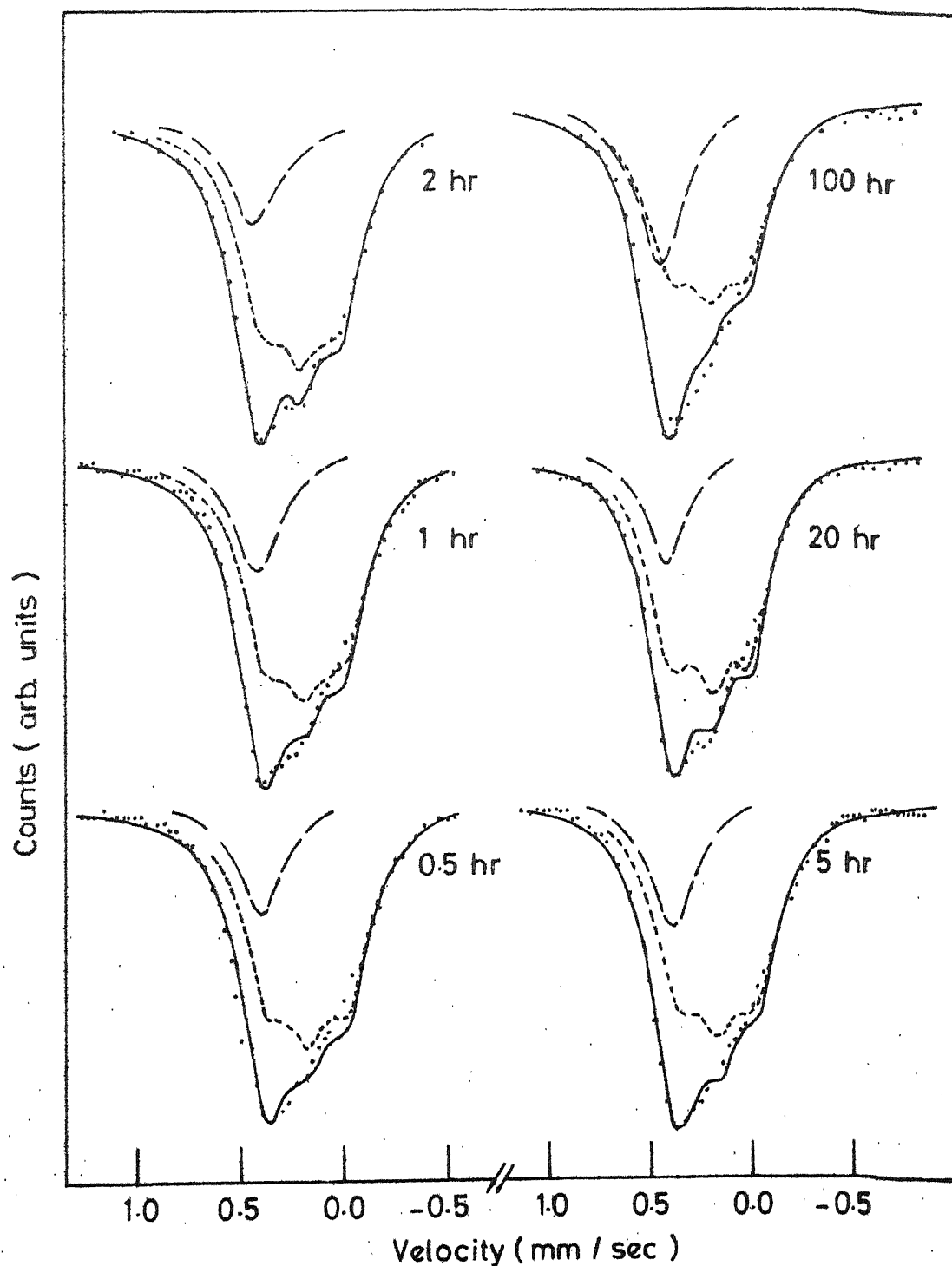


Fig.5.8(a) Room temperature Mössbauer spectra of Al-Fe (5.8 wt % Fe) samples annealed at 550 °C for various times.

Table 5.4 (a) Observed amounts of various phases in Al-Fe (5.8 wt % Fe) samples annealed at 550 °C for various lengths of time. These results are based on our Mössbauer measurements.

Annealing time hours	Peak width mm/sec	Amount of various phases Present	
		$\text{Al}_{13}\text{Fe}_4$ %	Monomer %
0.5	$0.28 \pm .01$	80.4	19.6
1.0	$0.28 \pm .01$	79.1	20.9
2.0	$0.28 \pm .01$	81.4	18.6
5.0	$0.29 \pm .01$	76.6	23.4
20.0	$0.20 \pm .01$	80.7	19.3
100.0	$0.28 \pm .01$	69.0	31.0

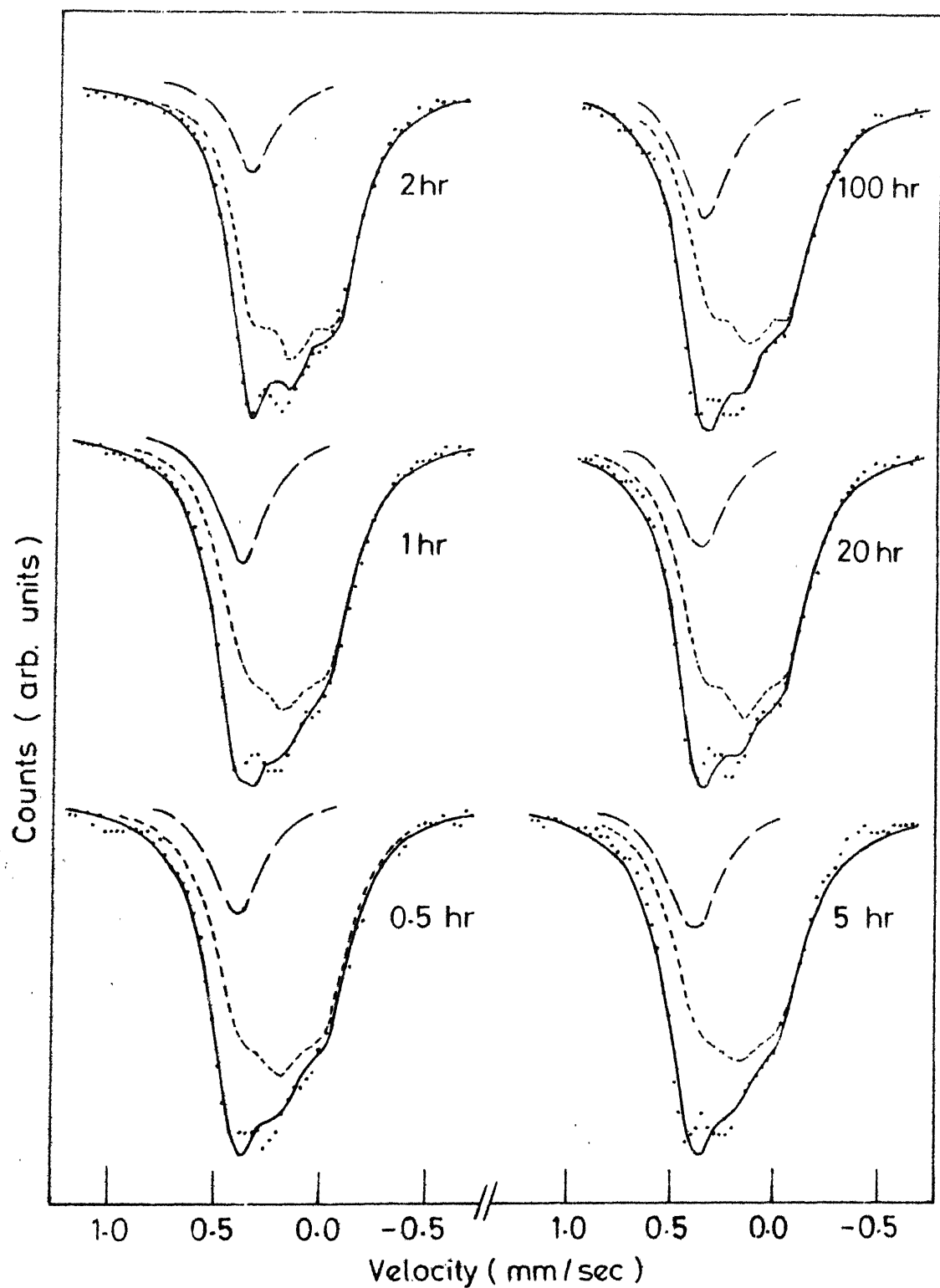


Fig.5.8 (b) Mössbauer spectra of Al-Fe sample (with 9.94 wt% Fe) annealed (heat-treated) at 550°C for various times.

Table 5.4 (b) Same as Table 5.4 (a) but for Al-Fe (9.94 wt % Fe) samples.

Annealing time hours	Peak width mm/sec	Amount of various phases	
		$\text{Al}_{13}\text{Fe}_4$ %	Monomer %
0.5	0.31	80.2	19.8
1.0	0.30	78.8	21.2
2.0	0.27	85.0	15.0
5.0	0.34	77.2	22.8
20.0	0.30	81.4	18.6
100.0	0.30	77.9	22.1

recorded at 20 °C (RT), 100, 200, 300, 400, 500, 550 and 600 °C are shown in Fig. 5.9 (a). Mössbauer spectrum of as-received sample at 20 °C (RT) is also shown in Fig. 5.3.

Analysis of the Mössbauer spectra recorded at 100, 200 and 300 °C indicates the presence of the same phases as those observed in the as-received sample at RT. The spectra show a shift towards the lower velocity side due to well known temperature shift [21]. At 400 °C $\text{Al}_{13}\text{Fe}_4$ and monomer phases are present and at temperature 500 °C only equilibrium phase $\text{Al}_{13}\text{Fe}_4$ is present. We have fitted these spectra in terms of these phases, the results of these fits are given in Table 5.5(a). The quadrupole splitting and centre point of spectra were allowed to vary in these fits.

The quadrupole splitting ΔE for $\text{Al}_{13}\text{Fe}_4$ phase decreases from 0.40 mm/sec at room temperature (see Table 5.5) to 0.26 mm/sec at 600 °C. This decrease may be due to temperature effect on EFG given by the relation [22]

$$\Delta E(T) = \Delta E(0) (1 - B T^{3/2}) .$$

(b) Al-9.94 wt % Fe alloy

Mössbauer spectra of Al-Fe (9.94 wt % Fe) recorded at 20 (RT), 100, 200, 300, 400, 500, 550 and 600 °C are shown in Fig. 5.9 (b). The spectrum recorded at 20 °C is also shown in Fig. 5.5. The analysis of these spectra indicates that Al_5Fe_2 , $\text{Al}_{13}\text{Fe}_4$, monomer, dimer and

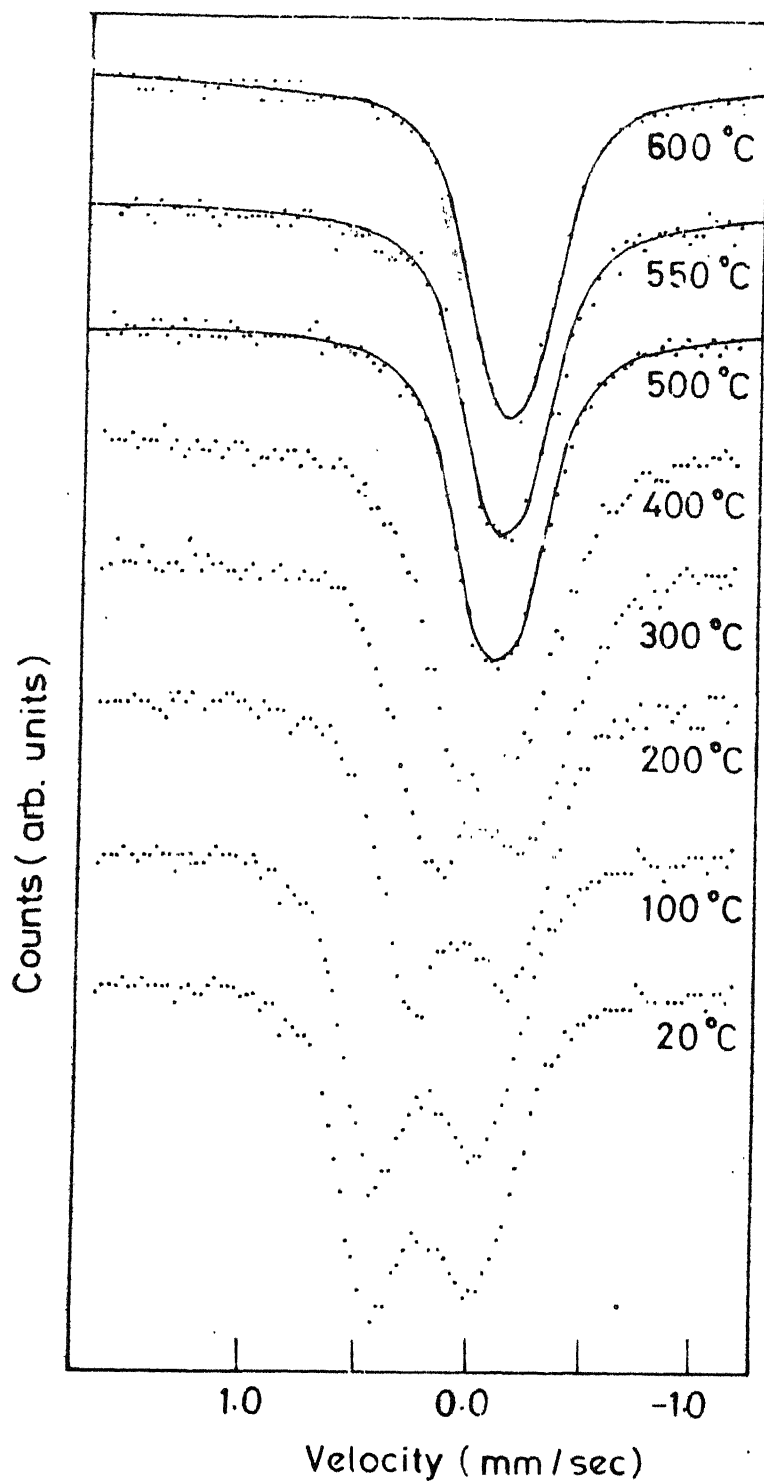


Fig.5.9(a) Mössbauer spectra of Al-Fe (5.8 wt% Fe) samples recorded at various temperatures. The solid lines represent the fits for the $\text{Al}_{13}\text{Fe}_4$ spectra.

Table 5.5 (a) Different iron phases present at various temperatures in Al-Fe (5.8 wt % Fe) sample and Mössbauer parameters of $\text{Al}_{13}\text{Fe}_4$ obtained from the analysis of Mössbauer spectra measured in-situ.

Temperature °C	Phases present	Mössbauer parameters of $\text{Al}_{13}\text{Fe}_4$ phase		
		Isomer shift (w.r.t. $\alpha\text{-Fe}$) mm/sec	Quadrupole splitting mm/sec	Peak-width mm/sec
20	Al_5Fe_2 , $\text{Al}_{13}\text{Fe}_4$, monomer and dimers.	0.20	0.40	$0.26 \pm .01$
100	-do-	-	-	-
200	-do-	-	-	-
300	-do-	-	-	-
400	$\text{Al}_{13}\text{Fe}_4$, monomer	$-.08 \pm .01$ $0.06 \pm .01^*$	$0.37 \pm .01$	$0.32 \pm .01$
500	$\text{Al}_{13}\text{Fe}_4$	$-0.08 \pm .01$	$0.28 \pm .01$	$0.30 \pm .01$
550	$\text{Al}_{13}\text{Fe}_4$	$-.11 \pm .01$	$0.27 \pm .01$	$0.30 \pm .01$
600	$\text{Al}_{13}\text{Fe}_4$	$-.12 \pm .01$	$0.26 \pm .01$	$0.29 \pm .01$

N.B. As explained in the text quantitative analysis of spectra recorded at 100, 200 and 300 °C could not be performed satisfactorily.

*IS value is for monomer phase.

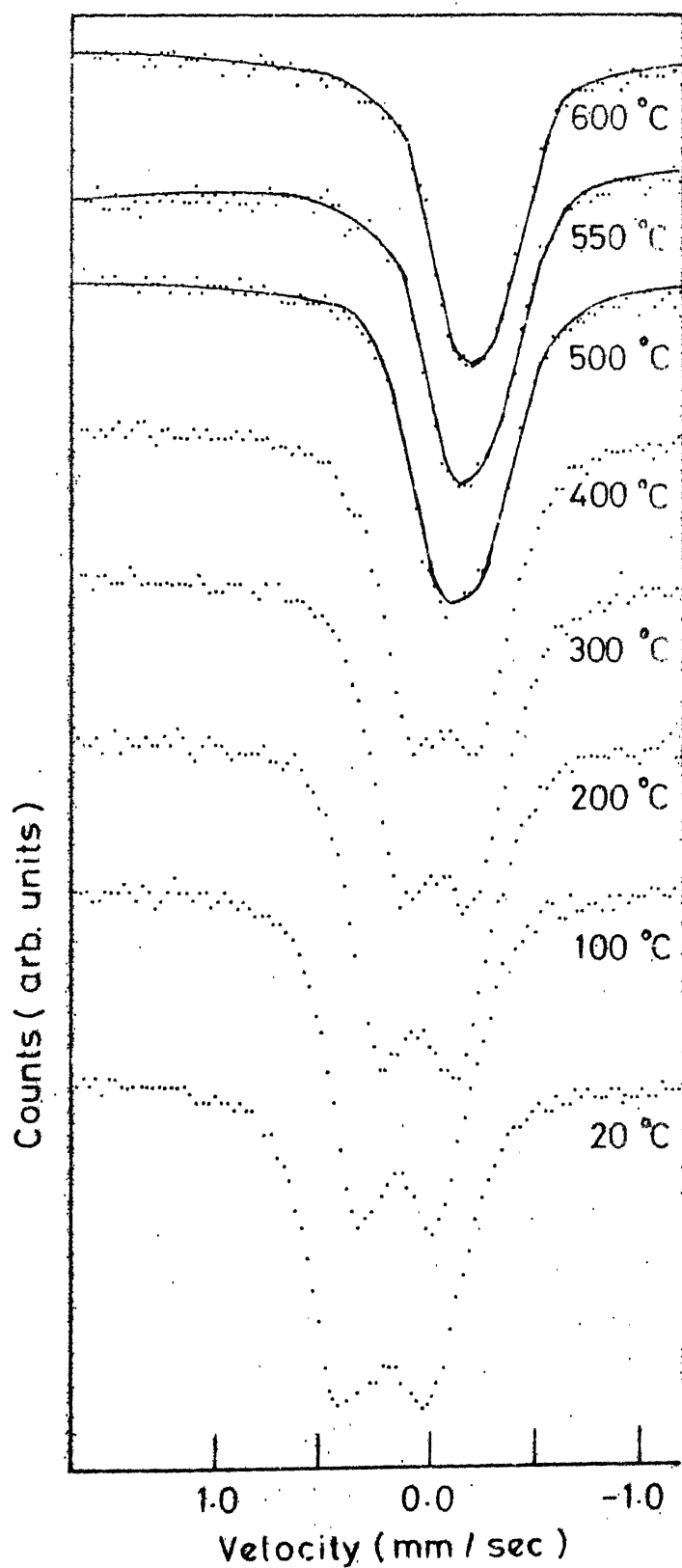


Fig.5.9(b) same as Fig.5.9(a) but for Al-Fe (9.94 wt % Fe) sample

Table 5.5 (b) Same as Table 5.5 (a) but for Al-Fe (9.94 wt % Fe) samples.

Temperature °C	Phases present	Mössbauer parameters of $\text{Al}_{13}\text{Fe}_4$ phase		
		Isomer shift (w.r.t. $\alpha\text{-Fe}$) mm/sec	Quadrupole splitting mm/sec	Peak-width mm/sec
20	Al_5Fe_2 , $\text{Al}_{13}\text{Fe}_4$, monomer dimers and clusters	0.20	0.40	$0.28 \pm .01$
100	--do--	--	--	--
200	--do--	--	--	--
300	--do--	--	--	--
400	--do--	--	--	--
500	$\text{Al}_{13}\text{Fe}_4$ and monomer	$-0.09 \pm .01$ $0.03 \pm .01$	$0.32 \pm .01$	$0.28 \pm .01$
550	$\text{Al}_{13}\text{Fe}_4$	$-0.12 \pm .01$	$0.30 \pm .01$	$0.23 \pm .01$
600	$\text{Al}_{13}\text{Fe}_4$	$-0.15 \pm .01$	$0.27 \pm .01$	$0.27 \pm .01$

N.B. As explained in the text, quantitative analysis of spectra recorded at 100, 200, 300 and 400 °C samples could not be performed satisfactorily.

*IS value is for monomer phase.

clusters are present upto 400 °C. At 500 °C $\text{Al}_{13}\text{Fe}_4$ and monomer phases alone are present and above 500 °C only $\text{Al}_{13}\text{Fe}_4$ phase is present. The results obtained from the analysis of these spectra is given in Table 5.5 (b). The quadrupole splitting for $\text{Al}_{13}\text{Fe}_4$ decreases with increase in temperature as observed for 5.8 wt % Fe alloys.

The spectra recorded at 100, 200 and 300 °C could not be analysed satisfactorily because many (3-4) phases are expected to be present and temperature variation of the Mössbauer parameters for these phases is not known and this situation brings in too many unknown variables making the fitting procedure very complicated. For a complete analysis, temperature variation of Mössbauer parameters of various phases should be known. To achieve this, single phase standard samples should be prepared and in-situ temperature variation of Mössbauer parameters should be observed. We could not carry out such studies but they are planned as a part of further work on Al-Fe alloys in our laboratory. Until then we prefer to leave our results in the form shown in Fig. 5.9 (a), (b) and Table 5.5 (a), (b).

Transmission electron microscopic studies on these samples have been carried out by Ramachandran [23]. The as-received sample of the 9.94 wt % Fe alloy shows a cellular structure (Fig. 5.10(a)) with typical cell size of 0.2 - 0.4 μm . Occasionally large insoluble particles ($\geq 1 \mu\text{m}$ in size) are

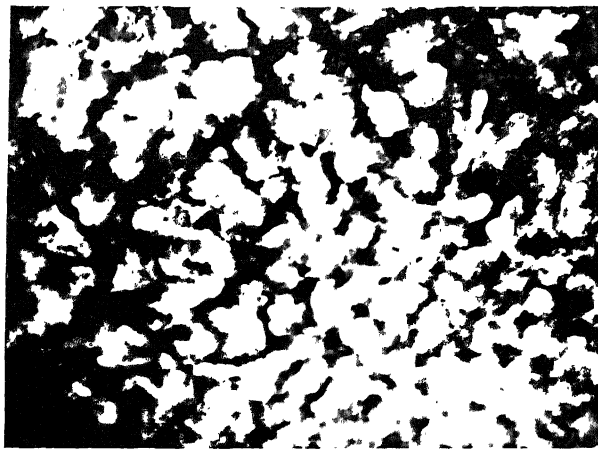


Fig. 5.10 (a) A typical transmission electron micrograph of as-received Al-Fe (9.94 wt % Fe) alloy.



Fig. 5.10 (b) A typical electron diffraction pattern of as-received Al-Fe (9.94 wt % Fe) alloy.



Fig. 5.10 (c) A single crystal spot pattern of an insoluble observed in as-received Al-Fe (9.94 wt % Fe) alloy.

found. A typical electron diffraction pattern of the as-received (9.94 wt % Fe) sample (shown in Fig. 5.10 (b) shows the presence of two phase, the aluminium-rich solid solution (FCC, $a = 4.05 \text{ \AA}$) (the spots in the diffraction pattern correspond to this phase with electron beam direction of $[1\ 1\ 2]$) and metastable Al_6Fe (orthorhombic, $a = 6.492 \text{ \AA}$, $b = 7.437 \text{ \AA}$ and $c = 8.788 \text{ \AA}$) (the ring pattern corresponds to this phase). A single crystal spot pattern obtained from an insoluble particle is shown in Fig. 5.10(c). It correspond to the orthorhombic phase Al_6Fe with electron beam direction of $[0\ 0\ 1]$.

Occasionally particles of the equilibrium phase $\text{Al}_{13}\text{Fe}_4$ (monoclinic, $a = 15.489 \text{ \AA}$, $b = 8.083 \text{ \AA}$, $c = 12.476$ and $\beta = 107^\circ, 43'$) are found. In case of samples annealed isochronally or isothermally at temperatures $\geq 500^\circ \text{C}$ only $\text{Al}_{13}\text{Fe}_4$ and solid solution are observed.

A comparison of results obtained with Mössbauer spectroscopy reveals a good agreement between the two studies in the case of annealed samples. However, in case of as-received sample Mössbauer spectroscopic show the presence of metastable phase Al_5Fe_2 while transmission electron microscopy indicate the presence of metastable phase Al_6Fe . Except this disagreement about the metastable phase, the results obtained by the two method are in reasonably good agreement.

5.4 SUMMARY

Mössbauer spectroscopic studies have been carried out on Al-Fe alloys (5.8 and 9.94 wt % Fe). The samples were heat-treated isothermally at 550 °C for 0.5, 1, 2, 5, 20 and 100 °C and isochronically for 1 hour at 200, 300, 400, 500, 550 and 600 °C. The Mössbauer spectra of heat-treated samples were recorded at room temperature. In-situ measurements were also carried out in the temperature range 20 °C to 600 °C. The results of our Mössbauer studies can be summarized as follows.

- (1) In the as-received sample metastable phase Al_5Fe_2 , equilibrium phase $\text{Al}_{13}\text{Fe}_4$ and isolated iron states (monomer, dimer and cluster) are present.
- (2) On heat-treatment at various temperatures for 1 hr the metastable phase and isolated iron atom states are found to decrease while equilibrium phase $\text{Al}_{13}\text{Fe}_4$ increase with heat-treatment at higher temperature.
- (3) Samples annealed at 550 °C for various times have only $\text{Al}_{13}\text{Fe}_4$ and monomers. The relative amounts of these phase remains unchanged (within $\pm 5\%$) with time of annealing.
- (4) In-situ measured Mössbauer spectra of the two alloy samples show the presence of Al_5Fe_2 , $\text{Al}_{13}\text{Fe}_4$, monomer and dimer phases upto 400 °C in 5.8 wt % Fe and upto 450 °C in 9.94 wt % Fe alloy. Above these

temperatures only $\text{Al}_{13}\text{Fe}_4$ phase is found to be present. The Mössbauer parameters for the $\text{Al}_{13}\text{Fe}_4$ phase at higher temperature are calculated from these spectra. The quadrupole splitting decreases due to the well known temperature effect.

Difficulties encountered in analysis of the Mössbauer data are discussed and scope of future work is given. The results are compared with those of electron microscopy.

REFERENCES

1. I.J. Polmear, Light Metals, Metallurgy of Light Metals, p. 15, Edward Arnold, London (1981)
2. H. Jones, J. Mater. Sci. 19, 1043 (1984)
3. A. Tonejc and A. Bonefacic, J. Appl. Phys. 40, 419 (1969)
4. I.R. Hughes and H. Jones, J. Mater. Sci. 11, 1781 (1976)
5. H. Jones, Mater. Sci. Eng. 5, 1 (1969)
6. M.R. Burden and H. Jones, Fizika 2, (Suppl. 2) paper 7 (1970)
7. M. Hansen, Constitution of binary alloys, p. 137 (1958)
8. P.W. Fisher and W.L. Baun, J. Appl. Phys. 38, 229 (1967)
9. H. Westengen, Z. Metallkde 73, 360 (1982)
10. T.R. Ramachandran et al., (to be published)
11. R. Nathans, M.T. Rigott and C.G. Shull, J. Phys. Chem. Solids 6, 38 (1958)
12. H.R. Lesoille and P.M. Gielen, Phys. Stat. Sol. 37, 127 (1970)
13. Kenske Oki, Shin-ichi Towata, Masaharu Taniya and Tetsuo Eguchi, Trans. Japan Institute Metals 22, 771 (1981) and 20, 451 (1979)
14. G.H. Huffman and R.H. Fisher, J. Appl. Phys. 38, 735 (1967)
15. S. Nasu, U. Gonser, R.S. Preston, J. Phys. Cl 41, C1-385 (1980) and reference therein.

16. S. Nasu, U. Gonser, P.H. Shingu and Y. Murakami, J. Phys. F 4, L24 (1974)
17. R.H. Bush, C.A. Stickels, L.W. Hobbs, Scripta Met. 1, 75 (1967)
18. R.S. Preston and R. Gerlach, Phys. Rev. B3, 1519 (1971)
19. A. Vertes et al., Scripta Met. 16, 145 (1982)
20. R.S. Preston, Metal Trans. 3, 1831 (1972)
21. P.K. Tseng and S.L. Ruby, Phys. Rev. 172, 249 (1968)
22. J. Christiansen, P. Heubes, R. Keitel, W. Klinger, W. Loeffler, W. Sandner and W. Witthuhn, Z. Physik B24, 177 (1976)
23. T.R. Ramachandran, Private Communication.